



**HAL**  
open science

# Convection in the primitive mantle in interaction with global magma oceans

Adrien Morison

► **To cite this version:**

Adrien Morison. Convection in the primitive mantle in interaction with global magma oceans. Earth Sciences. Université de Lyon, 2019. English. NNT : 2019LYSEN061 . tel-02482874v1

**HAL Id: tel-02482874**

**<https://theses.hal.science/tel-02482874v1>**

Submitted on 18 Feb 2020 (v1), last revised 28 Feb 2020 (v2)

**HAL** is a multi-disciplinary open access archive for the deposit and dissemination of scientific research documents, whether they are published or not. The documents may come from teaching and research institutions in France or abroad, or from public or private research centers.

L'archive ouverte pluridisciplinaire **HAL**, est destinée au dépôt et à la diffusion de documents scientifiques de niveau recherche, publiés ou non, émanant des établissements d'enseignement et de recherche français ou étrangers, des laboratoires publics ou privés.



Numéro National de Thèse : 2019LYSEN061

**THÈSE de DOCTORAT DE L'UNIVERSITÉ DE LYON**  
opérée par  
**l'École Normale Supérieure de Lyon**

**École Doctorale N° 52**  
**Physique et Astrophysique de Lyon (PHAST)**

**Discipline de doctorat : Sciences de la Terre**  
**Spécialité de doctorat : Géodynamique**

Soutenue publiquement le 15/11/2019, par :

**Adrien MORISON**

---

**Convection dans le manteau  
primitif en interaction avec  
des océans de magma globaux**

---

Devant le jury composé de :

RIBE, Neil	Dir. de recherche	Univ. Paris-Sud	Rapporteur
ČADEK, Ondřej	Professeur	Charles University	Rapporteur
MICHAUT, Chloé	Professeure	ENS de Lyon	Examinatrice
CARDIN, Philippe	Dir. de recherche	Univ. Grenoble Alpes	Examineur
LABROSSE, Stéphane	Professeur	ENS de Lyon	Directeur de thèse



*Quidquid latine dictum sit, altum videtur.*



# Résumé

Un scénario couramment considéré lors de la formation des planètes telluriques est celui des océans de magma. L'énergie d'accrétion ainsi que celle dégagée par la désintégration d'éléments radioactifs de courtes périodes est en effet largement suffisante pour fondre une large portion voire l'entièreté du manteau terrestre, formant dans ce dernier cas un océan de magma global. La dépendance en pression de la température de solidification et le fort gradient du profil isentropique dans le manteau inférieur peut amener à une cristallisation de cet océan de magma global par le milieu. Ceci conduit à une situation où la partie solide du manteau primitif est encadrée par deux océans de magma globaux : un en surface, et un basal.

Cette thèse se focalise sur deux aspects scientifiques d'un tel système. D'une part, les océans de magma ayant une composition similaire à celle du solide, la matière en convection dans le solide n'est pas nécessairement arrêtée à l'interface entre le solide et le liquide mais peut la traverser par fusion/cristallisation si le temps de changement de phase est court devant le temps de construction de topographie du solide au sein du liquide par force visqueuse. Une analyse de stabilité linéaire ainsi que des simulations numériques directes montrent que cette possibilité de changement de phase affecte considérablement la convection dans la partie solide. Le nombre de Rayleigh critique est abaissé, les structures convectives ont une plus grande longueur d'onde, et le flux de chaleur transporté à travers la couche solide peut être de plusieurs ordres de grandeurs plus important qu'avec des conditions aux limites classiques.

Le deuxième aspect étudié durant cette thèse est celui de l'évolution à long terme du manteau primitif. En couplant le modèle de convection dans le solide avec des modèles simples d'évolution des océans de magma, nous avons construit un modèle d'évolution global du manteau primitif suivant l'évolution thermo-compositionnelle des océans de magma globaux et de la partie solide. Une analyse de stabilité linéaire montre que la convection dans la partie solide démarre avant même que l'océan de magma en surface soit entièrement cristallisé. Une simulation numérique directe préliminaire montre que la cristallisation fractionnée de l'océan de magma basal peut conduire à la formation de larges piles thermochimiques en base du manteau solide, similaires aux structures de faibles vitesses sismiques (LLSVP) observées de nos jours.

La présence d'océans de magma globaux peut donc avoir d'importantes répercussions sur l'évolution à long terme de la Terre : d'une part via les structures thermiques et compositionnelles mises en place par la cristallisation fractionnée des océans et la convection dans le solide ; d'autre part, le bilan énergétique global peut être considérablement affecté par le fort flux de chaleur extrait par le manteau solide du fait des conditions de changement de phase.



# Abstract

A common scenario considered during the formation of Earth-like bodies is that of magma oceans. Indeed, the accretion energy as well as the heat produced by the radioactive decay of short-period elements is more than enough to melt entirely the primitive mantle, thereby forming a global magma ocean. The pressure-dependence of the solidification temperature as well as the steep isentropic temperature profile at the base of the mantle could lead to a crystallization of that global magma ocean from the middle. The primitive solid mantle could therefore be bounded by two global magma oceans: one above and one below.

This PhD thesis focuses on two aspects of such a system. First, the solid part of the mantle and the magma oceans being of similar composition, convecting matter in the solid is not necessarily stopped by the solid/liquid interface but could instead go through it by melting/freezing provided that the phase change timescale is short enough compared to the viscous timescale needed to build a solid topography in the liquid oceans. A linear stability analysis and direct numerical simulations show the phase change at the boundary greatly affects convection in the solid part of the mantle. The critical Rayleigh number decreases, convective patterns have a larger wavelength, and the heat flux carried through the solid increases of up to several orders of magnitude compared to cases with classical boundary conditions.

The second aspect explored in this thesis is the long-term evolution of the primitive mantle. Coupling convection in the solid with simple evolution models for the magma oceans allowed us to build a global evolution model of the primitive mantle monitoring the thermo-compositional evolution of the solid mantle and magma oceans. A linear stability analysis shows convection sets in the solid before the surface magma ocean crystallizes entirely. A preliminary direct numerical simulation shows the fractional crystallization of the basal magma ocean may lead to the formation of large thermo-chemical piles at the base of the solid mantle. These piles are similar to the large low-shear velocity provinces (LLSVP) observed today.

The presence of global magma oceans could therefore have important consequences on the long-term evolution of the Earth: first, fractional crystallization of the magma oceans and convection in the solid part affect the resulting thermal and compositional structures; and second, the global heat budget could be tremendously affected by the high heat flux carried out by the solid part owing to the phase change boundary conditions.



# Acknowledgements

The document you are currently reading, be it on paper or screen, synthesizes the scientific work I produced in the last few years. It would not be complete without a nod to the various people that I had the chance to have by my side during this adventure. The order in which those acknowledgements are written is purely arbitrary and does not purposefully represent any order of importance.

To my parents Bernard and Nadine, I thank you for giving me life, an important prerequisite to being able to pursue any form of academic activity. I am grateful to you for raising me and being a constant support throughout my existence. All those years would not have been as colourful without my four sisters. For all your support, shared laughs and inside jokes, I am grateful to you Aurore – cheers to Fred and Éloïse, Gaëlle, Laëtitia and Vanina – tip of the hat to Victor!

A PhD project involves an advisor, and I consider myself extremely lucky that mine was Stéphane. I thank you for offering me to work with you and trusting me with this research project. I am grateful for all the things you taught me about this fine art that is scientific research, but also for the good times and beers we shared during these few years. It has been a real pleasure working with you!

I also want to thank Renaud, Thierry, Fred, Fabien, and Roberto, who collaborated with me in Lyon on this project. Thank you for your insights and contributions to this work, and thank you for always doing so in a cheerful manner.

During this thesis I had the chance to go on several missions. This wouldn't have been possible without Marie-Jeanne, who handled these matters very efficiently and always in good spirits. I also wish to thank Emmanuelle for her professionalism and efficiency regarding the organization of teaching activities in the geology laboratory. Thank you both for your communicative good mood!

I want to thank my lunch companions Stéphane, Fred, Pierre, Patrick, Cyril (and the others that were here less often) for all the deep discussions about the optimal amount of crème brûlée that should reside on a meal tray (the answer is apparently a full ladle).

I conducted most of my thesis in one of the offices allotted to PhD students that is wittily called *Thesarium*. I shared this office with many people during the years that I want to thank for making this office a pleasant and comfortable place. Many thanks Mathieu, Théo, Jean-Alexis, Hélène, Nadège, Anaïs, Julie, Adrien “Riri”, Auguste, Marie, Samuel, Pierre-Jean, Thibaut, and Adrien for bearing with my bad puns and even laughing at them, and for all the good times we spent in and out of the office. Thank you for all the various talks, ranging from insightful scientific discussions to the careful elaboration of a badger-based mass unit. Cheers! I also take this opportunity to thank Nils Olav. Even though he didn't share our office despite being in every way qualified, he reminds us anybody can get things done by winging them.

---

I am also very grateful to the other PhD students and postdoc working in our lab for all the shared laughs, beers, and good times. Thank you Delphine, Quentin, Mélie, Fanny, Arnaud, Damian, Jean, Chloé, Cédric, Sylvain, Pauline, Lucia and Robin! I address special thanks to Briscard “Florian”, Victor, and Rémi for their shared love of beer and dubious jokes (not necessarily in that order).

I thank Alexandre and Nicolas, long-time friends of mine whose presence I always appreciate, for always being ready to share a few beers and have a good laugh!

Another aspect of my thesis is that it was a joint project with the Geophysical Fluid Dynamics group at ETH Zürich. I had the great pleasure to work in collaboration with Daniela, PhD student of the GFD group on the same project. I thank you of course for your valuable and rigorous contributions on the project, but also for your upbeat attitude and always welcoming me well when I visited your group. It has been wonderful and I look forward to working with you again in the future!

I also thank members of the GFD group with whom I collaborated closely. Paul, for your expertise in numerical methods, letting us use StagYY, and including me in your karaoké nights; Maxim for your valuable insights on the geochemical and petrological implications of the project as well as your kindness; Antoine for being rigorous and your deadpan humour; and Patrick for your precious help with managing developments of StagYY.

My stays in Zürich would not have been as enjoyable without the friends I had there. I am very thankful to Federico, Antonio, CJ, Anna, Kar Wai, and Jessica for welcoming me and all the good times we had over there!

I am very thankful to the members of the jury Chloé Michaut, Neil Ribe, Ondřej Čadek, Philippe Cardin and Stéphane Labrosse for accepting to review my work, allowing me to defend my thesis and granting me my PhD.

Finally, although I mentioned them already, I thank once again Sam, Delphine and Briscard for their unyielding efforts to make my post-defense party an amazing time. I also thank Adrien and the Groove General Store for providing the much appreciated musical ambiance!

# Contents

<b>Résumé</b>	<b>5</b>
<b>Abstract</b>	<b>7</b>
<b>Acknowledgements</b>	<b>9</b>
<b>Contents</b>	<b>11</b>
<b>1 Introduction</b>	<b>15</b>
1.1 The thermal catastrophe . . . . .	16
1.2 Evidence for global magma oceans in terrestrial bodies . . . . .	19
1.3 Possible consequences of magma oceans on solid-state convection . . . . .	22
1.4 Focus of this thesis . . . . .	23
<b>2 Constant solid thickness thermal problem</b>	<b>25</b>
2.1 Conservation equations . . . . .	26
2.2 Boundary conditions . . . . .	27
2.3 Dynamic pressure choice . . . . .	30
2.4 Dimensionless equations . . . . .	31
<b>3 Linear stability analysis of the static thermal problem</b>	<b>33</b>
3.1 Motionless reference state . . . . .	33
3.2 Poloidal potential formulation . . . . .	34
3.3 Perturbation equations . . . . .	36
3.4 Eigenvalue formulation . . . . .	37
3.5 Results . . . . .	39
3.6 Analytical study of the translation mode . . . . .	47
3.6.1 Buoyancy – topographic weight equilibrium . . . . .	47
3.6.2 Critical Rayleigh number . . . . .	48
3.7 Concluding remarks . . . . .	49
<b>4 Numerical simulations of the thermal problem</b>	<b>51</b>
4.1 Implementation in StagYY . . . . .	51
4.2 Flow-through condition at the bottom boundary . . . . .	55
4.3 Flow-through condition at the top boundary . . . . .	61
4.4 Flow-through condition at both boundaries . . . . .	66
4.5 Concluding remarks . . . . .	72

<b>5</b>	<b>Magma ocean evolution models coupled with the solid</b>	<b>73</b>
5.1	Evolution model of the Top Magma Ocean (TMO) . . . . .	74
5.1.1	Dimensional model . . . . .	74
5.1.2	Dimensionless equations . . . . .	80
5.2	Evolution model of the Basal Magma Ocean (BMO) . . . . .	82
5.2.1	Dimensional model . . . . .	82
5.2.2	Dimensionless equations . . . . .	86
5.3	Fixed-front approach in the solid . . . . .	89
5.3.1	Mathematical background . . . . .	89
5.3.2	Dimensional equations . . . . .	91
5.3.3	Dimensionless equations . . . . .	92
<b>6</b>	<b>Timescale of overturn in a magma ocean cumulate</b>	<b>95</b>
6.1	Abstract . . . . .	95
6.2	Introduction . . . . .	96
6.3	Methods . . . . .	97
6.3.1	Composition and temperature reference profiles . . . . .	98
6.3.2	Crystallization time scale . . . . .	101
6.3.3	Set of dimensionless equations . . . . .	102
6.3.4	Phase change boundary condition . . . . .	103
6.3.5	Determination of overturn timescale . . . . .	104
6.4	Results . . . . .	105
6.5	Discussion . . . . .	110
6.6	Conclusions . . . . .	113
6.7	A – Composition profile resulting from the fractional crystallization of the surface magma ocean . . . . .	114
6.8	B – Linear Stability . . . . .	115
<b>7</b>	<b>Preliminary non-linear coupled evolution model</b>	<b>119</b>
7.1	Implementation in StagYY . . . . .	119
7.2	Preliminary simulation with a Basal Magma Ocean . . . . .	122
<b>8</b>	<b>Concluding remarks and perspectives</b>	<b>129</b>
<b>A</b>	<b>Convection with phase change boundaries</b>	<b>131</b>
A.1	Abstract . . . . .	131
A.2	Introduction . . . . .	132
A.3	Conservation equations and boundary conditions . . . . .	134
A.4	The translation mode . . . . .	138
A.4.1	Linear stability analysis . . . . .	138
A.4.2	Steady state translation . . . . .	140
A.5	Non-translating modes with $\Phi^+ = \Phi^-$ . . . . .	143
A.5.1	Linear stability . . . . .	143
A.5.2	Weakly non-linear analysis . . . . .	151
A.6	Solutions with only one phase change boundary . . . . .	156
A.7	Conclusion . . . . .	160
A.8	A – Self-adjointness of operator $\mathbf{L}_c$ . . . . .	161
A.9	B – Expression of the non-linear terms . . . . .	162

---

<b>B</b>	<b>Mantle convection interacting with magma oceans</b>	<b>165</b>
B.1	Abstract . . . . .	165
B.2	Introduction . . . . .	166
B.3	Method . . . . .	167
	B.3.1 Governing equations . . . . .	167
	B.3.2 Treatment of the solid-liquid phase changes . . . . .	168
	B.3.3 Numerical approach and set-up . . . . .	170
B.4	Results . . . . .	171
	B.4.1 Convection with a magma ocean above and below . . . . .	172
	B.4.2 Convection with a magma ocean above or below . . . . .	178
B.5	Discussion . . . . .	184
B.6	Conclusions . . . . .	188
	<b>Bibliography</b>	<b>191</b>
	<b>List of Figures</b>	<b>201</b>
	<b>List of Tables</b>	<b>205</b>



# Chapter 1

## Introduction

The Earth is cooling down. The current heat flux through its surface inferred from direct measurements is about 45 TW (e.g. J. Davies and D. Davies 2009; Jaupart, Labrosse, et al. 2015; Lucazeau 2019). A significant part of this flux is contributed by the radioactive decay of the so-called heat producing elements, namely uranium 238, thorium 232, and potassium 40 which mainly reside in the Earth's mantle and the continental crust (Huang et al. 2013). Detections of neutrinos emitted by their desintegrations seem to indicate about half ( $\sim 25$  TW) of the total heat flux evacuated by the Earth can be imparted to radiocative decay (e.g. Korenaga 2011). The proportion of heat produced by internal heating is the Urey number  $U$  and is defined as

$$U = \frac{H}{Q} \quad (1.1)$$

where  $H$  is radiogenic heating and  $Q$  the total heat flux at the surface of the system. For today's Earth, this number is  $U \sim 0.5$ . The other half of the total heat flux is the residual from the primordial heat accumulated during accretion and early radiogenic heating. It is estimated around 5 – 15 TW can be assigned to core cooling (Lay et al. 2008), the remaining 5 – 15 TW corresponding to mantle cooling. Note that the balance between mantle and core cooling is still poorly constrained. Other processes such as tidal dissipation bring minor contributions to the overall heat budget of the Earth.

It is only since fairly recently that convection has been known to be the prominent heat transfer mechanism within the Earth. Lord Kelvin (1864) proposed conduction as the only heat transfer mechanism. Starting from a sphere with a homogeneous sub-solidus temperature and letting it cool down until the heat flux at its surface reaches today's value led him to conclude the Earth is only a few ten or hundred millions of years old. As shown by Richter (1986), merely adding internal heating to Lord Kelvin's model only raises slightly the obtained age for the Earth. Since the age of the Earth is constrained at 4.55 Gyr from radiogenic dating, this shows a crucial ingredient is missing to explain the current heat flow at the surface of the Earth.

Perry (1895) and later Holmes (1913) proposed convection as a way to obtain an age for the Earth of the order of a few billion years, even without any internal heating. Indeed, the heat flux at the surface of a convecting spherical domain is higher for a longer period of time than with a conductive model. Hence, for a given initial condition, a convective Earth requires more time than a conductive Earth for its surface heat flow to decrease to today's value. This is the first strong

argument in favor of a convecting mantle. The famous study of Strutt (1916) shows the critical Rayleigh number for thermal convection in a cartesian box heated from below with classical free-slip boundary conditions is  $\frac{27\pi^4}{4} \sim 657$ . This is several orders of magnitude lower than that of the mantle (roughly  $10^7$ ), which should hence convect. However, the great success of thermal convection comes from the fact it provides a physical motor for plate-tectonics (see Schubert et al. 2004, for a comprehensive historical background).

Convection is now widely studied as it is the prominent mechanism to explain planetary interiors dynamics and the associated heat transfer.

## 1.1 The thermal catastrophe

The constraints available to build a thermal evolution model for the Earth are the following:

1. its accretion age of 4.55 Gyr;
2. the current heat flux at the surface of the planet  $Q_0 = 45$  TW;
3. the current Urey ratio  $U_0 \sim 0.5$ ;
4. the potential temperature of the mantle  $T_0 \sim 1500$  K.

Christensen (1985) exposes a simple method to built parameterized thermal evolution models for the Earth; the gist of this method is shown hereafter. Even though simple, this model yields an issue that has not been resolved to this day, known as the thermal catastrophe.

Energy balance at the scale of the mantle gives the following equation on the time derivative of the mantle potential temperature  $T$ :

$$MC_p\dot{T} = H - Q. \quad (1.2)$$

$M$  is the mass of the mantle,  $C_p$  its heat capacity. Note that the flux coming from the core is neglected in such a model. This is based on the observation that the hot plumes originated at the Core Mantle Boundary (CMB) bring a small contribution to the overall heat flux at the top of the mantle (G. F. Davies 1988; Sleep 1990). Assuming this situation is representative of the Earth's thermal history, the heat flux through the CMB and therefore the core contribution to the mantle energy balance is minor (Stacey and Loper 1983). The internal heating  $H$  in the past can easily be computed in the past from today's value of about  $H_0 = 20 - 25$  TW:

$$H(t) = H_0 \exp\left(-\frac{t}{\tau_r}\right) \quad (1.3)$$

with  $\tau_r$  the radioactive decay timescale (about 3 Gyr) and  $t$  the time. By convention,  $t = 0$  at the present time and  $t = -4.55$  Gyr at the formation of the Earth.

Convection models offer a power law relationship between the heat flux carried out by a convective system,  $Q$ , and the Rayleigh number, Ra. The latter compares the buoyancy forces that are the motor of thermal convection with the kinematic

viscosity,  $\nu$ , and thermal diffusivity,  $\kappa$ , that dampen thermal convection. Its expression is

$$\text{Ra} = \frac{\alpha g \Delta T L^3}{\nu \kappa} \quad (1.4)$$

where  $\alpha$  is the coefficient of thermal expansivity,  $g$  the gravity acceleration,  $L$  the thickness of the system, and  $\Delta T$  the temperature difference across the domain. The heat flux verifies

$$Q = AS \frac{k \Delta T}{L} \text{Ra}^\beta \left( \frac{T}{\Delta T} \right)^{1+\beta} \quad (1.5)$$

where  $A$  is some coefficient,  $S$  the surface of the top boundary,  $k$  the conductivity, and  $\beta$  an exponent. Note that such a parametrization allows the temperature difference  $\Delta T$  to drop out of the equation, the potential temperature  $T$  becoming the only temperature scale describing the system. Boundary layer theory prescribes that  $Q$  should be independent on the thickness of the domain  $L$ , leading to  $\beta = 1/3$ . In practice, direct numerical simulations lead to values that are not exactly  $1/3$  but rather around  $0.3$  (e.g. Wolstencroft et al. 2009). Moreover, the viscosity  $\nu$  depends strongly on temperature. Denoting  $\nu_0$  the current bulk viscosity of the mantle, a simple power law that can be used to compute the viscosity as a function of the potential temperature is

$$\nu = \nu_0 \left( \frac{T}{T_0} \right)^{-n} \quad (1.6)$$

with  $n$  an exponent that can be determined from experimental measurements. A reasonable value would be  $n = 30$  (G. F. Davies 1979). Plugging eqs. (1.3), (1.5) and (1.6) in the heat balance eq. (1.2) leads to

$$MC_p \dot{T} = Q_0 \left( U_0 \exp \left( -\frac{t}{\tau_r} \right) - \left( \frac{T}{T_0} \right)^{1+\beta+\beta n} \right). \quad (1.7)$$

Solving eq. (1.7) backwards in time allows one to recover the past potential temperature of the mantle. Using  $U_0 = 0.5$  and  $\beta = 0.3$  leads to the so-called thermal catastrophe. Since today total heat flux  $Q_0$  is superior to the radiogenic heat production  $H_0$  (i.e.  $U_0 < 1$ ), the mantle is currently cooling down. Going backwards, the potential temperature increases. This leads to a large increase of  $(T/T_0)^{1+\beta+\beta n}$  (especially due to the large value of  $n$ , which represents the dependence of viscosity on temperature).  $\tau_r$  is too large for the internal heating to compensate that effect and keep  $\dot{T}$  more or less constant. This leads to an increase of the absolute value of  $\dot{T}$  with time and the potential temperature of the mantle quickly diverges. One could imagine that the opposite case would be possible if  $U_0$  were large enough: the radiogenic term in eq. (1.7) would dominate  $\dot{T}$ , leading to a temperature that would diverge towards negative values. This means that bounds exist on the value of today's Urey mantle  $U_0$  for the model eq. (1.7) to give a satisfactory potential temperature as far as 4.55 Gyrs in the past. Note that since the value  $n = 30$  for the viscosity law exponent is only valid for values of  $T$  that are fairly close to  $T_0$  and tends to under-estimate viscosity at higher temperatures (ibid.), a better model for the viscosity dependence on temperature would lead to a slightly larger range of acceptable values for  $U_0$ . This effect does not prevent however the thermal catastrophe.

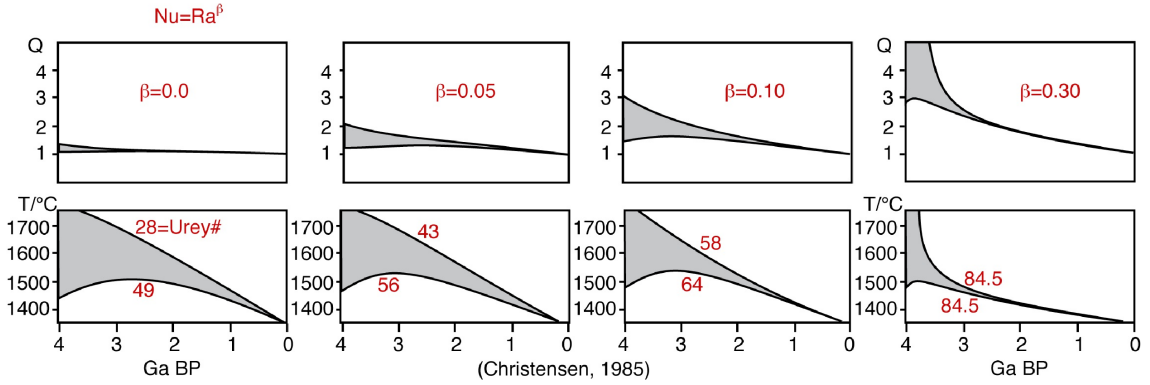


Figure 1.1: Figure from Christensen (1985). It shows the heat flux  $Q/Q_0$  (first line) and potential temperature  $T$  (second line) obtained by running backwards the model eq. (1.7). Each column is a different value of the heat flux exponent  $\beta$ , and the grey area represents model trajectories that result in non-diverging potential temperature and heat flux. The acceptable range of values for  $U_0$  is indicated in percent on each plot.

Figure 1.1, from Christensen (1985), shows the acceptable range for  $U_0$ , also exploring the effect of the  $\beta$  coefficient on that range. One can notice that for  $\beta = 0.3$  (which is the value obtained from numerical simulations), the acceptable range for  $U_0$  is very narrow around  $U_0 = 0.845$  and far off the estimated value of  $U_0 = 0.5$ . On the other hand, values of  $\beta$  for which  $U_0 \sim 0.5$  would be acceptable are  $\beta < 0.1$ , which is also far off the value obtained numerically.

Among possible explanations and ways around the thermal catastrophe are the two following:

- our understanding of mantle convection lacks a major physical ingredient that would lead to a radically different power law or even relationship between the heat flux and the Rayleigh number;
- the heat flux through the CMB is not negligible, and therefore cannot be ruled out eq. (1.2). A high flux from the core to the mantle would help mitigating the blowing effect of increasing  $T$  in the mantle going backwards in time owing to the term  $(T/T_0)^{1+\beta+\beta n}$ . Indeed, part of the heat would go into increasing the core temperature instead of that of the mantle (Labrosse, Hernlund, and Hirose 2015).

The second explanation is gaining traction in the community. The argument that the CMB heat flow should be low given the scarcity of hot plumes reaching the surface of the Earth is dubious, Labrosse (2002) indeed shows hot plumes originating from the CMB do not necessarily have enough buoyancy to reach the planet's surface. Moreover, higher heat fluxes from the core (of around 15 TW) have recently been proposed as estimations of the conductivity of the outer core are radically higher than previous estimates (e.g. Gomi et al. 2013; Koker et al. 2012; Pozzo et al. 2014). The heat flow that can be extracted from the core by the mantle throughout the history of the Earth hence needs to be investigated.

## 1.2 Evidence for global magma oceans in terrestrial bodies

Observation of a plagioclase-enriched crust and a KREEP layer (enriched in incompatible elements) underneath it at the surface of the Moon led to the hypothesis that these are manifestations of the crystallization of a global magma ocean, the so-called Lunar Magma Ocean (e.g. Wood et al. 1970). Numerous following studies suggested and studied the consequences of a global surface magma ocean for terrestrial planets including the Earth (e.g. Abe and Matsui 1986; Richter et al. 1998; Zahnle et al. 1988). Indeed, the heat accumulated during the accretion of such planetary bodies brings more than enough heat to melt the entire mantle. See Elkins-Tanton (2012), Labrosse, Hernlund, and Hirose (2015), and Solomatov (2015) for comprehensive reviews on the subject.

Since a surficial global magma ocean would have a gigantic Rayleigh number owing to the small viscosity of liquid, the convection is expected to be vigorous, resulting in a well-mixed magma ocean and a large heat flux at its boundary. Moreover, an interesting feature of global magma oceans made out of molten silicates is that the solidus is steeper with depth than the isentropic temperature profile of the magma ocean. As a result, the magma ocean crystallizes from the bottom up, forming a so-called Top Magma Ocean (TMO) lying on top of the primitive solid mantle. Due to the very large heat flux at the surface of the TMO, the latter is expected to crystallize on a short timescale, of the order of a few million years (Abe 1997; Lebrun et al. 2013; Sleep 2000).

An additional complexity arises from the effect of pressure and/or composition (which would vary with time if fractional crystallization is in effect) on the solidus and isentropic profiles in the magma ocean. In the lower part of the Earth mantle, it is possible that the solidus becomes less steep than the isentropic temperature profile, resulting in a crystallization starting from the middle of the mantle instead of the bottom (Boukaré, Ricard, et al. 2015; Caracas et al. 2019; Labrosse, Hernlund, and Coltice 2007; Nomura et al. 2011; Thomas, Liu, et al. 2012). In this situation, provided that solid crystals settle at an intermediate depth, two global magma oceans are formed: a Top Magma Ocean (TMO) as previously, and a Bottom Magma Ocean (BMO). Note that contrary to the TMO that is expected to crystallize quickly owing to the large heat flux at its surface, cooling of the BMO is limited by the heat flux carried out by convection in the solid mantle which should be much slower than in the magma ocean. Therefore, the crystallization of the BMO is expected to happen on a much longer timescale than that of the TMO, possibly of the order of a few Gyrs (Labrosse, Hernlund, and Coltice 2007). Figure 1.2, from Caracas et al. (2019), shows various scenarii in which crystallization of the mantle starts from the middle of the ocean, leading to the formation of a TMO and a BMO. In these scenarii, the first solid crystals form slightly below or above their neutral buoyancy depth where they settle. Once a rigid solid layer is formed, both oceans evolve in a rather individual fashion, the TMO crystallizing at a much faster pace than the BMO. Depending on where the first solid forms and whether fractional crystallization is prominent from the beginning of the crystallization or only sets in later, the composition of both magma oceans does not evolve exactly in the same way, which could have repercussions on the compositional structure of the future solid mantle.

The existence of a Basal Magma Ocean during Earth's history could explain a few seismological and geochemical observations. As hypothesized by Labrosse, Hernlund, and Coltice (2007), it could be a mean to produce the Large Low Shear Velocity Provinces seismically observed under Africa and the Pacific (Lekic et al. 2012) and thought to be thermo-chemically dense (e.g. Hernlund and McNamara 2015). Indeed, fractional crystallization of a BMO would lead to a dense FeO-enriched layer at the base of the mantle, which could be pushed around by convection in the solid mantle and accumulate as large piles. Moreover, some OIB plumes sampling these piles have a primitive-like signature in noble gasses such as Neon and Argon. Such a feature can be explained by the important fractionation associated with the crystallization of a BMO (Coltice et al. 2011).

Note that numerous physical complexities are associated with the cooling of magma oceans, making the study of their dynamics and evolution an extremely rich problem. For instance, the cooling of the TMO is deeply connected to the atmosphere dynamics and exchanges of gasses between the TMO and the atmosphere that can affect it (e.g. Lebrun et al. 2013). Moreover, due to fractional crystallization, compositional heterogeneities can form in a magma ocean and the solid that crystallizes from it, leading to double-diffusive convection and the associated numerical challenges to model such systems (e.g. Bouffard et al. 2017).

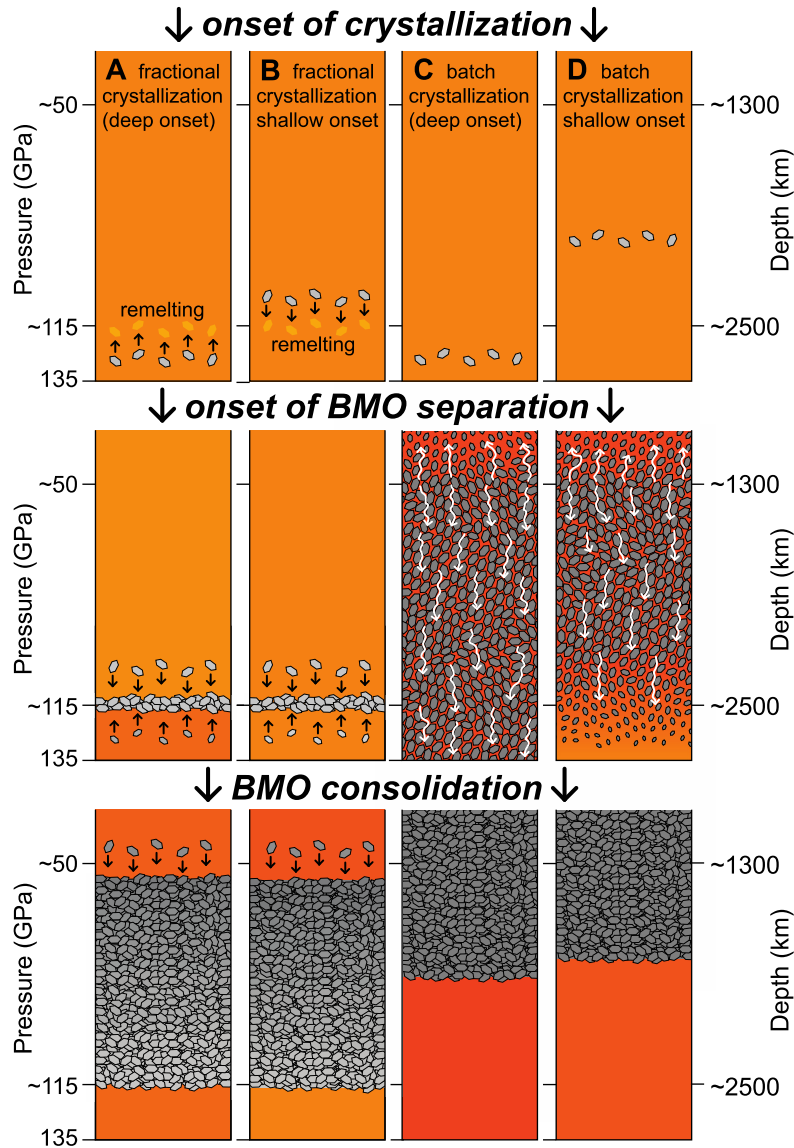


Figure 1.2: Crystal formation and settling leading to the formation of a Basal Magma Ocean in four different scenarios. Either the formation of the first crystals happens below or above their neutral buoyancy; and either fractional crystallization is effective from the beginning of the process or only at a later phase after a batch crystallization episode. From Caracas et al. (2019).

### 1.3 Possible consequences of magma oceans on solid-state convection

An aspect of convection models that should be treated with care is the choice of suitable boundary conditions. Indeed, they offer a strong constraint on the convective patterns and heat flux accessible to the modeled system.

Common mechanical boundary conditions applied to the mantle are free-slip and non-penetrative boundary conditions. Free-slip boundary condition states that the tangential stress applied at the domain boundary is null. This is a reasonable assumption, at least for the Earth, as the solid mantle is surrounded by the liquid outer core at the bottom and a gaseous atmosphere at the top, which are both several orders of magnitude less viscous than the solid mantle. Note that this stays valid for the solid layer of the primitive mantle when surrounded by magma oceans.

Non-penetrative boundary condition states that the normal velocity of the convective matter is null at the interface. This condition is generally applied directly at the position of the interface at rest (i.e. when no convection operates in the solid). This neglects the possibility of forming dynamic topography and the associated feedback on convection. This is often a reasonable assumption as the weight of the topography greatly limit its amplitude. However, as shown by Monnereau and Dubuffet (2002) and Ricard, Labrosse, et al. (2014), the convection pattern, thermal structure and heat flux can be greatly affected by dynamic topography when it is associated with volcanism (i.e. a strong heat transfer related to the topography itself) or fast erosion. In the case of a solid mantle surrounded by global magma oceans above and/or below it, non-penetrative boundary conditions are very likely not relevant to describe the dynamics of the solid. Indeed, the solid is in contact with a liquid of similar composition and therefore dynamic topography at the solid/liquid boundary can be erased as it is formed by melting and freezing. Alboussière et al. (2010) introduced for the inner core (which is essentially a very similar system) a phase change boundary condition, allowing exchange of matter by melting and freezing between the solid inner core and the liquid outer core. As shown by Alboussière et al. (2010), Deguen, Alboussière, et al. (2013), Lasbleis et al. (2015), and Mizzon and Monnereau (2013), this boundary condition exhibits a translation convection mode for the inner core (see fig. 1.3), as well as a higher heat flux. A positive topography of solid intruding the liquid melts on one hemisphere while a negative topography freezes on the other, the inner core being maintained in place by a wind of matter going through it. Deguen (2013) presents the linear stability of a similar problem but with a different geometry: instead of a full sphere with a phase change boundary condition at its top, he considers the case of a solid spherical shell surrounded by an ocean of similar composition above and/or below it. Such a setup could be representative of the situation in icy satellites with a solid layer on top of an ocean (e.g. Čadek et al. 2016) as well as the situation of a terrestrial mantle crystallizing from the bottom-up or from the middle of a global magma ocean. The linear stability analysis of this system performed by Deguen (2013) shows the phase change boundary condition leads to convective patterns with higher wavelengths than in the classical non-penetrative case (see fig. 1.4). There even is the possibility of a translation mode with both boundaries open, and an almost-translation mode with some deformation in the bulk when only the top boundary is open. A question that is not answered by the linear stability analysis is how these convec-

tion modes affect the heat flux carried out through the solid domain. However, they involve very little to no deformation, therefore diminishing the role of viscosity and probably leading to a higher heat flux than the classical case. This could affect the heat budget scaling law presented as eq. (1.7), and therefore the conditions leading to thermally catastrophic scenarii.

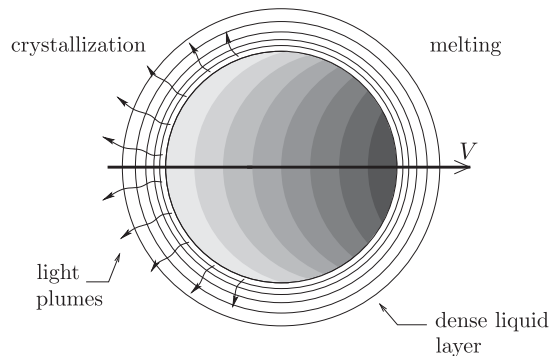


Figure 1.3: Depiction of the translation mode obtained with the flow through boundary condition at the inner core boundary. The shades of grey represent the temperature field in the inner core (higher temperatures are in darker shades). From Deguen, Alboussière, et al. (2013).

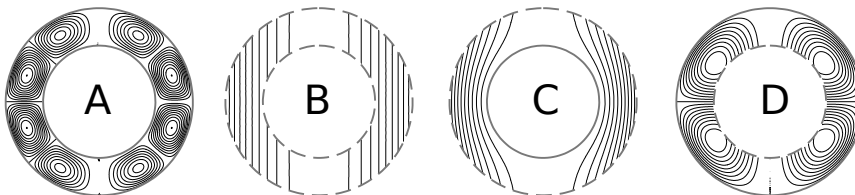


Figure 1.4: Linearly most unstable modes of convection in a spherical shell with internal heating and a gravity varying linearly with the radius. The 4 cases presented here are classical non-penetrative boundary conditions (A), phase change condition at both boundaries (B), phase change boundary only at the top (C), and phase change boundary only at the bottom (D). From Deguen (2013).

## 1.4 Focus of this thesis

In this study, we focus on convection in the primitive solid mantle of Earth-like bodies. We consider the general case where this solid layer can be bounded by global magma oceans above and/or below. As discussed previously, the boundary condition we apply at the interface between the solid and the magma oceans allows matter to traverse it by fusion and crystallization.

The overall goal of this thesis is to study the consequences of the existence of global magma oceans on solid-state convection and on the heat budget of the Earth. Increasingly complex models and methods are used to explore this question.

First, we focus on a purely thermal modelling of our system with a solid of constant thickness. All chemical aspects of the problem are left out, and no-net freezing nor melting of the magma oceans occurs, avoiding the need for an evolution model of

the magma oceans themselves. Chapter 2 presents the conservation equations and boundary conditions verified by the primitive solid mantle. Chapter 3 details the linear stability analysis of this problem. Chapter 4 presents non-linear simulations, hereby completing the study of the purely-thermal and constant-thickness system.

Then, chapter 5 details a much more complete model, taking chemical aspects into consideration (through fractionation at the boundary) as well as the long-term evolution of the system by allowing net-freezing and melting of the magma oceans. Chapter 6 presents a linear stability analysis of this evolution model to assess the timescale at which solid-state convection sets in when crystallizing a Top Magma Ocean. Finally, chapter 7 presents a preliminary fully non-linear numerical resolution of the evolution model.

## Chapter 2

# Constant solid thickness thermal problem

In the three following chapters, we focus on the simplest instance of the considered problem. We put aside for now the long term evolution of the system, and hence consider a solid mantle of constant thickness (no net crystallization of the magma oceans). The solid part of the crystallizing mantle is considered to be a spherical shell of external radius  $R^+$  and internal radius  $R^-$ . Its thickness is denoted  $L = R^+ - R^-$ . For generality purpose, we consider global magma oceans can exist above and/or below the solid layer. They are also considered to be spherical shells. The Top Magma Ocean (TMO) extends from the external solid boundary  $R^+$  to the surface of the planet at radius  $R_T$ ; the interface between the TMO and the solid layer is called the Top Ocean-Mantle Boundary (TOMB). The Basal Magma Ocean (BMO) extends from the Core Mantle Boundary (CMB) at radius  $R_c$  to the internal solid boundary  $R^-$ ; the interface between the BMO and the solid layer is called the Bottom Ocean-Mantle Boundary (BOMB). See fig. 2.1 for a visual representation of these layers.

We focus in the three following chapters on the thermal part of the problem and therefore neglect any compositional effects. The aim is to see what are the dynamical consequences of the presence of magma oceans in contact with the solid primitive mantle, without mixing these with dynamical effects due to compositional variations in the solid.

Moreover, the studied system is merely the solid part of the crystallizing mantle. The presence of magma oceans is parameterized with boundary conditions at the top and bottom boundaries of the solid domain. Such a vision is of course overly simplistic, but as shown in the following chapters, it allows us to isolate and understand interesting consequences of the presence of magma oceans on solid-state convection. This chapter describes the conservation equations that apply to the solid layer, and the boundary conditions applied at the TOMB and the BOMB. Finally, making these equations and associated boundary conditions dimensionless exhibits the controlling parameters of this simplified system.

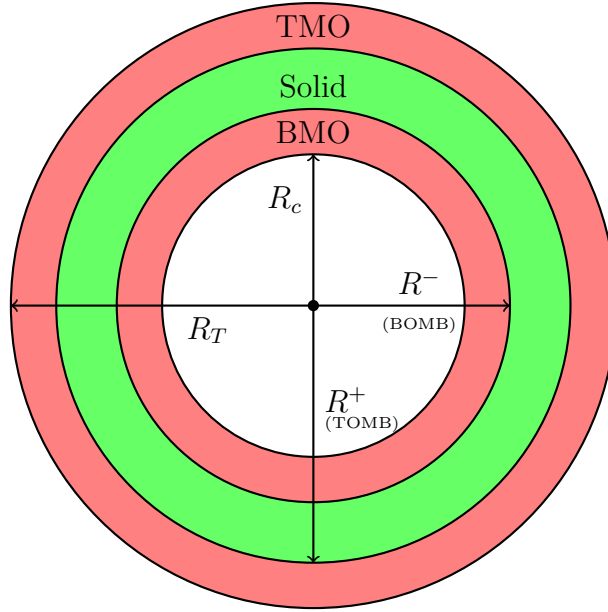


Figure 2.1: Equatorial view of the problem setup. We consider a solid layer (green) surrounded by global magma oceans (red) above and/or below that solid. The radii associated with the various interface positions are labelling the relevant arrows.

## 2.1 Conservation equations

The velocity  $\mathbf{u} = (u_r, u_\theta, u_\phi)$ , pressure  $P$  and temperature  $T$  fields in the solid are linked together by a set of conservation equations. For the sake of simplicity, the viscosity  $\eta$  and thermal diffusivity  $\kappa$  are assumed to be uniform throughout the mantle. The gravity acceleration  $\mathbf{g} = -g\hat{\mathbf{r}}$  is radial and its intensity  $g$  is uniform. This work is done under the Boussinesq approximation where all density variations are considered negligible except, of course, in the buoyancy term which is the motor of thermal convection. Moreover, the solid mantle has an extremely large Prandtl number, which means inertia terms are negligible compared to the viscous forces. We hence consider the solid mantle is an infinite Prandtl number fluid with no inertia. Under these assumptions, the mass, momentum and energy conservation equations are the following (e.g. Chandrasekhar 1961):

$$\nabla \cdot \mathbf{u} = 0, \quad (2.1)$$

$$\mathbf{0} = -\nabla P + \eta \nabla^2 \mathbf{u} - \rho_\alpha g \hat{\mathbf{r}}. \quad (2.2)$$

$$\frac{\partial T}{\partial t} + \mathbf{u} \cdot \nabla T = \kappa \nabla^2 T. \quad (2.3)$$

$\rho_\alpha$  is the density used in the buoyancy term. It is related to the temperature field via the thermal expansion coefficient  $\alpha$  which is considered constant. Denoting  $\rho$  the reference density at a temperature  $T_0$ , the buoyancy density  $\rho_\alpha$  can be expanded as

$$\rho_\alpha = \rho (1 - \alpha(T - T_0)). \quad (2.4)$$

Note moreover that in this problem, we do not consider internal heating occurring in the solid. Only heat advection and diffusion are included in eq. (2.3). This is justified here by the fact that heat producing elements (U, K, Th) are refractory

(e.g. Huang et al. 2013) and therefore are expected to reside in the magma oceans rather than the solid.

## 2.2 Boundary conditions

The boundary positions  $r = R^-$  (BOMB) and  $r = R^+$  (TOMB) correspond to the case where no convection operates in the solid, and the solid and liquid layers are at thermodynamical equilibrium. In this case – referred to as “the equilibrium case” in this chapter – both boundaries are spherical, and at the phase change temperatures  $T^-$  and  $T^+$ . Moreover, no heat is gained or lost by the overall system (which would result in a net melting or freezing of the magma oceans). In practice, if convection operates in the solid layer, matter at the boundary departs from its equilibrium position and therefore forms a topography  $h$  with respect to it. This topography is either a solid residing in a liquid or a liquid residing in a solid of the same composition, and therefore prone to melting or freezing. This phase change can act as an erosion mechanism of the topography, effectively resulting in an exchange of matter between the solid and the liquid layers. The goal of this chapter is to write boundary conditions accounting for this possibility. Such a system comprises a large wealth of complexities and therefore several assumptions need be made in order to ease its study. A few of these assumptions are alleviated in chapter 5. Figure 2.2 illustrates what happens as the actual solid-liquid boundary is deformed around its equilibrium position. The topography with respect to the equilibrium position is denoted  $h^+$  at the TOMB and  $h^-$  at the BOMB; it is by convention positive when oriented towards a higher radial position. The actual liquid/solid interface of the system is then at  $r = R^- + h^-$  for the bottom boundary and  $r = R^+ + h^+$  for the top boundary.

The normal stress continuity writes:

$$2\eta \frac{\partial u_r}{\partial r}(h_s) - P(h_s) = -P(h_l), \quad (2.5)$$

where  $f(h_s)$  is the quantity  $f$  at the solid side of the boundary, and  $f(h_l)$  is the quantity  $f$  at the liquid side of the boundary. Note that the viscosity of the liquid is several orders of magnitude smaller than that of the solid; viscous forces on the liquid side are therefore neglected. The pressure is then written as the sum between the hydrostatic pressure  $\bar{P}$  and the dynamic pressure  $p$ :

$$\begin{aligned} 2\eta \frac{\partial u_r}{\partial r}(h_s) - p(h_s) \underbrace{-\bar{P}_0 + \rho_s g h}_{-\bar{P}(h_s)} \\ = -p(h_l) \underbrace{-\bar{P}_0 + \rho_l g h}_{-\bar{P}(h_l)}. \end{aligned} \quad (2.6)$$

where  $\bar{P}_0$  is the hydrostatic pressure at the boundary in the motionless equilibrium position. Moreover, the dynamic pressure  $p(h_l)$  in the liquid can be neglected since its time average value is null and the dynamics of the liquid part is expected to be fast compared to the one of the solid. Equation (2.6) becomes

$$2\eta \frac{\partial u_r}{\partial r}(h_s) - p(h_s) + \Delta \rho g h = 0 \quad (2.7)$$

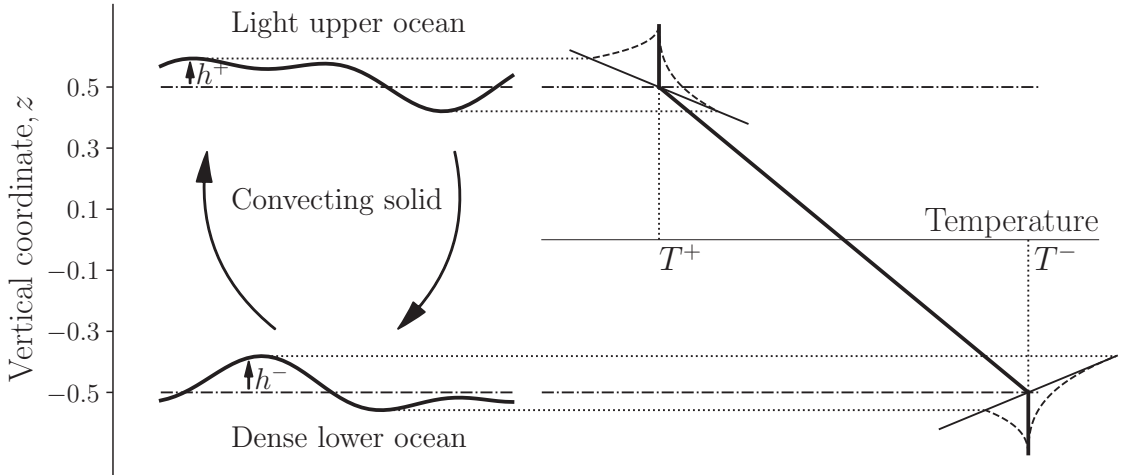


Figure 2.2: Dynamic topography at the boundaries. Note that the curvature has been removed and the height of topography exaggerated for readability purpose. The horizontal dot-dashed lines at  $z = \pm 1/2$  correspond to the equilibrium position of the boundaries  $r = R^\pm$  when no convection operates in the solid and there is no net freezing or melting of the magma oceans. Matter departing from the boundary creates a topography  $h$ . The thick line on the right side is the superisentropic temperature profile in the motionless steady state. The temperature at the topography follows the melting temperature (thin solid line), and therefore departs from the isentropic profile in the liquid. Figure from Labrosse, Morison, et al. (2018).

where  $\Delta\rho = \rho_s - \rho_l$  is the density contrast between the solid and the liquid. Note that for the system to be mechanically stable,  $\Delta\rho$  should be positive at the top boundary and negative at the bottom boundary. The last variable that needs to be connected to the dynamics of the solid mantle is the topography  $h$ . At the TOMB, a positive (resp. negative) topography  $h^+$  is formed by solid (liquid) matter that goes toward the liquid (solid) part but that has not melted (crystallized) yet. Conversely, at the BOMB, a positive topography  $h^-$  corresponds to liquid matter going toward the solid but that has not frozen yet.

The topography  $h^\pm$  is formed by the velocity of the solid itself  $u_r$  as well as the freezing-front velocity  $V_r$ . This freezing-front velocity is chosen positive along the outward radial direction. A positive value of  $V_r$  corresponds to freezing at the TOMB, and melting at the BOMB. Its lagrangian derivative hence verifies

$$\frac{Dh^\pm}{Dt} = u_r + V_r. \quad (2.8)$$

Moreover, energy conservation at the boundary is given by Stefan's law:

$$\rho_s L_h V_r = (\mathbf{q}_l - \mathbf{q}_s) \cdot \hat{\mathbf{r}} \quad (2.9)$$

where  $L_h$  is the latent heat of crystallization and  $\mathbf{q}$  is the heat flux on either side of the boundary. Assuming the topography is at thermodynamic equilibrium, the temperature at the boundary  $T(h)$  is the melting temperature at the relevant pressure. It is related to the melting temperature at the equilibrium position of the boundary  $T^\pm$  as follows:

$$T(h^\pm) = T^\pm - \frac{\partial T_L}{\partial P} \rho_l g h^\pm. \quad (2.10)$$

$\frac{\partial T_L}{\partial P}$  is the Clapeyron slope, considered constant on the pressure range across the topography  $h$ .

Solving this set of equations at both boundaries requires a full convection model in the liquid to determine the heat flux in the liquid  $\mathbf{q}_l$ . However, the timescale at which the liquid evolves is much shorter than that of the solid. This makes solving Navier-Stokes in a consistent way for both the solid and liquid layers impractical with our current computing power. The liquid behavior at the timescale at which solid-state convection operates is therefore parameterized. The parametrization we use is the one that was introduced for the core in Deguen, Alboussière, et al. (2013). Assuming advection dominates heat transport, one can write

$$\mathbf{q}_l \cdot \hat{\mathbf{r}} \sim \rho_l C_{p,l} v' \delta T \quad (2.11)$$

where  $v'$  is the typical fluid velocity in the liquid and  $\delta T$  is the temperature departure from the average temperature profile in the liquid at the topography. The average temperature profile is assumed to be isentropic as convection in magma oceans is expected to be vigorous (e.g. Solomatov 2015). This leads to

$$\delta T = \left( \frac{\partial T}{\partial P} \Big|_S - \frac{\partial T_L}{\partial P} \right) \rho_l g h. \quad (2.12)$$

Moreover, the heat flux from the solid  $\mathbf{q}_s \cdot \hat{\mathbf{r}}$  is considered small compared to the one carried out in the liquid and is therefore neglected in eq. (2.9). Injecting eqs. (2.11) and (2.12) in eq. (2.9) gives the following expression for the freezing velocity  $V_r$ :

$$V_r = -\frac{h}{\tau_\phi} \quad (2.13)$$

with  $\tau_\phi$  the phase change timescale

$$\tau_\phi = \frac{\rho_s L h}{\rho_l^2 g C_{p,l} v' (\partial_P T_L - \partial_P T_S)}. \quad (2.14)$$

$\tau_\phi$  is the timescale at which heat is carried in the magma ocean from the topographies that freeze to the topographies that melt.

Moreover, convection in the solid operates at much longer timescales than convection in the liquid and melting/freezing, meaning the time derivative of topography in eq. (2.8) can be neglected ( $Dh/Dt \sim 0$ ). Plugging eq. (2.13) in eq. (2.8) yields the following expression for the topography  $h$

$$h = u_r \tau_\phi. \quad (2.15)$$

Substituting  $h$  with its expression in eq. (2.7) and assuming the topography is small compared to the thickness of the domain, one obtains the following boundary condition applied at  $r = R^\pm$

$$\Delta \rho g \tau_\phi u_r + 2\eta \frac{\partial u_r}{\partial r} - p = 0. \quad (2.16)$$

Note that the topography  $h$  is now an implicit variable of the problem that can be computed *a posteriori*. This boundary condition and its effects on solid-state

convection is extensively discussed in Deguen (2013), Deguen, Alboussière, et al. (2013), Labrosse, Morison, et al. (2018), and Morison et al. (2019).

Assuming viscous forces in the liquid are negligible, the shear stress continuity at each boundary is written:

$$\begin{aligned}\tau_{r\theta} &= \eta \left( r \frac{\partial}{\partial r} \left( \frac{u_\theta}{r} \right) + \frac{1}{r} \frac{\partial u_r}{\partial \theta} \right) = 0, \\ \tau_{r\phi} &= \eta \left( r \frac{\partial}{\partial r} \left( \frac{u_\phi}{r} \right) + \frac{1}{r \sin \theta} \frac{\partial u_r}{\partial \phi} \right) = 0.\end{aligned}\tag{2.17}$$

Those equations are applied directly to the reference boundary  $R^\pm$ , the topography  $h$  being considered small.

Finally, boundary conditions on the temperature field are required. We assume in this study that the solid/liquid phase transition occurs at a laterally constant temperature. Hence, neglecting the topography, Dirichlet conditions are used at both boundaries:

$$T(r = R^-) = T^-, \quad T(r = R^+) = T^+.\tag{2.18}$$

## 2.3 Dynamic pressure choice

Applying the boundary condition eq. (2.16) at both boundaries might lead to a non-zero average radial velocity at a boundary. This would be equivalent to a net-freezing of one magma ocean and a net-melting of the other. We want to decouple completely net-freezing or melting of the magma oceans (related to the long term evolution of the system) and dynamical freezing or melting at the boundaries (related to the dynamic topography formed by viscous forces). To this effect, the dynamic pressure needs to be chosen to ensure the boundary condition eq. (2.16) cannot yield a non-zero average radial velocity. In the rest of this document,  $\langle \bullet \rangle$  denotes the lateral mean of a quantity. As previously,  $+$  and  $-$  superscripts denote quantities evaluated at the top and bottom boundary respectively.

Denoting  $T_p$  the temperature profile such that  $T = T_p$  yields  $p = 0$ , the Stokes eq. (2.2) becomes

$$\mathbf{0} = -\nabla p + \eta \nabla^2 \mathbf{u} + \rho g \alpha (T - T_p) \hat{\mathbf{r}}.\tag{2.19}$$

Integrating the Stokes equation over the entire solid domain  $\Omega$  and projecting on  $\hat{\mathbf{r}}$  gives:

$$0 = \int_+ \left( 2\eta \frac{\partial u_r}{\partial r} - p \right) dS - \int_- \left( 2\eta \frac{\partial u_r}{\partial r} - p \right) dS + \int_\Omega \rho g \alpha (T - T_p) dV.\tag{2.20}$$

Plugging the phase change boundary condition eq. (2.16) in eq. (2.20) leads to

$$\Delta \rho^+ g \tau_\phi^+ (R^+)^2 \langle u_r \rangle^+ + |\Delta \rho^-| g \tau_\phi^- (R^-)^2 \langle u_r \rangle^- = \rho g \alpha \int_{R^-}^{R^+} (\langle T \rangle - T_p) r^2 dr.\tag{2.21}$$

Finally, mass conservation gives us:

$$(R^+)^2 \langle u_r \rangle^+ = (R^-)^2 \langle u_r \rangle^-.\tag{2.22}$$

This leads to

$$(\Delta\rho^+\tau_\phi^+ + |\Delta\rho^-\tau_\phi^-) (R^+)^2 \langle u_r \rangle^+ = \rho\alpha \int_{R^-}^{R^+} (\langle T \rangle - T_p) r^2 dr. \quad (2.23)$$

Equation (2.23) shows the average topography at the boundaries  $\tau_\phi^\pm \langle u_r \rangle^\pm$  is directly proportional to the average buoyancy of the bulk. Choosing  $T_p$  equal to  $\langle T \rangle$  therefore ensures the average topography (and average radial velocity) is zero at all time. Defining the dynamic pressure as  $p = P - \langle P \rangle$ , the Stokes eq. (2.2) becomes

$$\mathbf{0} = -\nabla p + \eta \nabla^2 \mathbf{u} + \rho g \alpha (T - \langle T \rangle) \hat{\mathbf{r}}. \quad (2.24)$$

## 2.4 Dimensionless equations

The equations are made dimensionless in order to reduce the number of parameters describing the physical problem. The scales for distance, time, mass and temperature are respectively the thickness of the domain  $L = R^+ - R^-$ , the thermal diffusive timescale  $\frac{L^2}{\kappa}$ , the mass  $\eta \frac{L^3}{\kappa}$  and the temperature difference  $\Delta T = T^- - T^+$  between the two interfaces. The dimensionless temperature  $\tilde{T}$  is defined as:

$$\tilde{T} = \frac{T - T^+}{\Delta T}. \quad (2.25)$$

Using the same symbols for dimensionless and dimensional quantities, the non dimensional conservation equations write

$$\nabla \cdot \mathbf{u} = \mathbf{0} \quad (2.26)$$

$$\mathbf{0} = -\nabla p + \nabla^2 \mathbf{u} + \text{Ra}(T - \langle T \rangle) \hat{\mathbf{r}} \quad (2.27)$$

$$\frac{\partial T}{\partial t} + \mathbf{u} \cdot \nabla T = \nabla^2 T \quad (2.28)$$

where Ra is the Rayleigh number defined as:

$$\text{Ra} \equiv \frac{\rho g \alpha \Delta T L^3}{\eta \kappa}. \quad (2.29)$$

This dimensionless number compares the buoyancy forces which drive the convection to the momentum and heat diffusion coefficients which limit the convection.

With eq. (2.25), the boundary conditions for the temperature are straightforward:

$$\begin{aligned} T^- &= T(R^-) = 1; \\ T^+ &= T(R^+) = 0. \end{aligned} \quad (2.30)$$

The free-slip boundary condition eq. (2.17) gives:

$$\begin{aligned} r \frac{\partial}{\partial r} \left( \frac{u_\theta}{r} \right) + \frac{1}{r} \frac{\partial u_r}{\partial \theta} &= 0, \\ r \frac{\partial}{\partial r} \left( \frac{u_\phi}{r} \right) + \frac{1}{r \sin \theta} \frac{\partial u_r}{\partial \phi} &= 0. \end{aligned} \quad (2.31)$$

Finally, the normal stress continuity condition eq. (2.16) leads to:

$$\pm \Phi^\pm u_r + 2 \frac{\partial u_r}{\partial r} - p = 0. \quad (2.32)$$

$\Phi^+$  and  $\Phi^-$  are the dimensionless phase change numbers of the top and bottom interfaces, defined as

$$\Phi^\pm \equiv \frac{|\Delta\rho|^\pm gL}{\eta} \tau_\phi. \quad (2.33)$$

These parameters are ratios between the phase change timescale  $\tau_\phi$  and the timescale needed to build topography by viscous forces. These numbers represent the resistance of the melting/freezing boundaries to the flow of matter through them. If  $\Phi \rightarrow 0$  at one interface, the boundary condition eq. (2.32) reduces to a normal stress free condition, meaning the interface is fully permeable. Physically, melting and freezing of matter is much quicker than viscous building of topography, allowing matter to pass easily through the interface. The height of the topography is indeed limited by the rate at which it is melted/frozen away instead of its buoyancy. On the contrary, if  $\Phi \rightarrow \infty$ , the boundary condition eq. (2.32) imposes that  $u_r = 0$ , which corresponds to the impermeable boundary condition. Physically, viscous building of topography is fast enough for the height of the topography to be limited by its weight rather than melting or freezing, hence preventing matter from crossing the boundary.

After making the equations dimensionless, only four parameters are necessary to describe the system. The inner radius  $R^-$  characterizing the geometry (the outer radius being  $R^+ = 1 + R^-$  since lengths are made dimensionless with the thickness of the domain), the Rayleigh number  $Ra$  describing the strength of convection, and the two phase change numbers  $\Phi^\pm$  parameterizing the behavior of the two interfaces with the magma oceans.

# Chapter 3

## Linear stability analysis of the static thermal problem

A first approach to study the system described in chapter 2 is a linear stability analysis. We study here the stability of the conductive state in the solid, varying the phase change numbers  $\Phi^\pm$  as well as the geometry of the system defined by the dimensionless position of the internal boundary  $R^-$ . The approach presented here is akin to that used by Deguen (2013) who studies a similar problem with three differences:

- the gravity acceleration is considered constant in our study while it varies linearly with the radial position in Deguen (ibid.);
- we neglect internal heating in our study, while Deguen (ibid.) considers a volumetrically heated domain;
- the Rayleigh number is defined with the temperature difference and the domain thickness in our study, but with the volumetric heating rate and the outer radius in Deguen (ibid.); comparison of the critical Rayleigh number values between the two studies should therefore be made with care.

### 3.1 Motionless reference state

The system of partial differential equations formed by the conservation eqs. (2.26) to (2.28) and their boundary conditions eqs. (2.30) to (2.32) exhibits a purely conductive (i.e. motionless) steady solution. This solution is denoted by an overline in this chapter. Since it is a steady motionless state, we have

$$\bar{\mathbf{u}} = \mathbf{0} \tag{3.1}$$

and

$$\nabla^2 \bar{T} = 0. \tag{3.2}$$

The latter equation along with the boundary conditions on temperature eq. (2.30) lead to a reference temperature  $\bar{T}$  that is laterally constant and varies with the radius as

$$\bar{T} = \frac{R^+ R^-}{r} - R^-. \tag{3.3}$$

Injecting this in the Stokes eq. (2.27) gives

$$\nabla \bar{p} = \mathbf{0}. \quad (3.4)$$

Therefore,  $\bar{p}$  is constant throughout the solid domain. Since it should be null to satisfy the phase change boundary condition eq. (2.32), one obtains

$$\bar{p} = 0. \quad (3.5)$$

Introducing the temperature anomaly  $\Theta = T - \bar{T}$ , the conservation equations become:

$$\nabla \cdot \mathbf{u} = 0; \quad (3.6)$$

$$\mathbf{0} = -\nabla p + \nabla^2 \mathbf{u} + \text{Ra} (\Theta - \langle \Theta \rangle) \hat{\mathbf{r}}; \quad (3.7)$$

$$\frac{\partial \Theta}{\partial t} + \mathbf{u} \cdot \nabla (\Theta + \bar{T}) = \nabla^2 \Theta. \quad (3.8)$$

The boundary conditions on  $\Theta$  are  $\Theta = 0$  at both boundaries.

## 3.2 Poloidal potential formulation

Since the fluid is considered isoviscous and incompressible, the velocity field can be reduced to a scalar field, the poloidal potential  $\mathcal{P}$  defined as (e.g. Ribe 2007; Ricard and Vigny 1989):

$$\mathbf{u} = \nabla \times \nabla \times (\mathcal{P} \mathbf{r}). \quad (3.9)$$

One can notice that the poloidal potential is related to the stream vector  $\Psi$ :

$$\mathbf{u} = \nabla \times \Psi \iff \Psi = \nabla \times (\mathcal{P} \mathbf{r}). \quad (3.10)$$

The three components of the velocity field are then:

$$u_r = \frac{1}{r} \mathcal{L}^2 \mathcal{P}, \quad (3.11)$$

$$u_\theta = \frac{\partial}{\partial \theta} \left( \frac{1}{r} \frac{\partial}{\partial r} (r \mathcal{P}) \right), \quad (3.12)$$

$$u_\phi = \frac{1}{\sin \theta} \frac{\partial}{\partial \phi} \left( \frac{1}{r} \frac{\partial}{\partial r} (r \mathcal{P}) \right). \quad (3.13)$$

$\mathcal{L}^2$  is the scalar operator defined as:

$$\begin{aligned} \mathcal{L}^2 \bullet &\equiv \frac{\partial}{\partial r} \left( r^2 \frac{\partial \bullet}{\partial r} \right) - r^2 \nabla^2 \bullet \\ &= -\frac{1}{\sin \theta} \frac{\partial}{\partial \theta} \left( \sin \theta \frac{\partial \bullet}{\partial \theta} \right) - \frac{1}{\sin^2 \theta} \frac{\partial^2 \bullet}{\partial \phi^2}. \end{aligned} \quad (3.14)$$

Using the following properties (e.g. Dormy 1997):

$$\mathcal{L}^2 \bullet = (\nabla \times \nabla \times (\bullet \mathbf{r})) \cdot \mathbf{r}, \quad (3.15)$$

$$\nabla \times \nabla \times \mathbf{u} = -\nabla \times \nabla \times (\mathbf{r} \nabla^2 \mathcal{P}), \quad (3.16)$$

one can find the poloidal formulation of the momentum conservation equation:

$$(\nabla \times \nabla \times \text{eq. (3.7)}) \cdot \mathbf{r} \iff \mathcal{L}^2 \left( \nabla^4 \mathcal{P} - \frac{\text{Ra}}{r} \Theta \right) = 0. \quad (3.17)$$

Since the poloidal and temperature fields are assumed to be “smooth”, this equation means that the quantity  $\nabla^4 \mathcal{P} - \frac{\text{Ra}}{r} \Theta$  is constant with respect to the  $\phi$  and  $\theta$  directions. This constant can be taken equal to zero without any loss of generality, leading to

$$\nabla^4 \mathcal{P} = \frac{\text{Ra}}{r} \Theta. \quad (3.18)$$

Introducing  $\mathcal{Q}$  such as:

$$\mathcal{Q} \equiv \nabla^2 \mathcal{P}, \quad (3.19)$$

eq. (3.18) can be written

$$\nabla^2 \mathcal{Q} = \frac{\text{Ra}}{r} \Theta. \quad (3.20)$$

The heat conservation equation eq. (3.8) becomes:

$$\frac{\partial \Theta}{\partial t} + (\nabla \times \nabla \times (\mathcal{P} \mathbf{r})) \cdot \nabla \Theta = \nabla^2 \Theta + R^- R^+ \frac{1}{r^3} \mathcal{L}^2 \mathcal{P}. \quad (3.21)$$

Using eqs. (3.11) to (3.13), the free-slip boundary condition eq. (2.31) leads to:

$$\frac{\partial^2 \mathcal{P}}{\partial r^2} + (\mathcal{L}^2 - 2) \frac{\mathcal{P}}{r^2} = C_{\theta, \phi} \quad (3.22)$$

where  $C_{\theta, \phi}$  denotes an arbitrary constant along the  $\theta$  and  $\phi$  directions. The choice of  $C_{\theta, \phi}$  does not matter to perform the linear stability analysis since it is a term of harmonic degree 0 and therefore vanishes when equations are written for higher harmonic degrees. Degree-0 terms are ignored since they are forbidden by our definition of the dynamic pressure as shown in section 2.3.

Finally, since the dynamic pressure does not appear in the poloidal formulation of the momentum conservation eq. (3.20), it should be eliminated from the normal stress continuity boundary condition eq. (2.32). Denoting  $\boldsymbol{\omega} = \nabla \times \mathbf{u}$  the vorticity and recalling  $\nabla \cdot \mathbf{u} = \mathbf{0}$ , one can deduce that

$$\nabla^2 \mathbf{u} = -\nabla \times \boldsymbol{\omega}. \quad (3.23)$$

The projection of the momentum conservation eq. (3.7) along  $\hat{\boldsymbol{\theta}}$  gives

$$\frac{1}{r} \frac{\partial p}{\partial \theta} + (\nabla \times \boldsymbol{\omega}) \cdot \hat{\boldsymbol{\theta}} = 0. \quad (3.24)$$

Since there is no source of toroidal potential in the studied problem, there is no radial vorticity (e.g. Ribe 2007). Hence,

$$(\nabla \times \boldsymbol{\omega}) \cdot \hat{\boldsymbol{\theta}} = -\frac{1}{r} \frac{\partial}{\partial r} (r \omega_\phi). \quad (3.25)$$

With eqs. (3.11) and (3.12), one obtains:

$$\omega_\phi = (\nabla \times \mathbf{u}) \cdot \hat{\boldsymbol{\phi}} = \frac{1}{r} \left( \frac{\partial}{\partial r} (r u_\theta) - \frac{\partial u_r}{\partial \theta} \right) = \frac{\partial}{\partial \theta} (\nabla^2 \mathcal{P}). \quad (3.26)$$

Putting eqs. (3.25) and (3.26) in eq. (3.24) leads to:

$$\frac{\partial p}{\partial \theta} = \frac{\partial^2}{\partial \theta \partial r} (r \nabla^2 \mathcal{P}). \quad (3.27)$$

Performing a similar calculation on the  $\phi$  direction gives this relation between the dynamic pressure and the poloidal potential:

$$-p + \frac{\partial}{\partial r} (r \nabla^2 \mathcal{P}) = K_{\theta, \phi} \quad (3.28)$$

where  $K_{\theta, \phi}$  is an arbitrary constant along the  $\theta$  and  $\phi$  directions. This allows us to substitute the pressure in the phase change condition eq. (2.32):

$$\pm \Phi^\pm \frac{1}{r} \mathcal{L}^2 \mathcal{P} + \frac{\partial}{\partial r} \left( \frac{2}{r} \mathcal{L}^2 \mathcal{P} - r \mathcal{Q} \right) = K_{\theta, \phi}. \quad (3.29)$$

Note that as  $C_{\theta, \phi}$  in eq. (3.22), the actual value of  $K_{\theta, \phi}$  is irrelevant in this study.

### 3.3 Perturbation equations

Since  $\Theta$  is defined as the temperature difference to the conductive state, it already represents the perturbation of temperature with respect to the reference state. Perturbations of the poloidal potential  $\mathcal{P}$ ,  $\mathcal{Q}$  and the temperature field  $\Theta$  are developed using spherical harmonics as following:

$$\begin{aligned} \mathcal{P} &= \sum_{l=1}^{\infty} \sum_{m=-l}^l P_l^m(r) Y_l^m(\theta, \phi) e^{\sigma_l t}, \\ \mathcal{Q} &= \sum_{l=1}^{\infty} \sum_{m=-l}^l Q_l^m(r) Y_l^m(\theta, \phi) e^{\sigma_l t}, \\ \Theta &= \sum_{l=1}^{\infty} \sum_{m=-l}^l T_l^m(r) Y_l^m(\theta, \phi) e^{\sigma_l t}. \end{aligned} \quad (3.30)$$

Note that the  $l = 0$  harmonic is not taken into account since it corresponds to the motionless conductive state.

In the frame of linear stability analysis, one can study each mode  $(l, m)$  in an independent way. For a given problem  $(R^-, \Phi^+, \Phi^-)$ , the goal of the analysis is to determine which mode is the most unstable and what is its associated critical Rayleigh number  $\text{Ra}_c$ . Moreover, the problem is degenerated in terms of lateral orientation. Hence, the growth rate  $\sigma_l$  of any given mode  $(l, m)$  only depends on  $l$ . For readability purposes,  $m$  indices are dropped.

The differential operators can easily be written for any mode  $l$ . Indeed, spherical harmonics are eigenfunctions of the  $\mathcal{L}^2$  operator. Applying  $\mathcal{L}^2$  to a given mode reduces to:

$$\mathcal{L}^2 \bullet = l(l+1) \bullet. \quad (3.31)$$

The laplacian operator applied to a given mode is then:

$$\mathcal{D}_l^2 \bullet \equiv \frac{\partial^2 \bullet}{\partial r^2} + \frac{2}{r} \frac{\partial \bullet}{\partial r} - \frac{l(l+1)}{r^2} \bullet. \quad (3.32)$$

The conservation equations eqs. (3.19) to (3.21) can be written as (the only neglected non-linear term being the advection  $\mathbf{u} \cdot \nabla \Theta$ ):

$$Q_l = \mathcal{D}_l^2 P_l, \quad (3.33)$$

$$\mathcal{D}_l^2 Q_l = \frac{\text{Ra}}{r} T_l, \quad (3.34)$$

$$(\sigma_l - \mathcal{D}_l^2) T_l = R^- R^+ \frac{l(l+1)}{r^3} P_l. \quad (3.35)$$

Finally, the boundary conditions eqs. (2.30), (3.22) and (3.29) can be written as:

$$(T_l)^\pm = 0, \quad (3.36)$$

$$\left( \frac{d^2 P_l}{dr^2} \right)^\pm + [l(l+1) - 2] \left( \frac{P_l}{r^2} \right)^\pm = 0, \quad (3.37)$$

$$\pm \Phi^\pm l(l+1) \left( \frac{P_l}{r} \right)^\pm + \frac{d}{dr} \left( \frac{2l(l+1)}{r} P_l - r Q_l \right)^\pm = 0. \quad (3.38)$$

Note that the lateral constants  $C_{\theta,\phi}$  and  $K_{\theta,\phi}$  do not appear in those equations since they are of degree  $l = 0$ . Also, as mentioned previously, the linearized equations are independent of the order  $m$  of the considered mode.

### 3.4 Eigenvalue formulation

Using a Chebyshev-collocation approach (e.g. Canuto et al. 1985; Guo et al. 2012), the system defined by eqs. (3.33) to (3.38) can be formulated as a generalized eigenvalue problem. Chebyshev polynomials are used to expand the perturbations along the radial direction. Each vertical mode  $P_l$ ,  $Q_l$  and  $T_l$  is entirely characterized by  $N + 1$  Chebyshev-Gauss-Lobatto nodal points at  $z_i = \cos \frac{i\pi}{N}$  with  $i = 0 \dots N$ . To map the  $z \in [-1, 1]$  space to the  $r \in [R^-, R^+]$  space, one uses the following transformation:

$$r_i = \frac{z_i + 1}{2} + R^-. \quad (3.39)$$

Each vertical mode can then be represented by a vector with  $N + 1$  components. For example, the toroidal potential vertical mode  $P_l$  is represented by  $\mathbf{P}$ , the vector such as  $\mathbf{P}_i = P_l(r_i)$ . Similarly,  $Q_l$  and  $T_l$  are represented by  $\mathbf{Q}$  and  $\mathbf{T}$ .

With such a formalism, the successive radial derivatives of each vertical mode at any nodal point can be computed with the help of a differentiation matrix  $\mathbf{d}$ :

$$\frac{\partial^k \mathbf{P}}{\partial r^k} = \mathbf{d}^k \mathbf{P}. \quad (3.40)$$

Note that for numerical precision reasons, the powers of  $\mathbf{d}$  are computed separately instead of directly as the successive powers of  $\mathbf{d}$ . The differentiation matrices  $\mathbf{d}^k$  are calculated with the help of a Python adaptation of DMSUITE (Weideman and Reddy 2000). The Python package is available at <https://github.com/labrosse/dmsuite>.



The neutral Rayleigh number  $\text{Ra}_n$  is the Rayleigh number such as  $\mathcal{R}(\sigma(\text{Ra}_n)) = 0$  where  $\mathcal{R}$  denotes the real part. Finally, for a given problem  $\Pi$ , one can compute the neutral Rayleigh number as a function of the harmonic degree  $l$  of the perturbation. The degree  $l_c$  for which  $\text{Ra}_n(l)$  is minimal is the most unstable mode of the problem  $\Pi$ . The associated Rayleigh number  $\text{Ra}_c = \text{Ra}_n(l_c)$  is the critical Rayleigh number of  $\Pi$ .

### 3.5 Results

A simple way to test the linear stability analysis is to perform the analysis with classical non-permeable free-slip condition at both boundaries for which linear analysis have already been obtained. For comparison, in cartesian geometry, one gets a critical Rayleigh number  $\text{Ra}_c = 657.52$  and an associated wavenumber  $k_x = 2.23$  (Strutt 1916). In a spherical shell of aspect ratio  $\gamma \equiv R^-/R^+ = 0.55$ , the critical Rayleigh number is  $\text{Ra}_c = 711.95$ , associated with the harmonic degree  $l = 3$ . Again, this is in perfect agreement with the existing literature (e.g. Bercovici and Schubert 1988). Moreover, when  $\gamma \rightarrow 1$ , the geometry of the spherical shell tends towards a laterally infinite cartesian space. The critical Rayleigh number is hence expected to tend towards the value  $\text{Ra}_c = 657.52$  obtained for the cartesian geometry. With  $\gamma = 0.99$ , the obtained critical Rayleigh number is  $\text{Ra}_c = 657.528$  which is very close to the cartesian value.

In all the performed analyses, the growth rate  $\sigma$  has no imaginary part. All the modes at  $\text{Ra}_c$  presented here are hence non oscillating solutions.

Figures 3.1 and 3.2 show the most unstable mode and associated critical Rayleigh number for various cases. Since the linear problem we solve here is degenerated in terms of lateral orientation, all modes with the same harmonic degree  $l$  but different orders  $m$  have the same growth rate. We choose in figs. 3.1 and 3.2 to represent the critical mode of order  $m = l_c$  ( $l_c$  being the degree of the critical mode) in the equatorial plane  $\theta = \frac{\pi}{2}$ . Moreover, instead of showing the poloidal potential perturbation, we show instead isovalues of the stream vector component along  $\hat{\theta}$ . These are streamlines of the flow in the equatorial plane. Enforcing  $l = m$  leads to the following relationship between the  $\Psi_\theta$  component of the stream vector and the poloidal potential eigenmode  $P_l$ :

$$\Psi_\theta(r, \phi) = \mathcal{R} \left( ilP_l(r)Y_l^l \left( \frac{\pi}{2}, \phi \right) \right) \quad (3.47)$$

where  $\mathcal{R}$  denotes the real part.

The left column of fig. 3.1 shows the classical case with non-penetrative boundaries. The critical mode consists in nearly aspect-ratio-one convective rolls, and therefore a higher critical harmonic degree as the aspect ratio of the shell increases. We can see on the right column of fig. 3.1 the effects of a small phase change number at the bottom boundary while a classic non-penetrative condition is prescribed at the top boundary. Owing to the flow-through boundary condition, streamlines are not deviated by the boundary and can instead pass through it as matter melts (downwellings) or freezes (upwellings). Hence, as expected in section 2.4, a low value of the phase change number  $\Phi$  allows matter to cross the boundary. The return current necessary to conserve mass happens in the magma ocean. This leads to

convective patterns with a larger wavelength than the classical rolls, as well as a lower critical Rayleigh number as less deformation is involved in these modes than in the classical rolls.

The left column of fig. 3.2 shows that with a flow-through boundary condition with a small phase change number at the top boundary, the most unstable mode is a degree-one pattern regardless of the aspect ratio of the shell. Matter crystallizes on one hemisphere of the shell, goes through the other side avoiding the core, and finally melts on the other hemisphere. As shown in the right column of fig. 3.2, when both phase change numbers are small (i.e. both boundaries are flow through), streamlines go straight through the entire shell. All the cases shown on fig. 3.2 correspond to degree-one translation modes of convection. The solid shell departs from its equilibrium position but is constantly recycled and kept in place as it freezes on one side and melts on the other. When both boundaries are flow-through, this translation operates without any deformation in the solid. Convection is only limited by the rate at which melting and freezing can occur and, as shown in section 3.6, the critical Rayleigh number can be arbitrarily small and is proportional to  $\Phi^\pm$ . Note that this complete absence of deformation is valid in the frame of linear stability, the non-linear numerical simulations presented in the next chapter yield a slightly different result. Finally, when only the top boundary is flow-through, the translation is associated to some deformation in the solid, necessary for the convecting matter to go around the core.

Figures 3.3 to 3.5 show the effects of varying the phase change number on the critical Rayleigh number and associated critical harmonic degree. A first observation from these figures is that when both phase change numbers are high ( $\Phi^\pm \gtrsim 10^2$ ), the system exhibits the same critical Rayleigh numbers and wavelengths as with the classical non-penetrative free-slip boundary conditions. This is expected from the definition of the phase change number  $\Phi$ , as discussed in section 2.4. As either or both phase change number decrease, the corresponding boundaries transition to the flow-through regime. The critical Rayleigh number and associated harmonic degree decrease as the boundary condition allows for larger wavelength modes of convection. When only one boundary is flow-through (figs. 3.3 and 3.4), the critical Rayleigh number decreases of roughly one order of magnitude. As shown in section 3.6, the critical Rayleigh number can be arbitrarily small when both boundaries are flow-through and the translation regime is the most unstable (see fig. 3.5). A remarkable feature visible on fig. 3.4 and fig. 3.5 is that a small value of  $\Phi^+$  (smaller than about 10) leads to a degree-one translation mode regardless of the aspect ratio of the shell  $\gamma$  or the value of  $\Phi^-$  (a large value for the latter leads to a translation mode with deformation as discussed above).

Finally, figs. 3.6 to 3.8 show the effect of varying the aspect ratio of the shell on the stability of several harmonics degree in three setups: flow-through condition only at the bottom (fig. 3.6), only at the top (fig. 3.7), and at both boundaries (fig. 3.8). As observed before, fig. 3.7 and fig. 3.8 show the degree-one mode is the most unstable for any aspect ratio. Moreover, one can notice the neutral Rayleigh number of other modes is much higher than that of the degree-one, showing the degree-one translation mode is strongly favored. The case of a flow-through boundary only at the bottom depicted in fig. 3.6 exhibits an interesting behavior. For aspect ratio lower than about 0.75, the most unstable mode corresponds to convective rolls that cross the boundary. These rolls are about twice as wide as the classical convective

rolls obtained with non-penetrative boundary conditions, as observed in fig. 3.1 for  $\gamma < 0.8$  (for  $\gamma = 0.2$  it is geometrically impossible for the rolls in the flow-through case to be wider than those in the non-penetrative case). However, for higher aspect ratios of the shell, instead of higher harmonic degrees corresponding merely to these wider rolls, the most unstable mode is of degree-one. This mode is the one shown for  $\gamma = 0.8$  on fig. 3.1, it corresponds to a mode where matter freezes on one inner hemisphere and melts on the other, akin to what happens in the translation mode excepts more deformation is involved in the solid. Note that this degree-one mode has a critical Rayleigh number close to that of other modes as visible on fig. 3.6, allowing competition between the degree-one mode and higher-degree modes at intermediate values of the aspect ratio  $\gamma$ . This contrasts strongly with the translation mode exhibited by cases with a flow-through condition at the top boundary (figs. 3.7 and 3.8) that is clearly the most unstable mode.

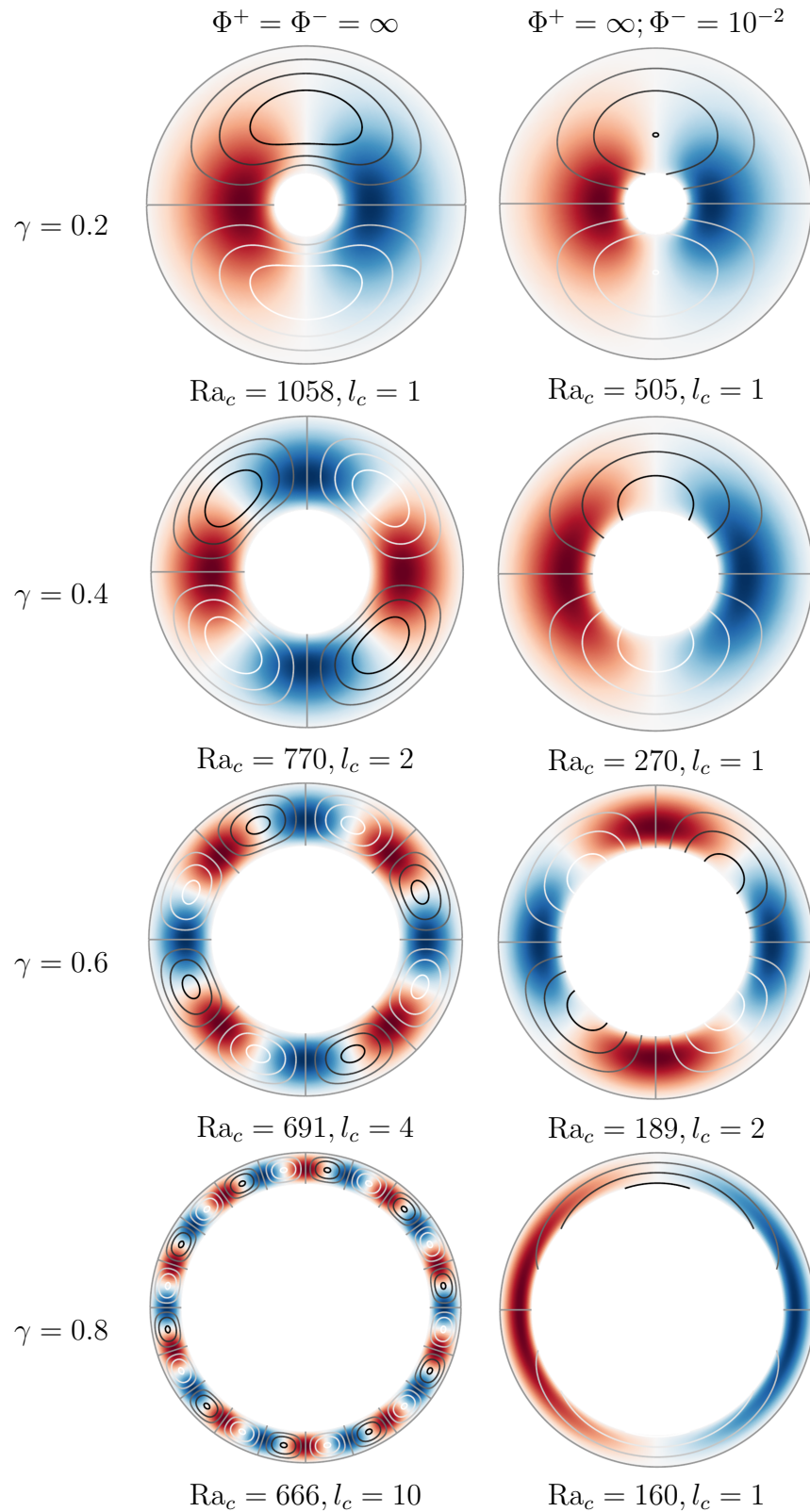


Figure 3.1: Temperature perturbation and streamlines of the most unstable mode for non-penetrative boundary conditions (left) and flow-through at the bottom (right). Each row is a different value of the aspect ratio  $\gamma$  of the shell. The critical Rayleigh number  $Ra_c$  and harmonic degree  $l_c$  are indicated under each figure.

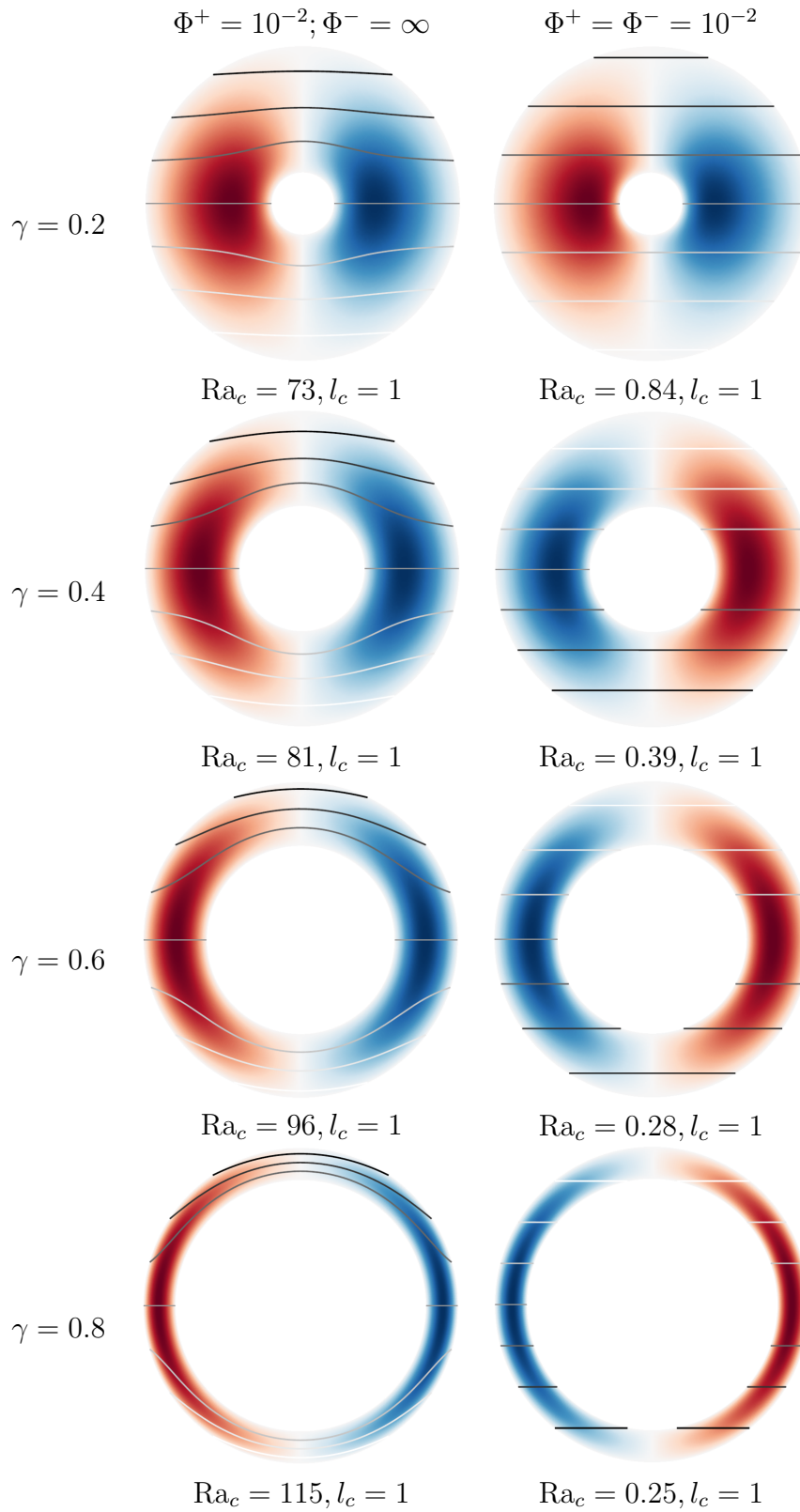


Figure 3.2: Temperature perturbation and streamlines of the most unstable mode for flow-through at the top (left) and flow-through at both boundaries (right). Each row is a different value of the aspect ratio  $\gamma$  of the shell. The critical Rayleigh number  $\text{Ra}_c$  and harmonic degree  $l_c$  are indicated under each figure.

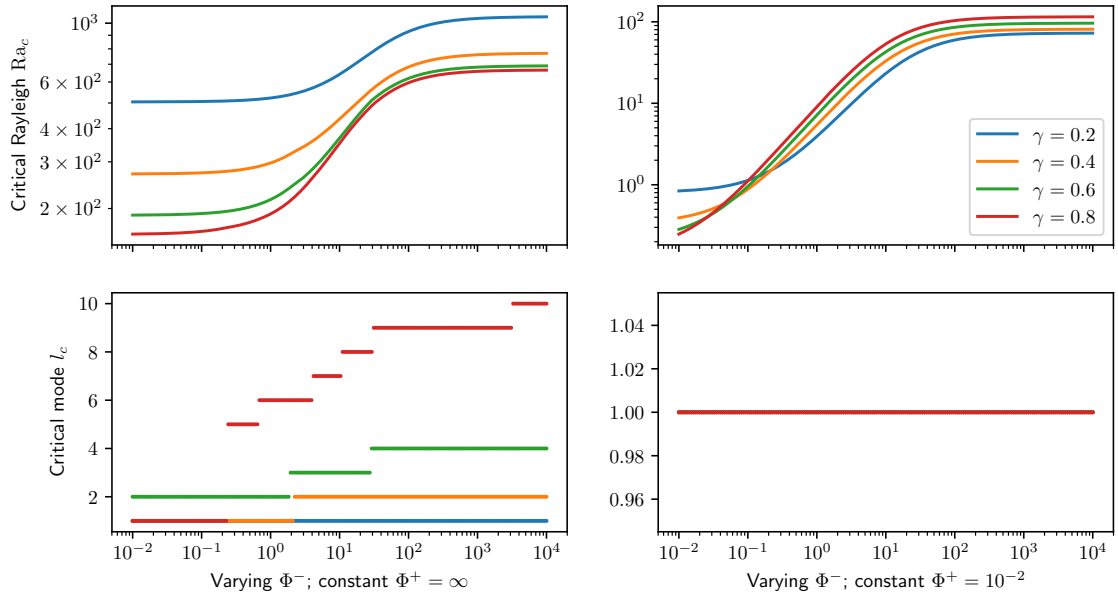


Figure 3.3: Critical Rayleigh number and associated harmonic degree for varying  $\Phi^-$  and various aspect ratios. Left: top boundary is non-penetrative, right: top boundary is flow-through.

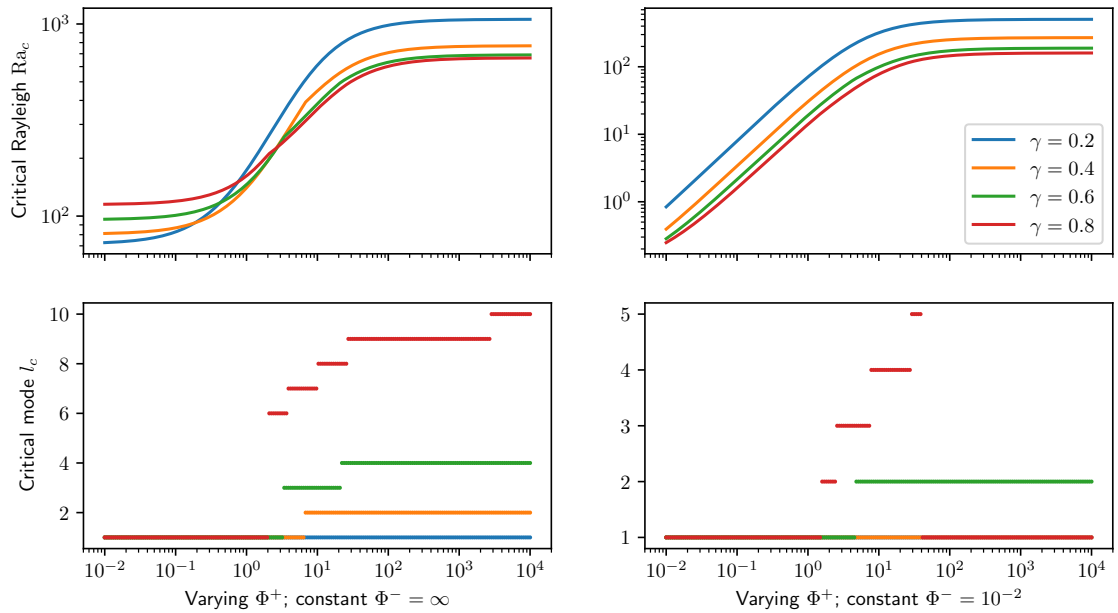


Figure 3.4: Critical Rayleigh number and associated harmonic degree for varying  $\Phi^+$  and various aspect ratios. Left: bottom boundary is non-penetrative, right: bottom boundary is flow-through.

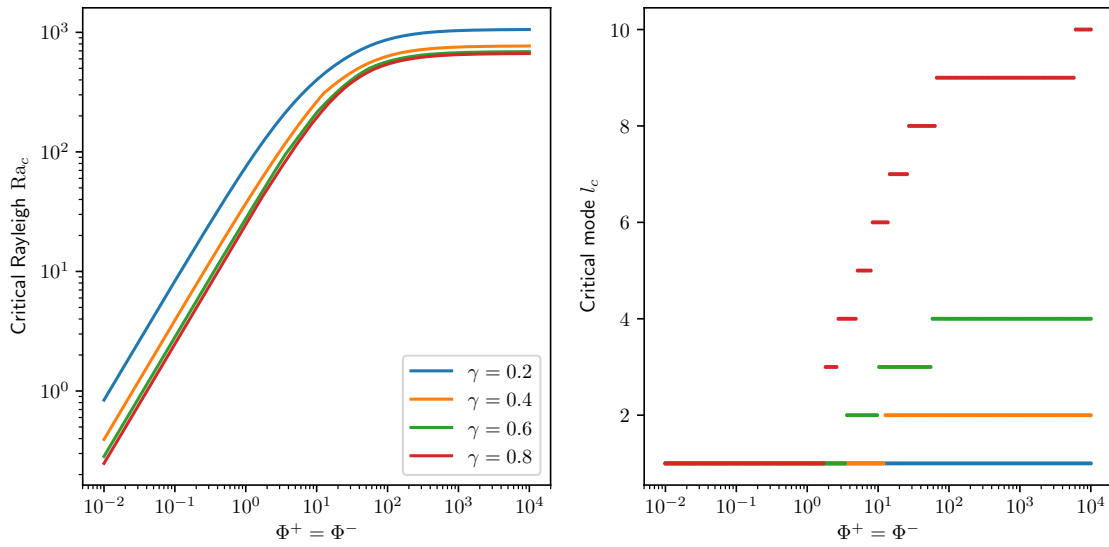


Figure 3.5: Critical Rayleigh number and associated harmonic degree for varying  $\Phi^+ = \Phi^-$  and various aspect ratios.

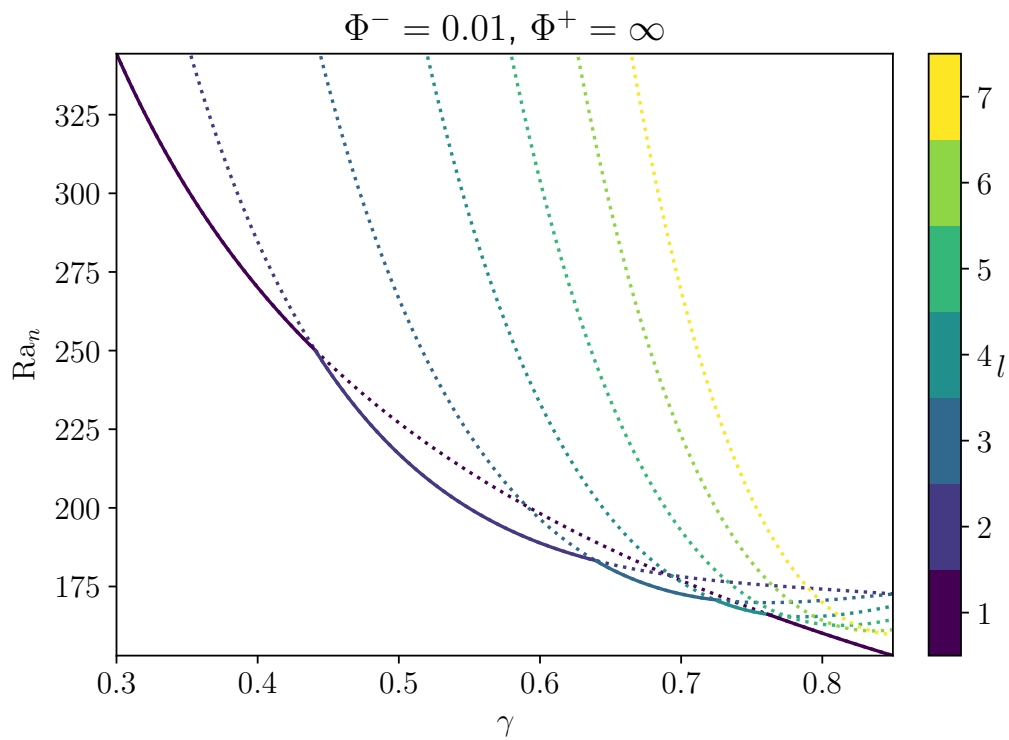


Figure 3.6: Neutral Rayleigh number of several modes as a function of the aspect ratio of the spherical shell. Boundary conditions are flow-through at the bottom and non-penetrative at the top.

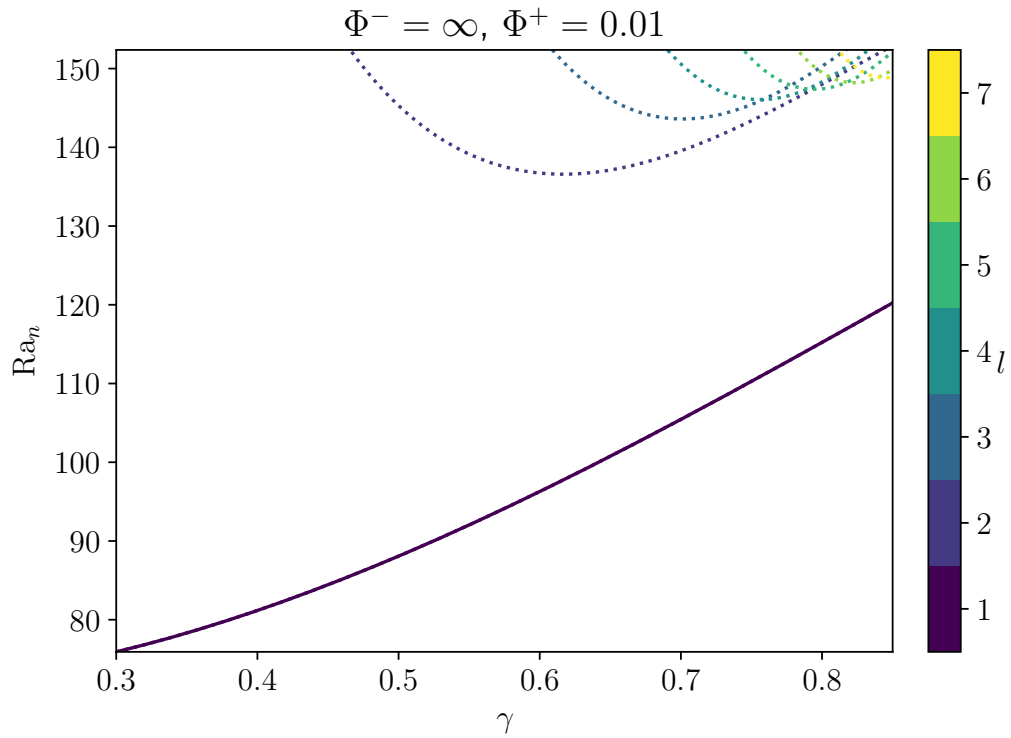


Figure 3.7: Neutral Rayleigh number of several modes as a function of the aspect ratio of the spherical shell. Boundary conditions are non-penetrative at the bottom and flow-through at the top.

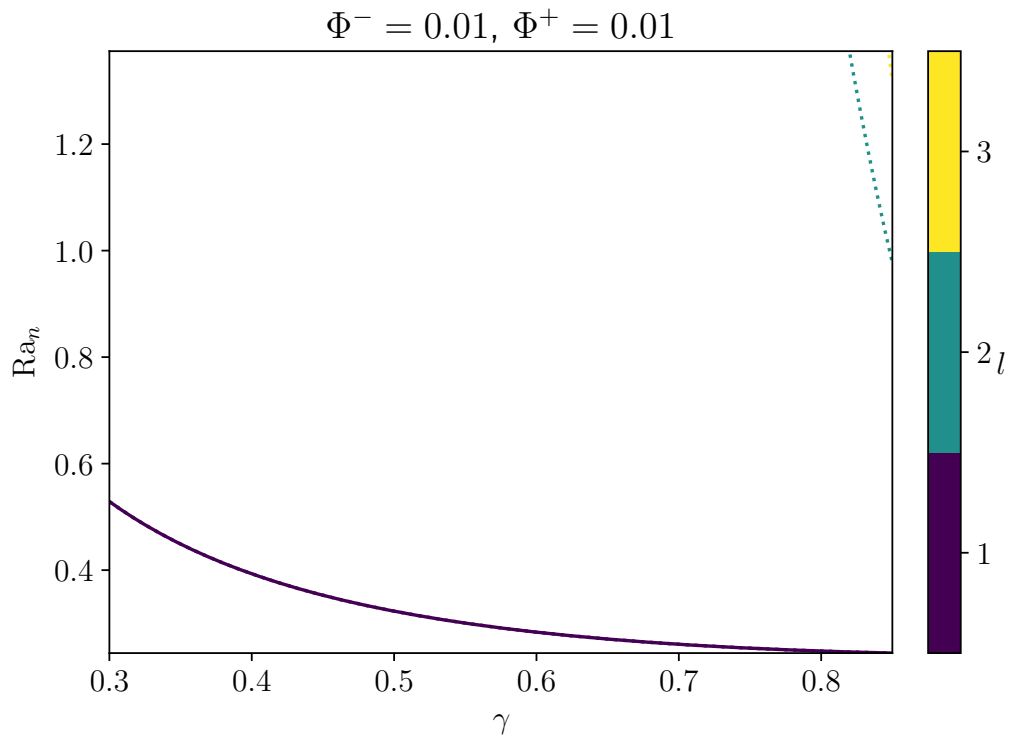


Figure 3.8: Neutral Rayleigh number of several modes as a function of the aspect ratio of the spherical shell. Boundary conditions are flow-through at both boundaries.

## 3.6 Analytical study of the translation mode

The degree-one translation solution is the dominating convection regime when both phase change numbers  $\Phi^\pm$  are small. This section presents an analytical determination of the critical Rayleigh number of this mode of convection.

In this section,  $U\hat{\mathbf{t}}$  denotes the translation velocity.  $U$  is its amplitude and  $\hat{\mathbf{t}}$  a unit vector along the translation direction. The colatitude is chosen as  $\theta = (\hat{\mathbf{t}}, \hat{\mathbf{r}})$ , see fig. 3.9 for a schematic of the setup.

### 3.6.1 Buoyancy – topographic weight equilibrium

Integrating the Stokes eq. (2.27) over the entire domain  $\Omega$  yields

$$\begin{aligned} \mathbf{0} &= \int_+ (-p\hat{\mathbf{r}} + (\nabla u + \nabla u^T) \cdot \hat{\mathbf{r}}) dS \\ &\quad - \int_- (-p\hat{\mathbf{r}} + (\nabla u + \nabla u^T) \cdot \hat{\mathbf{r}}) dS \\ &\quad + \int_\Omega \text{Ra} (T - \langle T \rangle) \hat{\mathbf{r}} dV. \end{aligned} \quad (3.48)$$

Plugging the free-slip boundary condition eq. (2.31) and the phase change boundary condition eq. (2.32) in eq. (3.48) leads to

$$\int_\Omega \text{Ra} (T - \langle T \rangle) \hat{\mathbf{r}} dV = \int_+ \Phi^+ u_r \hat{\mathbf{r}} dS + \int_- \Phi^- u_r \hat{\mathbf{r}} dS. \quad (3.49)$$

Equation (3.49) shows the buoyancy of the domain (left-hand-side) compensates the total weight of the dynamical topographies (right-hand-side).

One can expand the temperature and velocity fields as series of Legendre polynomials. Projecting eq. (3.49) along the translation direction  $\hat{\mathbf{t}}$  gives the following relation between their degree one components:

$$\text{Ra} \int_{R^-}^{R^+} \underbrace{\int_0^\pi T \cos \theta \sin \theta d\theta}_{\frac{2}{3}T_1} r^2 dr = ((R^+)^2 \Phi^+ + (R^-)^2 \Phi^-) \underbrace{\int_0^\pi u_r \cos \theta \sin \theta d\theta}_{\frac{2}{3}u_{r=1} = \frac{2}{3}U}. \quad (3.50)$$

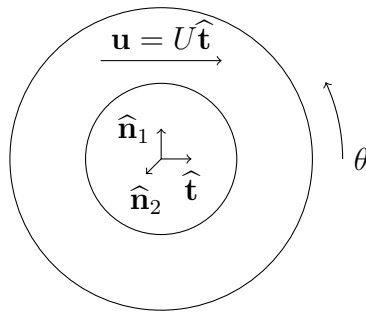


Figure 3.9: Physical setup and chosen frame in a degree-one translation case. This figure is drawn in the  $\varphi = 0$  plane. The system is axisymmetric around  $\hat{\mathbf{t}}$  (i.e.  $\varphi$ -invariant).

This yields the following relation between the translation velocity  $U$  and the degree-one  $T_1$  of the temperature field

$$U = \frac{\text{Ra}}{(R^+)^2\Phi^+ + (R^-)^2\Phi^-} \int_{R^-}^{R^+} T_1 r^2 dr. \quad (3.51)$$

### 3.6.2 Critical Rayleigh number

The linear growth rate of  $T_1$  is

$$\frac{\partial T_1}{\partial t} = -U \frac{\partial \bar{T}}{\partial r} + \mathcal{D}_1^2 T_1 \quad (3.52)$$

where  $\bar{T}$  is the reference conductive profile eq. (3.3), which is also the degree-zero component of the temperature field. The advection of the degree-two component  $T_2$  is neglected as it is a non-linear term. If the Rayleigh number is at the critical value for the degree-one mode of convection (i.e. the translation mode), then the growth rate of  $T_1$  should be zero. Solving eq. (3.52) for  $\frac{\partial T_1}{\partial t} = 0$  (with  $T_1^\pm = 0$ ) and injecting the solution in eq. (3.51) therefore gives us an equation for the critical Rayleigh number of the translation mode.

$$\begin{aligned} \mathcal{D}_1^2 T_1 = U \frac{\partial \bar{T}}{\partial r} &= -U R^- R^+ \frac{1}{r^2} \\ \Leftrightarrow T_1 = \frac{U}{2} R^- R^+ \left( 1 - \frac{(R^+)^2 - (R^-)^2}{(R^+)^3 - (R^-)^3} r + \frac{(R^+)^2 (R^-)^3 - (R^+)^3 (R^-)^2}{(R^+)^3 - (R^-)^3} \frac{1}{r^2} \right) \end{aligned} \quad (3.53)$$

This leads to:

$$\text{Ra}_c = 24 \frac{((R^+)^2\Phi^+ + (R^-)^2\Phi^-)((R^+)^3 - (R^-)^3)}{R^+ R^- ((R^+)^2 + 4R^+ R^- + (R^-)^2)}. \quad (3.54)$$

Introducing the aspect ratio  $\gamma \equiv \frac{R^-}{R^+}$ , one obtains:

$$\text{Ra}_c = 24 \frac{(\Phi^+ + \gamma^2\Phi^-)(1 - \gamma^3)}{\gamma(1 - \gamma)(\gamma^2 + 4\gamma + 1)}. \quad (3.55)$$

Note that the critical Rayleigh number of the translation mode is directly proportional to  $\Phi^+ + \gamma^2\Phi^-$ . It can therefore be arbitrarily small as the values of these phase-change parameters decrease. Indeed, since no deformation occurs in the solid, the only limiting factor for convection to happen in the translation regime is the rate at which melting and freezing can occur. Moreover, as  $\gamma$  gets close to 1, the geometry of the system gets closer to that of an infinite cartesian layer. One can notice that

$$\lim_{\gamma \rightarrow 1} \text{Ra}_c = 12(\Phi^+ + \Phi^-), \quad (3.56)$$

which is the linear critical Rayleigh number of the translation mode in cartesian geometry (Labrosse, Morison, et al. 2018).

## 3.7 Concluding remarks

Even though a simple approach, the linear stability analysis exposed in this section sheds light on the dramatic consequences of the flow-through boundary condition on convection in the primitive solid mantle. Note that the results obtained for our system are similar to those of Deguen (2013) for a shell with a gravity increasing with radius and internal heating. This is not surprising given the strong effects of the phase change boundary condition on the behaviour of the flow. These boundary conditions drastically decrease the critical Rayleigh number, affecting the onset of convection in a primitive mantle crystallizing from global magma oceans, as extensively discussed in chapter 6. The geometry of the flow in the solid is also greatly affected by the possibility for matter to cross the boundary: the expected convective patterns exhibit a much larger wavelength than with classical non-penetrative boundary conditions.

It should be kept in mind that the results are only meaningful close to the critical Rayleigh number when non-linear terms play a minor role. Direct numerical simulations are necessary to capture the dynamics of the system at higher Rayleigh numbers and to obtain amplitude for convective velocities, temperature profiles, and associated heat fluxes. This is the goal of the next chapter.



# Chapter 4

## Numerical simulations of the thermal problem

The linear stability analysis exposed in chapter 3 offers interesting insights on the effect of the flow-through boundary condition used to parameterize the exchange of matter between the primitive solid mantle and global magma oceans. Namely, the critical Rayleigh number is drastically lowered, and the convective patterns exhibit larger wavelengths. However, the linear stability analysis brings little information on the dynamics of the system as the Rayleigh number departs from the critical value and non-linear terms become important. It is also unable to yield finite-amplitude informations on the system, such as heat flow and velocities. In order to obtain information about these aspects, we choose here to perform direct numerical simulations of the non-linear system. This chapter presents an exploration of the parameter space of our problem, namely the phase change numbers  $\Phi^\pm$ , the aspect ratio of the shell  $\gamma = R^-/R^+$  and the Rayleigh number Ra.

### 4.1 Implementation in StagYY

Non-linear numerical simulations are done with the StagYY code from Tackley (2008), which can handle 2D and 3D spherical and cartesian geometries. In this study, due to the high computational cost of 3D calculations, we merely use the 2D spherical annulus geometry introduced by Hernlund and Tackley (2008). The surface ratio between the inner surface and the outer surface of a spherical annulus is the same as that of the full spherical shell. This leads to values of common diagnostics, such as the heat flux, that are closer to those obtained with 3D simulations than when using simpler 2D geometries such as a cylindrical slice.

The resolution of the conservation eqs. (2.26) to (2.28) and the associated boundary conditions is a two-step process. First, the mass and momentum conservation equations along with the associated boundary conditions are discretized and written in the form of a large sparse matrix equation with the pressure and velocity fields as unknowns and the buoyancy term as right-hand-side. This system is solved using the direct solvers UMFPack (Davis 2004) and MUMPS (Amestoy, Duff, et al. 2001; Amestoy, Buttari, et al. 2019). Then, an advection-diffusion scheme is used to solve the heat conservation equation, with the temperature field at the next step as unknown. At the next time step, the temperature field previously calculated is used to update the buoyancy term in the momentum conservation equation, and the same

process is repeated until the desired number of time steps is reached.

Regarding the heat advection scheme, MPDATA (Smolarkiewicz and Margolin 1998) and TVD (Harten 1983) are both implemented in StagYY. However, as shown in fig. 4.1, the use of MPDATA produces important numerical oscillations with the phase change boundary conditions. We hence used the TVD scheme which does not exhibit such oscillations, adapting it to handle non-zero normal velocities at the boundaries.

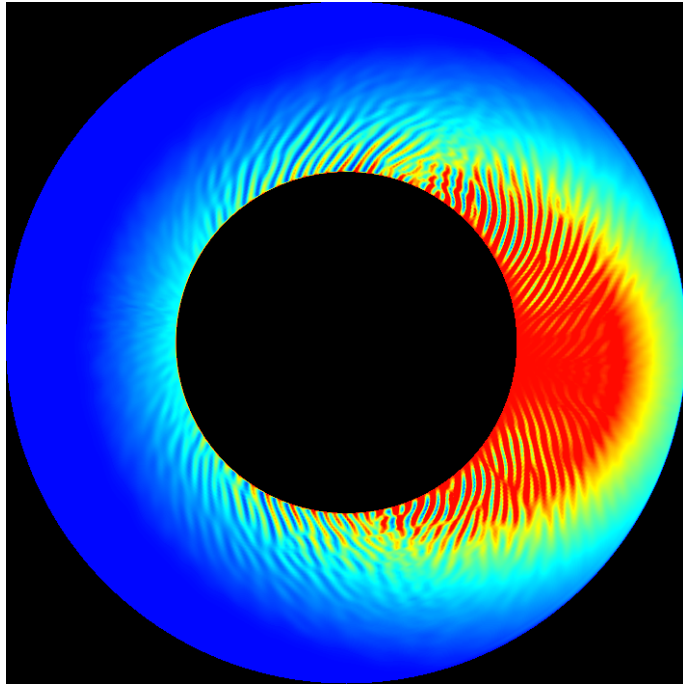


Figure 4.1: Temperature field obtained with the MPDATA advection-diffusion scheme. The important numerical oscillations that arise make this scheme unusable for the present study.

The normal stress continuity condition eq. (2.32) was the only missing equation in the existing sparse matrix solver already implemented in StagYY. Discretization of that boundary condition is described hereafter. Figure 4.2 shows the staggered grid used in StagYY near the boundaries. Since  $u_r(0)$  and  $u_r(n_r)$  are the velocities at the bottom and top interfaces, one only needs to evaluate the velocity gradient  $\partial u_r / \partial r$  and the dynamic pressure  $p$  at the interface as a function of the velocity and pressure interior points. Three interior points are used to do so, this leads to a boundary condition written to the third order while other equations are discretized to the second order. We made this choice because the boundary layer obtained with the flow-through boundary condition can be extremely thin and its resolution is the main numerical challenge issued by our system. Using a third order discretization for the boundary instead of merely refining the grid in order to properly resolve the boundary layer leads to better performances.

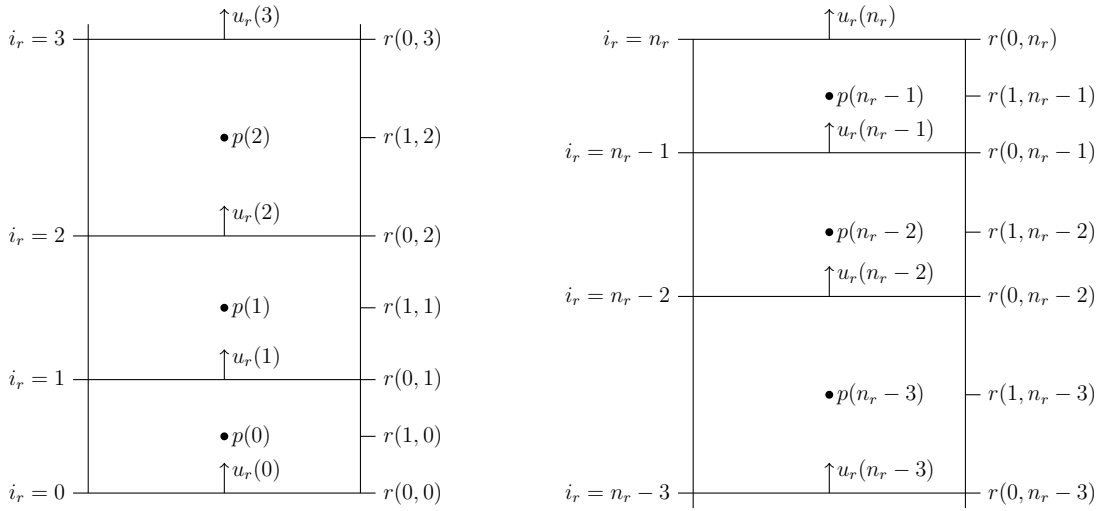


Figure 4.2: Staggered grid used in StagYY near the bottom boundary (left) and the top boundary (right). The domain is decomposed in  $n_r$  interior cells along the radial direction. Note that to ease the resolution of the boundary layers, the cell thickness decreases near the boundary. The pressure (as well as the temperature) is evaluated at the center of the cells, whereas the velocities are evaluated on the faces of the cells.  $r(0, i_r)$  is the radial position of the bottom face of the  $i_r$ -th cell;  $r(1, i_r)$  is the radial position of the center of that cell.  $u_r(i_r) = u_r(r(0, i_r))$  and  $p(i_r) = p(r(1, i_r))$ .  $u_r(0)$  and  $u_r(n_r)$  are then the radial velocities at the bottom  $R^- = r(0, 0)$  and top boundary  $R^+ = r(0, n_r)$  respectively.

### Velocity gradient at the bottom

With:

$$\begin{aligned} d_0 &= r(0, 1) - r(0, 0), & a_0 &= d_1^2 d_2^2 (d_2 - d_1), \\ d_1 &= r(0, 2) - r(0, 0), & a_1 &= d_0^2 d_2^2 (d_0 - d_2), \\ d_2 &= r(0, 3) - r(0, 0), & a_2 &= d_0^2 d_1^2 (d_1 - d_0), \end{aligned} \quad (4.1)$$

the following Taylor developments may be written:

$$u_r(1) = u_r(0) + d_0 \frac{\partial u_r}{\partial r}(R^-) + \frac{d_0^2}{2} \frac{\partial^2 u_r}{\partial r^2}(R^-) + \frac{d_0^3}{6} \frac{\partial^3 u_r}{\partial r^3}(R^-) + \mathcal{O}(\delta r^4); \quad (4.2)$$

$$u_r(2) = u_r(0) + d_1 \frac{\partial u_r}{\partial r}(R^-) + \frac{d_1^2}{2} \frac{\partial^2 u_r}{\partial r^2}(R^-) + \frac{d_1^3}{6} \frac{\partial^3 u_r}{\partial r^3}(R^-) + \mathcal{O}(\delta r^4); \quad (4.3)$$

$$u_r(3) = u_r(0) + d_2 \frac{\partial u_r}{\partial r}(R^-) + \frac{d_2^2}{2} \frac{\partial^2 u_r}{\partial r^2}(R^-) + \frac{d_2^3}{6} \frac{\partial^3 u_r}{\partial r^3}(R^-) + \mathcal{O}(\delta r^4). \quad (4.4)$$

$\delta r = 1/n_r$  is the typical cell thickness along the radial direction. The linear combination  $a_0(4.2) + a_1(4.3) + a_2(4.4)$  gives the following expression for the velocity gradient at the bottom boundary:

$$\frac{\partial u_r}{\partial r}(R^-) = \frac{a_0 u_r(1) + a_1 u_r(2) + a_2 u_r(3) - (a_0 + a_1 + a_2) u_r(0)}{d_0 a_0 + d_1 a_1 + d_2 a_2} + \mathcal{O}(\delta r^3). \quad (4.5)$$

### Pressure at the bottom

With:

$$\begin{aligned} h_0 &= r(1, 0) - r(0, 0), \\ h_1 &= r(1, 1) - r(0, 0), \\ h_2 &= r(1, 2) - r(0, 0), \end{aligned} \quad (4.6)$$

the following Taylor developments may be written:

$$p(0) = p^- + h_0 \frac{\partial p}{\partial r}(R^-) + \frac{h_0^2}{2} \frac{\partial^2 p}{\partial r^2}(R^-) + \mathcal{O}(\delta r^3); \quad (4.7)$$

$$p(1) = p^- + h_1 \frac{\partial p}{\partial r}(R^-) + \frac{h_1^2}{2} \frac{\partial^2 p}{\partial r^2}(R^-) + \mathcal{O}(\delta r^3); \quad (4.8)$$

$$p(2) = p^- + h_2 \frac{\partial p}{\partial r}(R^-) + \frac{h_2^2}{2} \frac{\partial^2 p}{\partial r^2}(R^-) + \mathcal{O}(\delta r^3). \quad (4.9)$$

The linear combination  $h_1 h_2 (h_2 - h_1)(4.7) + h_0 h_2 (h_0 - h_2)(4.8) + h_0 h_1 (h_1 - h_0)(4.9)$  gives the following expression for the dynamic pressure at the boundary:

$$p^- = \frac{h_1 h_2 (h_2 - h_1) p(0) + h_0 h_2 (h_0 - h_2) p(1) + h_0 h_1 (h_1 - h_0) p(2)}{(h_1 - h_0)(h_2 - h_0)(h_2 - h_1)} + \mathcal{O}(\delta r^3). \quad (4.10)$$

### Discretized equation at the bottom

Equations (4.5) and (4.10) allow us to write eq. (2.32) at the bottom boundary under the discretized form:

$$\begin{aligned} (-\Phi^- + c_{w0})u_r(0) + c_{w1}u_r(1) + c_{w2}u_r(2) + c_{w3}u_r(3) \\ + c_{p0}p(0) + c_{p1}p(1) + c_{p2}p(2) = \mathcal{O}(\delta r^3) \end{aligned} \quad (4.11)$$

where:

$$\begin{aligned} c_{w0} &= -2 \frac{a_0 + a_1 + a_2}{d_0 a_0 + d_1 a_1 + d_2 a_2}, & c_{p0} &= -\frac{h_1 h_2}{(h_1 - h_0)(h_2 - h_0)}, \\ c_{w1} &= 2 \frac{a_0}{d_0 a_0 + d_1 a_1 + d_2 a_2}, & c_{p1} &= \frac{h_0 h_2}{(h_1 - h_0)(h_2 - h_1)}, \\ c_{w2} &= 2 \frac{a_1}{d_0 a_0 + d_1 a_1 + d_2 a_2}, & c_{p2} &= -\frac{h_0 h_1}{(h_2 - h_0)(h_2 - h_1)}, \\ c_{w3} &= 2 \frac{a_2}{d_0 a_0 + d_1 a_1 + d_2 a_2}. \end{aligned} \quad (4.12)$$

### Discretized equation at the top

With:

$$\begin{aligned} d_0 &= r(0, n_r - 1) - r(0, n_r), & h_0 &= r(1, n_r - 1) - r(0, n_r), \\ d_1 &= r(0, n_r - 2) - r(0, n_r), & h_1 &= r(1, n_r - 2) - r(0, n_r), \\ d_2 &= r(0, n_r - 3) - r(0, n_r), & h_2 &= r(1, n_r - 3) - r(0, n_r), \end{aligned} \quad (4.13)$$

the same developments as for the bottom boundary may be written. Hence, the discretized version of eq. (2.32) at the top boundary is

$$\begin{aligned} (\Phi^+ + c_{w0})u_r(n_r) + c_{w1}u_r(n_r - 1) + c_{w2}u_r(n_r - 2) + c_{w3}u_r(n_r - 3) \\ + c_{p0}p(n_r - 1) + c_{p1}p(n_r - 2) + c_{p2}p(n_r - 3) = \mathcal{O}(\delta r^3) \end{aligned} \quad (4.14)$$

with the coefficients expressed in eq. (4.12).

Using eqs. (4.11) and (4.14), the implementation of the phase change boundary condition in StagYY is straightforward: one merely needs to add the  $c_w$  and  $c_p$  coefficients in the sparse matrix involved in the resolution of the Stokes equation.

## 4.2 Flow-through condition at the bottom boundary

We focus in this section on the situation where the top boundary is non-penetrative while the phase change condition is applied at the bottom boundary. Figure 4.3 shows the behaviour of the system as the phase change number at the bottom,  $\Phi^-$ , and the super-critical Rayleigh number,  $Ra/Ra_c$ , vary.  $Ra_c$  is the linear critical Rayleigh number calculated using the method exposed in chapter 3. The aspect ratio is  $\gamma = 0.6$  for all the cases on fig. 4.3. These numerical simulations confirm the two main conclusions previously drawn from the linear stability analysis.

- Large values of the phase change number  $\Phi^-$  lead to a classical non-penetrative boundary (cases with  $\Phi^- = 10^3$ ). Lower values of the phase change number lead to a boundary that allows matter to flow through as can be seen with the opening of the streamlines as  $\Phi^-$  decreases.
- Large values of  $\Phi^-$ , hence a non-penetrative boundary, lead to nearly aspect-ratio-1 rolls corresponding to a degree-4 flow with the chosen aspect ratio  $\gamma = 0.6$ . Decreasing  $\Phi^-$  leads to wider convection patterns. One can indeed observe a competition between degree-4 and wider degree-3 convective patterns on cases with  $Ra/Ra_c \geq 10$  and  $\Phi^- \leq 10$ . These cases are not stationary but instead exhibit oscillations as the two harmonic degrees compete. Note that these oscillations were not predicted by the linear stability analysis, and the most linearly unstable mode is a degree-2 pattern (see fig. 3.1). This shows the shortcomings of linear stability analysis to predict the behaviour of this system, even at a rather low super-critical Rayleigh number of  $10^{1/2}$ .

On top of the aforementioned oscillations, the numerical simulations exhibit interesting features that could not be captured by a linear stability analysis.

- Rayleigh-Bénard convection in a spherical shell with non-penetrative boundaries leads to rather large cold downwellings and narrower hot plumes due to the smaller surface of the hot bottom boundary compared to the cold top boundary. As can be seen on fig. 4.3, the flow-through boundary condition at the bottom leads to a strikingly different thermal structure for small values of  $\Phi^-$ . Owing to inward advection of hot material at the bottom boundary, most of the shell is filled with wide hot upwellings, while cold downwellings are narrow. This is similar to convection with internal heating, even though none is involved in this system. Note that since the bottom boundary allows matter to cross it, cold downwellings do not spread when reaching the interface. Instead, they pass through it, reaching the bottom boundary temperature by the means of a diffusive thermal boundary layer.

- As the Rayleigh number increases, the cold narrow downwellings become thinner (like the top thermal boundary layer) and associated to a higher vertical velocity so as to conserve the overall mass of solid. This narrowing and acceleration of downwellings induces a numerical challenge. Indeed, the diffusive thermal boundary layer at the base of downwelling becomes extremely thin. Moreover, as the bottom boundary is isothermal and conservation of mass imposes that the average radial velocity is zero through the boundary, no net advection can occur through that boundary. Therefore, in order to properly assess the heat flux carried out by the system, the thin and narrow diffusive boundary layer at the base of downwellings needs to be well resolved as it is the only mechanism to carry heat through the bottom boundary of the domain.

Figure 4.4 shows the effects of decreasing the phase change number  $\Phi^-$  for various values of the aspect ratio  $\gamma$  of the shell. The simulations on this figure are performed at  $Ra/Ra_c = 10^{1/2}$ . As noticed on fig. 4.3, it shows decreasing the phase change number leads to a boundary allowing the matter to flow-through, and large hot upwellings. One can note that even though the Rayleigh number is fairly close to the linear critical value, the unstable modes are not the one predicted by the linear stability analysis. However, as predicted by the latter, convective patterns do tend to have a larger wavelength when the boundary is flow-through instead of penetrative (see  $\gamma = 0.4$  and  $\gamma = 0.8$  on fig. 4.4, surprisingly  $\gamma = 0.6$  does not exhibit this effect).

Figures 4.5 to 4.7 show common diagnostics, namely the average temperature, root-mean-square velocity and heat flux, as functions of the Rayleigh number for several values of the phase change number  $\Phi^-$ . These figures show simulations performed with  $\gamma = 0.6$ , similar results are obtained for other aspect ratios. As deduced from figs. 4.3 and 4.4, fig. 4.5 shows the average temperature of the domain is dramatically increased by a flow-through bottom boundary, from  $T_{\text{avg}} \sim 0.3$  for the classical case ( $\Phi^- = 10^3$ ) to  $T_{\text{avg}} \sim 0.9$  for the flow-through case ( $\Phi^- < 10$ ). Note that the average temperature increases with the Rayleigh number for a given  $\Phi^-$  as the cold downwellings get thinner. Figure 4.6 shows that, for a given Rayleigh number  $Ra$ , decreasing  $\Phi^-$  leads to fluid velocities that are roughly twice as large for the flow-through case ( $\Phi^- \lesssim 10$ ) than for the non-penetrative case ( $\Phi^- \gtrsim 10^3$ ). This can be understood by the fact that less deformation (i.e. less viscous forces) is involved in the solid as streamlines are open with a flow-through boundary condition. Therefore, similar values of the Rayleigh number (i.e. buoyancy forces) can lead to more vigorous convection with a flow-through boundary condition. Note however that the power law followed by the root-mean-square velocity  $u_{\text{rms}}$  is roughly the same as that of the classical case, namely  $u_{\text{rms}} \propto Ra^{2/3}$  (e.g. Turcotte and Oxburgh 1967). Finally, fig. 4.7 shows an interesting outcome of the flow-through boundary condition: the heat flux carried out through the solid is twice as high with  $\Phi^- \lesssim 10$  than with a non-penetrative boundary ( $\Phi^- \gtrsim 10^3$ ). Akin to the rms velocity, the Nusselt number  $Nu$  follows the same power law with a flow-through boundary than in the classical case, that is  $Nu \propto Ra^{1/3}$  (ibid.).

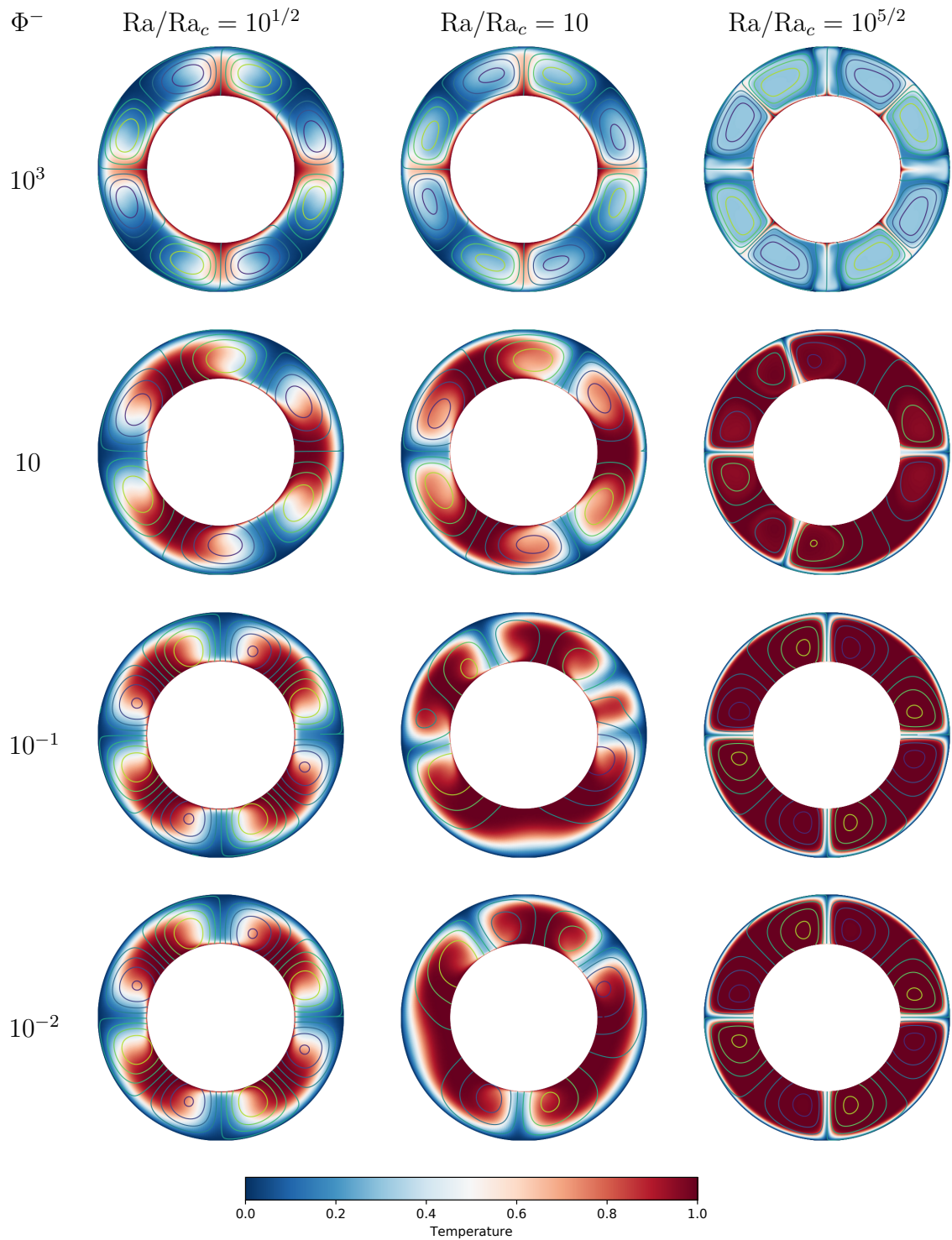


Figure 4.3: Temperature fields and streamlines for various values of the phase change number (left column) when the bottom boundary is flow-through. The top boundary is non-penetrative. The aspect ratio is  $\gamma = 0.6$  for all simulations.

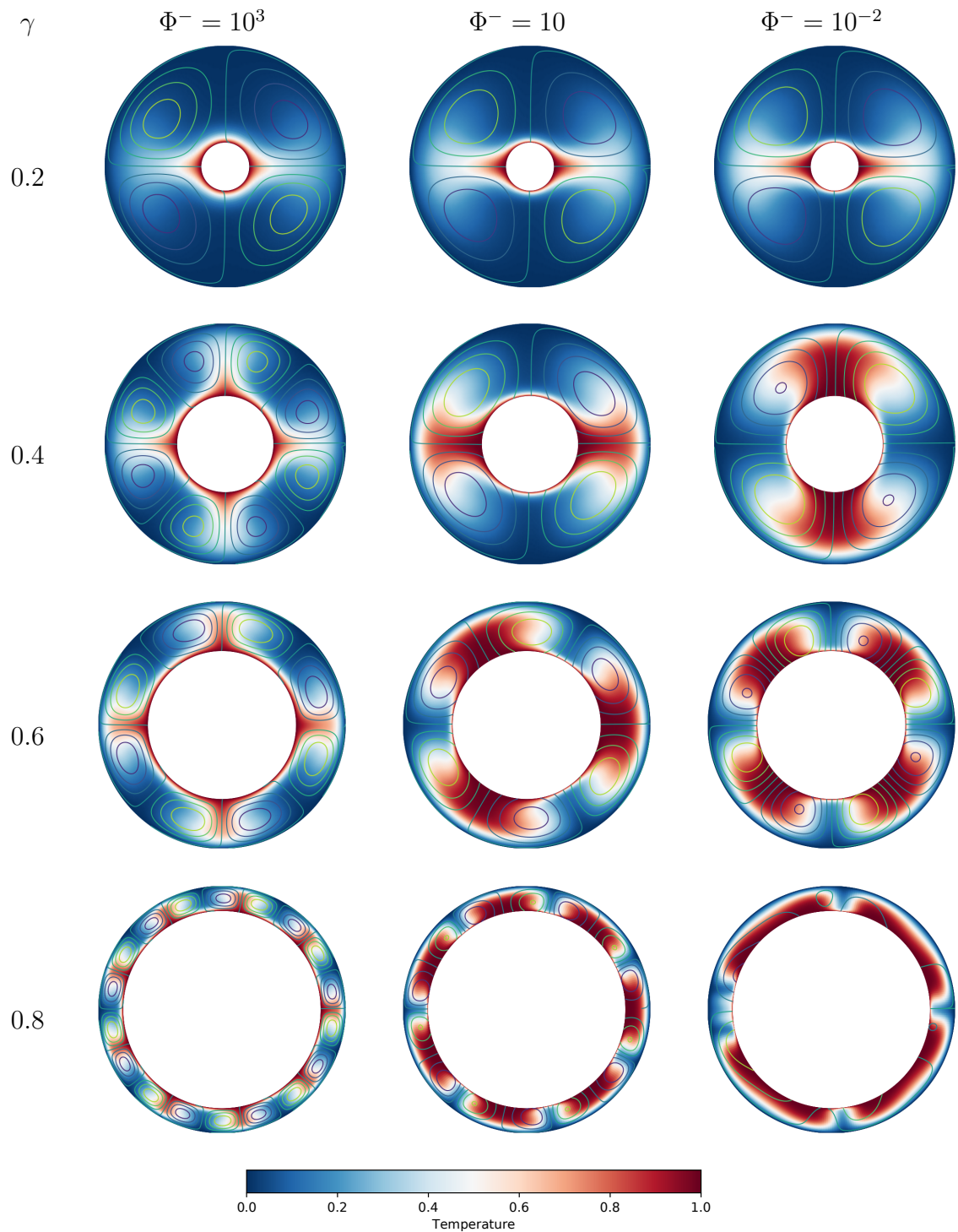


Figure 4.4: Temperature fields and streamlines for various values of the phase change number and aspect ratio  $\gamma$  when the bottom boundary is flow-through. The top boundary is non-penetrative. The super-critical Rayleigh is  $Ra/Ra_c = 10^{1/2}$  for all simulations.

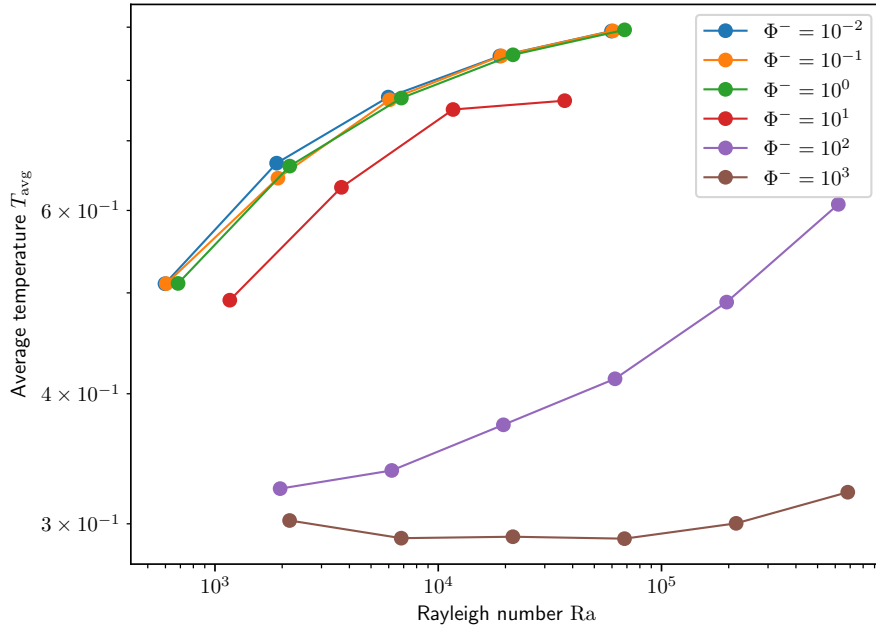


Figure 4.5: Average temperature as a function of Rayleigh number for various values of  $\Phi^-$ . The top boundary condition is non-penetrative. In these simulations,  $\gamma = 0.6$ .

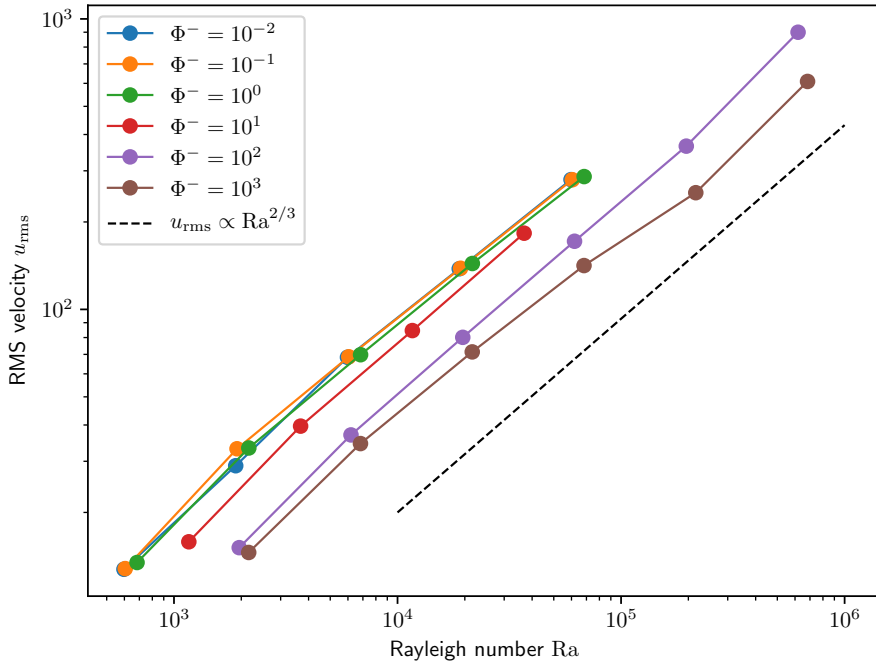


Figure 4.6: Root-mean-square velocity as a function of Rayleigh number for various values of  $\Phi^-$ . The top boundary condition is non-penetrative. In these simulations,  $\gamma = 0.6$ .

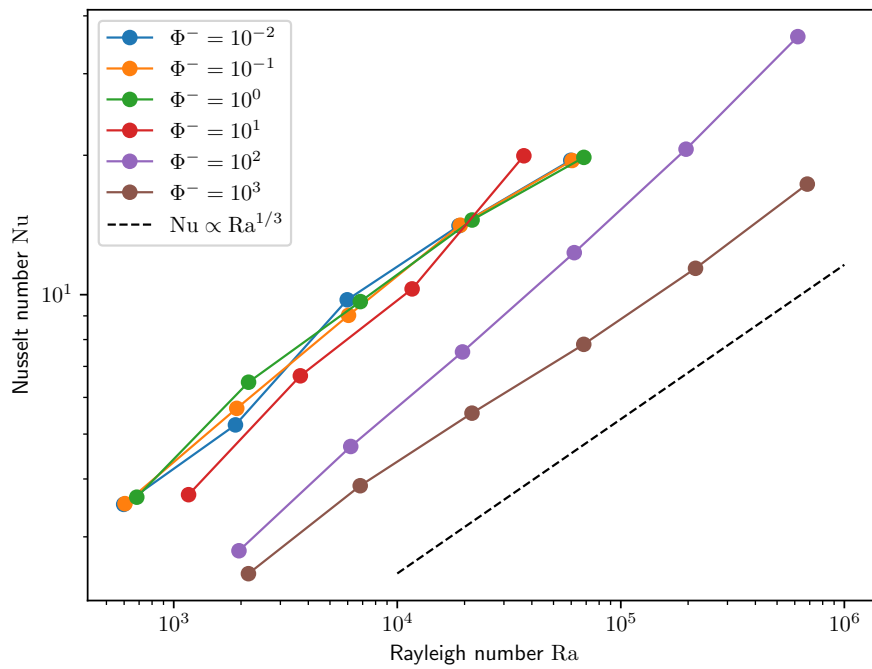


Figure 4.7: Nusselt number as a function of Rayleigh number for various values of  $\Phi^-$ . The top boundary condition is non-penetrative. In these simulations,  $\gamma = 0.6$ .

### 4.3 Flow-through condition at the top boundary

We focus now on the situation where the bottom boundary is non-penetrative and explore the effects of changing the phase change number at the top boundary  $\Phi^+$ . This case is somewhat symmetrical to the one explored in the previous section 4.2, with a few differences that are stressed here.

Figures 4.8 and 4.9 show the behaviour of the system when varying the control parameters of the problem: the phase change number at the top boundary,  $\Phi^+$ , the super-critical Rayleigh number,  $Ra/Ra_c$  and the aspect ratio of the shell,  $\gamma$ . As for the system with a phase change boundary condition at the bottom, high values of  $\Phi^+$  correspond to a classical non-penetrative boundary, leading to nearly aspect-ratio-1 rolls, while low values of  $\Phi^+$  lead to a flow-through top boundary that the convective matter can cross via melting and freezing. Low values of  $\Phi^+$  lead to wider patterns of convection. Moreover, owing to the flow-through condition, cold material is advected inward to form large cold downwellings, and hot upwellings get thinner as  $\Phi^+$  decreases and  $Ra/Ra_c$  increases. A striking difference with linear stability analysis is that while the latter shows the degree-1 convection mode is by far the linearly most unstable when  $\Phi^+$  is small (fig. 3.4), none of the models shown on figs. 4.8 and 4.9 exhibits such a pattern. This is even the case at  $Ra/Ra_c = 10^{1/2}$  even though other modes are not linearly unstable (fig. 3.7).

Figure 4.10 shows the flow-through boundary at the bottom leads to an important decrease of the average temperature of the domain, from roughly 0.3 when the boundary is non-penetrative ( $\Phi^+ \geq 10^3$ ) to values as low as  $3 \times 10^{-2}$  when the boundary is flow-through ( $\Phi^+ \lesssim 10$ ). Note the strong dependence of the average temperature on the Rayleigh number for a given phase change number. This dependence is due to the hot upwellings getting thinner as the Rayleigh number is increased when the top boundary is flow-through. Similarly to what is observed for the case with a flow-through bottom boundary, the root-mean-square velocity is twice as large with flow-through boundary condition but follows the classical case scaling  $u_{\text{rms}} \propto Ra^{2/3}$  as shown on fig. 4.11. The heat flux however does not seem to be as dramatically affected by the flow-through boundary at the top of the domain, as can be seen on fig. 4.12. It is slightly increasing when  $\Phi^+$  decreases, but the difference is surprisingly not as strong as in the case of a flow-through boundary at the bottom.

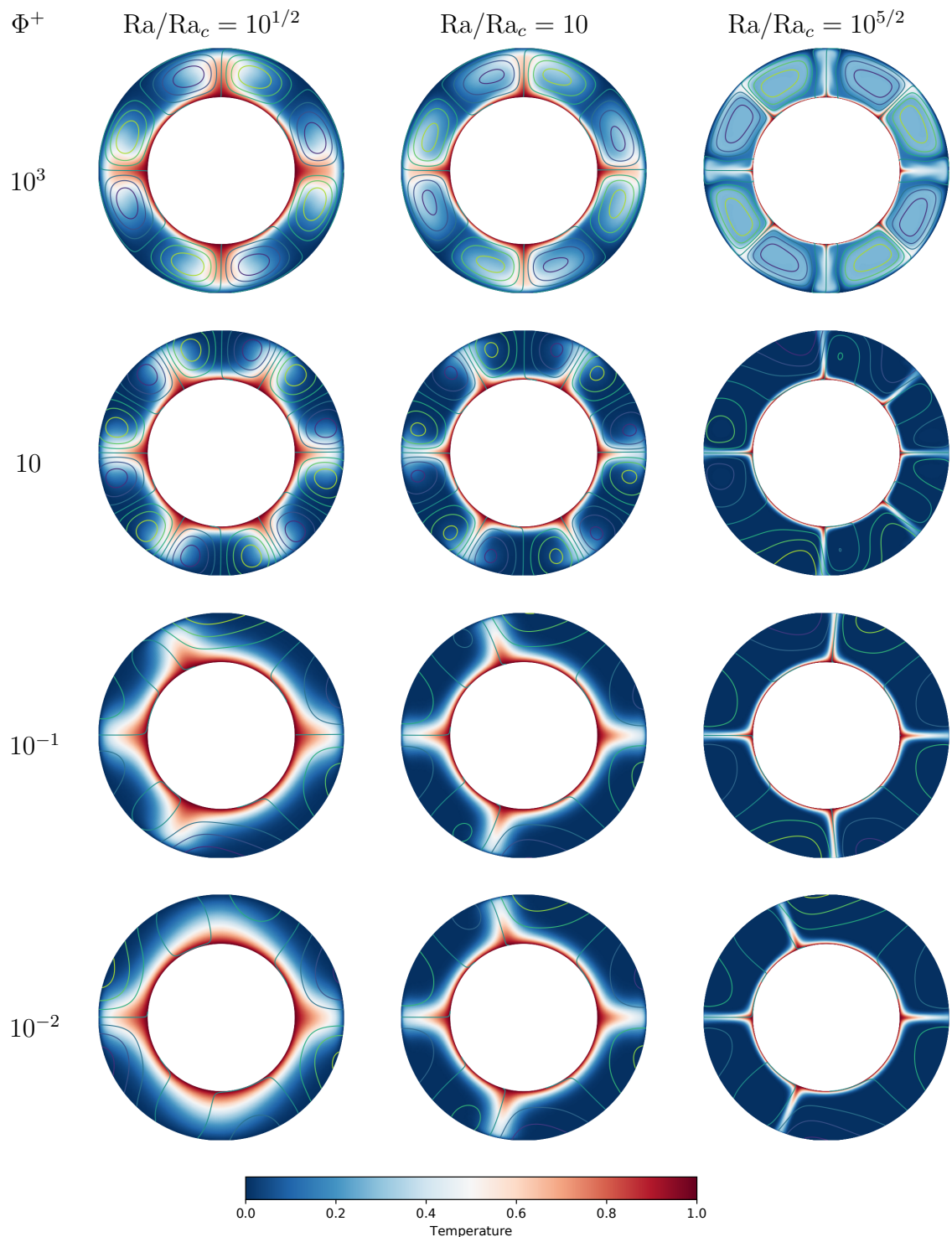


Figure 4.8: Temperature fields and streamlines for various values of the phase change number (left column) when the top boundary is flow-through. The bottom boundary is non-penetrative. The aspect ratio is  $\gamma = 0.6$  for all simulations.

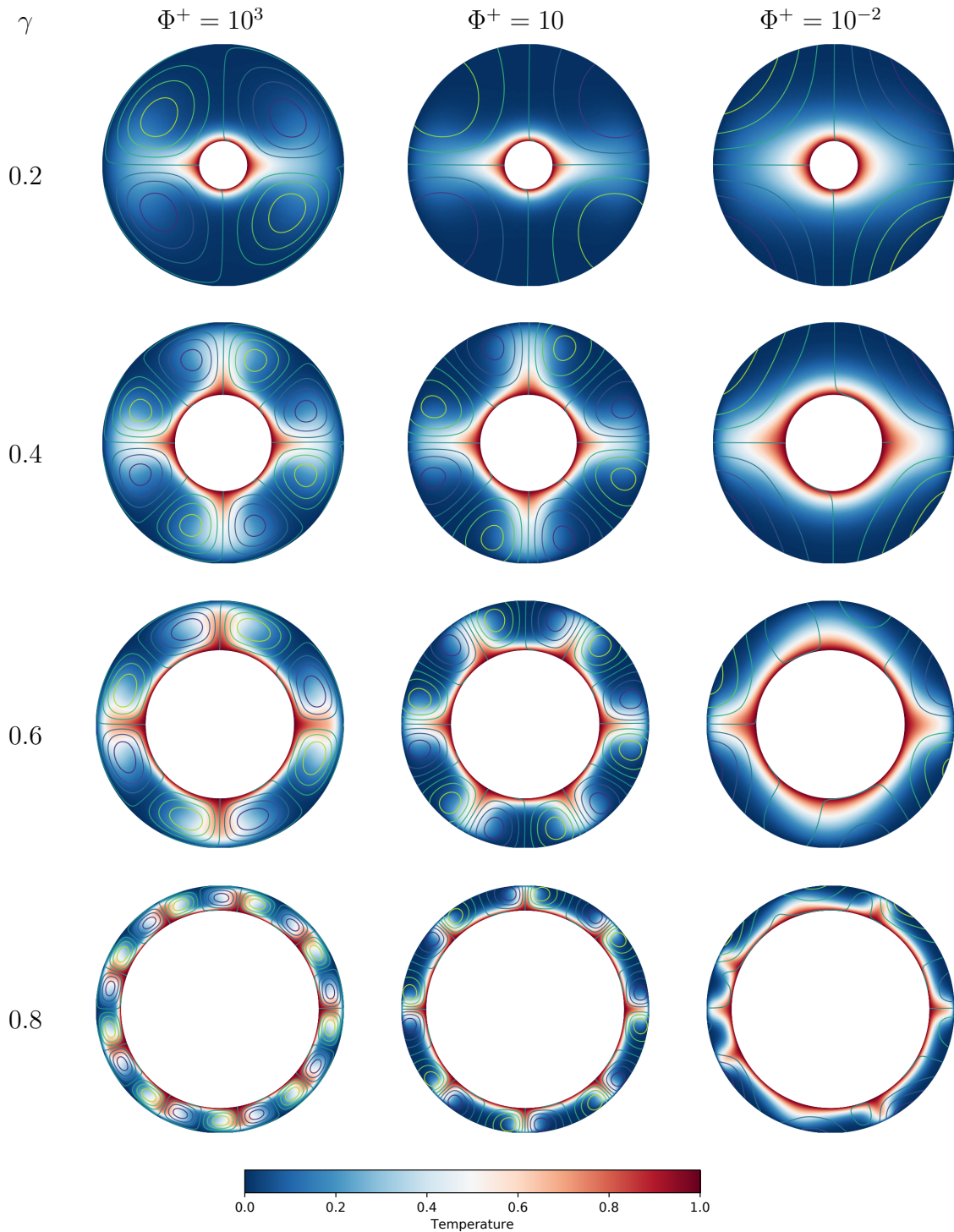


Figure 4.9: Temperature fields and streamlines for various values of the phase change number and aspect ratio  $\gamma$  when the top boundary is flow-through. The bottom boundary is non-penetrative. The super-critical Rayleigh is  $Ra/Ra_c = 10^{1/2}$  for all simulations.

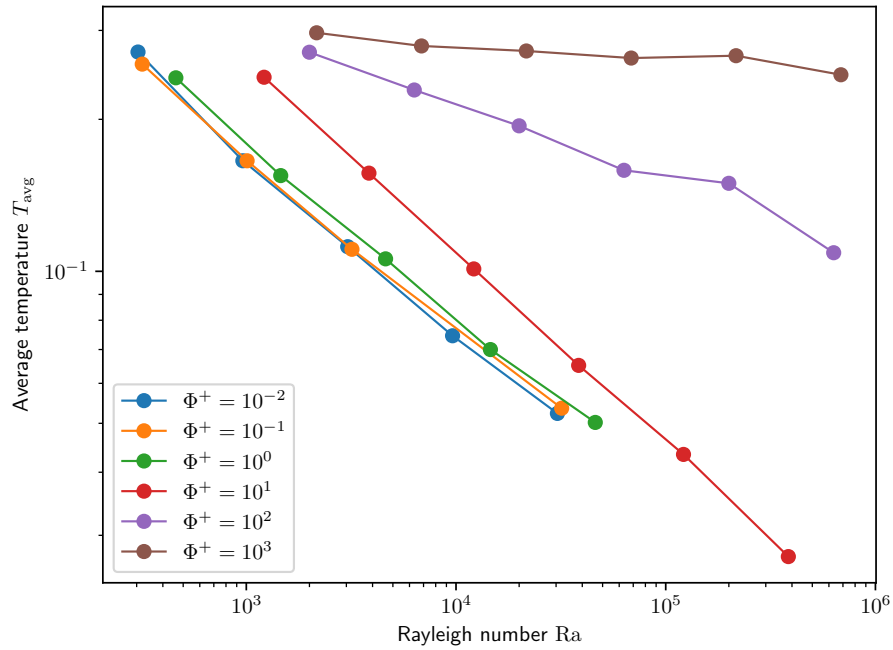


Figure 4.10: Average temperature as a function of Rayleigh number for various values of  $\Phi^+$ . The bottom boundary condition is non-penetrative. In these simulations,  $\gamma = 0.6$ .

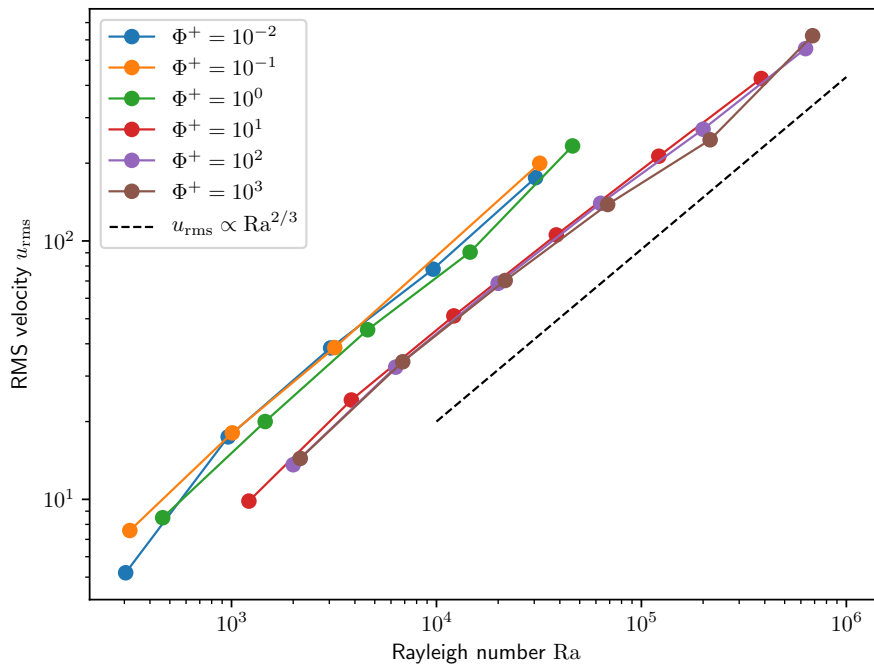


Figure 4.11: Root-mean-square velocity as a function of Rayleigh number for various values of  $\Phi^+$ . The bottom boundary condition is non-penetrative. In these simulations,  $\gamma = 0.6$ .

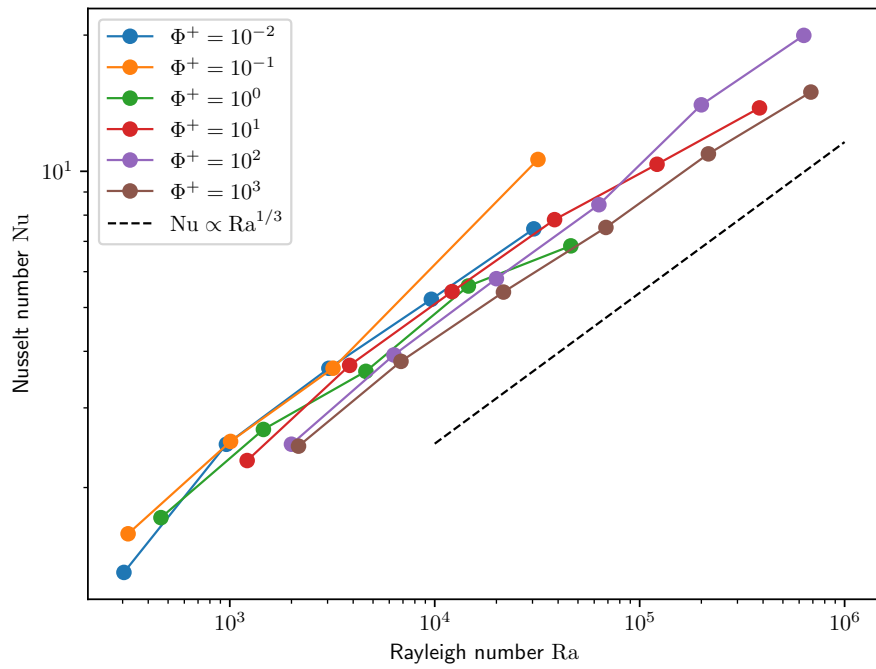


Figure 4.12: Nusselt number as a function of Rayleigh number for various values of  $\Phi^+$ . The bottom boundary condition is non-penetrative. In these simulations,  $\gamma = 0.6$ .

## 4.4 Flow-through condition at both boundaries

The last case we will focus on has both boundaries verifying a phase change condition. Both phase change numbers are considered equal in this section  $\Phi^+ = \Phi^-$ .

Figures 4.13 and 4.14 show decreasing both phase change numbers leads to a situation where both boundaries are flow-through. Convective patterns that emerge from this setup involve very little deformation in the solid and exhibit large wavelengths of degree-two or even degree-one. Cold downwellings and hot upwellings are rather large, with the transition between hot and cold regions getting sharper as the Rayleigh number increases. Indeed, a higher Rayleigh number leads to higher flow velocities, and hence leaves less time to thermal diffusion to smear out the temperature gradient between hot and cold regions. Note also that the very notion of cold downwelling and hot upwelling does not fully describe the convective patterns obtained with two flow-through boundaries. See for example the  $\Phi^\pm = 10^{-1}$  row on fig. 4.13 where cold regions are dragged by the hot upwellings owing to viscous forces, and therefore move upwards even though they are negatively buoyant.

A particularly interesting regime yielded by this system with two flow-through boundaries is the degree-one translation mode. The shell continuously melts on one side and freezes on the other, and is kept in place by a constant wind of convecting solid matter going through the entire shell. This convection mode involves very little deformation in the solid shell. Moreover, building up on the analytical study of the stability of this mode in section 3.6, we can determine an approximation for the translation velocity as a function of  $\text{Ra}$ ,  $\Phi^\pm$  and  $\gamma$ . Equilibrium between the buoyancy available in the bulk of the domain and the weight of the topography leads to eq. (3.51), relating the translation velocity  $U$  and the degree-one mode of temperature  $T_1$ . It is copied here for readability purposes:

$$U = \frac{\text{Ra}}{(R^+)^2\Phi^+ + (R^-)^2\Phi^-} \int_{R^-}^{R^+} T_1 r^2 dr. \quad (4.15)$$

Given an arbitrary temperature field, one can hence compute the corresponding translation velocity (note that this solution would not necessarily be stationary, and that the full non-linear system would include other velocity modes). Figure 4.15 is the idealized temperature field in the translation regime at high Rayleigh number. The hot upwelling is merely modeled as a tangent cylinder at temperature  $T^- = 1$  along the translation direction. The rest of the domain is considered to be at  $T^+ = 0$ . Note that to ease the computation, we use a spherical frame where the colatitude  $\theta$  is the angle with respect to the translation direction. The system is invariant along the longitude  $\phi$  in this frame. In this setup, one obtains

$$T_1(r) = \frac{3}{2} \int_0^\pi T(r, \theta) \cos \theta \sin \theta d\theta = \frac{3}{2} \int_0^{\arcsin\left(\frac{R^-}{r}\right)} \cos \theta \sin \theta d\theta = \frac{3}{4} \left(\frac{R^-}{r}\right)^2. \quad (4.16)$$

Injecting  $T_1$  in eq. (4.15) gives:

$$U = \frac{3}{4} \text{Ra} \frac{\gamma^2}{\Phi^+ + \gamma^2\Phi^-} = 18 \frac{\text{Ra}}{\text{Ra}_c} \frac{\gamma(1 - \gamma^3)}{(1 - \gamma)(\gamma^2 + 4\gamma + 1)} \quad (4.17)$$

where  $\text{Ra}_c$  is the critical Rayleigh number eq. (3.55). The translation velocity is proportional to the Rayleigh number, which contrasts greatly with the usual scaling for convective velocity  $u_{\text{rms}} \propto \text{Ra}^{2/3}$ .

Figure 4.16 shows the effect of decreasing  $\Phi^\pm$  on the average temperature of the domain. It decreases slightly as  $\Phi^\pm$  decreases, although not as much as in the flow-through only at the top case.

Figure 4.17 shows the root-mean-square velocity as a function of the Rayleigh number for various values of  $\Phi^\pm$ , with  $\gamma = 0.6$ . The numerical results are compared with the ideal velocity given by eq. (4.17). As expected, large values of  $\Phi^\pm \geq 10^3$ , corresponding to non-penetrative boundary conditions, yield a root-mean-square velocity scaling as  $u_{\text{rms}} \propto \text{Ra}^{2/3}$ . Moreover, even though not all cases exhibit a translation mode, velocities for low values of  $\Phi^\pm$  are remarkably well approximated by the ideal velocity eq. (4.17). Note that  $U$ , and hence likely  $u_{\text{rms}}$  too can be arbitrarily large as  $\Phi^\pm$  decreases since it is inversely proportional to the critical Rayleigh number which itself is proportional to  $\Phi^\pm$  (see section 3.6).

Finally fig. 4.18 shows the effect of the flow-through boundary on the heat flux. Again, large values of the phase change numbers lead to the classical case  $\text{Nu} \propto \text{Ra}^{1/3}$ . Low values of the phase numbers lead both to a dramatic increase of the heat flux, and to much more efficient power law  $\text{Nu} \propto \text{Ra}$ . As for the velocity, the heat flux is expected to become arbitrarily large as  $\Phi^\pm$  decreases. Note that both scalings, namely velocity and heat flux proportional to the Rayleigh number, are similar to those obtained analytically in cartesian geometry for high Rayleigh numbers (Labrosse, Morison, et al. 2018, in appendix A).

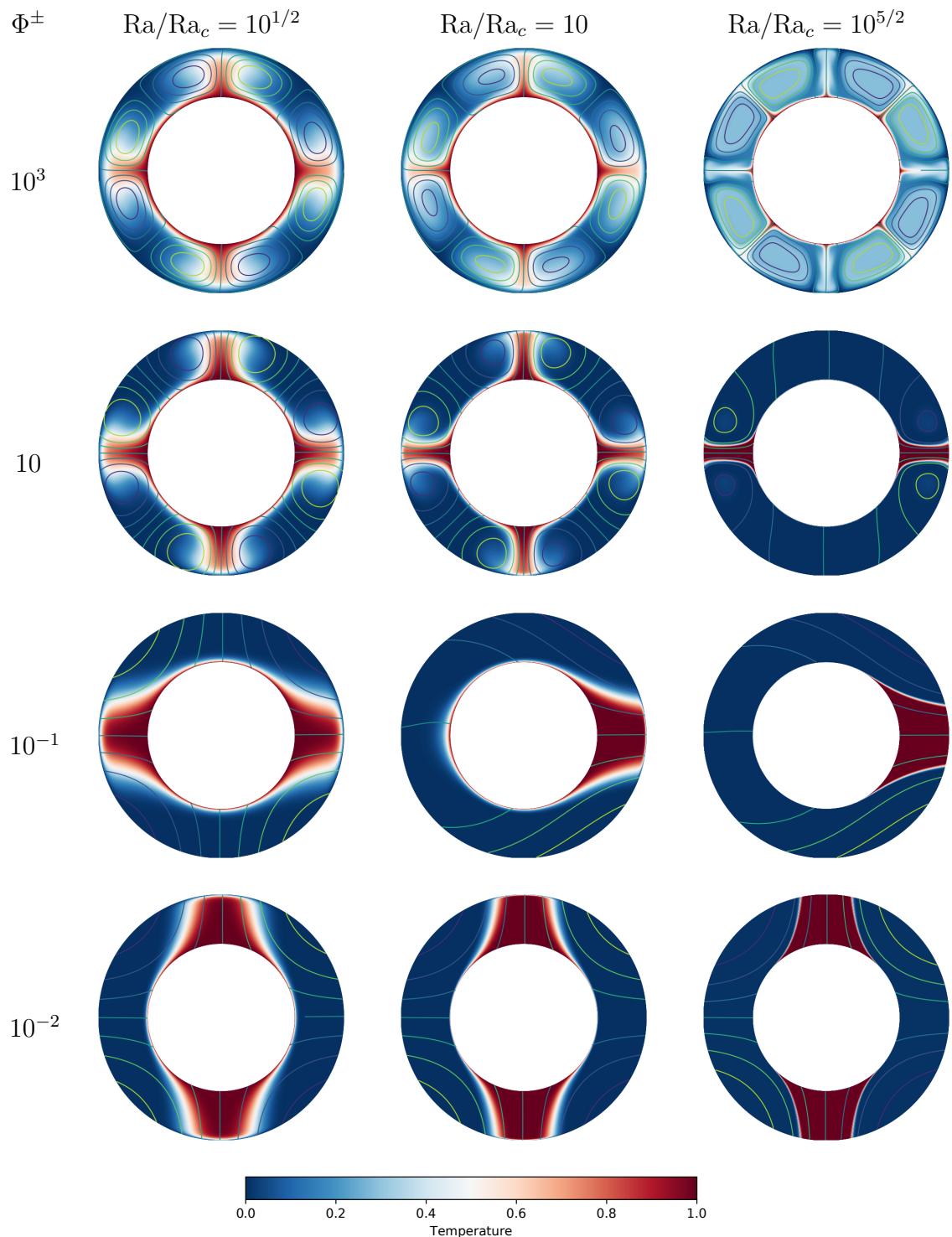


Figure 4.13: Temperature fields and streamlines for various values of the phase change number (left column) when both boundaries are flow-through. The aspect ratio is  $\gamma = 0.6$  for all simulations.

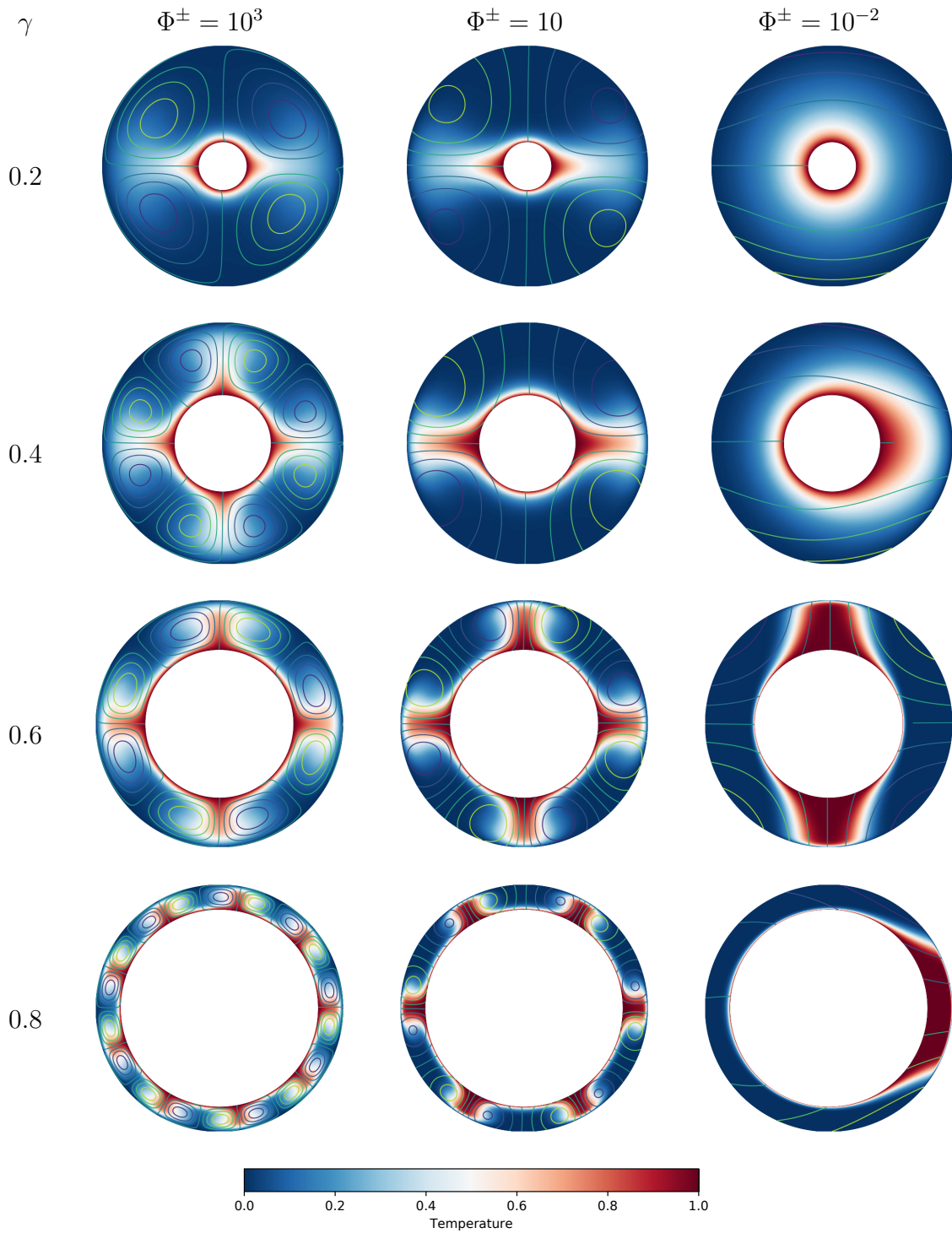


Figure 4.14: Temperature fields and streamlines for various values of the phase change number and aspect ratio  $\gamma$  when the both boundaries are flow-through. The super-critical Rayleigh is  $Ra/Ra_c = 10^{1/2}$  for all simulations.

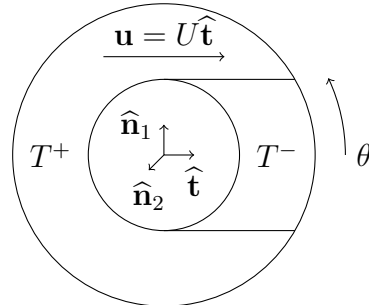


Figure 4.15: Idealized temperature field in the translation regime, in the  $\varphi = 0$  plane. The field is axisymmetric around  $\hat{\mathbf{t}}$  (i.e.  $\varphi$ -invariant).

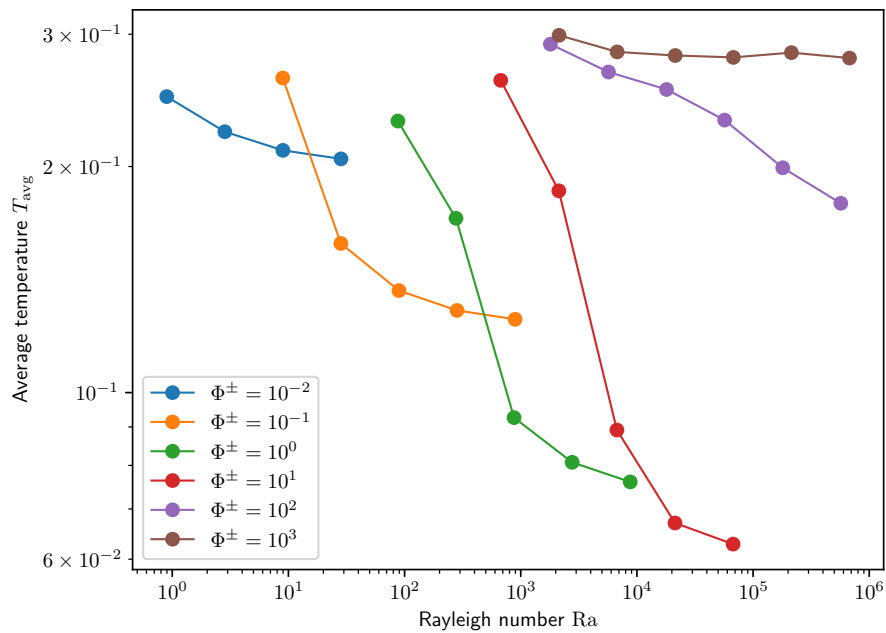


Figure 4.16: Average temperature as a function of Rayleigh number for various values of  $\Phi^+ = \Phi^-$ . In these simulations,  $\gamma = 0.6$ .

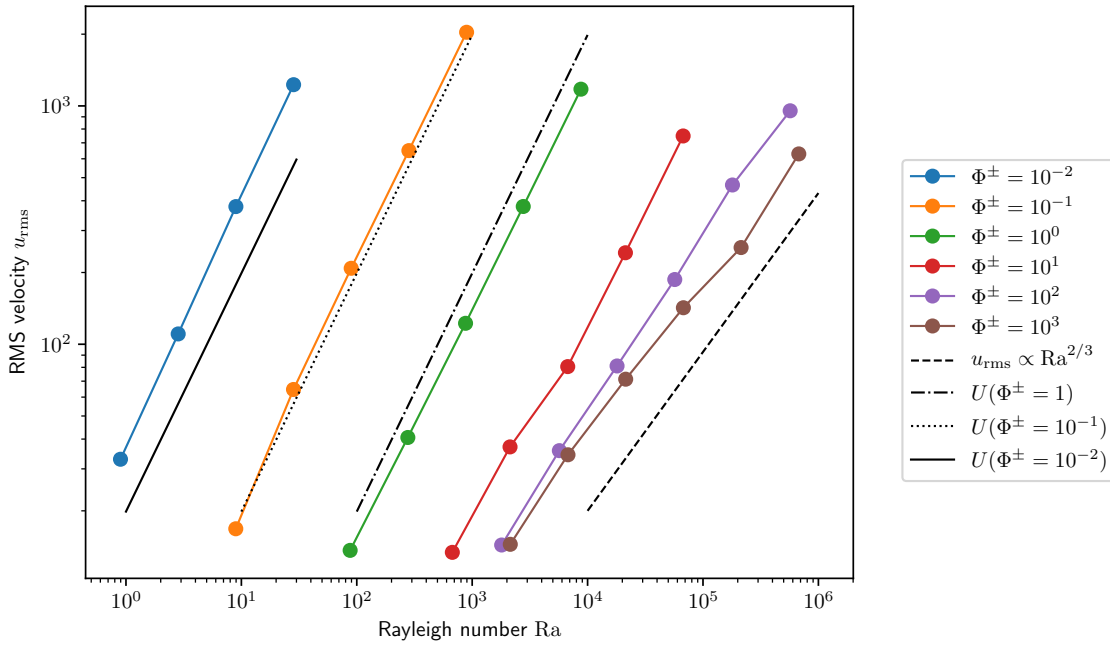


Figure 4.17: Root-mean-square velocity as a function of Rayleigh number for various values of  $\Phi^+ = \Phi^-$ . In these simulations,  $\gamma = 0.6$ . The black lines are the ideal translation velocity computed with eq. (4.17).

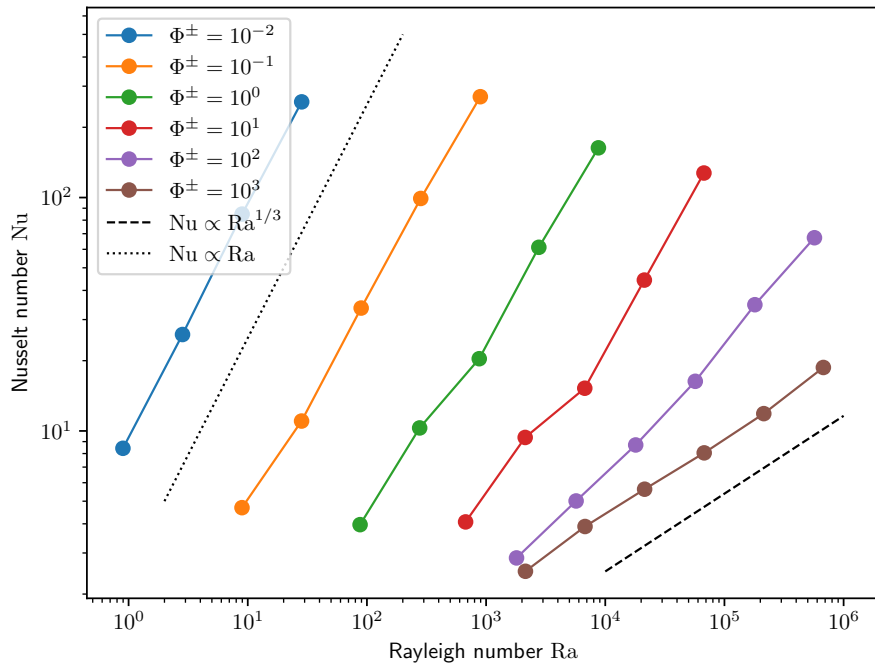


Figure 4.18: Nusselt number as a function of Rayleigh number for various values of  $\Phi^+ = \Phi^-$ . In these simulations,  $\gamma = 0.6$ .

## 4.5 Concluding remarks

Direct numerical simulations bring several informations that complete the linear stability analysis. It confirms that low values of phase change numbers lead to flow-through boundary conditions. These greatly affect the thermal structure of the mantle flow: up- and/or downwellings are large, and convective patterns exhibit wider wavelengths. This leads to convection with less deformation involved in the solid compared to cases with classical non-penetrative boundary conditions. The root-mean-square velocity is increased, roughly twice when one boundary is flow-through, and to arbitrarily large values when both boundaries are open. The heat flux is also twice as important when the bottom boundary is flow-through, and arbitrarily large when both boundaries are flow-through. Note that for Earth-like planets, the phase change numbers are expected to be small (unless the magma ocean is stably stratified and inefficient at carrying heat laterally). Morison et al. (2019, in chapter 6) propose  $\Phi^+ \sim 10^{-5}$  at the top boundary. For the bottom boundary, taking convective velocities in the basal magma ocean of the order of those in today's core would lead to  $\Phi^- \sim 10^{-3}$ . Hence, if global magma oceans existed at some point throughout Earth's history, they are likely to have had tremendous effects on the heat budget of the planet. Full evolutionary models are necessary to explore this hypothesis, and a rather crude but computationally tractable attempt at building such a model is presented in the next chapter.

# Chapter 5

## Magma ocean evolution models coupled with the solid

As seen in the previous chapters, the presence of magma oceans has tremendous consequences on the convection in the solid part of the primitive mantle. Convection sets in the solid more easily since the critical Rayleigh number is lower, convective patterns have a larger wavelength with less deformation, and the heat flux is increased. However, the models presented before are simplistic since no net-freezing of the magma oceans is allowed. This prevents drawing any conclusions regarding the long term evolution of the primitive mantle. Two aspects of the problem are added in this chapter.

- As heat is evacuated from the system, the magma oceans cool down and crystallize, thickening the solid part.
- Assuming fractional crystallization of the magma oceans, their composition and that of the solid evolve with time. This can play a role on convection in the solid due to the effect of composition on buoyancy, and this can also play a role on the evolution of the thickness of the solid due to the effect of composition on the melting temperature.

The dynamics and evolution of magma oceans is a complicated subject with several aspects. Keeping in mind this study is focused on the long term evolution of the solid part of the primitive mantle, several simplifications are necessary for the problem to be computationally tractable.

The dynamics of magma oceans itself is hard to model. The parameters are out of reach even to state-of-the-art convection codes (high Rayleigh number, low Ekman number). Moreover, fractional crystallization can create a layer enriched in incompatible elements at the top or the base of magma oceans, potentially leading to double-diffusive convection involving very large Lewis numbers for which few studies have been conducted to this day (e.g. Bouffard et al. 2017). However, the dynamics of magma oceans is expected to be much faster than that of the solid owing to their small viscosity. Since we are mainly interested in convection in the solid, we assume the oceans are well-mixed and laterally homogeneous. For the sake of simplicity, we neglect double-diffusive convection phenomena in the liquid altogether.

Another process that requires simplification is the crystallization of magma oceans. It raises several complex questions such as whether isolated crystals in

magma oceans settle or are entrained and potentially melt back, what is the compaction length needed to fully drive out the liquid trapped in a matrix of crystals, what is the rheology of that matrix and that of the new solid, whether the crystallization is fractional, if so what is the phase diagram of the mixture composing the magma ocean... Rather than trying to have a realistic model dealing with all these aspects at once, we make the following assumptions.

- We neglect the thickness of the mush and the compaction layer at the interface between the solid and the liquid, therefore we assume the matter is completely solid on one side of the boundary and completely liquid on the other side.
- We consider fractional crystallization of the magma oceans, using a simple-loop phase diagram between two end-members (MgO and FeO enriched end-members of a silicate). This is a crude simplification of the chemistry of the mantle, the goal being to see the dynamical effects of the enrichment of the newly formed solid in a dense incompatible element (the iron) as crystallization of magma oceans progresses.
- The temperature at the solid/liquid interface is chosen as that of the liquidus of the liquid composition, which is also that of the solidus of the newly formed solid composition. It is called the melting temperature in the following chapters. This temperature varies with time as the pressure at the interface and the composition of the magma oceans vary.

To be able to treat in a self-consistent way the evolution of the magma oceans and that of the solid part of the primitive mantle, a model describing the evolution of the magma oceans under the set of hypotheses mentioned above is needed. Energy conservation written at the scale of the magma oceans is used to build this model. The evolution model for the Top Magma Ocean (TMO) is presented in the following section. The evolution model for the Basal Magma Ocean (BMO) is very similar and is presented in the next section, stressing the main differences with the TMO evolution model. These evolution models are similar to that of the core proposed in Labrosse (2015).

## 5.1 Evolution model of the Top Magma Ocean (TMO)

### 5.1.1 Dimensional model

Energy conservation integrated on the entire magma ocean is

$$\int_{\text{TMO}} \rho \left( T \frac{\partial s}{\partial t} + \mu \frac{\partial \xi}{\partial t} \right) dV = Q_L + Q_R + Q^+ - Q^s. \quad (5.1)$$

The left hand side is the rate of change of internal energy in the volume of the TMO, balanced by the latent heat associated to melting and freezing,  $Q_L$ , the radiogenic heating,  $Q_R$ , the heat flux through the Top Ocean/Mantle Boundary (TOMB),  $Q^+$ , and the heat flux through the surface of the planet,  $Q^s$ . The various terms appearing in eq. (5.1) as well as the phase diagram are described in the rest of this subsection.

### Phase diagram at the boundary

The melting temperature  $T^+$  depends on pressure and composition, and will therefore vary with time as the position of the TOMB (hence its pressure) and the composition of the ocean change. Its time derivative verifies:

$$\dot{T}^+ = -\frac{\partial T_L}{\partial P} \rho g \dot{R}^+ + \frac{\partial T_L}{\partial \xi} \dot{\xi}^+. \quad (5.2)$$

$\dot{\xi}^+$  itself can be written as a linear function of  $\dot{R}^+$  through conservation of the heavy component:

$$\frac{d(M_{\text{TMO}} \xi^+)}{dt} = M_{\text{TMO}} \dot{\xi}^+ - 4\pi (R^+)^2 \rho \xi^+ \dot{R}^+ = I^+, \quad (5.3)$$

where  $I^+$  is the upward flux of FeO through the TOMB. We assume the flux of FeO across the upper boundary of the TMO to be null.  $I^+$  depends on the net freezing/melting occurring at the boundary, which has two contributions.

- Dynamic melting and freezing occur owing to the phase change boundary condition eq. (2.32), associated to the radial velocity of the convecting solid  $u_r$ . At the TOMB, a positive velocity  $u_r$  induces the melting of an intrusion of solid in the magma ocean; while a negative velocity induces the freezing of an intrusion of liquid in the solid layer.
- Net freezing or melting of the TMO at a velocity  $\dot{R}^+$ . A positive  $\dot{R}^+$  corresponds to a freezing TMO while a negative  $\dot{R}^+$  corresponds to a melting TMO.

This leads to

$$I^+ = \int_+ \rho (\xi_\phi^{-u_r} u_r - \xi_\phi^{\dot{R}^+} \dot{R}^+) dS \quad (5.4)$$

where  $\xi_\phi^v$  is the composition of the solid associated with a freezing rate  $v$ . We assume here that a newly crystallized solid (case  $v > 0$ ) has a composition  $\xi_f$  corresponding to the fractional crystallization of the solid; and that a solid of composition  $\xi_s$  that melts (case  $v < 0$ ) pumps iron from the liquid so as to reach the liquidus composition and melt, which is mathematically equivalent to directly melting the solid without altering its composition. Denoting  $K$  the partition coefficient of FeO defined as

$$K \equiv \frac{\xi_f(1 - \xi^+)}{\xi^+(1 - \xi_f)}, \quad (5.5)$$

$\xi_\phi^v$  verifies

$$\xi_\phi^v = \begin{cases} \frac{K \xi^+}{1 - \xi^+(1 - K)} & v \geq 0; \\ \xi_s & v < 0. \end{cases} \quad (5.6)$$

This implements a simple loop phase diagram between two pure phases, that can be seen as pure FeO and pure MgO. Of course, this phase diagram is simplistic compared to that of the actual mantle, but it allows us to model the enrichment of the magma ocean in heavy components owing to fractional crystallization.

Combining eqs. (5.3) and (5.4) gives the following relation between  $\dot{\xi}^+$  and  $\dot{R}^+$ :

$$\left( \int_+ \rho \xi_\phi^{\dot{R}^+} dS - 4\pi (R^+)^2 \rho \xi^+ \right) \dot{R}^+ + \frac{4\pi}{3} \rho (R_T^3 - (R^+)^3) \dot{\xi}^+ = \int_+ \rho \xi_\phi^{-u_r} u_r dS. \quad (5.7)$$

$\dot{\xi}^+$  and therefore  $\dot{T}^+$  are hence entirely determined by  $\dot{R}^+$  using eqs. (5.2) and (5.7).

### Entropy contribution to internal energy $T\partial_t s$

As discussed previously, we assume the magma ocean is well mixed. The specific entropy  $s$  and the composition of the TMO, defined as the FeO massic concentration  $\xi^+$ , are therefore considered uniform in the entire volume of the TMO. To avoid treating entropy explicitly, the heat term  $T\partial_t s$  is written using the heat capacity  $C_p$  as  $C_p\partial_t T$ . Moreover, the isentropic temperature profile in the TMO verifies:

$$\frac{\partial T}{\partial r} = -\frac{\alpha g T}{C_p}. \quad (5.8)$$

The temperature at the Top Ocean/Mantle Boundary (TOMB, at  $r = R^+$ ) is the melting temperature denoted  $T^+$ . Integrating eq. (5.8) gives the temperature profile in the TMO. Neglecting variations of  $\alpha$  and  $C_p$  with depth, this leads to

$$T(r) = T^+ \exp\left(\frac{\alpha(R^+ - r)}{C_p}\right). \quad (5.9)$$

It is well known variations of  $\alpha$  are important at the scale of the whole mantle (Ricard 2015), the assumption of a constant  $\alpha$  should therefore be alleviated to study systems exhibiting thick magma oceans.

Due to the very large Rayleigh number of magma oceans, convection is very efficient leading to a small super-isentropic temperature difference across the magma ocean (Labrosse, Hernlund, and Coltice 2007; Ulvrova et al. 2012). The boundary layer on the liquid side at the TOMB and its associated temperature and composition jump are therefore neglected. The treatment of the boundary layer at the surface of the planet is explicated later on in this subsection.

Neglecting spatial and time variations of  $\rho$ ,  $C_p$ ,  $g$  and  $\alpha$ , the cooling term  $Q_c$  expands as:

$$\begin{aligned} Q_c &\equiv \int_{\text{TMO}} \rho C_p \frac{\partial T}{\partial t} dV \\ &= 4\pi \rho C_p \left( \dot{T}^+ + \frac{\alpha g T^+}{C_p} \dot{R}^+ \right) \int_{R^+}^{R_T} r^2 \exp\left(\frac{\alpha g (R^+ - r)}{C_p}\right) dr. \end{aligned} \quad (5.10)$$

### Compositional contribution to internal energy $\mu\partial_t \xi$

The TMO is assumed to be well-mixed. At any given time, its FeO mass fraction  $\xi$  is therefore constant throughout the entire magma ocean. It is denoted  $\xi^+$  and is only a function of time.

Moreover, the chemical potential difference between the two end-members  $\mu = \mu_{\text{FeO}} - \mu_{\text{MgO}}$  verifies (e.g. Braginsky and Roberts 1995; Lister and Buffett 1995)

$$\frac{\partial \mu}{\partial r} = -\beta g. \quad (5.11)$$

$\beta$  is the chemical expansivity defined as

$$\beta \equiv -\left. \frac{1}{\rho} \frac{\partial \rho}{\partial \xi} \right|_{P,s} = \rho \left. \frac{\partial \mu}{\partial P} \right|_{s,\xi}. \quad (5.12)$$

Note that since FeO is the heavy end-member of the considered phase-diagram,  $\beta$  is negative. Assuming constant  $\beta$  and  $g$ , integrating eq. (5.11) gives

$$\mu - \mu^+ = \beta g(R^+ - r) \equiv \mu' \quad (5.13)$$

where  $\mu^+$  is the chemical potential difference at the TOMB. Its value can be estimated from the difference at ambient condition of enthalpy of formation  $\Delta H^0$ , heat capacity  $\Delta C_p^0$  and entropy  $\Delta S^0$  between the two end-members:

$$\mu^+ = \Delta H^0 + \Delta C_p^0(T^+ - T^0) - \Delta S^0(T^+ - T^0) + \beta g(R_T - R^+). \quad (5.14)$$

The second term on the right-hand-side integrates the effect of temperature on the enthalpy of formation, the third term is the difference between enthalpy and free-energy, and the last term is the effect of pressure on the chemical potential difference.

Neglecting spatial variations of  $g$  and  $\beta$ , the compositional contribution  $Q_\xi$  to the energy budget is written as

$$\begin{aligned} Q_\xi &\equiv \int_{\text{TMO}} \rho \mu \frac{\partial \xi}{\partial t} dV \\ &= \rho \beta g \dot{\xi}^+ (R^+ V_{\text{TMO}} - \pi(R_T^4 - (R^+)^4)) + \rho \dot{\xi}^+ \mu^+ V_{\text{TMO}}. \end{aligned} \quad (5.15)$$

### Latent heat $Q_L$

The latent heat term  $Q_L$  is related to the rate of freezing and melting, which can occur through two mechanisms: the net freezing of the magma ocean at a rate  $\dot{R}^+$ , and the dynamical melting and freezing owing to the flow-through boundary condition at a rate  $u_r$ . Integrating these two contributions over the TOMB leads to:

$$Q_L = \int_+ \rho L_h (\dot{R}^+ - u_r) dS. \quad (5.16)$$

Moreover, the latent heat  $L_h$  expands as

$$L_h = T^+ \Delta s + \mu^+ \Delta \xi = T^+ (s_l - s_s) + \mu^+ (\xi^+ - \xi_s). \quad (5.17)$$

Assuming  $\Delta s$  to be laterally constant and since the lateral average of  $u_r$  is null (see section 2.3), this leads to

$$Q_L = 4\pi(R^+)^2 \rho T^+ \Delta s \dot{R}^+ + \int_+ \rho \mu^+ \Delta \xi (\dot{R}^+ - u_r) dS. \quad (5.18)$$

### Radiogenic heating $Q_R$

Several elements are responsible for radiogenic heating in the primitive mantle. For the sake of simplicity, all the heat producing elements (HPE) are treated as one element with an associated half-life  $\tau_{\text{HPE}}$  and partition coefficient  $K_{\text{HPE}}$ . The concentration of HPE is denoted  $c^+$ . The radiogenic heating  $Q_R$  is then

$$Q_R = \rho c^+ R_H \exp\left(\ln\left(\frac{1}{2}\right) \frac{t}{\tau_{\text{HPE}}}\right) V_{\text{TMO}} \quad (5.19)$$

where  $R_H$  is the massic heat production. Conservation of HPE is similar to that of FeO:

$$\frac{d(M_{\text{TMO}c^+})}{dt} = M_{\text{TMO}}\dot{c}^+ - 4\pi(R^+)^2\rho c^+\dot{R}^+ = I_{\text{HPE}}^+ \quad (5.20)$$

where  $I_{\text{HPE}}^+$  is the upward flux of HPE through the TOMB. That flux depends on the net freezing/melting occurring at the boundary:

$$I_{\text{HPE}}^+ = \int_+ \rho(c_\phi^{-u_r}u_r - c_\phi^{\dot{R}^+}\dot{R}^+)dS \quad (5.21)$$

where  $c_\phi^v$  is the relevant solid composition similarly to what is done for FeO eq. (5.6):

$$c_\phi^v = \begin{cases} \frac{c^+K_{\text{HPE}}}{1 - c^+(1 - K_{\text{HPE}})} & v \geq 0; \\ c_s & v < 0. \end{cases} \quad (5.22)$$

Combining eqs. (5.20) and (5.21) gives the following relation between  $\dot{c}^+$  and  $\dot{R}^+$ :

$$\left( \int_+ \rho c_\phi^{\dot{R}^+} dS - 4\pi(R^+)^2\rho c^+ \right) \dot{R}^+ + \frac{4\pi}{3}\rho(R_T^3 - (R^+)^3)\dot{c}^+ = \int_+ \rho c_\phi^{-u_r}u_r dS. \quad (5.23)$$

Note that the decay of HPE is directly taken into consideration in the radiogenic heating eq. (5.19) rather than in the evolution of  $c^+$ . This is to ease the implementation in StagYY. This leads to a slight error in the evolution of  $c^+$  (since  $c_\phi^v$  depends on the actual value of  $c^+$  when  $v \geq 0$ ), but this error should be less than that made with the assumption that the crystallization is purely fractional with a constant partition coefficient. Once again, the goal of this model is only to capture the broad behaviour of the system, which should not be strongly affected by this approximation.

### Energy flux through the TOMB $Q^+$

The energy flux through the TOMB  $Q^+$  is expanded as:

$$Q^+ = Q_T^+ + \mu^+I^+. \quad (5.24)$$

Note that a chemical term  $\mu^+I^+$  appears in the energy flux.  $\mu^+$  is the chemical potential difference at the boundary eq. (5.14) and  $I^+$  is the flux of FeO through the boundary eq. (5.4). The thermal flux  $Q_T^+$  is determined by our model of convection in the solid.

### Energy flux at the surface $Q^s$

At the surface of the planet, we consider that there is no flux of FeO. The energy flux hence has only a thermal contribution  $Q^s = Q_T^s$ . King et al. (2012) showed that the scaling law for the heat flux in a rotating fluid (such as the surface magma ocean) depends on how the quantity  $\text{Ra}_{\text{TMO}}\text{Ek}_{\text{TMO}}^{3/2} = \frac{\alpha g \Delta T \nu^{1/2}}{\kappa (2\Omega)^{3/2}}$  compares to 1, with  $\text{Ek}_{\text{TMO}}$  the Ekman number and  $\text{Ra}_{\text{TMO}}$  the Rayleigh number in the TMO. A conservative lower bound with the thermal expansivity  $\alpha \sim 10^{-5} \text{K}^{-1}$ , the gravity

$g \sim 10 \text{ m/s}^2$ , the super-isentropic temperature difference  $\Delta T \sim 1 \text{ K}$ , the kinematic viscosity  $\nu \sim 10^{-5} \text{ m}^2/\text{s}$ , the thermal diffusivity  $\kappa \sim 10^{-6} \text{ m}^2/\text{s}$  and the rotation rate  $\Omega \sim 10^{-4} \text{ s}^{-1}$  is  $\text{Ra}_{\text{TMO}} \text{Ek}_{\text{TMO}}^{3/2} \sim 10^5 \gg 1$ . We then consider the heat flux is not controlled by rotation and scales as  $\text{Nu} = 0.16 \text{Ra}_{\text{TMO}}^{2/7} (\Gamma^+)^{6/7}$  with  $\Gamma^+ = (R_T - R^+)/L_M$  the dimensionless thickness of the TMO. Note that this scaling does not depend on the Prandtl number in the range of values explored by King et al. (ibid.), i.e.  $1 \leq \text{Pr} \leq 100$ . Since  $\text{Pr} \sim 10$  is a reasonable value for a magma ocean, we assume this scaling holds for our study. We neglect variations of  $\text{Ra}_{\text{TMO}}$  with time and assume the magma ocean behaves like a gray body at its upper surface. Heat flow conservation at the surface gives the following equation for the surface temperature  $T_s$ :

$$\frac{k(T_p - T_s)}{L_M} 0.16 \text{Ra}_{\text{TMO}}^{2/7} (\Gamma^+)^{-1/7} = \varepsilon \sigma (T_s^4 - T_\infty^4). \quad (5.25)$$

$T_p = T^+ \exp\left(\frac{\alpha g (R^+ - R_T)}{C_p}\right)$  is the potential temperature at the surface,  $T_\infty$  is the black body equilibrium temperature,  $\sigma$  is the Stefan-Boltzmann constant and  $\varepsilon$  the emissivity. This equation on  $T_s$  is of the form  $(T_s^4 - T_\infty^4) + a(T_s - T_p) = 0$  with  $a > 0$ . This equation for  $T_s$  has a unique solution in  $[T_\infty, T_p]$ , and hence can easily be solved via dichotomy. Once the surface temperature  $T_s$  is determined, the heat flux can be calculated either with the heat flux scaling law or by plugging it back in the gray-body flux expression:

$$Q_T^s = 4\pi R_T^2 \varepsilon \sigma (T_s^4 - T_\infty^4). \quad (5.26)$$

The emissivity should depend on the atmosphere dynamics and composition (particularly its water content) and vary with time. Taking this effect into account would require an atmosphere model (e.g. Abe 1997; Lebrun et al. 2013). For the sake of simplicity, we assume the emissivity to be constant, tuning its value to obtain a crystallization timescale that matches the ones of Lebrun et al. (2013).

### Energy conservation as a linear function of $\dot{R}^+$

Plugging the expressions for several terms detailed in this subsection, the energy conservation equation can be written as

$$\begin{aligned} 0 = & - \underbrace{Q_c - \rho \beta g \dot{\xi}^+ (R^+ V_{\text{TMO}} - \pi (R_T^4 - (R^+)^4))}_{E_{\xi_1}} \\ & + \underbrace{4\pi (R^+)^2 \rho T^+ \Delta s \dot{R}^+}_{Q_{L,H}} - \underbrace{\int_+ \rho \mu^+ \xi_s (\dot{R}^+ - u_r) dS}_{E_{\xi_2}} + Q_R + Q_T^+ - Q_T^s. \end{aligned} \quad (5.27)$$

Terms in  $\dot{\xi}^+$  are expressed as a linear function of  $\dot{R}^+$  with the iron conservation eq. (5.3) combined with the expression of  $I^+$  eq. (5.4):

$$\dot{\xi}^+ = \frac{1}{M_{\text{TMO}}} \left( 4\pi (R^+)^2 \rho \xi^+ - \int_+ \rho \xi_\phi \dot{R}^+ dS \right) \dot{R}^+ + \frac{1}{M_{\text{TMO}}} \int_+ \rho \xi_\phi^{-u_r} u_r dS. \quad (5.28)$$

Similarly, terms in  $\dot{T}^+$  are expressed as a linear function of  $\dot{R}^+$  using the phase diagram eq. (5.2) and the previous expression eq. (5.28):

$$\begin{aligned} \dot{T}^+ = & \left( \frac{1}{M_{\text{TMO}}} \left( 4\pi(R^+)^2 \rho \xi^+ - \int_+ \rho \xi_\phi^{\dot{R}^+} dS \right) \frac{\partial T_L}{\partial \xi} - \frac{\partial T_L}{\partial P} \rho g \right) \dot{R}^+ \\ & + \frac{\partial T_L}{\partial \xi} \frac{1}{M_{\text{TMO}}} \int_+ \rho \xi_\phi^{-u_r} u_r dS. \end{aligned} \quad (5.29)$$

The energy conservation equation therefore allows us to compute  $\dot{R}^+$  at a given instant in our model. Then, plugging  $\dot{R}^+$  back in eqs. (5.28) and (5.29) gives us  $\dot{\xi}^+$  and  $\dot{T}^+$ . Similarly,  $\dot{c}^+$  is given by the HPE conservation eq. (5.23).

### 5.1.2 Dimensionless equations

The magma ocean evolution equations are made dimensionless with the following scales.

- $L_M$ , the total thickness of the mantle (solid and both oceans), considered constant in this study for simplicity. For the Earth,  $L_M = 2900$  km.
- $\Delta T_M$ , an arbitrary reference temperature difference. In practice it is taken as a guesstimate for the melting temperature difference between the top and the bottom of the mantle, so that the dimensionless temperature across the solid  $\Delta T / \Delta T_M$  is of order one. The chosen value is  $\Delta T_M = 4000$  K.
- $\rho$ , the reference density of the considered materials. For the Earth's mantle,  $\rho = 4000$  kg/m<sup>3</sup>.
- $\kappa = k / (\rho C_p)$ , the diffusion coefficient  $\kappa = 10^{-6}$  m<sup>2</sup>/s, associated with the conductivity  $k = 4$  W/(mK) and the heat capacity  $C_p = 10^3$  J K<sup>-1</sup> kg<sup>-1</sup>.

The dimensionless parameters arising from the non-dimensionalization are shown in table 5.1.

The dimensionless equations are shown hereafter using the same symbols as for dimensional quantities.

The conservation of FeO leads to

$$\dot{\xi} = \underbrace{\frac{1}{V_{\text{TMO}}} (4\pi(R^+)^2 \xi - I_\xi^+)}_{a_\xi} \dot{R}^+ + \underbrace{\frac{1}{V_{\text{TMO}}} I_{u\xi}^+}_{b_\xi}. \quad (5.30)$$

The two compositional integrals are defined as:

$$I_\xi^+ = \int_+ \xi_\phi^{R^+} dS; \quad (5.31)$$

$$I_{u\xi}^+ = \frac{1}{\Gamma} \int_+ \xi_\phi^{-u_r} u_r dS. \quad (5.32)$$

The  $1/\Gamma$  factor comes from the non-dimensionalization of velocities in the solid with  $L$  instead of  $L_M$ . See section 5.3 for details.

Symbol	Expression	Description	Nominal value
$\Gamma$	$\frac{L}{L_M}$	Solid thickness	Time dependent
$\Gamma^+$	$\frac{R_T - R^+}{L_M}$	TMO thickness	Time dependent
$T_0^+$	$\frac{T^+(t=0)}{\Delta T_M}$	Initial TOMB temperature	Run dependent
$\xi_0^+$	$\xi^+(t=0)$	Initial TMO FeO content	Run dependent
$c_0^+$	$c^+(t=0)$	Initial TMO HPE content	Run dependent
$B_\xi$	$-\frac{\beta}{\alpha \Delta T_M}$	Compositional buoyancy	5
Di	$\frac{\alpha g L_M}{C_p}$	Dissipation number	0.58
$T_{LP}$	$\frac{\rho g L_M}{\Delta T_M} \frac{\partial T_L}{\partial P}$	Pressure dependence of melting temperature	0.53 (Andraut, Petitgirard, et al. 2012)
$T_{L\xi}$	$\frac{1}{\Delta T_M} \frac{\partial T_L}{\partial \xi}$	Composition dependence of melting temperature	-0.125
St	$\frac{\Delta s}{C_p}$	Stefan number	0.3
$\Delta H^0$	$\frac{\Delta H^0}{C_p \Delta T_M}$	FeO-MgO enthalpy difference at ambient conditions	2.8 (Haynes and Lide 2011)
$\Delta C_p^0$	$\frac{\Delta C_p^0}{C_p}$	FeO-MgO heat capacity difference at ambient conditions	-0.2 (Haynes and Lide 2011)
$\Delta S^0$	$\frac{\Delta S^0}{C_p}$	FeO-MgO entropy difference at ambient conditions	-0.05 (Haynes and Lide 2011)
$R_H$	$\frac{R_{H,d} \rho L_M^2}{k \Delta T_M}$	Specific radiogenic heat production	20
$\tau_{\text{HPE}}$	$\frac{\tau_{\text{HPE},d} \kappa}{L_M^2}$	HPE half-life	0.02
$\text{Ra}_{\text{TMO}}$	$\frac{\rho \alpha g \Delta T_O L_M^3}{\eta \kappa}$	Rayleigh number in the TMO	$10^{30}$
$T_\infty$	$\frac{T_\infty}{\Delta T_M}$	Gray body equilibrium temperature	$6.4 \times 10^{-2}$
$E_{GB}$	$\frac{\varepsilon \sigma L_M \Delta T_M^3}{k}$	Gray body coefficient	$2 \times 10^5$

Table 5.1: Dimensionless parameters for the Top Magma Ocean evolution.

The melting temperature then verifies

$$\dot{T}^+ = (T_{L\xi}a_\xi - T_{LP})\dot{R}^+ + T_{L\xi}b_\xi. \quad (5.33)$$

The secular cooling term  $Q_c$  becomes

$$Q_c = 4\pi I_c (T_{L\xi}a_\xi - T_{LP} + \text{Di}T^+) \dot{R}^+ + 4\pi I_c T_{L\xi}b_\xi \quad (5.34)$$

with

$$I_c = \int_{R^+}^{R_T} r^2 \exp(\text{Di}(R^+ - r)) dr. \quad (5.35)$$

The thermal contribution to the latent heat is

$$Q_{L,H} = 4\pi(R^+)^2 T^+ \text{St} \dot{R}^+. \quad (5.36)$$

The compositional terms become

$$E_{\xi 1} = B_\xi \text{Di}(R^+ V_{\text{TMO}} - \pi(R_T^4 - (R^+)^4))(a_\xi \dot{R}^+ + b_\xi); \quad (5.37)$$

$$E_{\xi 2} = \mu^+ (I_{u\xi}^+ - I_\xi^+ \dot{R}^+). \quad (5.38)$$

where  $\mu^+$  is

$$\mu^+ = \Delta H^0 + \Delta C_p^0(T^+ - T^0) - \Delta S^0(T^+ - T^0) - B_\xi \text{Di}\Gamma^+. \quad (5.39)$$

The flux at the surface verifies

$$Q_T^s = 4\pi E_{GB} R_T^2 (T_s^4 - T_\infty^4), \quad (5.40)$$

with the surface temperature  $T_s$  being solution of

$$(T_s^4 - T_\infty^4) + \frac{0.16 \text{Ra}_{\text{TMO}}^{2/7} (\Gamma^+)^{-1/7}}{E_{GB}} (T_s - T^+ \exp(\text{Di}(R^+ - R_T))) = 0. \quad (5.41)$$

Finally, the energy balance simply is

$$Q_c = E_{\xi 1} + E_{\xi 2} + Q_L + Q_R + Q_T^+ - Q_T^s. \quad (5.42)$$

## 5.2 Evolution model of the Basal Magma Ocean (BMO)

### 5.2.1 Dimensional model

The evolution model of the Basal Magma Ocean is very similar to that of the Top Magma Ocean presented in the previous section. The main differences are the signs of some terms, and of course the CMB heat flux is treated in a different way than the surface heat flux. This section follows the same layout as the previous one, underlining the key differences. Energy conservation on the BMO gives

$$\int_{\text{BMO}} \rho \left( T \frac{\partial s}{\partial t} + \mu \frac{\partial \xi}{\partial t} \right) dV = Q_L + Q_R + Q^c - Q^-. \quad (5.43)$$

Note that the only difference with eq. (5.1) are the signs of the surface fluxes. The flux from the core  $Q^c$  is a positive contribution to the energy balance of the BMO while the flux extracted by the mantle  $Q^-$  is a negative contribution.

### Phase diagram at the boundary

The melting temperature at the BOMB,  $T^-$ , depends on pressure and composition, leading to

$$\dot{T}^- = -\frac{\partial T_L}{\partial P} \rho g \dot{R}^- + \frac{\partial T_L}{\partial \xi} \dot{\xi}^-. \quad (5.44)$$

Conservation of FeO gives a linear relation between  $\dot{\xi}^-$  and  $\dot{R}^-$ :

$$\frac{d(M_{\text{BMO}} \xi^-)}{dt} = M_{\text{BMO}} \dot{\xi}^- + 4\pi (R^-)^2 \rho \xi^- \dot{R}^- = -I^-. \quad (5.45)$$

$I^-$  is the upward flux of iron through the BOMB (we do not consider a flux of iron through the CMB). That flux depends on the net freezing/melting occurring at the boundary:

$$I^- = \int_- \rho (\xi_\phi^{u_r} u_r - \xi_\phi^{\dot{R}^-} \dot{R}^-) dS. \quad (5.46)$$

Similarly to what is done for the TMO,  $\xi_\phi^v$  is the composition of the solid associated with a freezing-front velocity  $v$ . Note that  $u_r > 0$  and  $\dot{R}^- < 0$  are the cases corresponding to the crystallization of a new solid, instead of  $u_r < 0$  and  $\dot{R}^+ > 0$  for the TMO. Denoting  $K$  the partition coefficient of FeO,  $\xi_\phi^v$  follows

$$\xi_\phi^v = \begin{cases} \frac{K \xi^-}{1 - \xi^- (1 - K)} & v \geq 0; \\ \xi_s & v < 0. \end{cases} \quad (5.47)$$

Combining eqs. (5.45) and (5.46) gives:

$$\left( 4\pi (R^-)^2 \rho \xi^- - \int_- \rho \xi_\phi^{\dot{R}^-} dS \right) \dot{R}^- + \frac{4\pi}{3} \rho ((R^-)^3 - R_c^3) \dot{\xi}^- = - \int_- \rho \xi_\phi^{u_r} u_r dS. \quad (5.48)$$

### Entropy contribution to internal energy $T \partial_t s$

As for the TMO, we assume the BMO is well-mixed and its temperature profile is therefore isentropic:

$$\frac{\partial T}{\partial r} = -\frac{\alpha g T}{C_p}. \quad (5.49)$$

The temperature at the Basal Ocean/Mantle Boundary (BOMB, at  $r = R^-$ ) is the melting temperature  $T^+$ . Integrating eq. (5.49) gives the temperature profile in the BMO:

$$T = T^- \exp\left(\frac{\alpha (R^- - r)}{C_p}\right). \quad (5.50)$$

Both boundary layers in the BMO are neglected in its energy balance. Moreover, spatial and time variations of  $\rho$ ,  $C_p$ ,  $g$  and  $\alpha$  are neglected, leading to

$$\begin{aligned} Q_c &\equiv \int_{\text{BMO}} \rho C_p \frac{\partial T}{\partial t} dV \\ &= 4\pi \rho C_p \left( \dot{T}^- + \frac{\alpha g T^-}{C_p} \dot{R}^- \right) \int_{R_c}^{R^-} r^2 \exp\left(\frac{\alpha g (R^- - r)}{C_p}\right) dr. \end{aligned} \quad (5.51)$$

### Compositional contribution to internal energy $\mu\partial_t\xi$

Similarly to what is done for the TMO, the BMO is considered to be well-mixed. Its FeO content  $\xi$  is therefore only a function of time, it is denoted  $\xi^-$ .

The chemical potential difference between the two end-members  $\mu = \mu_{\text{FeO}} - \mu_{\text{MgO}}$  verifies

$$\frac{\partial\mu}{\partial r} = -\beta g \quad (5.52)$$

with  $\beta$  the compositional expansivity. Integrating this equation gives

$$\mu - \mu^- = \beta g(R^- - r) \equiv \mu' \quad (5.53)$$

where  $\mu^-$  is the chemical potential difference at the BOMB.

As for the TOMB, its value is estimated from the difference at ambient condition of enthalpy  $\Delta H^0$ , heat capacity  $\Delta C_p^0$  and entropy  $\Delta S^0$  between the two end-members:

$$\mu^- = \Delta H^0 + \Delta C_p^0(T^- - T^0) - \Delta S^0(T^- - T^0) + \beta g(R_T - R^-). \quad (5.54)$$

The compositional contribution  $Q_\xi$  to the energy budget of the BMO is therefore

$$\begin{aligned} Q_\xi &\equiv \int_{\text{BMO}} \rho\mu \frac{\partial\xi}{\partial t} dV \\ &= \rho\beta g\dot{\xi}^- (R^- V_{\text{BMO}} - \pi((R^-)^4 - R_c^4)) + \rho\dot{\xi}^- \mu^- V_{\text{BMO}}. \end{aligned} \quad (5.55)$$

### Latent heat $Q_L$

The latent heat term for the BMO present one difference with the TMO case: melting and freezing correspond to opposite signs of radial velocities. This leads to

$$Q_L = \int_{-} \rho L_h (u_r - \dot{R}^-) dS. \quad (5.56)$$

The latent heat  $L_h$  expands as

$$L_h = T^- \Delta s + \mu^- \Delta\xi = T^- (s_l - s_s) + \mu^- (\xi^- - \xi_s). \quad (5.57)$$

Plugging this in eq. (5.56) gives

$$Q_L = -4\pi(R^-)^2 \rho T^- \Delta s \dot{R}^- + \int_{-} \rho\mu^- \Delta\xi (u_r - \dot{R}^-) dS. \quad (5.58)$$

### Radiogenic heating $Q_R$

As for the TMO, the radiogenic heating in the BMO is associated to the concentration in heat producing element (HPE), denoted  $c^-$ , with an associated half-life  $\tau_{\text{HPE}}$ . The radiogenic heating  $Q_R$  is then

$$Q_R = \rho c^- R_H \exp\left(\ln\left(\frac{1}{2}\right) \frac{t}{\tau_{\text{HPE}}}\right) V_{\text{BMO}} \quad (5.59)$$

where  $R_H$  is the massic heat production. Conservation of HPE is similar to that of FeO:

$$\frac{d(M_{\text{BMO}} c^-)}{dt} = M_{\text{BMO}} \dot{c}^- + 4\pi(R^-)^2 \rho c^- \dot{R}^- = I_{\text{HPE}}^- \quad (5.60)$$

where  $I_{\text{HPE}}^-$  is the upward flux of HPE through the BOMB. That flux depends on the net freezing/melting occurring at the boundary:

$$I_{\text{HPE}}^- = \int_- \rho(c_\phi^{u_r} u_r - c_\phi^{-\dot{R}^-} \dot{R}^-) dS. \quad (5.61)$$

$c_\phi^v$  is the relevant solid composition similarly to what is done for FeO eq. (5.47):

$$c_\phi^v = \begin{cases} \frac{K_{\text{HPE}} c^-}{1 - c^-(1 - K_{\text{HPE}})} & v \geq 0; \\ c_s & v < 0. \end{cases} \quad (5.62)$$

Combining eqs. (5.60) and (5.61) gives the following relation between  $\dot{c}^-$  and  $\dot{R}^-$ :

$$\left(4\pi(R^-)^2 \rho c^- - \int_- \rho c_\phi^{-\dot{R}^-} dS\right) \dot{R}^- + \frac{4\pi}{3} \rho ((R^-)^3 - R_c^3) \dot{c}^- = - \int_- \rho c_\phi^{u_r} u_r dS. \quad (5.63)$$

### Energy flux through the BOMB $Q^-$

Similarly to flux through the TOMB  $Q^+$ , the energy flux through the BOMB  $Q^-$  is expanded as:

$$Q^- = Q_T^- + \mu^- I^- \quad (5.64)$$

with  $\mu^-$  the chemical potential difference at the boundary eq. (5.54) and  $I^-$  the flux of FeO through the boundary eq. (5.46). The thermal flux  $Q_T^-$  is determined by our model of convection in the solid.

### Core contribution to the energy budget

We neglect the FeO flux between the core and the mantle for the sake of simplicity. The energy flux from the core is therefore purely thermal  $Q^c = Q_T^c$ . We use here the core cooling model proposed by Labrosse (2015) for an entirely liquid core. This model connects directly the heat flux extracted from the core  $Q^c$  to the time derivative of the temperature at the CMB  $T_c$ .

$$Q^c = - \underbrace{\frac{4\pi}{3} \rho_N C_{pN} L_\rho^3}_{P_{c,d}} \frac{f_C\left(\frac{R_c}{L_\rho}, \gamma\right)}{\left(1 - \frac{R_c^2}{L_\rho^2} - A_\rho \frac{R_c^4}{L_\rho^4}\right)^\gamma} \dot{T}_c. \quad (5.65)$$

$\rho_N$  is the density at the center of the core,  $C_{pN}$  the assumed constant heat capacity of the core,  $L_\rho$  and  $A_\rho$  the structure parameters describing the density variation with radius in the core,  $\gamma$  the Grüneisen parameter of the core and

$$\begin{aligned} f_C(x, \gamma) &= 3 \int_0^x u^2 (1 - u^2 - A_\rho u^4)^{1+\gamma} du \\ &= x^3 \left(1 - \frac{3}{5}(\gamma + 1)x^2 - \frac{3}{14}(\gamma + 1)(2A_\rho - \gamma)x^4 + \mathcal{O}(\delta x^6)\right). \end{aligned} \quad (5.66)$$

As the thermal boundary layers at both boundaries of the core are thin and with a small temperature difference across them compared to that at the scale of the whole core,  $T_c$  can be related to  $T^-$  assuming an adiabatic profile in the core

$$T_c = T^+ \exp\left(\frac{\alpha g(R^- - R_c)}{C_p}\right). \quad (5.67)$$

Hence,  $\dot{T}_c$ , and therefore  $Q^c$ , can be expressed as a linear function of  $\dot{T}^-$  and  $\dot{R}^-$ :

$$\dot{T}_c = \left(\dot{T}^- + \frac{\alpha g T^-}{C_p} \dot{R}^-\right) \exp\left(\frac{\alpha g(R^- - R_c)}{C_p}\right). \quad (5.68)$$

### Energy conservation as a linear function of $\dot{R}^-$

Plugging the expressions for all the terms in the energy conservation eq. (5.43) gives

$$0 = - \underbrace{Q_c - \rho\beta g \dot{\xi} (R^- V_{\text{BMO}} - \pi((R^-)^4 - R_c^4))}_{E_{\xi_1}} - \underbrace{-4\pi(R^-)^2 \rho T^- \Delta s \dot{R}^-}_{Q_{L,H}} + \underbrace{\rho\mu^- \int_- \xi_s (\dot{R}^- - u_r) dS}_{E_{\xi_2}} + Q_R + Q_T^c - Q_T^-. \quad (5.69)$$

The strategy to solve this equation is, as for the TMO, to develop terms in  $\dot{\xi}^-$  using the FeO conservation eq. (5.48)

$$\dot{\xi}^- = \frac{1}{M_{\text{BMO}}} \left( \int_- \rho \xi_\phi^{-\dot{R}^-} - 4\pi(R^-)^2 \rho \xi^- dS \right) \dot{R}^- - \frac{1}{M_{\text{BMO}}} \int_- \rho \xi_\phi^{u_r} u_r dS. \quad (5.70)$$

Terms in  $\dot{T}^-$  are expanded as linear functions of  $\dot{R}^-$  using the phase diagram eq. (5.44)

$$\begin{aligned} \dot{T}^- = & \left( \frac{1}{M_{\text{BMO}}} \left( \int_- \rho \xi_\phi^{-\dot{R}^-} - 4\pi(R^-)^2 \rho \xi^- dS \right) \frac{\partial T_L}{\partial \xi} - \frac{\partial T_L}{\partial P} \rho g \right) \dot{R}^- \\ & - \frac{\partial T_L}{\partial \xi} \frac{1}{M_{\text{BMO}}} \int_- \rho \xi_\phi^{u_r} u_r dS. \end{aligned} \quad (5.71)$$

The energy conservation equation is then used to compute  $\dot{R}^-$  at a given instant in our model. Plugging  $\dot{R}^-$  back in eqs. (5.63), (5.70) and (5.71) gives us  $\dot{c}^-$ ,  $\dot{\xi}^-$  and  $\dot{T}^-$ .

### 5.2.2 Dimensionless equations

The basal magma ocean evolution equations are made dimensionless with the same scales as the top magma ocean. The dimensionless parameters arising from the non-dimensionalization are shown in table 5.2.

The dimensionless equations are shown hereafter using the same symbols as for dimensional quantities.

The conservation of FeO leads to

$$\dot{\xi} = \underbrace{\frac{1}{V_{\text{BMO}}} (I_\xi^- - 4\pi(R^-)^2 \xi)}_{a_\xi} \dot{R}^+ - \underbrace{\frac{1}{V_{\text{BMO}}} I_{u\xi}^-}_{b_\xi} \quad (5.72)$$

Symbol	Expression	Description	Nominal value
$\Gamma$	$\frac{L}{L_M}$	Solid thickness	Time dependent
$\Gamma^-$	$\frac{L_M}{R^- - R_c}$	Initial BMO thickness	Time dependent
$T_0^-$	$\frac{L_M}{T^-(t=0) - \Delta T_M}$	Initial BOMB temperature	Run dependent
$\xi_0^-$	$\xi^-(t=0)$	Initial BMO FeO content	Run dependent
$c_0^-$	$c^-(t=0)$	Initial BMO HPE content	Run dependent
$B_\xi$	$-\frac{\beta}{\alpha \Delta T_M}$	Compositional buoyancy	5
Di	$\frac{\alpha g L_M}{C_p}$	Dissipation number	1.74
$T_{LP}$	$\frac{\rho g L_M}{\Delta T_M} \frac{\partial T_L}{\partial P}$	Pressure dependence of melting temperature	0.53 (Andrault, Petitgirard, et al. 2012)
$T_{L\xi}$	$\frac{1}{\Delta T_M} \frac{\partial T_L}{\partial \xi}$	Composition dependence of melting temperature	-0.125
St	$\frac{\Delta s}{C_p}$	Stefan number	0.3
$\Delta H^0$	$\frac{\Delta H^0}{C_p \Delta T_M}$	MgO-FeO enthalpy difference at ambient conditions	2.8 (Haynes and Lide 2011)
$\Delta C_p^0$	$\frac{\Delta C_p^0}{C_p}$	MgO-FeO heat capacity difference at ambient conditions	-0.2 (Haynes and Lide 2011)
$\Delta S^0$	$\frac{\Delta S^0}{C_p}$	MgO-FeO entropy difference at ambient conditions	-0.05 (Haynes and Lide 2011)
$R_H$	$\frac{R_{H,d} \rho L_M^2}{k \Delta T_M}$	Specific radiogenic heat production	20
$\tau_{\text{HPE}}$	$\frac{\tau_{\text{HPE},d} \kappa}{L_M^2}$	HPE half-life	0.02
$P_c$	$\frac{F_{c,d}}{\rho C_p L_M^3}$	Core cooling contribution, see eq. (5.65)	3.67

Table 5.2: Dimensionless parameters for the Basal Magma Ocean evolution.

The two compositional integrals are defined as:

$$I_{\xi}^{-} = \int_{-} \xi_{\phi}^{-\dot{R}^{-}} dS; \quad (5.73)$$

$$I_{u\xi}^{-} = \frac{1}{\Gamma} \int_{-} \xi_{\phi}^{u_r} u_r dS. \quad (5.74)$$

The  $1/\Gamma$  factor comes from the non-dimensionalization of velocities in the solid with  $L$  instead of  $L_M$ . See section 5.3 for details.

The melting temperature then verifies

$$\dot{T}^{-} = (T_{L\xi} a_{\xi} - T_{LP}) \dot{R}^{-} + T_{L\xi} b_{\xi} \quad (5.75)$$

The secular cooling term  $Q_c$  becomes

$$Q_c = 4\pi I_c (T_{L\xi} a_{\xi} - T_{LP} + \text{Di}T^{-}) \dot{R}^{-} + 4\pi I_c T_{L\xi} b_{\xi} \quad (5.76)$$

with

$$I_c = \int_{R_c}^{R^{-}} r^2 \exp(\text{Di}(R^{-} - r)) dr. \quad (5.77)$$

The thermal contribution to the latent heat is

$$Q_{L,H} = -4\pi (R^{-})^2 T^{-} \text{St} \dot{R}^{-}. \quad (5.78)$$

The compositional terms become

$$E_{\xi 1} = B_{\xi} \text{Di}(R^{-} V_{\text{BMO}} - \pi((R^{-})^4 - R_c^4))(a_{\xi} \dot{R}^{-} + b_{\xi}); \quad (5.79)$$

$$E_{\xi 2} = \mu^{-} \left( I_{\xi}^{-} \dot{R}^{-} - I_{u\xi}^{-} \right). \quad (5.80)$$

where  $\mu^{-}$  is

$$\mu^{-} = \Delta H^0 + \Delta C_p^0 (T^{-} - T^0) - \Delta S^0 (T^{-} - T^0) + B_{\xi} \text{Di}(\Gamma^{-} - 1). \quad (5.81)$$

The flux at the CMB verifies

$$Q_T^c = -P_c \dot{T}^c \quad (5.82)$$

with the CMB temperature

$$T^c = T^{-} \exp(\text{Di}(R^{-} - R_c)). \quad (5.83)$$

The energy balance is

$$Q_c = E_{\xi 1} + E_{\xi 2} + Q_L + Q_R + Q_T^c - Q_T^{-}. \quad (5.84)$$

## 5.3 Fixed-front approach in the solid

The last problem to tackle to be able to solve self-consistently the convection in the solid part and the evolution of both magma oceans according to the previously described evolution models is that the thickness of the solid part  $L = R^+ - R^-$  will change with time as it crystallizes (or melts). A possible approach is to add layers of cells to the numerical domain as the solid thickens (e.g. Ballmer et al. 2017; Maurice et al. 2017). However, this method would be difficult to implement in StagYY and raises several questions with no clear answers such as when to add such a layer, what thickness should it have, and what should be the information inside to reduce as much as possible discretization related effects. We choose instead to use a constant computational domain on which we project more and more physical domain as the solid thickens. This is done by building a dimensionless radius that is between 1 and 2 at all time and writing the conservation equations in this new frame (e.g. Crank 1984). This dimensionless radius  $\tilde{r}$  is defined as

$$\tilde{r} \equiv \frac{r - R^-}{L} + 1. \quad (5.85)$$

Note that  $R^-$  and  $L$  both depend on time, which introduces additional terms in the conservation equations when expressing them in this frame. Such an approach eliminates the need to change the computational domain as the geometry of the system changes. It is referred to as a fixed-front approach in this document.

### 5.3.1 Mathematical background

For the sake of clarity, we present here a simple mathematical description of non-dimensionalisation of a generic set of partial differential equations with scales whose definition depends on time. Note that two aspects need to be considered in doing so. First, contrary to the classical case where scales are constant, the non-dimensional basis vectors are not merely proportional to the dimensional ones, leading to additional terms when expressing partial derivatives from one frame to the other. Second, the dimensionless variables themselves are not merely proportional to the dimensional ones, leading to additional terms when expressing the equations applying to these dimensionless variables. These two aspects are briefly discussed in a general manner hereafter.

Let  $\mathbf{x}$  be any point of a dimensional frame. For our purposes, it is taken as a spherical frame  $\mathbf{x} = (t, r, \theta, \phi)$ . Let  $f$  be a dimensional function defined on this frame, such as the temperature or velocity fields involved in convection problems. The same point in the associated dimensionless frame is denoted  $\tilde{\mathbf{x}}$ , and the dimensional function defined on the dimensionless frame is denoted  $f'$  and is such that  $f(\mathbf{x}) = f'(\tilde{\mathbf{x}})$ . The Jacobian matrix  $\mathbf{J}$  associated to the transformation from the dimensionless frame to the dimensional one is

$$\mathbf{J}_{ij} = \frac{\partial \tilde{\mathbf{x}}_i}{\partial \mathbf{x}_j}. \quad (5.86)$$

Partial derivatives in one frame are related to partial derivatives in the other as

$$\frac{\partial f}{\partial \mathbf{x}_j} = \sum_i \mathbf{J}_{ij} \frac{\partial f'}{\partial \tilde{\mathbf{x}}_i}. \quad (5.87)$$

In the classic cases where  $\mathbf{x}_i$  and  $\tilde{\mathbf{x}}_i$  are proportional,  $\mathbf{J}$  is diagonal which leads to derivatives that are merely proportional to one another. In our case with the dimensionless radius built as described in eq. (5.85), the off-diagonal term  $\partial\tilde{r}/\partial t$  is non-zero, leading to

$$\frac{\partial f}{\partial t} = \frac{\partial f'}{\partial \tilde{t}} \frac{\partial \tilde{t}}{\partial t} + \frac{\partial f'}{\partial \tilde{r}} \frac{\partial \tilde{r}}{\partial t}. \quad (5.88)$$

This shows time derivatives in the dimensional frame become time derivatives associated with an advection at velocity  $\partial\tilde{r}/\partial t$  in the dimensionless frame. This advection accounts for the fact that more and more physical domain is projected in the dimensionless frame as the solid mantle thickens. Other derivatives are not affected by non-zero off-diagonal terms.

The second aspect that deserves attention is that the dimensionless function  $\tilde{f}$  associated with the dimensionless variable  $f$  can be built with a non-constant scale. In our problem, this is the case of the temperature, made dimensionless with the temperature difference between the two solid/liquid interfaces that varies with time. Keeping on with our generic example, given a time-varying scale  $F(t) = F'(\tilde{t})$  for  $f$  and a function  $f_0(t) = f'_0(\tilde{t})$ , one can build a dimensionless function  $\tilde{f}$  such as:

$$f(\mathbf{x}) = (F'\tilde{f} + f'_0)(\tilde{\mathbf{x}}). \quad (5.89)$$

Since  $F$  and  $f_0$  are merely functions of  $t$ , plugging eq. (5.89) in eq. (5.88) leads to:

$$\frac{\partial f}{\partial t} = F \left( \frac{\partial \tilde{f}}{\partial \tilde{t}} \frac{\partial \tilde{t}}{\partial t} + \frac{\partial \tilde{f}}{\partial \tilde{r}} \frac{\partial \tilde{r}}{\partial t} \right) + \tilde{f} \frac{\partial F}{\partial t} + \frac{\partial f_0}{\partial t} \quad (5.90)$$

The two last terms are null in the classical case where the scales and offset values do not depend on time.

Finally, the definition of the dimensionless radius eq. (5.85) yields a dimensionless curvature term

$$\lambda \equiv \frac{R^-}{L} - 1 \quad (5.91)$$

when expanding the  $\tilde{\nabla}$  operator in the dimensionless frame. For example the gradient expands as

$$\tilde{\nabla} f = \frac{1}{L} \tilde{\nabla} f = \frac{1}{L} \begin{pmatrix} \frac{\partial f}{\partial \tilde{r}} \\ \frac{1}{\tilde{r} + \lambda} \frac{\partial f}{\partial \theta} \\ \frac{1}{(\tilde{r} + \lambda) \sin \theta} \frac{\partial f}{\partial \phi} \end{pmatrix}, \quad (5.92)$$

and the divergence expands as

$$\begin{aligned} \tilde{\nabla} \cdot \mathbf{u} &= \frac{1}{L} \tilde{\nabla} \cdot \mathbf{u} = \frac{1}{L} \left( \frac{1}{(\tilde{r} + \lambda)^2} \frac{\partial((\tilde{r} + \lambda)^2 u_r)}{\partial \tilde{r}} \right. \\ &\quad \left. + \frac{1}{(\tilde{r} + \lambda) \sin \theta} \frac{\partial(u_\theta \sin \theta)}{\partial \theta} \right. \\ &\quad \left. + \frac{1}{(\tilde{r} + \lambda) \sin \theta} \frac{\partial u_\phi}{\partial \phi} \right). \end{aligned} \quad (5.93)$$

### 5.3.2 Dimensional equations

Conservation equations and associated boundary conditions are similar to the ones introduced in chapter 2. We introduce a conservation equation for the major element composition, namely the FeO mass fraction  $\xi$ , as well as internal heating and the associated heat producing elements (HPE) concentration  $c$ .

Mass and momentum conservation equations are

$$\nabla \cdot \mathbf{u} = 0, \quad (5.94)$$

$$\mathbf{0} = -\nabla p + \eta \nabla^2 \mathbf{u} + \delta \rho g \hat{\mathbf{r}}. \quad (5.95)$$

Composition transport equations are

$$\frac{\partial \xi}{\partial t} + \mathbf{u} \cdot \nabla \xi = 0, \quad (5.96)$$

$$\frac{\partial c}{\partial t} + \mathbf{u} \cdot \nabla c = 0. \quad (5.97)$$

Note that we assume for both FeO and HPE that their diffusion is negligible compared to that of heat (limit case of infinite Lewis numbers). The only transport mechanism affecting them is advection. Finally, the heat equation is

$$\frac{\partial T}{\partial t} + \mathbf{u} \cdot \nabla T = \kappa \nabla^2 T + h. \quad (5.98)$$

The temperature and FeO content both affect the buoyancy term as

$$\delta \rho = \rho \alpha (T - \langle T \rangle) + \rho \beta (\xi - \langle \xi \rangle). \quad (5.99)$$

Finally, internal heating is related to the HPE content as

$$h = c \frac{R_H}{C_p} \exp \left( \ln \left( \frac{1}{2} \right) \frac{t}{\tau_{\text{HPE}}} \right). \quad (5.100)$$

The mechanical boundary conditions are the same as in chapter 2, namely free-slip and phase change boundary condition:

$$r \frac{\partial}{\partial r} \left( \frac{u_\theta}{r} \right) + \frac{1}{r} \frac{\partial u_r}{\partial \theta} = r \frac{\partial}{\partial r} \left( \frac{u_\phi}{r} \right) + \frac{1}{r \sin \theta} \frac{\partial u_r}{\partial \phi} = 0, \quad (5.101)$$

$$\Delta \rho g \tau_\phi u_r + 2\eta \frac{\partial u_r}{\partial r} - p = 0. \quad (5.102)$$

The thermal boundary condition is the same as previously, with the temperature at a boundary equal to the melting temperature:

$$T(R^\pm) = T^\pm. \quad (5.103)$$

These temperature evolves with time as the pressure at the boundary and the composition of the oceans vary, according to eqs. (5.2) and (5.44). Finally, regarding the compositional fields  $\xi$  and  $c$ , their fluxes at the boundaries are imposed by the melting/freezing associated with the dynamics of the solid (owing to the flow-through boundary condition), and with the net motion of the solid/liquid interface (owing to the evolution of both magma oceans). New solid resulting from the freezing has a composition as described by eqs. (5.6), (5.22), (5.47) and (5.62).

Symbol	Expression	Description	Nominal value
Ra	$\frac{\rho g \alpha \Delta T_M L_M^3}{\eta \kappa}$	Rayleigh number	$10^7$
$B_\xi$	$-\frac{\beta}{\alpha \Delta T_M}$	Compositional buoyancy	5
$\Phi^\pm$	$\frac{ \Delta \rho  g \tau_\phi L}{\eta}$	Phase change number	$10^{-3}$
$R_H$	$\frac{R_H L_M^2}{\kappa C_p \Delta T_M}$	Heat production	20
$\tau_{\text{HPE}}$	$\frac{\tau_{\text{HPE}} \kappa}{L_M^2}$	HPE half-life	0.02

Table 5.3: Dimensionless parameters for the dynamics of the solid.

### 5.3.3 Dimensionless equations

The scales for length, velocity, mass and temperature all depend on time and are defined as:  $L = R^+ - R^-$ ,  $\frac{\kappa}{L}$ ,  $\frac{\eta L^3}{\kappa}$ ,  $\Delta T = T^- - T^+$ . To ensure the dimensionless time  $\tilde{t}$  is monotonic, it is built with a constant scale, i.e.  $t = \frac{L_M^2}{\kappa} \tilde{t}$ .

Moreover, the dimensionless temperature is defined as:

$$\tilde{T} = \frac{T - T^+}{\Delta T}. \quad (5.104)$$

This leads to constant boundary conditions on temperature.

These variable scales for length and temperature yield two dimensionless numbers depending on time. The dimensionless thickness of the solid is

$$\Gamma = \frac{L}{L_M}. \quad (5.105)$$

The dimensionless temperature scale is

$$\mathbb{T} = \frac{\Delta T}{\Delta T_M}. \quad (5.106)$$

The dimensionless parameters controlling the convection in the solid are shown in table 5.3.

The dimensionless equations in the solid are written here using the same symbol as the corresponding dimensional quantities. The Stokes and mass conservation equations become:

$$0 = \nabla \cdot \mathbf{u} \quad (5.107)$$

$$\mathbf{0} = -\nabla p + \nabla^2 \mathbf{u} + \mathbb{T} \Gamma^3 \text{Ra} \delta \rho \hat{\mathbf{r}} \quad (5.108)$$

where

$$\delta \rho = \left( T - \frac{B_\xi}{\mathbb{T}} \xi \right) - \left\langle T - \frac{B_\xi}{\mathbb{T}} \xi \right\rangle. \quad (5.109)$$

Compositional conservation equations are

$$\Gamma^2 \frac{\partial \xi}{\partial t} + \mathbf{u} \cdot \nabla \xi = 0, \quad (5.110)$$

$$\Gamma^2 \frac{\partial c}{\partial t} + \mathbf{u} \cdot \nabla c = 0. \quad (5.111)$$

The dimensionless heat conservation equation is

$$\Gamma^2 \frac{\partial T}{\partial t} + \mathbf{u} \cdot \nabla T + \Gamma \left( (1-r)\dot{R}^+ + (r-2)\dot{R}^- \right) \frac{\partial T}{\partial r} + \frac{\Gamma^2}{\mathbb{T}} (\dot{\mathbb{T}}T + \dot{T}^+) = \nabla^2 T + h. \quad (5.112)$$

The internal heating is related to the HPE content as

$$h = c \frac{\Gamma^2}{\mathbb{T}} R_H \exp \left( \ln \left( \frac{1}{2} \right) \frac{t}{\tau_{\text{HPE}}} \right). \quad (5.113)$$

The phase change boundary condition is:

$$\pm \Phi^\pm u_r + 2 \frac{\partial u_r}{\partial r} - p = 0 \quad (5.114)$$

The free-slip boundary condition becomes

$$(r+\lambda) \frac{\partial}{\partial r} \left( \frac{u_\theta}{r+\lambda} \right) + \frac{1}{r+\lambda} \frac{\partial u_r}{\partial \theta} = (r+\lambda) \frac{\partial}{\partial r} \left( \frac{u_\phi}{r+\lambda} \right) + \frac{1}{(r+\lambda) \sin \theta} \frac{\partial u_r}{\partial \phi} = 0. \quad (5.115)$$



# Chapter 6

## Timescale of overturn in a magma ocean cumulate

This chapter is a paper written by A. Morison, S. Labrosse, R. Deguen and T. Alboussière published in 2019 in *Earth and Planetary Science Letters* (Morison et al. 2019). It focuses on the timescale of overturn of the solid part of the mantle when crystallizing a Top Magma Ocean. The approach used in this chapter is a linear stability analysis and therefore present numerous simplifications to the models discussed previously.

### 6.1 Abstract

The formation and differentiation of planetary bodies are thought to involve magma oceans stages. We study the case of a planetary mantle crystallizing upwards from a global magma ocean. In this scenario, it is often considered that the magma ocean crystallizes more rapidly than the time required for convection to develop in the solid cumulate. This assumption is appealing since the temperature and composition profiles resulting from the crystallization of the magma ocean can be used as an initial condition for convection in the solid part. We test here this assumption with a linear stability analysis of the density profile in the solid cumulate as crystallization proceeds. The interface between the magma ocean and the solid is a phase change interface. Convecting matter arriving near the interface can therefore cross this boundary via melting or freezing. We use a semi-permeable condition at the boundary between the magma ocean and the solid to account for that phenomenon. The timescale with which convection develops in the solid is found to be several orders of magnitude smaller than the time needed to crystallize the magma ocean as soon as a few hundreds kilometers of cumulate are formed on a Mars- to Earth-size planet. The phase change boundary condition is found to decrease this timescale by several orders of magnitude. For a Moon-size object, the possibility of melting and freezing at the top of the cumulate allows the overturn to happen before complete crystallization. The convective patterns are also affected by melting and freezing at the boundary: the linearly most-unstable mode is a degree-1 translation mode instead of the approximately aspect-ratio-one convection rolls found with classical non-penetrative boundary conditions. The first overturn of the crystallizing cumulate on Mars and the Moon could therefore be at the origin of their observed degree-1 features.

## 6.2 Introduction

A common scenario considered for the formation of terrestrial planets is the crystallization of a global magma ocean from the bottom-up, because the liquidus of silicate magmas increases with pressure more steeply than the isentropic temperature, at least at low to moderate mantle pressure (Andrault, Bolfan-Casanova, Nigro, et al. 2011; Boukaré, Ricard, et al. 2015; Fiquet et al. 2010; Thomas and Asimow 2013). The crystallization of the surface magma ocean is expected to be rapid, around 1 Myr (e.g. Abe 1997; Lebrun et al. 2013). This has led several authors to assume convection in the solid part of the crystallizing mantle does not start until the mantle is entirely crystallized (e.g. Abe 1997; Elkins-Tanton, E. M. Parmentier, et al. 2003; Elkins-Tanton, Zaranek, et al. 2005; Hess and E. M. Parmentier 1995; E. Parmentier et al. 2002; Zhang et al. 2013). However, this assumption deserves scrutiny since the compositional and thermal structure of the mantle after complete crystallization could be widely different if solid-state convection does set in during its crystallization.

Two processes might lead to the destabilization of the solid mantle during its crystallization. First, assuming fractional crystallization, the surface magma ocean gets enriched in incompatible elements. As a secondary result, the new solid formed at the solid/liquid boundary gets richer and richer in these elements as crystallization progresses. Iron is such an element and its abundance is such that it affects significantly the density of both the solid and the liquid. The solid formed at the end of the crystallization is richer in iron than the solid formed at the beginning of the crystallization, leading to an unstable setup with material denser at the top than at the bottom of the solid mantle.

The second process that can further destabilize the solid mantle is the temperature gradient in the solid. The solidus temperature increases with pressure, and is steeper than the isentropic temperature profile. Assuming the temperature in the solid stays close to the solidus, the resulting profile is hence unstable. This effect is enhanced by fractional crystallization and the associated enrichment of the solid in incompatible elements: their presence further decreases the solidus temperature and the compositional gradient discussed above induces an even steeper solidus.

Numerical simulations including these processes suggest it is possible for solid-state convection to set in prior to the entire crystallization of the surface magma ocean (e.g. Boukaré, E. Parmentier, et al. 2018; Maurice et al. 2017). Whether convection in the mantle starts during or after the crystallization of the surface magma ocean is found to have profound implications on the preservation of compositional heterogeneities as well as the dynamics of the mantle (Ballmer et al. 2017; Tosi et al. 2013). These results further confirm the need to assess the parameters controlling the onset of convection in the primitive mantle.

A dynamical feature of the solid cumulate in contact with a magma ocean that has not been accounted for in the past studies is the possibility of exchange of matter at the boundary between the solid and the ocean via melting and freezing. We use a boundary condition developed for the inner core boundary (Deguen, Alboussière, et al. 2013) to take this effect into account. This boundary condition is expected to have important effects on the convection pattern and heat flux as well as the timescale with which convection sets in (Deguen 2013; Labrosse, Morison, et al. 2018).

Our aim is to assess how the timescale at which convection starts in the solid cumulate compares with the time needed to crystallize a surface magma ocean. Different scenarios are explored to determine the parameters controlling the onset of convection in the magma ocean cumulate. We consider the case where fractional crystallization happens during the entire cooling history of the magma oceans as well as the case where no compositional fractionation occurs. We explore the classical case for which no matter crosses the boundary between the magma ocean and the solid cumulate, and also the case with a boundary that allows matter transfer across it. The study is applied to the Earth, Mars, and the Moon.

## 6.3 Methods

We consider a mantle that is initially fully molten and crystallizes from the bottom or some intermediate depth upward. The goal of the present study is to determine the timescale for convection to start in the solid part of the mantle as the magma ocean crystallizes.

For the sake of simplicity, we assume the compaction length to be small and neglect the thickness of a mush layer at the phase change interface. Matter on one side of the boundary is entirely liquid while matter on the other side is entirely solid. We nonetheless allow for compositional fractionation to occur as the mantle crystallizes. The temperature at the solid/liquid boundary is denoted  $\mathcal{T}_m$  and referred to as the melting temperature.

Depending on how the temperature profile in the magma ocean compares with the profile of the melting temperature, two situations can occur. Either the solidification of the ocean progresses from the bottom up, or the solidification starts from an intermediate depth leading to a setup in which the solid part of the mantle is surrounded by two magma oceans. In this second scenario, the crystallization of the surface magma ocean (SMO) is thought to be a lot faster than the crystallization of the basal magma ocean (BMO) (Labrosse, Hernlund, and Coltice 2007).

We assume the solid mantle is a spherical shell of internal radius  $R^-$  and external radius  $R^+$ . Since the crystallization of the BMO is much slower than the crystallization of the SMO, we assume  $R^-$  to be constant even for the case where the solid shell is surrounded by two magma oceans. The presence or absence of a BMO however affects the boundary condition applied at the bottom boundary of the solid mantle (see section 6.3.4).

As the magma ocean cools down,  $R^+$  increases to reach the total radius of the planetary body, denoted by  $R_T$ . The temperature at the top boundary of the solid follows the melting temperature. The composition of the solid changes as well with the radius if we assume fractional crystallization occurs. For the sake of simplicity, we only consider fractionation of iron. The mass fraction of FeO, denoted by  $C$ , varies between 0 (e.g. Forsterite) and 1 (e.g. Fayalite). Although simplistic, such a model allows us to study the effect of the density gradient due to fractional crystallization on the dynamics of the solid. Figure 6.1 shows the composition and temperature profiles at two different times. We assume the velocity of the freezing front  $\dot{R}^+$  does not vary laterally and that the SMO is well mixed, the temperature and compositional fields in the resulting solid hence only vary with the radial position (as long as no solid-state convection operates).

In this section, we introduce the simple phase diagram we use to compute the

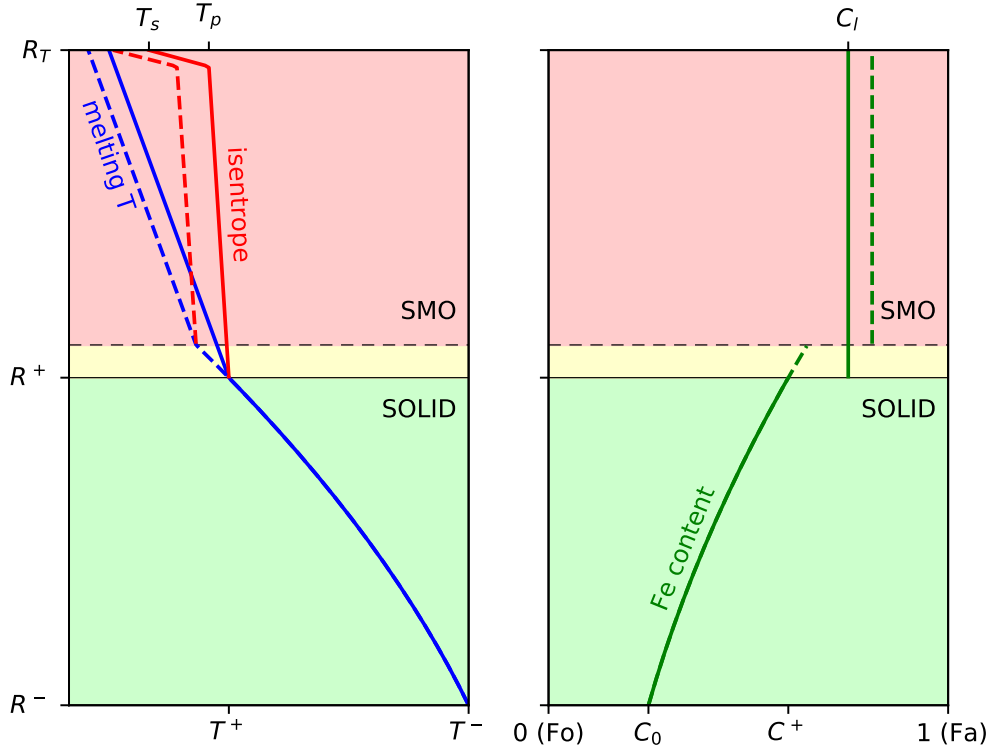


Figure 6.1: Temperature and composition reference profiles. Solid lines are the profiles at time  $t$ , dashed lines the profiles at time  $t + \delta t$ . The green area is the solid mantle at time  $t$ . The yellow area represents the part of the surface magma ocean (SMO, in red) that has crystallized during  $\delta t$ . All the annotations on the axes are written at time  $t$  (see table 6.1 for the meaning of symbols). Notice how the melting temperature decreases between the two instants owing to the enrichment in iron of the surface magma ocean. The slopes of the curves are exaggerated for readability purpose.

resulting temperature and composition profiles in the solid under the assumption that no convection occurs in the solid (section 6.3.1). This serves as base state which stability against overturning motion is studied. We don't treat the full dynamics of the overturn but compute, using a linear stability analysis, the growth rate of an overturning instability to compare it to the crystallization rate of the magma ocean. The latter is computed using a magma ocean cooling model which gives  $R^+$  as a function of time, as described in section 6.3.2.

### 6.3.1 Composition and temperature reference profiles

Under the assumption that no convection occurs during crystallization, one can determine the resulting temperature and compositional profiles in the cumulate. These profiles are used as reference profiles in order to perform the linear stability analysis (section 6.3.5).

We consider a magma ocean crystallizing from some depth  $R^-$  up to its top radius  $R_T$ . The mass fraction of the heavy component (FeO) is  $C(r)$  in the solid and

Symbol	Description	Earth	Moon	Mars
<b>Input parameters</b>				
$R^-$	Internal radius of the solid shell	3871 km*	737 km	2090 km
$R_T$	Total radius of the planet	6371 km	1737 km	3390 km
$\mathcal{T}^-$	Temperature at the bottom boundary <sup>†</sup>	4500 K	1500 K	2400 K
$\mathcal{T}_\infty$	Black body equilibrium temperature	255 K	255 K	212 K
$\varepsilon$	Emissivity <sup>¶</sup>	$10^{-4}$	1	$10^{-3}$
$g$	Gravity acceleration	9.81 m/s <sup>2</sup>	1.62 m/s <sup>2</sup>	3.71 m/s <sup>2</sup>
$\text{Ra}_S$	Rayleigh number of SMO	$10^{30}$	$10^{28}$	$5 \times 10^{28}$
$\alpha$	Thermal expansion coefficient		$10^{-5} \text{ K}^{-1}$	
$C_p$	Heat capacity		$10^3 \text{ J K}^{-1}$	
$\kappa$	Thermal diffusivity		$10^{-6} \text{ m}^2/\text{s}$	
$L_h$	Latent heat		$4 \times 10^5 \text{ J kg}^{-1}$	
$\sigma$	Stefan-Boltzmann constant	$5.67 \times 10^{-8} \text{ W m}^{-2} \text{ K}^{-4}$		
$\rho$	Reference density		$4 \times 10^3 \text{ kg/m}^3$	
$\Delta\rho_m$	Solid/liquid density contrast		$2 \times 10^2 \text{ kg/m}^3$	
$\eta$	Viscosity in the solid		$10^{18} \text{ Pa s}$	
$C_{l_0}$	Iron content of the primitive SMO <sup>‡</sup>		0.1	
$D$	Solid/liquid partition coefficient of iron <sup>‡</sup>		0.6	
$\beta$	Compositional expansion coefficient		-0.33	
$\partial\mathcal{T}_m/\partial P$	Clapeyron slope		$2 \times 10^{-8} \text{ K Pa}^{-1}$	
$\partial\mathcal{T}_m/\partial C$	Dependence of $\mathcal{T}_m$ on iron content		-700 K	
<b>Computed dimensional variables</b>				
$L_M$	Final thickness of solid mantle $R_T - R^-$	2500 km	1000 km	1300 km
$\mathcal{T}_m$	Melting temperature	$\mathcal{T}_m(P, C)$ described by eq. (6.4)		
$\mathcal{T}^+$	Temperature at the top boundary	$\mathcal{T}^+(t)$ with eq. (6.5)		
$\mathcal{T}_p$	Potential temperature at the surface	$\mathcal{T}_p(t)$ with eq. (6.8)		
$\mathcal{T}_s$	Temperature at the surface of the planet	$\mathcal{T}_s(t)$ with eq. (6.9)		
$R^+$	External radius of the solid shell	$R^+(t)$ with eq. (6.10)		
$L$	Thickness of the solid shell	$L = R^+ - R^-$		
$C_0$	Iron content of the first solid	$K C_{l_0} = 0.06$		
$C_l$	Iron content of the SMO	$K C_l(t) = C^+(t)$ with eq. (6.2)		
$\tau_{\text{Stokes}}$	Stokes time	$\eta L^2 / (\Delta\rho g L_M^3)$		
<b>Dimensionless numbers</b>				
$\text{Ra}(t)$	Thermal Rayleigh number	$\rho g \alpha \Delta T L^3 / (\eta \kappa)$		
$\text{Rc}(t)$	Compositional Rayleigh number	$\rho g \beta L^3 / (\eta \kappa)$		
$W(t)$	Freezing front velocity (Peclet number)	$L \dot{R}^+ / \kappa$		
$\Gamma(t)$	Thickness of the solid part	$L / L_M$		
$\Gamma_S(t)$	Thickness of the SMO	$(R_T - R^+) / L_M$		
$\Phi^\pm$	Phase change number <sup>§</sup>	$10^{-2}; \infty$		

Table 6.1: Symbols used in this paper. All quantities with a + superscript are evaluated at the top boundary ( $R^+$ ), while quantities with a - superscript are evaluated at the bottom boundary ( $R^-$ ). <sup>¶</sup> The emissivity values for the Earth and Mars are chosen so that the crystallization time scale of the SMO is of the order of 1 Myr (Lebrun et al. 2013). For the Moon, we neglect the effects of the atmosphere and assume a black body cooling. \* This choice assumes a 400 km thick basal magma ocean. Using  $R^- = 3471$  km does not change significantly the results. <sup>†</sup> From Andrault, Bolfan-Casanova, Nigro, et al. (2011), <sup>‡</sup> from Andrault, Petitgirard, et al. (2012). <sup>§</sup>  $10^{-2}$ : flow-through,  $\infty$ : non-penetrative. For the Moon and Mars, the possibility of a BMO is not considered and  $\Phi^- = \infty$  (see section 6.3.4 for details).

$C_l(t)$  in the liquid, assuming that no diffusion (nor convection) operates in the solid (therefore  $C$  does not depend on time) and convection mixes the liquid efficiently (therefore  $C_l$  depends only on time). At the freezing front, the phase relation is

$$C(R^+(t)) = DC_l(t) \quad (6.1)$$

with  $D$  the partition coefficient (considered constant) and  $R^+(t)$  the time-evolving radius of the freezing interface.

Assuming the magma ocean undergoes fractional crystallization, the composition profile in the cumulate is exponential. At the radial position  $r$  it is

$$C(r) = \begin{cases} C_0 \left( \frac{R_T^3 - (R^-)^3}{R_T^3 - r^3} \right)^{1-D} & \text{if } r < R_s \\ 1 & \text{if } r > R_s, \end{cases} \quad (6.2)$$

with

$$R_s = \left( (R^-)^3 C_0^{\frac{1}{1-D}} + R_T^3 \left( 1 - C_0^{\frac{1}{1-D}} \right) \right)^{1/3} \quad (6.3)$$

the value of  $R^+$  at which  $C_l$  reaches 1 (see section 6.7 for more details).

Since the diffusion timescale is much larger than the other time scales considered here, we assume the temperature profile in the cumulate stays close to the melting temperature. We take into account variations of the melting temperature  $\mathcal{T}_m$  due to both the pressure and the composition. A higher concentration in iron leading to a lower melting temperature, the resulting temperature profile in the solid is steeper than a constant-concentration solidus when fractional crystallization is accounted for (Figure 6.1). The melting temperature  $\mathcal{T}_m$  verifies:

$$\frac{d\mathcal{T}_m}{dr} = \frac{\partial \mathcal{T}_m}{\partial P} \frac{\partial P}{\partial r} + \frac{\partial \mathcal{T}_m}{\partial C} \frac{\partial C}{\partial r}. \quad (6.4)$$

With  $\frac{\partial P}{\partial r} = -\rho g$  and eq. (6.2), one obtains

$$\frac{d\mathcal{T}_m}{dr} = -\rho g \frac{\partial \mathcal{T}_m}{\partial P} + 3C(1-D) \frac{r^2}{R_T^3 - r^3} \frac{\partial \mathcal{T}_m}{\partial C}. \quad (6.5)$$

For the sake of simplicity, we assume  $\frac{\partial \mathcal{T}_m}{\partial P}$  and  $\frac{\partial \mathcal{T}_m}{\partial C}$  to be constant (see table 6.1 for values).

We denote  $T = \mathcal{T} - \mathcal{T}_{\text{adb}}$  the superisentropic temperature in the solid, with

$$\mathcal{T}_{\text{adb}} = \mathcal{T}^- \exp \left( \frac{\alpha g (R^- - r)}{C_p} \right) \quad (6.6)$$

the isentropic temperature profile in the solid, with  $\alpha$  the coefficient of thermal expansion,  $g$  the acceleration of gravity and  $C_p$  the heat capacity. We assume the variations of  $\alpha$ ,  $C_p$  and  $g$  with depth to be negligible. The reference superisentropic temperature (denoted  $\bar{T}$ ) gradient is then:

$$\frac{d\bar{T}}{dr} = -\rho g \frac{\partial \mathcal{T}_m}{\partial P} + 3C(1-D) \frac{r^2}{R_T^3 - r^3} \frac{\partial \mathcal{T}_m}{\partial C} + \frac{\alpha g}{C_p} \mathcal{T}^- \exp \left( \frac{\alpha g (R^- - r)}{C_p} \right). \quad (6.7)$$

### 6.3.2 Crystallization time scale

Assuming the temperature profile in the SMO to be isentropic and neglecting variations of  $\alpha$ ,  $g$  and  $C_p$  with depth, the potential temperature at the surface is:

$$\mathcal{T}_p = \mathcal{T}^+ \exp\left(\frac{-\alpha g(R_T - R^+)}{C_p}\right). \quad (6.8)$$

Note that we are neglecting the temperature drop across the boundary layer at the bottom of the magma ocean. This is justified by the very small viscosity of the magma and the main buoyancy force coming from cooling to the atmosphere at the top surface.

King et al. (2012) showed that the scaling law for the heat flux in a rotating fluid (such as the surface magma ocean) depends on how the quantity  $\text{Ra}_S \text{Ek}_S^{3/2} = \frac{\alpha g \Delta T \nu^{1/2}}{\kappa (2\Omega)^{3/2}}$  compares to 1, with  $\text{Ek}_S$  the Ekman number and  $\text{Ra}_S$  the Rayleigh number in the SMO. A conservative lower bound with the thermal expansivity  $\alpha \sim 10^{-5} \text{ K}^{-1}$ , the gravity  $g \sim 10 \text{ m/s}^2$ , the super-isentropic temperature difference  $\Delta T \sim 1 \text{ K}$ , the kinematic viscosity  $\nu \sim 10^{-5} \text{ m}^2/\text{s}$ , the thermal diffusivity  $\kappa \sim 10^{-6} \text{ m}^2/\text{s}$  and the rotation rate  $\Omega \sim 10^{-4} \text{ s}^{-1}$  is  $\text{Ra}_S \text{Ek}_S^{3/2} \sim 10^5 \gg 1$ . We then consider the heat flux is not controlled by rotation and scales as  $\text{Nu} = 0.16 \text{Ra}_S^{2/7} \Gamma_S^{6/7}$  with  $\Gamma_S = (R_T - R^+)/L$  the dimensionless thickness of the SMO (ibid.). Note that this scaling does not depend on the Prandtl number in the range of values explored by King et al. (ibid.), i.e.  $1 \leq \text{Pr} \leq 100$ . Since  $\text{Pr} \sim 10$  is a reasonable value for a magma ocean, we assume this scaling holds for our study. We neglect variations of  $\text{Ra}_S$  with time and assume the magma ocean behaves like a gray body at its upper surface. Heat flow conservation at the surface gives the following equation for the surface temperature  $\mathcal{T}_s$ :

$$\frac{k(\mathcal{T}_p - \mathcal{T}_s)}{L_M} 0.16 \text{Ra}_S^{2/7} \Gamma_S^{-1/7} = \varepsilon \sigma (\mathcal{T}_s^4 - \mathcal{T}_\infty^4) \quad (6.9)$$

where  $\mathcal{T}_\infty$  is the black body equilibrium temperature,  $\sigma$  is the Stefan-Boltzmann constant and  $\varepsilon$  the emissivity. The emissivity should depend on the atmosphere dynamics and composition (particularly its water content) and vary with time. Taking this effect into account would require an atmosphere model (e.g. Abe 1997; Lebrun et al. 2013). For the sake of simplicity, we assume the emissivity to be constant, tuning its value to obtain a crystallization timescale that matches the ones of Lebrun et al. (2013) (see table 6.1 for values).

As the SMO crystallizes (i.e.  $R^+$  increases with time), we assume the temperature at the top of the solid mantle  $\mathcal{T}^+$  follows the solidus (eq. (6.5)), and the temperature profile in the SMO follows an isentropic profile. As  $R^+$  grows, two phenomena produce heat that should be evacuated: the crystallization itself with an associated latent heat  $L_h$ , and the cooling of the magma ocean. Assuming this heat is entirely evacuated through radiation in the atmosphere modeled as a gray body, one obtains the following equation:

$$\varepsilon \sigma R_T^2 (\mathcal{T}_s^4 - \mathcal{T}_\infty^4) = \rho L_h R^{+2} \frac{dR^+}{dt} - \rho C_p \frac{d}{dt} \left( \int_{R^+}^{R_T} \mathcal{T}^+ \exp\left(\frac{\alpha g(R^+ - r)}{C_p}\right) r^2 dr \right). \quad (6.10)$$

The last term of this equation can be developed (keeping in mind that the lower bound of the integral  $R^+$  depends on time). This yields the time derivative of  $\mathcal{T}^+$ , which is written as a derivative with respect to  $R^+$  using the chain rule. One obtains an ordinary differential equation on  $R^+(t)$  whose numerical integration gives the position of the interface between the solid and the surface magma ocean as a function of time.

### 6.3.3 Set of dimensionless equations

$L = R^+ - R^-$ ,  $L_M^2/\kappa$ ,  $\kappa/L$ ,  $\eta L^3/\kappa$ ,  $\Delta T = T^- - T^+$  are used as scales for length, time, velocity, mass and temperature respectively. Note that  $R^+$  and  $T^+$  vary with time as the surface magma ocean crystallizes.  $L_M = R_T - R^-$  is the thickness of the solid mantle once the SMO is entirely crystallized. Note that all scales depend on time except the one for time itself, which is why  $\Gamma = L/L_M$  appears in the following equations. The dimensionless radial position is built as  $1 + (r - R^-)/L$  so that it is between 1 and 2 at all times. Similarly, the dimensionless temperature is chosen as  $(T - T^+)/\Delta T$  so that it is between 0 and 1 at all times.

Using the same symbols for dimensionless quantities, dimensionless conservation equations of mass, momentum, heat and iron fraction are written as:

$$\nabla \cdot \mathbf{u} = 0 \quad (6.11)$$

$$\mathbf{0} = -\nabla p + \nabla^2 \mathbf{u} + \text{Ra} (\Theta - \langle \Theta \rangle) \hat{\mathbf{r}} + \text{Rc} (c - \langle c \rangle) \hat{\mathbf{r}} \quad (6.12)$$

$$\Gamma^2 \frac{\partial \Theta}{\partial t} + \mathbf{u} \cdot \nabla (\Theta + \bar{T}) - \nabla^2 \Theta = W \left( (r - 1) \frac{\partial \Theta}{\partial r} + \left( \frac{\partial \bar{T}}{\partial r} \right)^+ \Theta \right) \quad (6.13)$$

$$\Gamma^2 \frac{\partial c}{\partial t} + \mathbf{u} \cdot \nabla (c + \bar{C}) = W (r - 1) \frac{\partial c}{\partial r}. \quad (6.14)$$

$\mathbf{u}$  is the velocity field,  $p$  the dynamic pressure,  $\Theta$  the temperature perturbation with respect to the reference profile  $\bar{T}$  and  $c$  the composition perturbation with respect to the reference profile  $\bar{C}$ .  $\langle x \rangle$  denotes the lateral average of the quantity  $x$ . Ra is the thermal Rayleigh number, Rc is the compositional Rayleigh number. The terms on the right hand side of eqs. (6.13) and (6.14) are due to the time dependence of the scales  $L$  and  $\Delta T$ , which brings new advection terms associated with the change of frame, with  $W = L\dot{R}^+/\kappa$  the dimensionless velocity of the freezing front. See table 6.1 for the definition and values of the various symbols.

Note that these equations are written under the assumption that  $\dot{R}^- = 0$ . Other terms would appear on the right hand side of eqs. (6.13) and (6.14) in the general case involving the crystallization of a basal magma ocean. For Earth's case, we assume the basal ocean crystallizes much slower than the surface ocean, and as such we neglect  $\dot{R}^-$  (Labrosse, Hernlund, and Coltice 2007). We assume the diffusion of the compositional field is negligible since the diffusion coefficient of composition is much smaller than that of heat. Moreover, diffusion of  $\bar{T}$  is neglected while that of  $\Theta$  is retained in order to ease the linear stability analysis. This is justified a posteriori by the fact that the diffusion timescale is much longer than the other timescales considered in this study.

### 6.3.4 Phase change boundary condition

In the classical Rayleigh-Bénard setup, convecting matter arriving near an horizontal boundary forms a topography whose height is limited by the weight viscous forces can sustain. This topography is often neglected and a non-penetrative boundary condition is assumed at the interface ( $u_r(R^+) = 0$ ). However, in the system studied here, the boundary between the magma ocean and the cumulate is a phase change interface. A topography of the solid with respect to the equilibrium position of the solid/liquid interface can then be eroded by melting or freezing. Provided that the melting/freezing time is short compared to the time needed to build the topography by viscous forces, it is thus possible to have a non-zero normal velocity across the interface. This is taken into account with the help of the boundary condition introduced for the inner core by Deguen, Alboussière, et al. 2013. This boundary condition, which translates the continuity of normal stress across the interface, is written in dimensional form as:

$$\Delta\rho_m g \tau_\phi u_r + 2\eta \frac{\partial u_r}{\partial r} - p = 0. \quad (6.15)$$

where  $\Delta\rho_m$  is the density difference between the solid and liquid phases and  $\tau_\phi$  is the phase change timescale. Note that our definition of the dynamic pressure (defined here as  $p = P - \langle P \rangle$ ) differs from that of  $\hat{p}$  used by *ibid.* The laterally constant term  $\Delta\rho_m g \tau_\phi \dot{R}$  is thus included in  $p$  instead of explicitly appearing in the boundary condition. The dimensionless form of the boundary condition is

$$\pm \Phi^\pm u_r + 2 \frac{\partial u_r}{\partial r} - p = 0 \quad (6.16)$$

where  $\Phi$  is the phase change number defined as:

$$\Phi^\pm = \frac{|\Delta\rho_m|^\pm g L \tau_\phi}{\eta} \quad (6.17)$$

(the superscript  $+$  denotes the interface between the SMO and the solid at  $R^+$  while the superscript  $-$  denotes the interface between the BMO and the solid at  $R^-$ ). Moreover, the continuity of tangential stress is simply written as a classic free-slip boundary condition.

The phase change timescale  $\tau_\phi$  is related to the time needed to transport latent heat in the magma ocean from the areas that freeze to the areas that melt (*ibid.*):

$$\tau_\phi = \frac{\rho L_h}{(\rho - \Delta\rho_m)^2 C_p (\partial_P \mathcal{T}_m - \partial_P \mathcal{T}_{\text{adb}}) g u'} \quad (6.18)$$

where  $u'$  is the velocity scale in the magma ocean. A reasonable value for the latter is  $u' \sim 1 \text{ m s}^{-1}$  (Lebrun et al. 2013). Using nominal values for the other parameters, we find that  $\tau_\phi \sim 10^4 \text{ s}$ . Plugging this in the expression of the phase change parameter eq. (6.17) yields  $\Phi \sim 10^{-5}$ .

The phase change number  $\Phi$  compares the phase change timescale  $\tau_\phi$  (i.e. the time needed to erode topography via melting and freezing) to the viscous timescale (i.e. the time needed to build topography with viscous forces). The value of  $\Phi$  allows to tune continuously the boundary condition between a non-penetrative classical condition ( $\Phi \rightarrow \infty$ ) and a fully permeable condition ( $\Phi \rightarrow 0$ ). Although this number should depend on time since  $L$  depends on time and  $\tau_\phi$  depends also on time but

in a non trivial way, it is kept constant in this study. Two extreme values are tested for the SMO/solid interface:  $\Phi = \infty$  which leads to the classical non-penetrative boundary condition and  $\Phi = 10^{-2}$  which leads to a flow-through boundary (we use this value rather than  $10^{-5}$  because the resolution of radial modes is more computationally demanding as  $\Phi$  decreases, while the overturn timescale is not affected as shown in the results). For the Earth, these two values are also considered at the bottom of the solid, accounting for the possible presence of a basal magma ocean (BMO, Labrosse, Hernlund, and Coltice 2007). For Mars and the Moon, we do not consider the possibility of a BMO and the bottom interface is hence non-penetrative,  $u_r(R^-) = 0$ . Rather than being realistic, these extreme constant values are used to study how the possibility of melting and freezing at the interface affects the stability of the solid, both in terms of onset time of overturn and preferred mode of motion. The estimated nominal value being  $\Phi \sim 10^{-5}$ , we expect the real system should be closer to the flow-through case than to the classical non-penetrative case.

### 6.3.5 Determination of overturn timescale

We start from a completely molten primitive mantle ( $R^+ = R^-$  and  $\mathcal{T}^+ = \mathcal{T}^-$ ). We numerically integrate eq. (6.10) to obtain  $R^+$  as a function of time (the potential surface temperature  $\mathcal{T}_p$  and the surface temperature  $\mathcal{T}_s$  are computed using eq. (6.8) and eq. (6.9)).

At each timestep of this integration, we compute the reference temperature and composition profiles in the solid as shown in section 6.3.1 as well as the dimensionless numbers  $\text{Ra}(t)$ ,  $\text{Rc}(t)$ ,  $W(t)$  and  $\Gamma(t)$ . Using a Chebyshev-collocation approach (e.g. Canuto et al. 1985; Guo et al. 2012), the set of linearized equations around the reference state is written as an eigenvalue problem (see section 6.8). Solving numerically this problem yields the growth rate and shape of the most unstable mode of overturn. The inverse of that growth rate is the timescale for convection to set in in the solid shell. We compute this timescale at each timestep of the evolution of the SMO. By comparing this timescale with the corresponding time in the evolution of the SMO, we can assess whether convection is able to take place before the entire magma ocean is crystallized. Three different models are considered for the bulk of the solid:

1. full model: compositional, thermal, and moving frame terms are taken into account;
2. thermal model: compositional terms are left out, modeling the ideal case where no fractional crystallization occurs and the sources of instability are purely thermal (eq. (6.14) and the corresponding buoyancy term in eq. (6.12) are ignored);
3. frozen-time model: moving frame terms are left out (i.e. right-hand side of eqs. (6.13) and (6.14)), resulting in a frozen-time approach where all long term evolution terms are ignored when studying the stability of the system at a given instant.

We also compare the timescale obtained by linear stability analysis with the Stokes time  $\tau_{\text{Stokes}} = \eta L^2 / (\Delta \rho g L_M^3)$  computed at each time to check whether this time is a relevant proxy of the stability of the solid mantle.

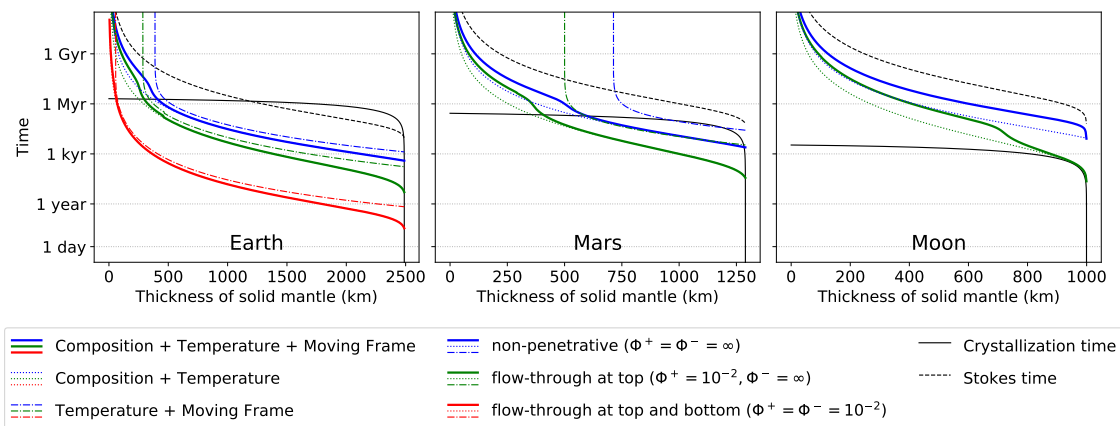


Figure 6.2: Growth time of the most unstable mode as a function of the crystallized mantle thickness for the Earth, Mars, and the Moon. The solid black line is the time necessary to crystallize the remaining surface magma ocean. Colors represent different boundary conditions: both horizontal boundaries non-penetrative (blue); flow-through boundary condition between the solid and the surface magma ocean to model the possibility of melting and freezing (see section 6.3.4 for details) (green); and flow-through boundary conditions for both horizontal boundaries assuming the presence of a basal magma ocean (red). Linestyles represent different approximations regarding compositional effects (fractional crystallization and effect on density) and moving frame contributions: both are taken into account (solid lines), compositional effects are neglected (dash-dotted lines), or moving frame terms are neglected (dotted lines). The black dashed line is the Stokes time for each thickness, given for comparison.

## 6.4 Results

The destabilization timescales for the Earth, Mars, and the Moon with various boundary conditions along with the time needed to crystallize the remaining SMO are shown on fig. 6.2. Comparison of the destabilization timescales obtained for various bulk setups and boundary conditions yields information regarding their contribution to the destabilization of the solid.

The simplest cases are the one neglecting the compositional effects on density. For such cases, the destabilization timescale tends to infinity for a given non-zero thickness of crystallized mantle. This thickness corresponds to the one needed for instabilities to overcome diffusion of perturbations of the reference state. In other words, it corresponds to the thickness above which the Rayleigh number in the solid part is above the critical Rayleigh number. For the Moon, this thickness is never reached and the Moon’s mantle stays stable with respect to purely thermal convection. For the Earth and Mars, this thickness is reached rather early, after  $\sim 500$  km of solid mantle is formed. As crystallization progresses, the thickness and the temperature contrast between the top and the bottom of the solid mantle increase. The available buoyancy in the system therefore increases. This leads to a strong decrease of the destabilization timescale, which becomes much shorter than the time needed to crystallize the remaining surface magma ocean (up to 6 orders of magnitude, depending on which boundary conditions are considered). This suggests that even in the purely thermal case, solid-state convection sets in before the mantle

is completely crystallized for planets larger than Mars.

The cases taking compositional effects on density into account are always unstable. This contrasts with the purely thermal cases and is due to the fact that diffusion of the composition field is neglected. There is no mechanism to damp perturbations around the reference state, the latter is hence always unstable. Similarly to what is observed for the thermal cases, the destabilization timescale drops dramatically as the solid mantle thickens. For the Earth and Mars, the destabilization timescale ends up being shorter than the crystallization time of the remaining SMO by several orders of magnitude. The case where moving frame terms are neglected exhibits a shorter destabilization time scale at small thickness. The moving frame terms play a stabilising role only at the beginning of mantle crystallization for the Earth and Mars but are significant through the entire Moon's mantle crystallization. The stabilising effect of the moving terms can be understood from the energy conservation eq. (6.13). Taking a temperature perturbation  $\theta > 0$  and the associated velocity perturbation  $u_r > 0$ , one can notice there is a competition between the advection term  $u_r \partial_r \bar{T} < 0$  and the moving frame term  $W(r-1) \partial_r \theta$  whose average is negative. The same reasoning can be made with a negative perturbation and on the iron conservation eq. (6.14).

For the Moon, the destabilization timescale is always greater than the time needed to crystallize the SMO. However, it should be noted that in this study the time to crystallize the SMO is computed assuming a well-mixed SMO with a surface behaving like a black body. The formation of a light solid crust enriched in plagioclase when around 80% of the SMO is crystallized is expected to slow down the solidification of the SMO by a few million years (e.g. Elkins-Tanton, Burgess, et al. 2011). This would leave enough time for convection to set in in the solid since the destabilization timescale we find is much shorter than that.

The three boundary conditions exhibits different destabilization timescales. The case where both boundaries are non-penetrative (which is the case classically considered) needs more time to destabilize than the case where the boundary between the surface magma ocean and the solid allows melting and freezing. Convective patterns obtained with a flow-through boundary are substantially different than the classical ones (fig. 6.3). Aspect-ratio-1 rolls are obtained with classical boundary conditions. However, when the top boundary allows phase change, a spherical-harmonic-degree-1 near-translation mode develops. Matter freezes on one side of the spherical shell, goes around the core or basal magma ocean, and melts on the other side. In the case with a basal magma ocean and its boundary with the solid of flow-through type, matter also crosses the inner boundary of the spherical shell, resulting in a true translation mode. These two translation modes involve very little or no deformation of the solid compared to the classical case, and therefore less viscous forces acting against convection. This explains the smaller destabilization timescale associated with these modes as well as the lower critical thickness in the purely thermal case.

fig. 6.4 shows the transition between the non-penetrative and the flow-through regime occurs over a rather short range of values of the phase change number.  $\Phi^+ \lesssim 1$  leads to near-translation while  $\Phi^+ \gtrsim 100$  leads to classical aspect-ratio-one rolls.

A notable feature on fig. 6.2 is the steep decrease of the destabilization timescales at the end of the crystallization when compositional terms are taken into account.

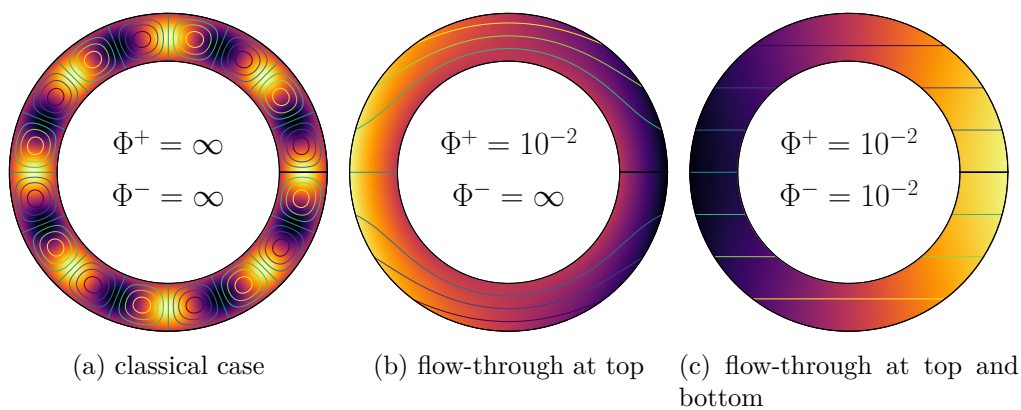


Figure 6.3: Most unstable convection modes for the Earth when a 1700 km thick mantle has crystallized, for different boundary conditions represented by the values of the  $\Phi$  parameters at the top and the bottom, as indicated. The dark zones represent negative temperature anomalies while the bright zones represent positive temperature anomalies. The streamlines are superimposed. Note that the linear stability analysis offers no constraint on the orientation and amplitude of these modes, only their harmonic degree and radial shape. (a): both boundaries non-penetrative, the convection rolls have an aspect ratio approximately equal to 1; (b): flow-through top boundary, the flow pattern is of spherical harmonic degree one, the streamlines go through the top boundary but go around the central part; (c): flow-through conditions at both boundaries, the flow pattern is of spherical harmonic degree one, the streamlines go through both boundaries, resulting in a translation mode of convection. Similar behavior is obtained for the other bodies.

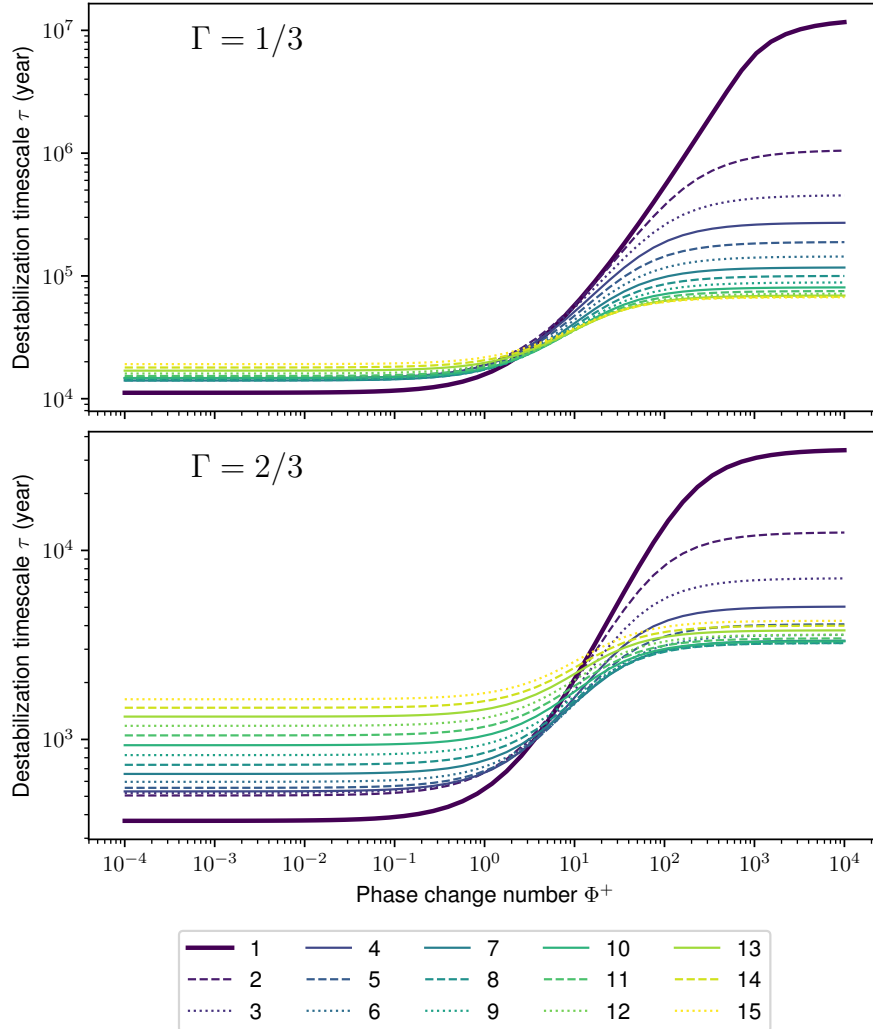


Figure 6.4: Destabilization timescale of several harmonics degree ( $l = 1$  to  $15$ ) as a function of the phase change number value for the Earth. The bottom boundary is non-penetrative. Top: 833 km are crystallized (mid-radius  $\bar{r} \sim 4288$  km), bottom: 1667 km are crystallized (mid-radius  $\bar{r} \sim 4704$  km). The most unstable mode is the one with the shortest destabilization timescale. One can notice that in the non-penetrative case ( $\Phi^+ \rightarrow \infty$ ), the most unstable mode corresponds to aspect-ratio-1 rolls. The typical roll size of the most unstable mode ( $\bar{r}\pi/l$ ) is roughly 900 km for the top case ( $l = 15$ ) and 1850 km for the bottom case ( $l = 8$ ). However, with a flow-through boundary ( $\Phi^+ \rightarrow 0$ ), the most unstable mode is the near-translation mode for both cases.

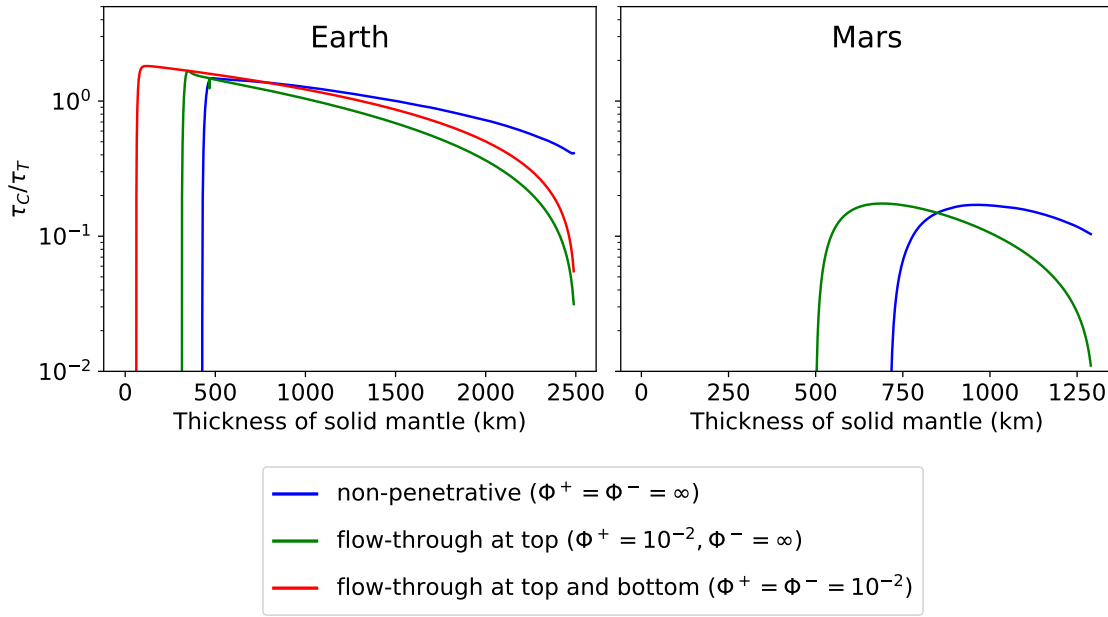


Figure 6.5: Ratio between the destabilization timescale obtained for the purely compositional case  $\tau_C$  (thermal terms are left out) and the timescale obtained for the purely thermal case  $\tau_T$  (compositional terms are left out). When this ratio is above one, it means the thermal reference profile is more unstable than the compositional reference profile. The Moon is not shown here since the purely thermal case is never unstable ( $\tau_T \rightarrow \infty$ ). The colors are the same as in fig. 6.2, blue: non-penetrative condition for both horizontal boundaries ( $\Phi^\pm = \infty$ ); green: flow-through condition at the boundary between the solid and the surface magma ocean; and red: flow-through condition at both horizontal boundaries.

That decrease is due to the strong (i.e. very unstable) compositional gradient appearing at the end of the crystallization. It does not affect the destabilization timescale obtained with non-penetrative boundary conditions; this can be explained by the fact that the strong compositional gradient is in a very thin layer at the top of the domain where vertical velocities vanish, and therefore does not contribute to the driving of the down- and up-welling currents.

A comparison between the purely thermal and purely compositional cases for the Earth and Mars is shown on fig. 6.5. The ratio between the destabilization timescales for these two cases is 0 before the critical thickness for the purely thermal case is reached. For Mars, the compositional profile is always more unstable than the thermal profile and controls the destabilization timescale of the system. For the Earth, however, the ratio between the two cases is fairly close to 1 for a large part of the crystallization history: neither the thermal nor the compositional profile dominates the destabilization timescale of the system.

fig. 6.6 shows that the destabilization timescale  $\tau_{\text{LSA}}$  is proportional to the Stokes time  $\tau_{\text{Stokes}} = \eta L^2 / (\Delta \rho g L_M^3)$ . Two effects alter this relation: moving frame terms whose effects are not included in the Stokes time, and the strong compositional gradient at the end of the crystallization whose effects depend on the boundary condition. It should be noted that the ratio  $\tau_{\text{LSA}} / \tau_{\text{Stokes}}$  depends on the body and the boundary conditions considered. Notably, permeable boundary conditions lead to a decrease of  $\tau_{\text{LSA}}$ .

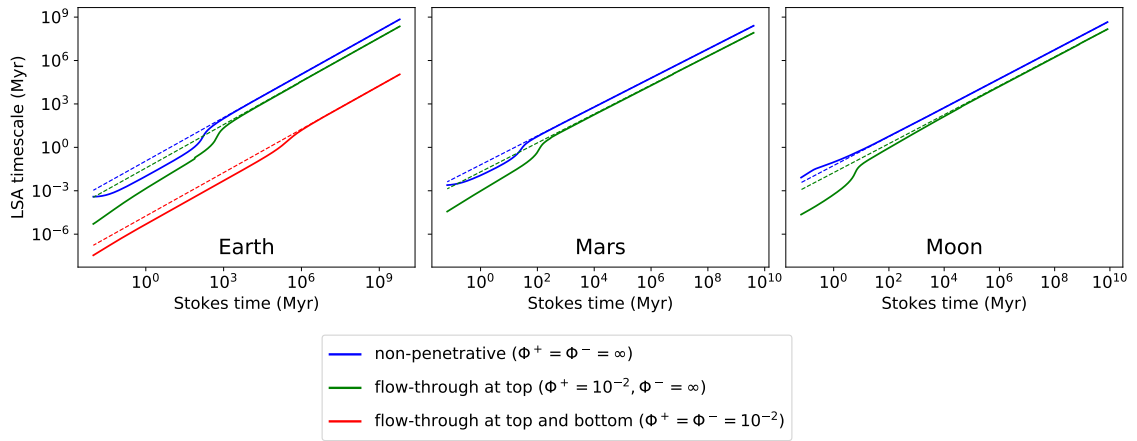


Figure 6.6: Growth time of the most unstable mode versus the Stokes time for the Earth, Mars, and the Moon. The solid line is the destabilization timescale obtained with the linear stability analysis  $\tau_{\text{LSA}}$  (case with all terms accounted for). The dashed lines correspond to  $\tau_{\text{LSA}} \propto \tau_{\text{Stokes}}$ . Composition, temperature and moving frame terms are all taken into account. The colors are the same as in fig. 6.2, blue: non-penetrative condition for both horizontal boundaries ( $\Phi^{\pm} = \infty$ ); green: flow-through condition at the boundary between the solid and the surface magma ocean; and red: flow-through condition at both horizontal boundaries.

## 6.5 Discussion

We showed for the Earth and Mars that the growth timescale of convective instabilities in a crystallizing mantle from the bottom up is several orders of magnitude smaller than the time needed to fully crystallize that mantle. This holds even without taking into account fractional crystallization and the unstable density gradient it induces. This contrasts with the assumptions made in several studies (Elkins-Tanton, E. M. Parmentier, et al. 2003; Hess and E. M. Parmentier 1995; Tosi et al. 2013) where the overturn is assumed to take place because of the compositionally induced density gradient after the entire mantle is crystallized. The numerical simulations performed by Ballmer et al. (2017) for Earth-like objects lead to a destabilization of the solid after a few Myr, and those performed by Maurice et al. (2017) for Mars-like objects lead to a destabilization after roughly 1 Myr. These times are not easily comparable to the timescales we compute via linear stability analysis since the physical problems are different in non-trivial ways: the simulations of Ballmer et al. (2017) are in a 2D aspect-ratio-1 cartesian box, those of Maurice et al. (2017) are in cylindrical geometry with a variable viscosity, a melt extraction mechanism and a solidus temperature that depends only on pressure. However, despite these differences, the destabilization time uncovered by these simulations are rather similar to the one we predict for the non-penetrative cases: of the order of 1 Myr for the Earth and 0.5 Myr for Mars. This confirms the linear growth rate of instabilities is a relevant proxy for the timescale at which convection sets in.

Moreover, allowing transfer of matter via melting and freezing at the interface between the solid and the surface magma ocean reduces dramatically the timescale with which solid-state convection can set in. It also changes the shape and harmonic degree of the most unstable mode: a degree-one translation mode is pre-

ferred. Therefore, the possibility of melting and freezing at the interface should be accounted for when studying the overturn of the primitive mantle of planetary bodies. For example, the case of the Moon is an interesting potential application. This body has a strong dichotomy: the near-side presents more mare basalts, more KREEP material, and a thinner crust than the far-side. Wasson and Warren (1980) already proposed that such features could be due to a slower cooling of the lunar magma ocean on the near side than on the far-side. A permeable boundary would allow the solid mantle to overturn with a dominant degree-one before the entire crystallization of the mantle (keeping in mind that the end of the crystallization is much slower than what we predict with our simple model, see Elkins-Tanton, Burgess, et al. (2011)). The mechanisms proposed to build a degree 1 at the scale of the Moon involve the dynamics of an entirely crystallized lunar mantle (e.g. E. Parmentier et al. 2002; Zhong et al. 2000). The possibility to form a degree one while the crystallization of the magma ocean is still ongoing is therefore worth exploring with more complete models to test whether this dominant degree-one can be conserved after crystallization of the magma ocean and/or helps the development of degree-one instabilities such as the ones predicted in the aforementioned studies. It is also tempting to associate the degree-one feature of Mars (the Marsian dichotomy) to the same process but, as explained above, the first degree-one overturn of the solid mantle is expected to happen long before its complete crystallization. Secondary overturning instabilities are possible after the first one that we cannot investigate with the tools presented above. A more complete study investigating the finite amplitude dynamics is necessary to understand the implications of this work to planets larger than the Moon.

It should be noted that several parameters involved in the problem are badly constrained. The viscosity of the solid mantle and even its rheology is such a parameter. It is highly dependent on how close the temperature in the solid is from the solidus and could easily vary by a few orders of magnitude (e.g. Solomatov 2015). Since the destabilization timescale scales as the Stokes time (fig. 6.6), it is directly proportional to the viscosity and could therefore vary by a few orders of magnitude. The strong relation between the viscosity of the cumulate and the overturn scaling has been investigated by Ballmer et al. (2017): their numerical experiments confirm the overturn onset scales as the Stokes time. It should be noted that our flow-through boundary conditions does not affect this result, it only reduces the proportionality factor between the Stokes time and the growth time of instabilities (fig. 6.6). This validates the general approach proposed by Boukaré, E. Parmentier, et al. (2018) to assess whether solid-state convection sets in before the magma ocean is entirely crystallized: they compare the Stokes time with the time needed to crystallize the magma ocean and their numerical experiments yields that syn-crystallization convection is possible when the ratio between these two times exceeds  $\sim 5 \times 10^4$ . This value however was determined with non-penetrative boundary conditions, the actual threshold should be a few orders of magnitude higher (meaning syn-crystallization convection is allowed for shorter solidification timescales) since the flow-through boundary condition leads to a faster destabilization of the cumulate for the same Stokes time. Another aspect that deserves care is that for Earth-sized bodies, the Stokes time should incorporate both the thermal and compositional density contrasts. Boukaré, E. Parmentier, et al. (ibid.) compare the “compositional” Stokes time with the solidification timescale; while this is perfectly valid for the Moon and

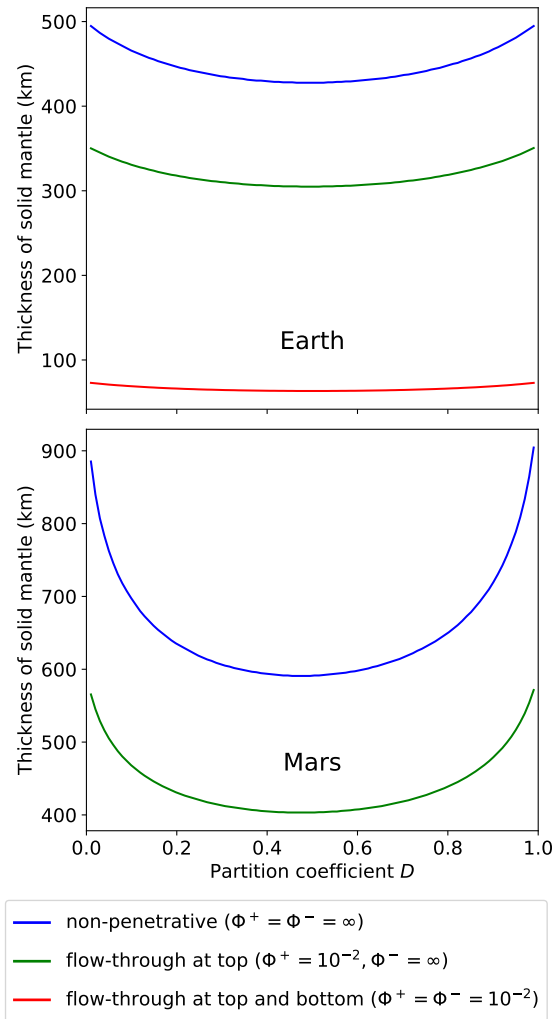


Figure 6.7: Thickness of the solid cumulate at which the destabilization timescale equals the time needed to crystallize the rest of the SMO for several values of the partition coefficient,  $D \in [0.01, 0.99]$ . The Moon is not shown here since the destabilization timescale is greater than the time needed to crystallize the SMO. The colors are the same as in fig. 6.2, blue: non-penetrative condition for both horizontal boundaries ( $\Phi^\pm = \infty$ ); green: flow-through condition at the boundary between the solid and the surface magma ocean; and red: flow-through condition at both horizontal boundaries.

Mars for which the thermal density contrast is much smaller than the compositional one, this does not hold for the Earth where both terms have similar magnitudes (fig. 6.5). The tremendous importance of the viscosity is why a viscosity of  $10^{18}$  Pa s is assumed in this study since it is a higher bound for the near-solidus viscosity (see Solomatov 2015, and references therein) and gives the most conservative estimate for the destabilizing time. The viscosity could be significantly lower if the melt fraction is important in the cumulate, Solomatov (ibid.) suggests  $10^{14}$  Pa s as a lower bound at 40% melt fraction (roughly the rheological transition). Another potential effect of viscosity that is neglected in the study is dynamical: since solid state convection occurs during the crystallization of the magma ocean, the temperature in the solid departs from the solidus temperature profile and as a result the viscosity increases. Moreover, the compositional profile becomes gravitationally stable with iron-enriched heavy material being transported from the top to the bottom of the solid. These two effects combined may lead to the stopping of the solid state convection (ibid.). Depending on the size of the magma ocean considered, it could then be possible either that the magma ocean crystallizes completely before convection may start again in the solid, or that convection sets in again in the solid before it is entirely crystallized. Studying this scenario requires a more complex method than a simple linear stability analysis since it involves a non-linear feedback between the dynamics of the solid part and its viscosity, temperature, and compositional fields.

Another unconstrained parameter is the partition coefficient of iron between the solid and liquid. An exploration of this parameter shows that the effect of the partition coefficient is rather limited for the Earth, and slightly more important for Mars (fig. 6.7). This is in agreement with figs. 6.2 and 6.5 showing the difference between the purely thermal case (corresponding to the extreme value  $D = 1$ ) and the purely compositional case is rather small for the Earth but more important for Mars.

Finally, our choice of a constant emissivity results in a roughly constant solidification rate, whereas more sophisticated cooling models including an atmosphere predict most of the mantle crystallizes quickly, and the solidification slows down when only a shallow magma ocean remains. Although such effects are important to build realistic solidification models, they should not affect dramatically our results. Indeed, a faster crystallization at the beginning would lead to a destabilization of the solid mantle at a larger thickness, but we expect this difference to be small since the destabilization timescale is rapidly much lower than the solidification timescale.

## 6.6 Conclusions

Upward crystallization of the silicate mantle of planets within a magma ocean is expected to produce a unstably stratified situation, because of both temperature and composition. In this study, we have addressed the question of whether the overturning instability develops faster than the time it takes to crystallize the magma ocean. To that end, we have developed a linear stability analysis tool to compute the growth rate of the fastest overturning mode and studied systematically the effect of the most important parameters: the planet's size (Moon to Earth size), the partition coefficient and the type of boundary condition between the solid and the liquid. In particular, we have introduced a boundary condition that accounts for the possibility of melting and freezing at the interface between the solid mantle and

the magma ocean.

This study shows convection is likely to start in the solid mantle of the Earth, Mars and the Moon before the entire crystallization of the surface magma ocean. Evolution models of the primitive mantle of planetary bodies should therefore account for convection and the associated mixing in the solid part of the crystallizing mantle.

This result holds for the Earth and Mars even without fractional crystallization and the unstable compositional gradient it creates in the cumulate. The value of the partition coefficient is found to have little impact on the timing of mantle overturn.

The timescale at which convection sets in scales as the Stokes time. Specifically, it is proportional to the viscosity of the solid. However, it should be kept in mind that these results are obtained assuming a newtonian rheology and a constant viscosity in the solid mantle. Given the central role of viscosity in this problem, better knowledge of the viscosity and rheology of the primitive solid mantle is of primary importance to study its dynamics.

Finally, the possibility of exchange of matter between the solid mantle and the magma ocean(s) should be accounted for in dynamical models of the primitive mantle since it greatly alters the pattern of convection as well as the destabilization timescale. It could even be a way of producing degree-one structures such as the ones observed on the Moon and Mars.

## Acknowledgements

We thank the editor Bruce Buffet and an anonymous reviewer for their useful remarks that helped to improve the clarity of our paper. This study is funded by the French Agence Nationale de la Recherche (grant number ANR-15-CE31-0018-01, MaCoMaOc).

## 6.7 A – Composition profile resulting from the fractional crystallization of the surface magma ocean

Conservation of the heavy component implies that

$$\frac{d}{dt} \left( \int_{R^-}^{R^+} C(r)r^2 dr + \frac{1}{3} (R_T^3 - R^{+3}) C_l \right) = 0, \quad (6.19)$$

where no compressibility effect on density is considered, allowing the bulk density to drop out of the equation. Using eq. (6.1) and  $\dot{C}_l = \dot{R}^+ \frac{dC_l}{dR^+}$ , assuming  $\dot{R}^+ > 0$  at all time and  $R^-$  constant:

$$\frac{1}{C_l} \frac{dC_l}{dR^+} = 3(1 - D) \frac{R^{+2}}{R_T^3 - R^{+3}}. \quad (6.20)$$

Using eq. (6.1), eq. (6.20) can be written for  $C$ :

$$\frac{1}{C} \frac{dC}{dR^+} - \frac{1}{D} \frac{dD}{dR^+} = 3(1 - D) \frac{R^{+2}}{R_T^3 - R^{+3}}. \quad (6.21)$$

Since  $C(r)$  does not depend on time, this equation holds for any  $r \leq R^+(t)$  (i.e. everywhere in the solid) and can be written as:

$$\frac{1}{C} \frac{dC}{dr} - \frac{1}{D} \frac{dD}{dr} = 3(1-D) \frac{r^2}{R_T^3 - r^3}. \quad (6.22)$$

Equation (6.22) is general and allows to take into account variations of  $D$ . However, it is useful to consider the limiting case of a constant partition coefficient  $D$ . In that case, a solution to this equation is

$$C = C_0 \left( \frac{R_T^3 - R^{-3}}{R_T^3 - r^3} \right)^{1-D}, \quad (6.23)$$

with  $C_0 = DC_{l0}$  the mass fraction of FeO in the first solid formed.

Note that eq. (6.23) diverges when  $r \rightarrow R_T$  but is in fact only valid as long as  $C < 1$  and  $C_l < 1$ . When  $C_l$  reaches 1, the solid formed has the same composition as the liquid. The complete solution therefore is

$$C = \begin{cases} C_0 \left( \frac{R_T^3 - R^{-3}}{R_T^3 - r^3} \right)^{1-D} & \text{if } r < R_s \\ 1 & \text{if } r > R_s, \end{cases} \quad (6.24)$$

with

$$R_s = \left( (R^-)^3 C_0^{\frac{1}{1-D}} + R_T^3 \left( 1 - C_0^{\frac{1}{1-D}} \right) \right)^{1/3} \quad (6.25)$$

the value of  $R^+(t)$  such that  $C_l(t) = 1$ .

## 6.8 B – Linear Stability

Since the solid is considered isoviscous and no source of toroidal flow is imposed at the boundaries, the velocity field can be expressed in terms of the scalar poloidal potential  $\mathcal{P}$ :  $\mathbf{u} = \nabla \times \nabla \times (\mathcal{P} \mathbf{r})$  (e.g. Ribe 2007; Ricard and Vigny 1989). Linearizing eqs. (6.11) to (6.14) around the reference state ( $\mathbf{u} = \mathbf{0}; \bar{T}; \bar{C}$ ) gives:

$$\mathcal{Q} = \nabla^2 \mathcal{P} \quad (6.26)$$

$$\nabla^2 \mathcal{Q} = \text{Ra} \frac{\Theta - \langle \Theta \rangle}{r + \lambda} + \text{Rc} \frac{c - \langle c \rangle}{r + \lambda} \quad (6.27)$$

$$\Gamma^2 \frac{\partial \Theta}{\partial t} + \frac{\partial \bar{T}}{\partial r} \frac{\mathcal{L}^2 \mathcal{P}}{r + \lambda} - \nabla^2 \Theta = W \left( (r-1) \frac{\partial \Theta}{\partial r} + \left( \frac{\partial \bar{T}}{\partial r} \right)^+ \Theta \right) \quad (6.28)$$

$$\Gamma^2 \frac{\partial c}{\partial t} + \frac{\partial \bar{C}}{\partial r} \frac{\mathcal{L}^2 \mathcal{P}}{r + \lambda} = W(r-1) \frac{\partial c}{\partial r}. \quad (6.29)$$

The boundary conditions on the temperature and composition perturbations are trivial:

$$\Theta^\pm = 0, \quad (6.30)$$

$$c^\pm = 0. \quad (6.31)$$

The boundary condition eq. (6.16) and the free-slip boundary condition are written in term of the poloidal potential as:

$$\pm\Phi^\pm \frac{1}{r+\lambda} \mathcal{L}^2 \mathcal{P} + \frac{\partial}{\partial r} \left( \frac{2}{r+\lambda} \mathcal{L}^2 \mathcal{P} - (r+\lambda) \mathcal{Q} \right) = 0 \quad (6.32)$$

$$\frac{\partial^2 \mathcal{P}}{\partial r^2} + (\mathcal{L}^2 - 2) \frac{\mathcal{P}}{(r+\lambda)^2} = 0. \quad (6.33)$$

$\lambda = R^-/L - 1$  is a curvature term due to the definition of the dimensionless radius.  $\mathcal{L}^2$  is the horizontal laplacian:  $\mathcal{L}^2 \bullet = \partial_r((r+\lambda)^2 \partial_r \bullet) - (r+\lambda)^2 \nabla^2 \bullet$ . The quantity  $\mathcal{Q}$  is introduced to ease the formulation of this system as an eigenvalue problem involving square matrices.

The perturbations  $\mathcal{P}$ ,  $\mathcal{Q}$ ,  $\Theta$  and  $c$  are developed using spherical harmonics, e.g.

$$\mathcal{P} = \sum_{l=1}^{\infty} \sum_{m=-l}^l \mathcal{P}_l(r) Y_l^m(\theta, \phi) e^{\sigma_l t} \quad (6.34)$$

where  $l$  and  $m$  are the spherical harmonics degree and order and  $\sigma_l$  is the growth rate associated to the harmonic degree  $l$ . The system is laterally degenerated and  $m$  does not affect the growth rate of the perturbation nor the shape of the radial modes  $\mathcal{P}_l(r)$ ,  $\mathcal{Q}_l(r)$ ,  $\Theta_l(r)$  and  $c_l(r)$ . These radial modes are discretized using a Chebyshev collocation approach (e.g. Canuto et al. 1985; Guo et al. 2012). Each radial mode is expressed as a vector whose components are the values at the  $N+1$  Chebyshev nodal points (respectively denoted  $\mathbf{P}$ ,  $\mathbf{Q}$ ,  $\mathbf{T}$  and  $\mathbf{C}$ ). Radial derivatives evaluated at the nodal points  $r_i = \frac{1}{2} \left( 3 + \cos \frac{i\pi}{N} \right)$  can then be expressed with a differentiation matrix  $\mathbf{d}$ , e.g.  $\partial_r \mathcal{P}(r_i) = (\mathbf{dP})_i$ . We formulate the system of linearized equations along with the associated boundary conditions as

$$\mathbf{LX} = \sigma_l \mathbf{RX} \quad (6.35)$$

with

$$\mathbf{X} = \begin{pmatrix} \mathbf{P} \\ \mathbf{Q} \\ \mathbf{T} \\ \mathbf{C} \end{pmatrix} \begin{matrix} 0 : N \\ 0 : N \\ 1 : N-1 \\ 1 : N-1 \end{matrix} \quad (6.36)$$

$$\mathbf{L} = \begin{pmatrix} 0 : N & 0 : N & 1 : N-1 & 1 : N-1 & \\ \mathbf{d}^2 + (l_2 - 2) \mathbf{r}_\lambda^{-2} & \mathbf{0} & \mathbf{0} & \mathbf{0} & 0 \\ \mathbf{D}^2 & -\mathbf{1} & \mathbf{0} & \mathbf{0} & 1 : N-1 \\ \mathbf{d}^2 + (l_2 - 2) \mathbf{r}_\lambda^{-2} & \mathbf{0} & \mathbf{0} & \mathbf{0} & N \\ l_2(\Phi^+ \mathbf{r}_\lambda^{-1} - 2\mathbf{r}_\lambda^{-2} + 2\mathbf{r}_\lambda^{-1} \mathbf{d}) & -(\mathbf{1} + \mathbf{r}_\lambda \mathbf{d}) & \mathbf{0} & \mathbf{0} & 0 \\ \mathbf{0} & \mathbf{D}^2 & -\mathbf{R} \mathbf{a} \mathbf{r}_\lambda^{-1} & -\mathbf{R} \mathbf{c} \mathbf{r}_\lambda^{-1} & 1 : N-1 \\ l_2(-\Phi^- \mathbf{r}_\lambda^{-1} - 2\mathbf{r}_\lambda^{-2} + 2\mathbf{r}_\lambda^{-1} \mathbf{d}) & -(\mathbf{1} + \mathbf{r}_\lambda \mathbf{d}) & \mathbf{0} & \mathbf{0} & N \\ -(\partial_r \bar{T}) l_2 \mathbf{r}_\lambda^{-1} & \mathbf{0} & \mathbf{D}^2 + W^+ ((\mathbf{r} - \mathbf{1}) \mathbf{d} + (\partial_r \bar{T})^+ \mathbf{1}) & \mathbf{0} & 1 : N-1 \\ -(\partial_r \bar{C}) l_2 \mathbf{r}_\lambda^{-1} & \mathbf{0} & \mathbf{0} & W^+ (\mathbf{r} - \mathbf{1}) \mathbf{d} & 1 : N-1 \end{pmatrix} \quad (6.37)$$

$$\mathbf{R} = \begin{pmatrix} & 0 : N & 0 : N & 1 : N - 1 & 1 : N - 1 \\ \mathbf{0} & \mathbf{0} & \mathbf{0} & \mathbf{0} & \\ \mathbf{0} & \mathbf{0} & \mathbf{0} & \mathbf{0} & \\ \mathbf{0} & \mathbf{0} & \Gamma^2 \mathbf{1} & \mathbf{0} & \\ \mathbf{0} & \mathbf{0} & \mathbf{0} & \Gamma^2 \mathbf{1} & \end{pmatrix} \begin{matrix} 0 : N \\ 0 : N \\ 1 : N - 1 \\ 1 : N - 1 \end{matrix} \quad (6.38)$$

where  $\mathbf{1}$  is the identity matrix,  $\underline{\mathbf{r}}_{ij} = r_i \mathbf{1}_{ij}$ ,  $\underline{\mathbf{r}}_\lambda = \underline{\mathbf{r}} + \lambda \mathbf{1}$ ,  $l_2 = l(l+1)$  and  $\mathbf{D}^2 = \mathbf{d}^2 + 2\underline{\mathbf{r}}_\lambda^{-1} \mathbf{d} - l_2 \underline{\mathbf{r}}_\lambda^{-2}$ . The extra row and column on top and right of the matrices are respectively the column and row indices of each of the submatrices. For example, the top left submatrix of the matrix  $\mathbf{L}$  is only the first row (hence the 0 on the extra column) of the matrix  $\mathbf{d}^2 + (l_2 - 2)\underline{\mathbf{r}}_\lambda^{-2}$ .

At a given instant during the crystallization, all the dimensionless numbers  $W$ ,  $\lambda$ ,  $\Gamma$ ,  $\text{Ra}$  and  $\text{Rc}$  appearing in the matrices  $\mathbf{L}$  and  $\mathbf{R}$  are known. For any harmonic degree  $l$  of the perturbation, finding its growth rate  $\sigma_l$  and associated vertical mode  $\mathbf{X}$  is an eigenvalue problem. The largest eigenvalue is the growth rate, and the associated eigenvector represent the vertical modes. At a given instant, we look for the harmonic degree  $l$  with the highest growth rate  $\sigma_l$ , which is then used to compute the dimensional destabilization time scale  $L_M^2/(\kappa\sigma)$ .



# Chapter 7

## Preliminary non-linear coupled evolution model

### 7.1 Implementation in StagYY

Our evolution model described in chapter 5 required several alterations to the existing convection code StagYY. Time-steps are composed of the following steps.

1. Compute the time-step  $\delta t$  to ensure numerical stability since an explicit scheme is used:

$$\delta t = \min \left( A \frac{(r + \lambda)\delta\phi}{u_\phi}; A \frac{\delta r}{u_r}; \frac{\delta r_{\min}}{|\dot{R}^\pm|_{\max}}; B(r + \lambda)^2\delta\phi^2; B\delta r^2 \right) \quad (7.1)$$

where  $A$  and  $B$  are safety factors smaller than 1. The first two terms correspond to advection by the flow velocity, the third term is due to the advection arising from the fixed-front method, and the last two terms account for heat diffusion.  $\lambda$  is the curvature term as defined by eq. (5.91).

2. Update magma ocean variables  $R^\pm$ ,  $T^\pm$ ,  $\xi^\pm$ ,  $c^\pm$  according to the time derivatives computed in the previous step (item 14).
3. Update geometrical variables to the new boundaries' positions  $R^\pm$ . In particular, the curvature term  $\lambda$  and pre-computed grid cell volumes of the spherical annulus  $(r + \lambda)^2\delta\theta\delta\phi\delta r$ .
4. Update the position and ideal mass of tracers to the new position of the boundaries, as explained hereafter.
5. Add new tracers in case of net freezing, and remove tracers in case of net melting of the magma oceans.
6. Update the coefficients of the matrix representing the Stokes equation since differential operators depend on the curvature term  $\lambda$  as explicitated by eqs. (5.92) and (5.93). This takes a heavy toll in terms of computational costs compared to the isoviscous cases in chapter 4. Indeed, the matrix being no longer constant, its LU factorization needs to be performed at every time-step instead of only once per simulation.

7. Update the temperature field owing to diffusion, advection (TVD scheme), and internal heating. Note that terms related to the fixed-front approach in eq. (5.112) are treated here.
8. Advect the tracers carrying compositional information (FeO content  $\xi$  and HPE content  $c$ ). This advection is performed only with the flow velocity. The advection term due to the fixed-front approach is handled in item 4.
9. Eliminate tracers that went out of the domain due to the phase change boundary conditions, add tracers where matter entered the domain.
10. Merge tracers that have a mass too low compared to the ideal tracer mass to keep the number of tracers roughly constant as magma oceans crystallize (more details after).
11. Interpolate tracers information on the grid.
12. Update the velocity and pressure fields by solving the Stokes equation with the new temperature (item 7) and FeO content (item 11) fields in the buoyancy term.
13. Compute diagnostics such as the heat flux out of the domain, average temperature, root-mean-square velocities, etc.
14. Compute the time derivatives  $\dot{R}^\pm$ ,  $\dot{T}^\pm$ ,  $\dot{\xi}^\pm$  and  $\dot{c}^\pm$  according to the evolution models described in chapter 5.

Tracers in StagYY each have a mass assigned to them, denoted  $m_t$  in this document. Dimensionless tracer masses are scaled with  $\rho L_M^3$ .

The dimensionless mass of the entire spherical annulus, scaled with  $\rho L_M^3$ , is

$$M = \frac{A}{3}((R^+)^3 - (R^-)^3). \quad (7.2)$$

$R^+$  and  $R^-$  are the TOMB and BOMB radii made dimensionless with  $L_M$ , and  $A$  is the surface coefficient

$$A = 2\pi\delta\theta. \quad (7.3)$$

Given a total number of tracers  $N$ , the ideal mass of one tracer (i.e. the mass such that every tracer has the same mass) is merely

$$m^{\text{ideal}} = \frac{M}{N} \quad (7.4)$$

Note that since  $M$  varies as the solid thickens or melts, and that the target number of tracers is constant, the ideal tracer mass changes between timestep  $n$  and the next timestep  $n + 1$  as

$$m_{n+1}^{\text{ideal}} = \frac{M_{n+1}}{M_n} m_n^{\text{ideal}}. \quad (7.5)$$

If the solid thickens,  $m^{\text{ideal}}$  increases but the mass of a given tracer  $m_t$  is constant since the mass scale  $\rho L_M^3$  is constant. Tracers hence slowly drift away from their ideal mass, becoming lighter than they should be and their number increasing as new tracers are added due to the net freezing (item 5). In order to maintain a constant

number of tracers, groups of tracers with a mass  $m_t < \frac{1}{2}m^{\text{ideal}}$  are merged together (item 10) using a merging routine originally developed in StagYY for eruption related routines.

Moreover, as stated in item 4, the radial position of each tracer needs to be advected so that their physical position stays the same while the frame changes due to the fixed-front approach. The position  $r^{n+1}$  at timestep  $n + 1$  is computed from that at timestep  $n$  as:

$$r_{n+1} = \frac{\Gamma_n(r_n + \lambda_n)}{\Gamma_{n+1}} - \lambda_{n+1}. \quad (7.6)$$

The last technical aspect that requires some care is that magma ocean evolution models in chapter 5 are made dimensionless with constant scales while the convective model in the solid uses scales (of distance and temperature) that vary with time. On top of that, magma oceans model are written assuming a 3D geometry, while numerical simulations are performed in a 2D spherical shell. Appropriate scaling of fluxes (heat and matter) is therefore required to connect the magma ocean evolution models with that of the solid part. These are described hereafter.

The mass of tracers that should be added in cells where dynamically freezing matter enters through the boundary (item 9) is

$$\delta m_t = \mp \frac{1}{\Gamma} u_r \delta t (R^\pm)^2 \delta \theta \delta \phi \quad (7.7)$$

The number of tracers added in a cell is chosen so that the mass of those tracers is as close as possible to the ideal tracer mass. Their positions are chosen randomly laterally and radially within a distance  $|u_r| \delta t / \Gamma^2$  of the boundary.

The mass of tracers to add owing to the net freezing of magma oceans (item 5) is

$$\delta m_t = \pm A \dot{R}^\pm (R^\pm)^2 \delta t. \quad (7.8)$$

Similarly to what is done for the dynamical-freezing tracers, the number of tracers is chosen so that their mass is as close as possible to the ideal tracer mass, and their positions are chosen randomly laterally and radially, within a distance  $|\dot{R}^\pm| \delta t / \Gamma$  of the boundary.

The dynamical exchange integrals  $I_{u\xi}^\pm$ , eqs. (5.32) and (5.74), are estimated as:

$$I_{u\xi}^\pm = \int_{\pm} \xi_\phi^{\mp u_r} u_r dS \simeq \frac{4\pi}{A} \left( \frac{(R^\pm)^2}{\Gamma} \delta \theta \delta \phi \sum_{\text{grid, inward}} \frac{\xi^\pm K}{1 - \xi^\pm (1 - K)} u_r + \frac{1}{\delta t} \sum_{\text{tracers, outward}} m_t \xi_t \right). \quad (7.9)$$

Tracers actually going out are used to evaluate the integrals over parts where dynamical melting occurs because it is more precise than integrating an interpolated field over the grid. A similar computation is performed with the HPE concentration.

The net fusion/crystallization integrals  $I_\xi^\pm$ , eqs. (5.31) and (5.73), are estimated as:

$$I_\xi^\pm \simeq \begin{cases} 4\pi (R^\pm)^2 \frac{\xi^\pm K}{1 - \xi^\pm (1 - K)} & \dot{R}^\pm \geq 0; \\ \frac{4\pi}{A} (R^\pm)^2 \delta \theta \delta \phi \sum_{\text{grid}} \xi & \dot{R}^\pm \leq 0. \end{cases} \quad (7.10)$$

A similar computation is performed with the HPE concentration. Note that when solving the energy balance eqs. (5.42) and (5.84) to determine  $\dot{R}^\pm$ , the sign of  $\dot{R}^\pm$  is not known. We assume first net crystallization  $\dot{R}^\pm \geq 0$  to evaluate  $I_\xi^\pm$ . If the energy balance equation then yields  $\dot{R}^\pm \leq 0$ ,  $I_\xi^\pm$  is computed again changing the assumed sign of  $\dot{R}^\pm$ .

## 7.2 Preliminary simulation with a Basal Magma Ocean

We present here a preliminary run with only a Basal Magma Ocean. Moreover, internal heating in the solid was disabled for this run due to problems with the conservation of HPE at the end of crystallization of the magma ocean. Parameters that are different from the nominal values in tables 5.2 and 5.3 are shown in table 7.1. The grid is 512 cells in the  $\phi$ -direction and 64 cells in the radial direction. The grid is refined in the radial direction up to a factor 20 at the bottom boundary and 5 at the top boundary. The number of tracers is about 650 thousands, i.e. an average of 20 tracers per grid-cell.

The initial condition taken for the composition of the solid is that of a uniform composition in thermodynamical equilibrium with the BMO. This is probably not a relevant initial condition since the fractional crystallization of a TMO would lead to an enriched solid mantle compared to the BMO. We make this choice so as to avoid compositional effects at the beginning of the crystallization of the BMO to focus on the thermal aspects of the problem. It would be worth to explore different initial conditions for the composition of the solid. The initial condition on temperature is that of a uniform bulk to be consistent with the initial uniform compositional field.

Figures 7.1 to 7.3 show snapshots of the temperature field, streamlines, and FeO mass fraction in the solid at various instants of the simulation. Figure 7.4 shows the corresponding time series.

At the beginning of the simulation (second row of fig. 7.1), convection in the solid is similar to what is obtained in the purely thermal case at constant solid thickness (chapter 4). The flow-through boundary condition at the bottom leads to wide hot upwellings and narrow downwellings, with little deformation in the solid compared to the classical case with nearly-aspect-ratio-1 rolls. As can be seen on the time series fig. 7.4, this convective mode is very efficient to extract heat from the BMO since it corresponds to a large heat flux at the BOMB. The flow velocities are at their maximum, and the average temperature is strongly increased. Since the initial solid and the BMO compositions are in equilibrium, the FeO mass fraction does not vary strongly in the solid at the beginning of the simulation.

This situation goes on for some time, even going through a phase where all downwellings are grouped in the same hemisphere, corresponding to a mode of convection dominated by a degree-one (third row of fig. 7.1,  $t = 4.5 \times 10^{-3}$ ). However, the thermal boundary layer ends up developing Rayleigh-Taylor instabilities, forming multiple narrow cold-downwellings (last row of fig. 7.1 and first of fig. 7.2). This is associated with a decrease of the heat flux extracted through the BOMB, the convective velocity, and the average temperature of the domain (fig. 7.4).

Shortly after, strong compositional variations start to appear in the solid as the BMO has been significantly enriched in FeO because of fractional crystallization.

Parameter	Description	Value
$\Gamma_0^-$	Initial BMO thickness	0.3
$T_0^-$	Initial BOMB temperature	0.7
$\xi_0^-$	Initial FeO concentration in the BMO	1/3
$\xi_0$	Initial FeO concentration in the solid	0.1
$B_\xi$	Compositional buoyancy	10
Ra	Rayleigh number	$3 \times 10^5$
$R_H$	Heat production in the solid	0
$\Phi^-$	Phase change number at BOMB	$10^{-2}$

Table 7.1: Parameters used for the simulation. Other parameters have the nominal values in tables 5.2 and 5.3.

Rows 2 and 3 of fig. 7.2 indeed show that a dense layer enriched in FeO starts to form at the base of the solid mantle. It is stable enough to stop most of the cold downwellings, thereby preventing them from going through the phase change interface while a BMO is still present. The convection in the solid then presents more classical patterns, the heat flux, flow velocities, and average temperature stay at values lower than at the beginning of the simulation.

The crystallization of the remaining BMO leads to the formation of an extremely dense layer enriched in FeO at the base of the mantle, as seen on fig. 7.3. It is pushed around and given the shape of piles by the flow in the solid mantle, but it is sufficiently dense to subsist over a very long timescale. Indeed, the last snapshot on fig. 7.3 at a dimensionless time  $t = 0.07$  would correspond to a total dimensional time of around 15 Gyrs. This is the first self-consistent evolution model that produces long-living LLSVP-like features that are chemically dense piles resulting from the crystallization of a Basal Magma Ocean, as proposed by Labrosse, Hernlund, and Coltice (2007). It should be kept in mind, however, that the Rayleigh number in this simulation is only  $3 \times 10^5$ , much lower than the estimated value of  $10^7$  or  $10^8$  for the Earth's mantle. Using a more realistic value should affect the lifetime, shape, or even existence of these piles. An exploration of the parameter space is therefore needed before drawing any decisive conclusion.

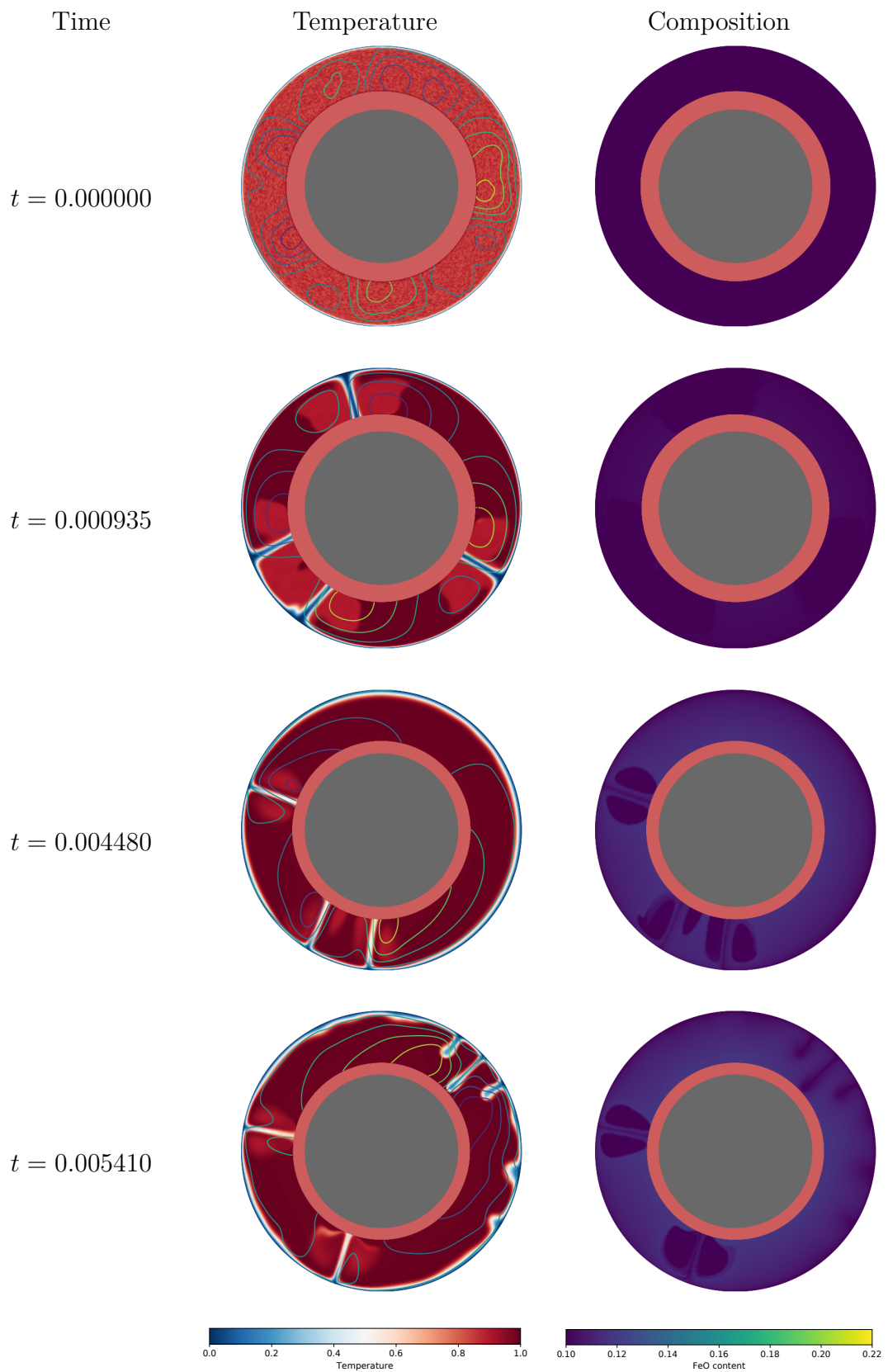


Figure 7.1: Temperature field with streamlines (left) and compositional field (right) at various times during the simulation. The red annulus at the base of the solid represents the BMO, the grey circle represents the core. For reference, a dimensionless time of 0.02 is about the age of the Earth.

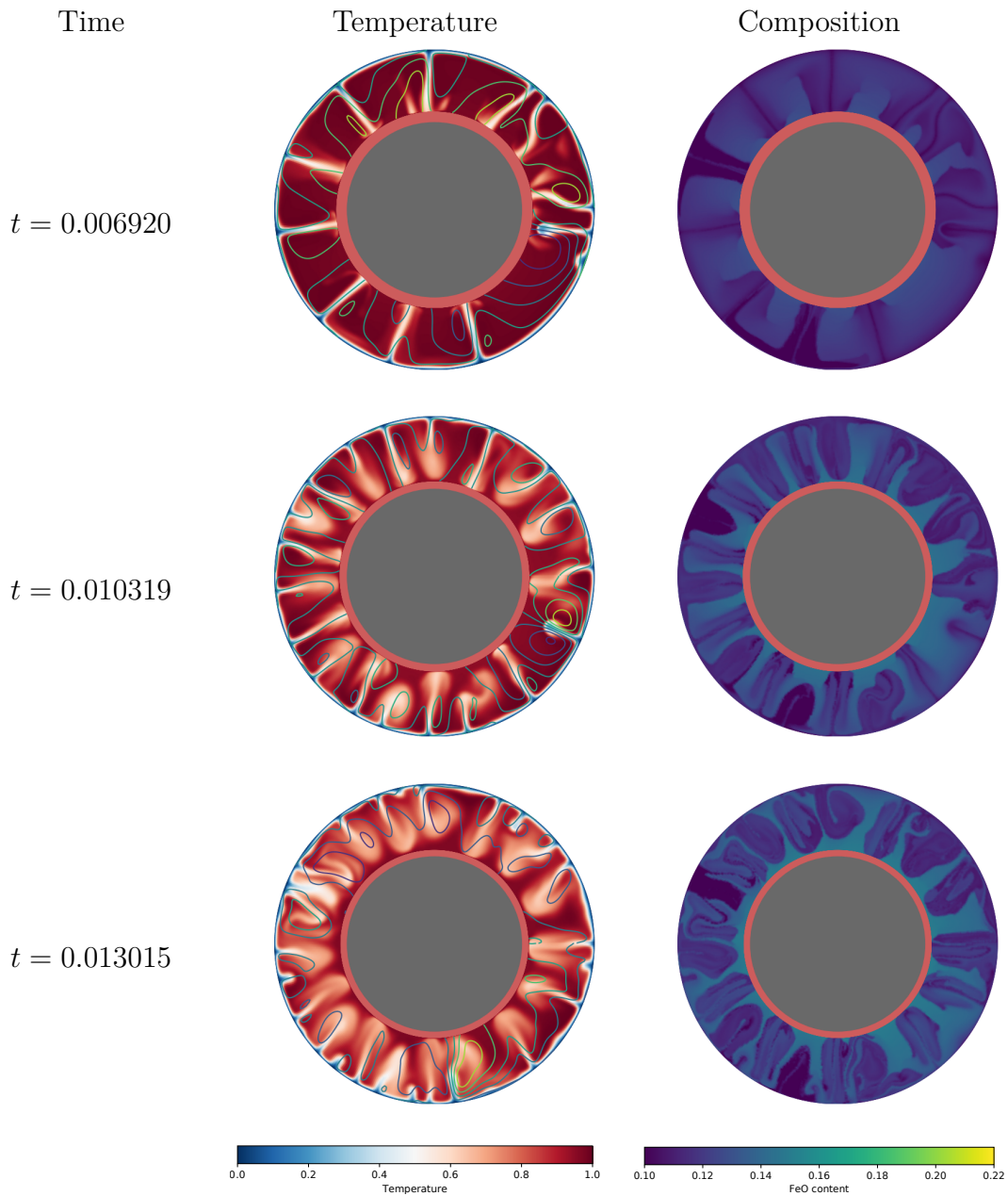


Figure 7.2: Temperature field with streamlines (left) and compositional field (right) at various times during the simulation. It is the same as fig. 7.1 for following times.

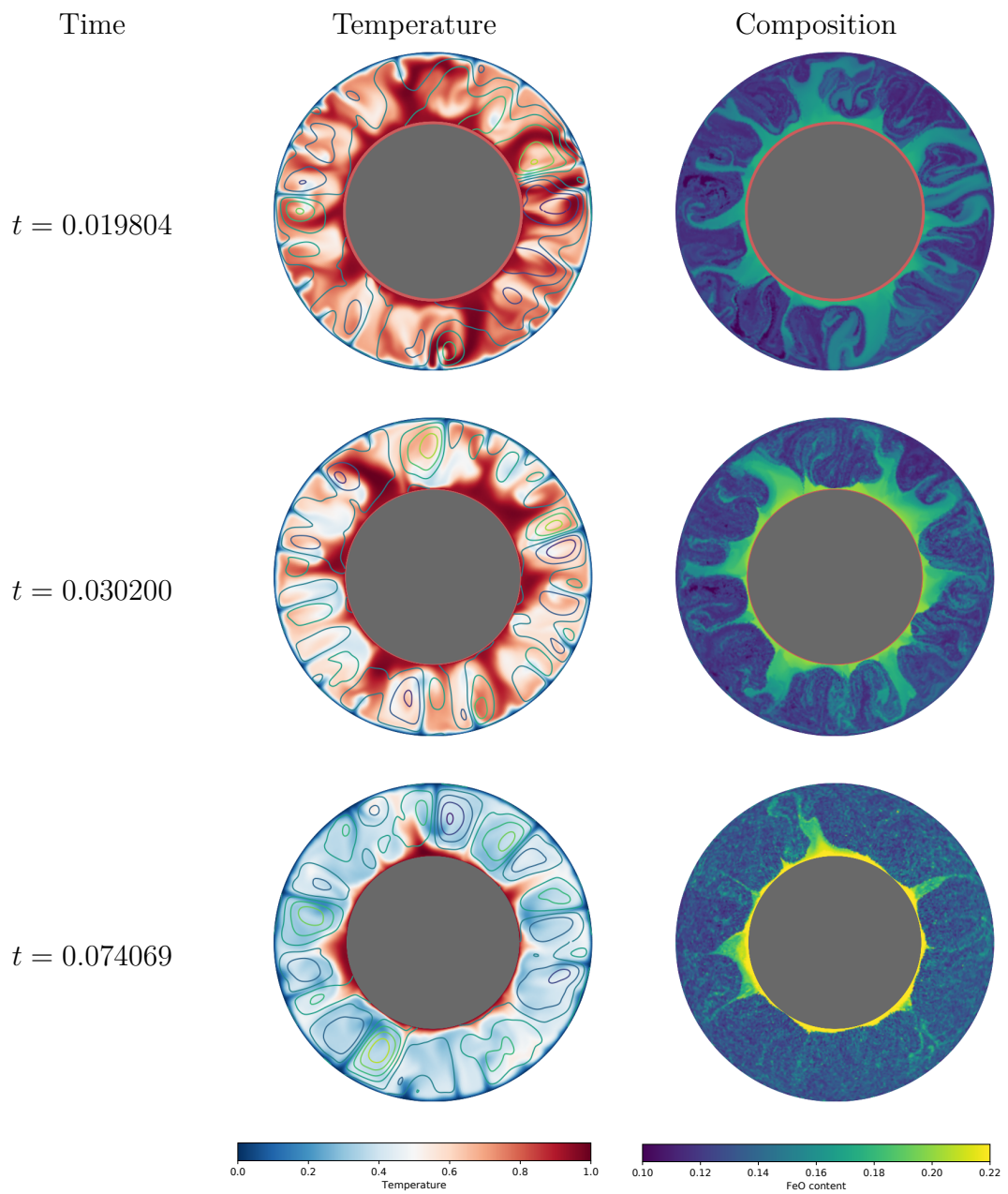


Figure 7.3: Temperature field with streamlines (left) and compositional field (right) at various times during the simulation. It is the same as figs. 7.1 and 7.2 for following times.

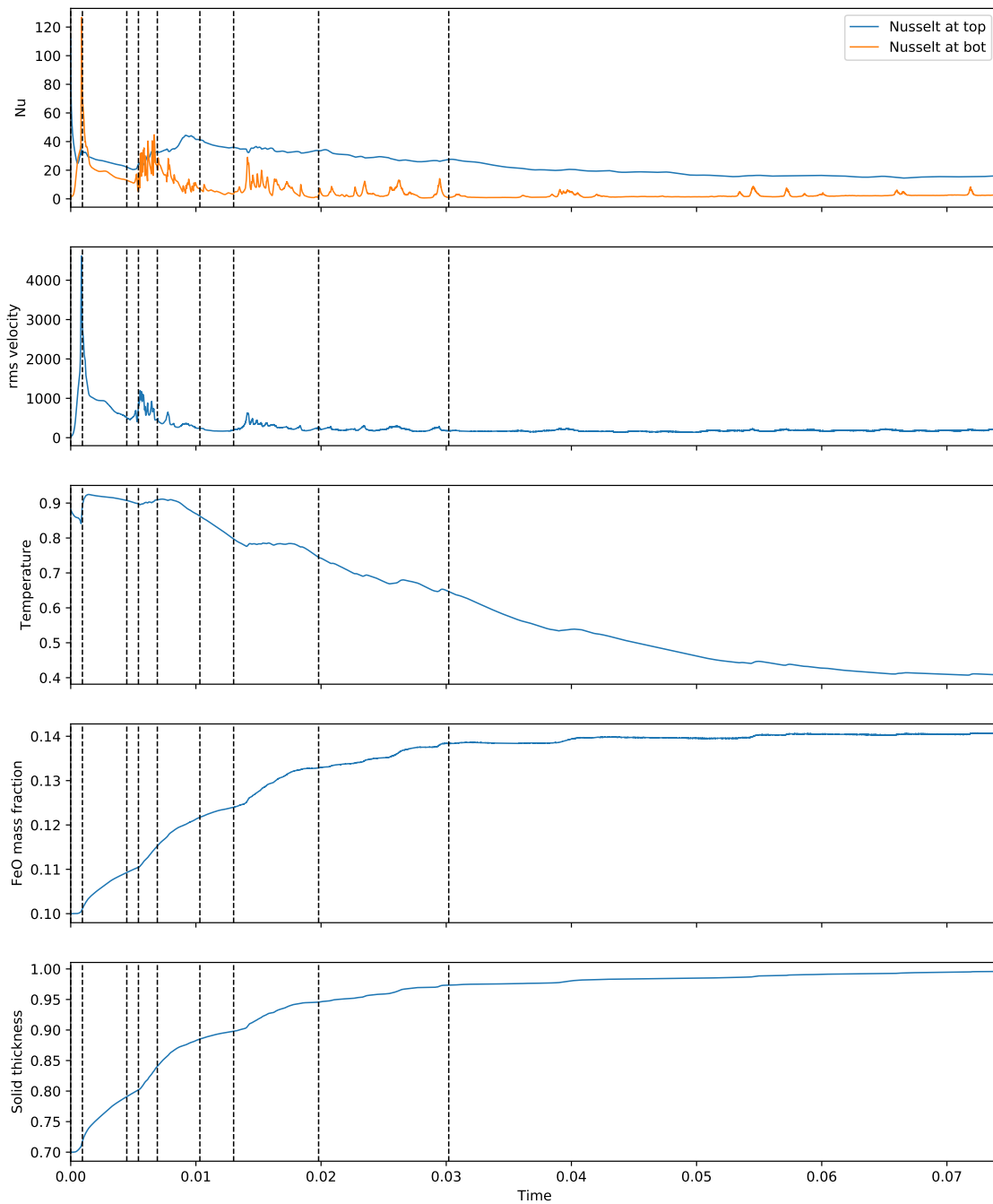


Figure 7.4: Time series. From top to bottom: heat flux at the outer surface and BOMB, root-mean-square velocity in the solid, average temperature in the solid, average FeO mass fraction in the solid, thickness of the solid layer. The dashed vertical lines correspond to the snapshots visible on figs. 7.1 to 7.3. Beware that the first and last snapshots are at the first and last timesteps, the corresponding dashed-lines are therefore not visible.



# Chapter 8

## Concluding remarks and perspectives

Throughout this thesis, we explored the consequences of the existence of global magma oceans on the dynamics of the primitive solid mantle. We mainly focused on the fact that the interface between the solid primitive mantle and a magma ocean is a phase change interface. Dynamic topography forming at the interface owing to viscous forces in the convecting solid mantle can therefore be melted/frozen away. This possibility for an exchange of matter at the boundary is strikingly different from the classical non-penetrative case. We take this mechanism into account with a phase change boundary condition allowing matter to go through the interface. The linear stability analysis of this system (chapter 3) revealed two drastic consequences of the phase change boundary condition: when the transfer of matter through the interface is efficient, linearly unstable patterns of convection have a larger wavelength than the classical non-penetrative case, involving less deformation in the solid and therefore leading to a lower critical Rayleigh number. Direct numerical simulations (chapter 4) showed moreover that the heat flux carried out by the solid is greatly increased by these boundary conditions, especially when both boundaries are flow-through. It could easily be a couple orders of magnitude larger than with classical boundary conditions. We built in chapter 5 an evolution model for the entire mantle coupling in a self-consistent manner the solid mantle and global magma oceans bounding it at either of both its boundaries. Computing the linear growth rate of a perturbation throughout the crystallization of a Top Magma Ocean showed it is likely that convection in the solid mantle starts in Earth-like bodies before the entire crystallization of the magma ocean (chapter 6). Finally, a preliminary fully non-linear simulation of the self-consistent evolution model showed promising results with the formation of LLSVPs-like features at the base of the solid mantle from the crystallization of a BMO.

It is clear from all these results that the possibility of exchange of matter between magma oceans and the primitive solid mantle has tremendous consequences on the dynamics and heat budget of the primitive Earth and is therefore a crucial ingredient that should be included in evolution models of the Earth. An important question that should be investigated through a more complete exploration of the parameter space of the coupled evolution model is whether the phase change boundary condition and the presence of global magma oceans would help solving the thermal catastrophe problem. Indeed, the enormous heat fluxes expected when two magma

oceans bound the solid mantle should provide an extremely efficient way to extract heat from the core. The self-consistent evolution model developed in this thesis offers a way to test this idea. Moreover, many complexities were left out in this thesis and deserve attention in the near future, some of them are listed below.

- Models featuring a TMO or even both magma oceans still require some tuning due to a problem of tracers mass conservation. Fixing these issues would be an important leap forward to routinely run self-consistent models following the entire cooling history of a global magma ocean crystallizing from the middle. The heat budget of such a system could be a way around the thermal catastrophe as discussed before.
- A way to form a BMO that was not considered here is to bring FeO and HPE enriched solid material (which could be issued from the fractional crystallization of a TMO) at the base of the solid mantle. Even though the present model does not allow yet the apparition of a BMO by this mechanism, it probably would not be excessively difficult to adapt it to study this setup.
- Hot upwellings in a primitive mantle close to its solidus would result in partial melting. In the case of a BMO, the volume involved could be considerable.
- Our current model assume an atmosphere behaving as a gray body of constant emissivity. Exchanges of gasses between a surface magma ocean and the atmosphere introduce an inter-dependence between the two layers that should be taken into account (e.g. Abe 1997; Lebrun et al. 2013).
- Fractional crystallization of the mantle would release FeO in the Top Magma Ocean, potentially forming a stable stratified layer at its base. This could affect both the phase change boundary condition and the self-consistent evolution model. Both are indeed based on the assumption that the magma ocean is vigorously convecting and well mixed, an assumption that could be challenged.
- A long standing issue in the community is that of the rheology of the solid mantle, and in particular what are the ingredients necessary for the onset of plate tectonics. The presence of a BMO naturally leads to convective patterns with very localized downwellings and large wavelength of convection, akin to what is observed in the tectonic plates regime. Of course, there is no longer a global BMO in today's mantle but it would be worth exploring whether its presence could ease the transition to a plate tectonics regime.

# Appendix A

## Rayleigh-Bénard convection in a creeping solid with melting and freezing at either or both its horizontal boundaries

This chapter is an article written by S. Labrosse, A. Morison, R. Deguen and T. Alboussière and published in 2018 in the Journal of Fluid Mechanics (Labrosse, Morison, et al. 2018). It presents a linear and a weakly non-linear stability analysis of the constant-thickness thermal problem described in chapter 2 in cartesian geometry.

### A.1 Abstract

Solid state convection can take place in the rocky or icy mantles of planetary objects and these mantles can be surrounded above or below or both by molten layers of similar composition. A flow toward the interface can proceed through it by changing phase. This behaviour is modeled by a boundary condition taking into account the competition between viscous stress in the solid, that builds topography of the interface with a timescale  $\tau_\eta$ , and convective transfer of the latent heat in the liquid from places of the boundary where freezing occurs to places of melting, which acts to erase topography, with a timescale  $\tau_\phi$ . The ratio  $\Phi = \tau_\phi/\tau_\eta$  controls whether the boundary condition is the classical non-penetrative one ( $\Phi \rightarrow \infty$ ) or allows for a finite flow through the boundary (small  $\Phi$ ). We study Rayleigh-Bénard convection in a plane layer subject to this boundary condition at either or both its boundaries using linear and weakly non-linear analyses. When both boundaries are phase change interfaces with equal values of  $\Phi$ , a non-deforming translation mode is possible with a critical Rayleigh number equal to  $24\Phi$ . At small values of  $\Phi$ , this mode competes with a weakly deforming mode having a slightly lower critical Rayleigh number and a very long wavelength,  $\lambda_c \sim 8\sqrt{2}\pi/3\sqrt{\Phi}$ . Both modes lead to very efficient heat transfer, as expressed by the relationship between the Nusselt and Rayleigh numbers. When only one boundary is subject to a phase change condition, the critical Rayleigh number is  $Ra_c = 153$  and the critical wavelength is  $\lambda_c = 5$ . The Nusselt number increases about twice faster with Rayleigh number than in the classical case with non-penetrative conditions and the average temperature diverges from  $1/2$  when the Rayleigh number is increased, toward larger values when the

bottom boundary is a phase change interface.

## A.2 Introduction

Rayleigh-Bénard convection is one of the main heat transfer mechanisms in natural sciences, responsible for most of the dynamics of the atmosphere and oceans (Pedlosky 1987), plate tectonics (Schubert et al. 2004), dynamo action in planetary cores (Roberts and King 2013). It is also one of the most generic example of pattern formation mechanism in fluid dynamics (e.g. Cross and Hohenberg 1993; Manneville 2004) and has therefore attracted a lot of attention for a century since the work of Lord Rayleigh (Strutt 1916). However, the mathematical and experimental studies of Rayleigh-Bénard convection have usually considered boundary conditions that are not fully relevant to the natural systems that justified them, their horizontal surfaces being generally considered as subjected to no-slip or free-slip boundary conditions. The former is valid for convection experiments in a tank and for the natural fluids bounded by much more viscous envelopes, like the liquid cores of terrestrial planets and the bottom of the ocean. The latter is often considered as an approximation for a free-surface condition, as applies to a fluid bounded by a much less viscous one. This is in particular the case of the solid planetary mantles that, on long timescales, behave like very viscous fluids (e.g. Jarvis and McKenzie 1980; McKenzie et al. 1974; Turcotte and Oxburgh 1967) and are bounded below and above by liquid or gaseous layers. This approximation neglects the effect of the topography on convection and some studies have been devoted to the modeling of these effects, which can be dramatic when it is associated to, for example, intense volcanism in hot planets (Monnereau and Dubuffet 2002; Ricard, Labrosse, et al. 2014).

In the present paper, we consider the effects of having horizontal boundaries at which a solid-liquid phase change occurs on Rayleigh-Bénard convection in the creeping solid, that has an infinite Prandtl number (Schubert et al. 2004). For simplicity, we consider a Newtonian fluid with a uniform high viscosity, neglecting the effects of more complex rheologies (e.g. Bercovici and Ricard 2014; Christensen and Yuen 1989; Davaille and Jaupart 1993; E. M. Parmentier 1978; Tackley 2000), that is bounded by a low viscosity liquid of the same composition as the convecting solid. The boundary between the liquid and the solid consists of a phase change whose position is controlled by a Clapeyron diagram relating pressure and temperature for phase equilibrium. In the context of planetary interiors, the pressure is largely dominated by the hydrostatic contribution and the interface is on average a horizontal surface. The stress field and associated dynamic pressure due to the dynamics of the solid leads to deformation of the interface with a viscous timescale  $\tau_\eta$ . The topography creates variations of the thermal gradient on the liquid side which drives a convective heat transfer in the liquid acting to erase the topography by transporting the latent heat released by freezing in topography lows to topography highs where melting occurs. Other sources of motions in the liquid can also contribute to this lateral heat transfer which happens on a timescale  $\tau_\phi$ , the expression of which being derived in section A.3. The ratio of the two timescales,  $\Phi = \tau_\phi/\tau_\eta$ , controls the behaviour of the boundary. For a large value of  $\Phi$ , the topography is set by the balance between the viscous stress in the solid and the buoyancy of the topography, the phase change acting on a too long timescale to affect the classical

behaviour of the free surface. The buoyancy of the topography is responsible for making the vertical velocity drop to zero at the interface, which leads to an effectively non-penetrating boundary condition. On the other hand, for low values of  $\Phi$ , the topography is erased by freezing and melting at a rate greater than the one at which it is generated. The removal of the associated buoyancy leads to a non-null velocity across the interface.

This situation has already been considered in the case of the dynamics of the Earth inner core (Alboussière et al. 2010; Deguen, Alboussière, et al. 2013; Mizzon and Monnereau 2013; Monnereau, Calvet, et al. 2010), which is the solid iron sphere at the center of the liquid iron core of the Earth. Deguen, Alboussière, et al. (2013) have derived a general formulation of the boundary condition for arbitrary values of  $\Phi$  and shown that the application of this boundary condition to a sphere considerably changes the dynamics by decreasing the critical Rayleigh number for the onset of thermal convection and allowing a new mode of convection, the translation mode, where no deformation occurs in the sphere, melting happens at the boundary of the advancing hemisphere and freezing occurs at the trailing boundary.

A similar situation arises for the ice shell of some satellites of giant planets in the solar system which are believed to host a liquid ocean below their ice layer (Čadek et al. 2016; Gaidos and Nimmo 2000; Khurana et al. 1998; Pappalardo et al. 1998; Soderlund et al. 2014; Tobie, Choblet, et al. 2003). Some of the largest of such satellites can also have a layer of high pressure ices below their ocean (Baland et al. 2014; Grasset et al. 2000; Sohl et al. 2003). Another situation that implies such a melt-solid interface arises on all terrestrial planets in their early stage when their silicate layer is completely or largely molten owing to the high energy of their accretion (Elkins-Tanton 2012; Solomatov 2015). Convection can start in the solid mantle during its crystallisation from the magma ocean, while a liquid layer persists above and/or below (Labrosse, Hernlund, and Coltice 2007). It is therefore interesting to consider convection in a layer, not a full sphere, when a phase change boundary condition applies at either or both its horizontal boundaries.

Deguen (2013) performed such a study in the case of a spherical shell with a central gravity linearly varying with radial position and showed that, again, a translation mode is possible and favoured in the linear stability analysis if both the upper and lower boundaries allow an easy phase change, that is if each has a low value of the  $\Phi$  parameter. The purpose of the present paper is to extend the analysis to the plane layer situation and perform the linear stability and weakly non-linear analysis as a function of the phase change parameters of both horizontal boundaries.

The boundary conditions are presented in section A.3, section A.4 presents the translation mode of convection, section A.5 presents the linear and weakly non-linear analysis in the case when both horizontal boundaries have the same value of the phase change parameter and section A.6 shows the case when phase change is only allowed on one boundary.

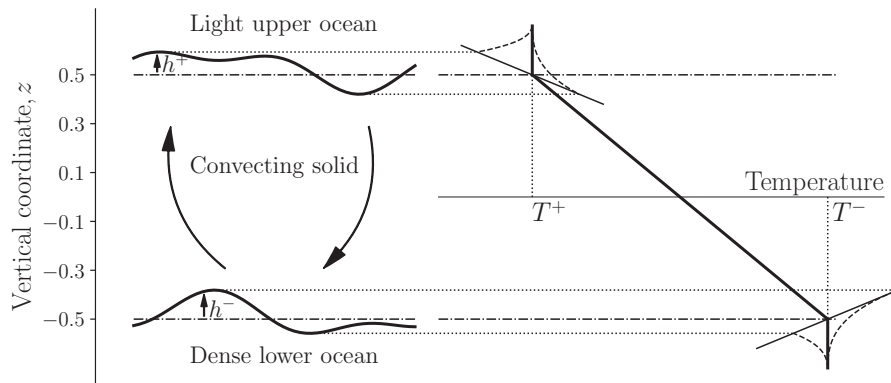


Figure A.1: Definition of the topography (exaggerated here for clarity) and the temperature for the boundary conditions. The dash-dotted lines are the reference positions for the conductive motionless solutions of the top and bottom boundaries. The right panel shows the reference temperature profile (thick solid line) intersecting the melting temperature at the top and bottom (thin solid lines) at temperatures  $T^+$  and  $T^-$ , respectively. Lateral variations of the topography make the intersection deviate laterally in temperature. Representative temperature profiles in the liquid sides are shown as dashed lines. In the context of planetary applications, the temperature profiles should be interpreted as deviations from the isentropic reference.

### A.3 Conservation equations and boundary conditions

We consider a layer of creeping solid that behaves like a Newtonian fluid on long timescales and that is bounded above or below or both by a liquid related to the solid by a phase change (fig. A.1). The temperature field at rest is solution of the thermal conduction problem with temperatures at the boundaries,  $T^+$  at the top and  $T^-$  at the bottom, that each equals the melting temperature  $T_m$  at the relevant pressure. Pressure, in the context of planetary interiors, is largely dominated by the hydrostatic part. The melting temperature therefore mainly depends on the vertical coordinate. The possibility of crossing the melting temperature at both the top and bottom of our computational domain requires either a non-linear dependence of  $T_m$  on pressure or, more easily, a compositional difference between the solid and both upper and lower liquid layers (Labrosse, Hernlund, and Coltice 2007). For simplicity here, we do not consider the dynamical effects of compositional variations. The vertical dependence of the melting temperature is linearised around the reference positions of the boundaries, owing to the smallness of their topographies compared to the total thickness of the layer,  $d$ .

The conduction temperature profile that is used as reference writes

$$T_0 = \frac{T^+ + T^-}{2} + \frac{z}{d} (T^+ - T^-), \quad (\text{A.1})$$

the reference for the vertical position  $z$  being at the center of the domain. Deviations from the conduction temperature profiles are made dimensionless using  $\Delta T = T - T^+$  as reference and denoted by  $\theta$ . In the following, superscripts  $^+$  and  $^-$  are used for quantities pertaining to the top and bottom boundaries, respectively, and omitted in equations that apply to both boundaries.

The crossing positions of the conduction solution with the melting temperature at the top and bottom are used as reference around which a topography height,  $h^+$  and  $h^-$ , is defined for each boundary, respectively (fig. A.1). These topographies can have either sign, positive upward, and need not average to 0, as will be shown below. At each phase change interface, two thermal boundary conditions are necessary to account for the moving boundary (Crank 1984). The temperature must equal the phase change temperature and the heat flux discontinuity across the interface must balance the release or consumption of latent heat,  $L$  (Stefan condition). The two thermal boundary conditions write

$$T(h) = T_m(h), \quad (\text{A.2})$$

$$\rho_s L v_\phi = \llbracket q \rrbracket, \quad (\text{A.3})$$

with  $v_\phi$  the freezing rate,  $\rho_s$  the density of the solid and  $\llbracket q \rrbracket$  the heat flux difference between the liquid and the solid sides. These boundary conditions apply to the deformed interface and need to be projected to the reference level that is used as boundary for the computation domain. Developing equation (A.2) to first order in  $h$  gives

$$T\left(\pm\frac{d}{2}\right) = T^\pm + \left(\frac{\partial T_m^\pm}{\partial z} - \frac{\partial T_0}{\partial z}\right) h^\pm. \quad (\text{A.4})$$

In dimensionless form, equation (A.4) writes

$$\theta\left(\pm\frac{1}{2}\right) = \left(1 + \frac{d}{\Delta T} \frac{\partial T_m^\pm}{\partial z}\right) \frac{h^\pm}{d}. \quad (\text{A.5})$$

In the following, we assume  $h^\pm/d$  to be small and we apply

$$\theta = 0, \quad z = \pm\frac{1}{2}. \quad (\text{A.6})$$

Turning to the second thermal boundary condition, the discontinuity of heat flow on the right-hand-side of equation (A.3) is assumed to be dominated by the convective heat flow on the low viscosity liquid side,  $f \sim \rho_l c_{pl} u_l \delta T_l$ , with  $\rho_l$  and  $c_{pl}$  the density and heat capacity of the liquid,  $u_l$  the characteristic liquid velocity and  $\delta T_l$  the temperature difference between the boundary and the bulk of the liquid. This difference results from variations of the topography (fig. A.1) and the vertical gradient of the melting temperature so that

$$f \sim -\rho_l c_{pl} u_l \left| \frac{\partial T_m}{\partial z} \right| h. \quad (\text{A.7})$$

The temperature difference  $h\partial T_m/\partial z$  is negligible on the solid side, but crucial for the convective heat flux on the liquid side. Fig. A.1 shows as dashed lines the typical local temperature profiles on the liquid side of each boundary for topography highs and lows, indicating that the implied lateral variations of heat flux density should lead to melting of regions where the solid protrudes in the liquid and freezing in depressed regions, tending toward erosion of the topography. This behaviour is ensured by the anti-correlation of  $f$  and  $h$  in equation (A.7), independently of the sign of  $\frac{\partial T_m}{\partial z}$ , and this applies to both top and bottom boundaries. The case of  $\frac{\partial T_m}{\partial z} < 0$  depicted here for the top boundary is the most usual and the opposite

case depicted here for the bottom boundary is encountered for water. Note, however, that in the context of planetary applications, the temperature considered here in the liquid layers and depicted on fig. A.1 is in fact the deviation from the reference isentropic temperature profile (Deguen, Alboussière, et al. 2013; Jeffreys 1930) and the pressure derivative of the actual melting temperature needs not be negative for having a liquid underlying the solid layer. Assuming that the convective heat flow on the liquid side dominates the right hand side of equation (A.3), we write

$$\rho_s L v_\phi \sim -\rho_l c_{pl} u_l \left| \frac{\partial T_m}{\partial z} \right| h. \quad (\text{A.8})$$

The freezing rate is related to the vertical velocity  $w$  across the boundary and the rate of change of the topography as

$$v_\phi^\pm = \pm \frac{\partial h^\pm}{\partial t} \mp w. \quad (\text{A.9})$$

Combining with equation (A.8) gives

$$w \mp \frac{\partial h}{\partial t} = \frac{\rho_l c_{pl} u_l}{\rho_s L} \left| \frac{\partial T_m}{\partial z} \right| h \equiv \frac{h}{\tau_\phi}, \quad (\text{A.10})$$

with

$$\tau_\phi = \frac{\rho_s L}{\rho_l c_{pl} u_l \left| \frac{\partial T_m}{\partial z} \right|} \quad (\text{A.11})$$

the characteristic phase change timescale for changing the topography by transferring latent heat from regions where it is released to places where it is consumed.  $u_l$  depends on the dynamics of the liquid which is not solved in this paper. The uncertainty in this quantity as well as the scaling coefficients implied by the  $\sim$  sign in equations (A.7) and (A.8) are all combined to make  $\tau_\phi$  the control parameter in our study.

Across the boundaries, the total traction must be continuous. Assuming that the topography is small (i.e. the horizontal gradient of  $h^\pm$  is small compared to 1,  $|\nabla_h h^\pm| \ll 1$ ), this writes for the vertical component

$$-P_s(h^\pm) + 2\eta \frac{\partial w}{\partial z} = -P_l(h^\pm) \quad (\text{A.12})$$

where  $P$  is total pressure,  $s$  and  $l$  are for the solid and liquid sides, respectively, and  $\eta$  is the dynamic viscosity of the solid. The total pressure on the solid and liquid sides is split into its hydrostatic part,  $P(0) - \rho_{s,l} g h^\pm$  ( $z = 0$  being the reference for  $h$  at each boundary) and the dynamic part  $p$ . On the liquid side, viscous stress and pressure fluctuations are neglected. With these assumptions, we get

$$-p + (\rho_s - \rho_l^\pm) g h^\pm + 2\eta \frac{\partial w}{\partial z} = 0. \quad (\text{A.13})$$

Note that the density difference across the phase change boundary,  $\Delta\rho^\pm = \rho_s - \rho_l^\pm$ , takes different signs at the top and bottom since the solid must be denser than the overlying liquid but less dense than the underlying one. Therefore  $\Delta\rho^+ > 0$  and  $\Delta\rho^- < 0$ .

The topography at each boundary is produced as a result of total stress in the solid, with a typical timescale  $\tau_\eta = \eta/|\Delta\rho^\pm|gd$  (the post-glacial rebound timescale, Turcotte and Schubert 2002), and erased by melting and freezing, as discussed above, with a timescale  $\tau_\phi$ . Both timescales are generally much shorter than the timescale for convection in the whole domain, so that we assume that the topography adjusts instantaneously to the competition between viscous stress and phase change. Therefore, we neglect  $\frac{\partial h}{\partial t}$  in equation (A.10) and combining it with equation (A.13) to eliminate  $h^\pm$ , we get

$$-p + \Delta\rho^\pm g\tau_\phi^\pm w + 2\eta\frac{\partial w}{\partial z} = 0. \quad (\text{A.14})$$

Introducing the phase change dimensionless number (Deguen 2013; Deguen, Alboussière, et al. 2013)

$$\Phi^\pm = \frac{\tau_{\phi^\pm}|\Delta\rho^\pm|gd}{\eta} \quad (\text{A.15})$$

equation (A.14) takes the dimensionless form

$$\pm\Phi^\pm w + 2\frac{\partial w}{\partial z} - p = 0, \quad z = \pm\frac{1}{2}. \quad (\text{A.16})$$

$\Phi^\pm$  is the ratio of the phase change timescale to the viscous deformation time scale. For large values of this parameter, the boundary condition (A.16) reduces to the usual non-penetration condition,  $w = 0$ , while for small values it allows a non zero mass flow through the boundary. The physical interpretation is straightforward: if  $\tau_\eta \ll \tau_{\phi^\pm}$ , topography evolves without the possibility of the phase change to happen and is limited by its own weight that has to be supported by viscous stress in the solid. In practice, this means that the flow velocity goes to zero at the free interface and is very small at the reference boundaries  $z = \pm 1/2$ , which is usually modeled as a non-penetrating boundary. In the other limiting case,  $\tau_\eta \gg \tau_{\phi^\pm}$ , topography is removed by phase change as fast as it is created by viscous stresses and this allows a flow across the boundary.

The liquid is assumed inviscid and therefore exerts no shear stress on the convecting solid. The topography of the boundary is assumed to be small and we approximate the horizontal component of the continuity condition for traction by a free-slip boundary condition at both horizontal boundaries,

$$\frac{\partial u}{\partial z} + \frac{\partial w}{\partial x} = 0, \quad z = \pm\frac{1}{2}. \quad (\text{A.17})$$

The dimensionless equations for the conservation of momentum, mass and energy are written in the classical Boussinesq approximation as

$$\frac{1}{Pr} \left( \frac{\partial \mathbf{v}}{\partial t} + \mathbf{v} \cdot \nabla \mathbf{v} \right) = -\nabla p + \nabla^2 \mathbf{v} + Ra\theta \hat{\mathbf{z}}, \quad (\text{A.18})$$

$$\nabla \cdot \mathbf{v} = 0, \quad (\text{A.19})$$

$$\frac{\partial \theta}{\partial t} + \mathbf{v} \cdot \nabla \theta = w + \nabla^2 \theta, \quad (\text{A.20})$$

where  $Pr = \nu/\kappa$  is the Prandtl number, with  $\nu$  and  $\kappa$  the momentum and thermal diffusivities,  $\mathbf{v} = (u, v, w)$  is the fluid velocity,  $p$  is the dynamic pressure,  $Ra =$

$\alpha\Delta Tgd^3/\kappa\nu$  is the Rayleigh number, with  $\alpha$  the thermal expansion coefficient, and  $\hat{z}$  is the upward vertical unit vector. These equations have been made dimensionless using the thickness of the layer  $d$  as length scale and the thermal diffusion time  $d^2/\kappa$  as timescale.

Since we are concerned here with convection in solid, albeit creeping, layers, we will generally consider the Prandtl number to be infinite in most of the calculations below.

## A.4 The translation mode

The boundary condition (A.16) discussed in the previous section permits a non-zero vertical velocity across the boundaries. If both boundaries are semi-permeable (finite values of both  $\Phi^+$  and  $\Phi^-$ ), the possibility of a uniform vertical translation arises. This situation has been explored systematically in the context of the dynamics of Earth's inner core (Alboussière et al. 2010; Deguen, Alboussière, et al. 2013; Mizzon and Monnereau 2013) and in spherical shells (Deguen 2013) but, in the case of a spherical geometry, the horizontally average vertical velocity is still null for a translation mode. Here we show that a translation mode with a uniform vertical velocity also exists in the case of a plane layer.

We search for a solution that is independent from the horizontal direction and therefore only has a vertical velocity,  $\mathbf{v} = w\hat{z}$ . The mass conservation equation (A.19) implies that  $w$  is independent of  $z$  and we consider two situations, the linear stability problem for which  $w = We^{\sigma t}$  and the steady state case for which  $w$  is constant. Similarly, we can write the temperature as  $\theta(z, t) = \Theta(z)e^{\sigma t}$  to study the onset of convection in that mode, and  $\theta$  as a function of  $z$  only at steady state and similar convention for pressure as  $p$  and  $P$ .

### A.4.1 Linear stability analysis

The conservation equations (A.18)- (A.20) linearized around the hydrostatic state reduce to two equations

$$\frac{\sigma}{Pr}W = -DP + Ra\Theta, \quad (\text{A.21})$$

$$\sigma\Theta = W + D^2\Theta, \quad (\text{A.22})$$

with  $D \equiv \frac{d}{dz}$ . For neutral stability,  $\sigma = 0$ , solving in turn equation (A.22) for  $\Theta$  and equation (A.21) for  $P$  subject to the boundary conditions (A.6) and (A.16) lead to

$$[Ra - 12(\Phi^+ + \Phi^-)]W = 0.$$

A non-trivial solution for  $W$  can then exist for

$$Ra = Ra_c = 12(\Phi^+ + \Phi^-), \quad (\text{A.23})$$

which is the condition for marginal stability of the translation mode.

This system of equations can also be solved for a finite value of  $\sigma$  in order to relate it to  $Ra$ . Equation (A.22) subject to boundary conditions  $\theta(\pm 1/2) = 0$  gives

$$\Theta = \frac{W}{\sigma} \left[ 1 - 2 \frac{\sinh(\sigma^{1/2}/2)}{\sinh(\sigma^{1/2})} \cosh(\sigma^{1/2}z) \right] \quad (\text{A.24})$$

Inserting this expression in Eq. (A.21) and solving for  $P$ , we obtain

$$P = cst + \left( \frac{Ra}{\sigma} - \frac{\sigma}{Pr} \right) Wz - 2Ra W \sigma^{-3/2} \frac{\sinh(\sigma^{1/2}/2)}{\sinh(\sigma^{1/2})} \sinh(\sigma^{1/2}z). \quad (\text{A.25})$$

Using the boundary condition (A.16) at  $z = 1/2$  allows to determine the integration constant, which gives

$$P = \Phi^+ W + \left( \frac{Ra}{\sigma} - \frac{\sigma}{Pr} \right) W(z - 1/2) - 2Ra W \sigma^{-3/2} \frac{\sinh(\sigma^{1/2}/2)}{\sinh(\sigma^{1/2})} [\sinh(\sigma^{1/2}z) - \sinh(\sigma^{1/2}/2)]. \quad (\text{A.26})$$

Finally, using the boundary condition at  $z = -1/2$ ,  $-\phi^- W = P(-1/2)$ , gives, after rearranging, the following dispersion equation:

$$0 = \frac{\sigma^2}{Pr(\Phi^+ + \Phi^-)} + \sigma + \frac{Ra}{\Phi^+ + \Phi^-} \left[ 2\sigma^{-1/2} \frac{\cosh \sigma^{1/2} - 1}{\sinh \sigma^{1/2}} - 1 \right]. \quad (\text{A.27})$$

An approximate solution for small  $\sigma$  can be obtained by developing the ratio of cosh and sinh functions to the second order in  $\sigma$ , which gives

$$\sigma = \frac{10}{1 + \frac{120}{Pr Ra}} \left( 1 - \frac{12(\Phi^+ + \Phi^-)}{Ra} \right). \quad (\text{A.28})$$

The critical Rayleigh number, obtained by setting  $\sigma = 0$ , is the same as that of Eq. (A.23). If  $Gr_T \equiv Pr Ra$  (similar to the Grashof number but with  $\kappa$  in place of  $\nu$ ) is large, the expression for the growth rate reduces to

$$\sigma = 10 \left( 1 - \frac{12(\Phi^+ + \Phi^-)}{Ra} \right). \quad (\text{A.29})$$

In the limit of a large  $\sigma$ ,

$$2\sigma^{-1/2} \frac{\cosh \sigma^{1/2} - 1}{\sinh \sigma^{1/2}} - 1 \rightarrow -1 \quad (\text{A.30})$$

and the dispersion relation reduces to

$$0 = \frac{\sigma^2}{Gr_T} + \frac{\Phi^+ + \Phi^-}{Ra} \sigma - 1. \quad (\text{A.31})$$

The positive root is

$$\sigma = \frac{\Phi^+ + \Phi^-}{Ra} \frac{Gr_T}{2} \left[ \sqrt{1 + \frac{4}{Gr_T} \left( \frac{Ra}{\Phi^+ + \Phi^-} \right)^2} - 1 \right] \quad (\text{A.32})$$

which reduces to

$$\sigma = \frac{Ra}{\Phi^+ + \Phi^-} \quad (\text{A.33})$$

in the limit of  $\frac{1}{Gr_T} \left( \frac{Ra}{\Phi^+ + \Phi^-} \right)^2 \ll 1$ . The growth rate in the large  $Gr_T$  limit is plotted as function of  $Ra/Ra_c$  on figure A.2.

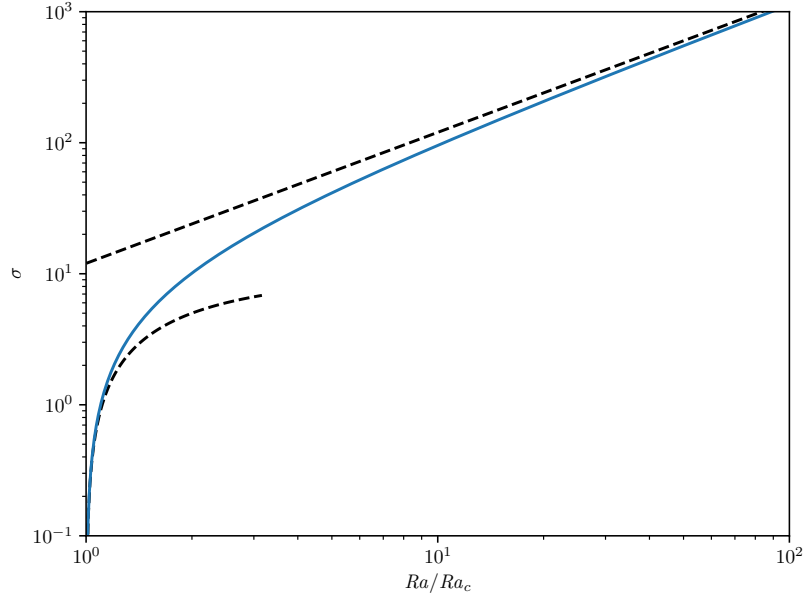


Figure A.2: Instability growth rate  $\sigma$  as a function of  $Ra/Ra_c$ , for infinite  $Gr_T$ , as given by the numerical solution of the full dispersion relation (solid blue line), and by the small and large  $\sigma$  approximations (black dashed lines).

#### A.4.2 Steady state translation

The steady state finite amplitude translation mode is solution of

$$0 = -Dp + Ra\theta, \quad (\text{A.34})$$

$$wD\theta = w + D^2\theta. \quad (\text{A.35})$$

Solving first the energy balance equation (A.35) subject to boundary conditions (A.6) gives

$$\theta = z + \frac{\cosh\left(\frac{w}{2}\right) - e^{wz}}{2 \sinh\left(\frac{w}{2}\right)} \Rightarrow T = \frac{1}{2} + \frac{\cosh\left(\frac{w}{2}\right) - e^{wz}}{2 \sinh\left(\frac{w}{2}\right)}. \quad (\text{A.36})$$

Using the momentum balance equation (A.34) and the boundary conditions (A.16) then gives

$$(\Phi^+ + \Phi^-) w = Ra \left[ \frac{\cosh\left(\frac{w}{2}\right)}{2 \sinh\left(\frac{w}{2}\right)} - \frac{1}{w} \right]. \quad (\text{A.37})$$

This transcendental equation relates the translation velocity  $w$  to the Rayleigh number.

Close to onset, assuming the Péclet number,  $|w|$ , to be small, equation (A.37) can be developed as function of  $(Ra - Ra_c)/Ra_c$  to give to leading order

$$w = \pm 2 \sqrt{15 \frac{Ra - Ra_c}{Ra_c}}. \quad (\text{A.38})$$

The corresponding temperature anomaly is

$$\theta = \frac{w}{8} (1 - 4z^2) + O(w^2), \quad (\text{A.39})$$

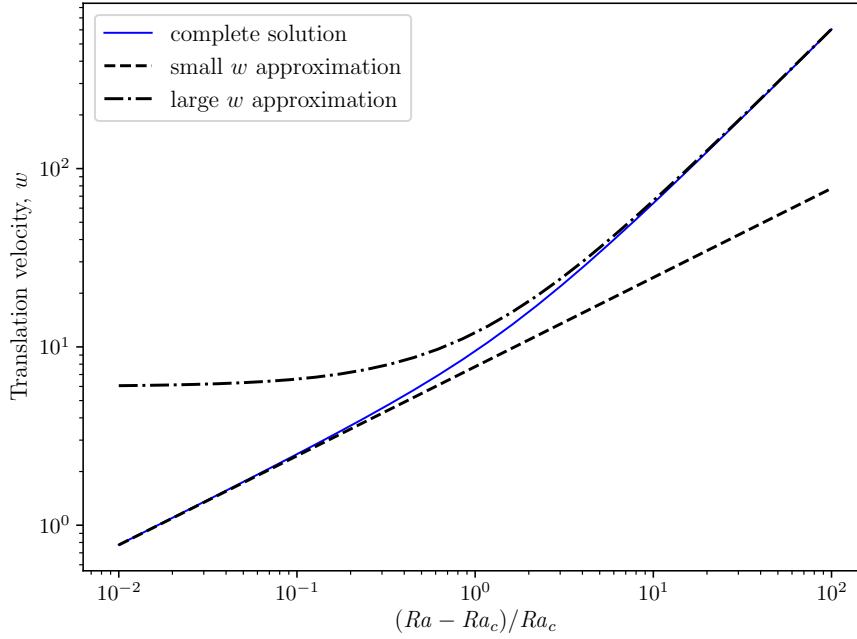


Figure A.3: Finite amplitude velocity in the translation mode. The dashed line is the small velocity approximation given by eq. (A.38), the dash-dotted line is the large velocity approximation given by eq. (A.40) and the solid line is the solution to the full equation (A.37).

showing that the temperature only differs from the conduction solution by an amount proportional to the Péclet number.

For a large Péclet number,  $|w| \gg 1$ , equation (A.37) reduces to

$$w \sim \pm \frac{Ra}{2(\Phi^+ + \Phi^-)} = \pm \frac{6Ra}{Ra_c}. \quad (\text{A.40})$$

Figure A.3 shows how the translation velocity  $|w|$  depends on Rayleigh number, computed using the full equation (A.37) and either the low or the large velocity development. It shows that the transition between the two regimes happens for  $Ra \sim 2Ra_c$ .

In the high Péclet number regime, the temperature anomaly takes a simple form:

$$\theta \sim z + \text{sgn}(w) \left[ \frac{1}{2} - e^{w(z - \text{sgn}(w)/2)} \right] \Rightarrow T \sim \frac{1}{2} [1 + \text{sgn}(w)] - \text{sgn}(w) e^{w(z - \text{sgn}(w)/2)}. \quad (\text{A.41})$$

The exponential in the last equation is negligible everywhere except close to the upper boundary ( $z = 1/2$ ; resp. lower boundary,  $z = -1/2$ ) when  $w \gg 1$  (resp.  $w \ll -1$ ). Therefore, the temperature is essentially equal to that imposed at the boundary the fluid originates from (0 at the top, 1 at the bottom) and adjusts to that of the opposite side in a boundary layer of thickness  $\delta \sim 1/w$ . In dimensional units,  $\delta$  is simply defined as the thickness that makes the Péclet number around 1:  $Pe = w\delta/\kappa \sim 1$ . Figure A.4 shows the temperature profiles for the upward and downward translation modes computed both with the exact (eq. A.36) and approximate (eq. A.41) expressions, showing that the approximation is quite good.

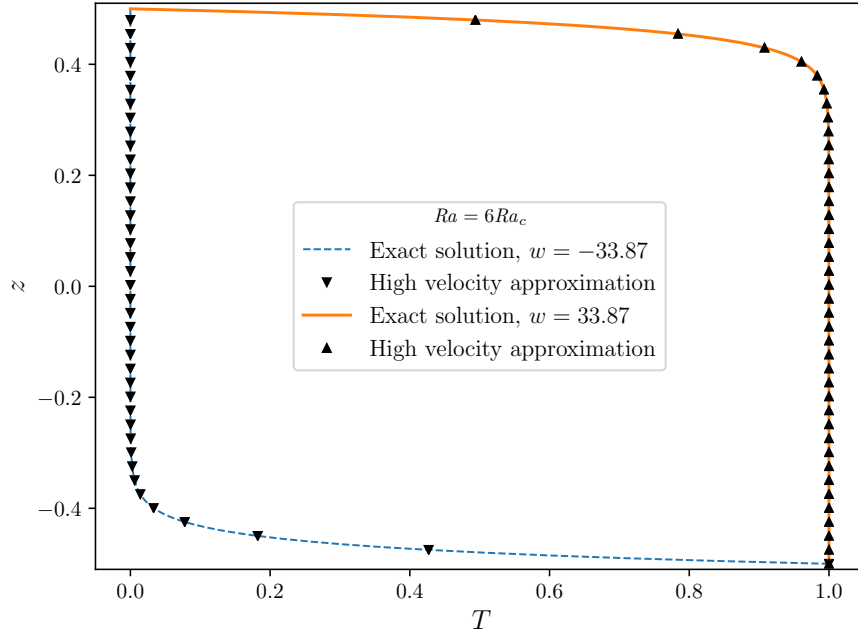


Figure A.4: Temperature profile in the translation mode for  $(Ra - Ra_c)/Ra_c = 5$ . The solid (resp. dashed) line is for the ascending (resp. descending) mode calculated using the full equation (A.36) and the up (resp. down) triangles are obtained using the approximate equation (A.41).

The steady state velocity given by equation (A.40) can also be obtained from a simple physical argument. In the steady translation regime, the (uniform) topography at each boundary is related to the translation velocity and the phase change timescale by

$$h^\pm = \tau_{\phi^\pm} w. \quad (\text{A.42})$$

In steady state, the excess (resp. deficit) weight of the cooler (resp. warmer) solid layer is balanced by the sum of pressure deviations from the hydrostatic equilibrium at both boundaries as

$$\alpha \rho_0 g \frac{\Delta T d}{2} = \Delta \rho^+ g h^+ + \Delta \rho^- g h^-, \quad (\text{A.43})$$

where the temperature in the solid layer has been assumed uniform, i.e. the contribution of the boundary layer to its buoyancy has been neglected. This gives for the translation velocity

$$w = \frac{\alpha \rho_0 g \Delta T d}{2(\Delta \rho^+ g \tau_{\phi^+} + \Delta \rho^- g \tau_{\phi^-})}. \quad (\text{A.44})$$

In dimensionless form, this is exactly equation (A.40).

It is also worth considering the heat transfer efficiency in the translation mode. Equation (A.35) can be integrated to show that  $wT - DT$  is independent of  $z$  and this implies that  $w = DT(-\frac{1}{2}) - DT(\frac{1}{2})$ , meaning that the difference between the conductive heat fluxes across the horizontal boundaries is equal to the advection by translation. Figure A.4 show that the heat flow (Nusselt number  $Nu$ ) should be computed on the exit side, where a boundary layer is produced:

$$Nu = -DT \left( \text{sgn}(w) \frac{1}{2} \right) = |w| - DT \left( -\text{sgn}(w) \frac{1}{2} \right) = |w| + \frac{w e^{-|w|/2}}{2 \sinh(w/2)}. \quad (\text{A.45})$$

The small and large  $|w|$  limit cases give

$$Nu = 1 + \frac{|w|}{2} = 1 + \sqrt{15 \frac{Ra - Ra_c}{Ra_c}}, \quad (\text{A.46})$$

$$Nu = |w| = 6 \frac{Ra}{Ra_c}, \quad (\text{A.47})$$

respectively. The large Rayleigh number behaviour is in striking contrast to the situation encountered for standard Rayleigh-Bénard convection for which  $Nu \sim Ra^\beta$  with  $\beta \sim 1/3$ .

## A.5 Non-translating modes with $\Phi^+ = \Phi^-$

In this section, we consider the situation with values of the phase change parameter of both boundaries equal,  $\Phi \equiv \Phi^+ = \Phi^-$ .

### A.5.1 Linear stability

Non-translating solutions can be obtained using standard approaches for the classical Rayleigh-Bénard problem. For the linear stability problem, a solution using separation of variables is sought, i.e.  $u = U(z)e^{ikx}e^{\sigma t}$  and similarly for  $w$ ,  $p$  and  $\theta$ . Linearized equations (A.18) to (A.20) reduce to

$$ikU + DW = 0, \quad (\text{A.48})$$

$$Pr [-ikP + (D^2 - k^2)U] = \sigma U, \quad (\text{A.49})$$

$$Pr [-DP + (D^2 - k^2)W + Ra\Theta] = \sigma W, \quad (\text{A.50})$$

$$W + (D^2 - k^2)\Theta = \sigma\Theta \quad (\text{A.51})$$

since, at the linear stage, the problem is fully degenerate in terms of orientation of the mode which can be taken as depending only on  $x$ . These equations must be complemented by boundary conditions applying at  $z = \pm \frac{1}{2}$ :

$$DU + ikW = 0, \quad (\text{A.52})$$

$$\pm \Phi^\pm W + 2DW - P = 0, \quad (\text{A.53})$$

$$\Theta = 0. \quad (\text{A.54})$$

This forms a generalized eigenvalue problem that we solve using a Chebyshev-collocation pseudo-spectral approach (e.g. Canuto et al. 1985; Guo et al. 2012). Given the Chebyshev-Gauss-Lobatto nodal point  $z_i = \cos \frac{i\pi}{N}$ ,  $i = 0 \dots N$ , in the interval  $[-1, 1]$ , the values of the  $z$ -dependent mode functions at  $z_i/2$  is noted as  $U_i$  for  $U$  and similarly for other variables. Division by 2 is required here to map the interval on which Chebyshev polynomials are defined onto  $[-\frac{1}{2}, \frac{1}{2}]$ . The  $k^{th}$  derivative of each function at the nodal points is related to the nodal values of the function itself by differentiation matrices:

$$\mathbf{U}^{(k)} = \mathbf{D}^{(k)} \cdot \mathbf{U}. \quad (\text{A.55})$$

The calculation of the differentiation matrices is done using a *python* adaptation<sup>1</sup> of DMSUITE (Weideman and Reddy 2000). With these differentiation matrices,

---

<sup>1</sup>available at <https://github.com/labrosse/dmsuite>



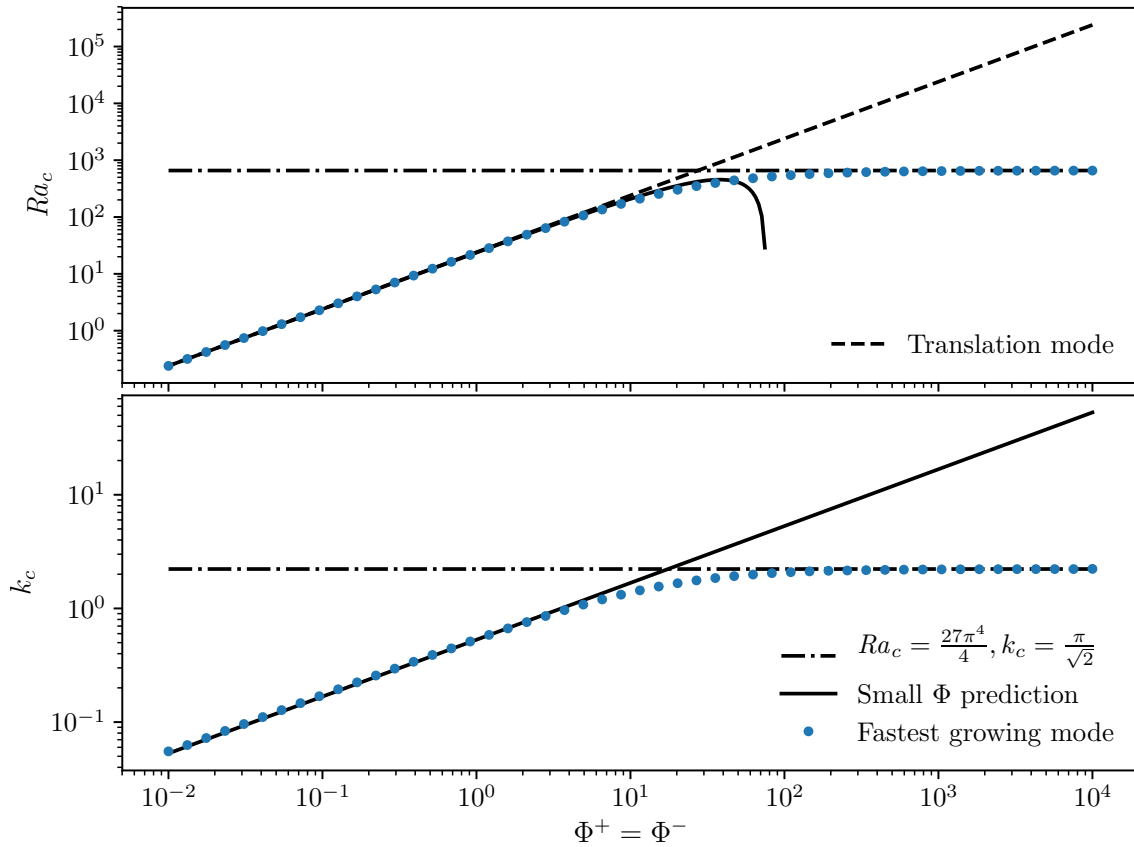


Figure A.5: Critical Rayleigh number (top) and wavenumber (bottom) as function of the phase change numbers, both taken equal here. Filled circles are results of the calculation using the Chebyshev-collocation technique, the dash-dotted lines represent the classical  $\Phi \rightarrow \infty$  limit, the dashed line in the upper panel represents the result for the translating mode (eq. A.23) and the solid lines represent the small  $\Phi$  leading order development.

the symmetry of the problem around  $z = 0$ , we write the temperature as

$$\Theta = \sum_{n=0}^N a_n z^{2n}. \quad (\text{A.58})$$

The Hermitian character of the linear problem (see appendix A.8) ensures that  $\sigma$  is real and, therefore,  $\sigma = 0$  at onset. Then  $W$  and  $U$  can be obtained using equations (A.51) and (A.48). Equations (A.49) and (A.50) then provide two expressions for  $DP$  and their equality implies several equations, one for each polynomial order considered. All the functions are developed to the same order as the temperature,  $2N$ . Note that even if the definition of  $\Theta$  for a given  $N$  only requires  $N + 1$  coefficients  $a_n$ , the development of the other profiles to the same order requires the inclusion of  $a_n$  for values up to  $n = N + 2$  because of the derivatives in the linear system. Using, for example,  $N = 2$  gives a pressure gradient  $DP$  that contains terms in  $z^{2n}$ ,  $n = 0..2$ , and provides therefore three independent equations for the equality between the two expressions. With the symmetry considered here, the boundary conditions (A.52)– (A.54) bring three additional equations for the coefficients  $a_n$ .

Setting first  $\Phi = 0$  leads to a non trivial solution only for  $Ra = 0$  and  $k = 0$ , the solution being equal to the low  $\Phi$  development of the translation solution. To go beyond that, each coefficient  $a_n$  is itself developed as a polynomial of  $\Phi$ :

$$a_n = \sum_{j=0}^J a_{n,j} \Phi^j. \quad (\text{A.59})$$

Similarly, the critical Rayleigh number  $Ra_c$  and the square of the critical wavenumber  $k^2$  are developed in powers of  $\Phi$ :

$$Ra_c = \sum_{j=0}^J r_j \Phi^j, \quad k_c^2 = \sum_{j=0}^J K_j \Phi^j. \quad (\text{A.60})$$

The three boundary conditions and the equations implied by the equality of the two pressure expressions are then written and solved for increasing degrees in the development in  $\Phi$ . In practice, we restrict ourselves to  $N = J = 2$ . At order 0 in  $\Phi$ , the set of linear equations can admit a non-trivial solution only if the determinant of the implied matrix is zero, which provides two possible values of  $r_0$ . The lowest one admits a minimum,  $r_0 = 0$ , for  $K_0 = 0$ . This implies  $a_{2,0} = a_{3,0} = a_{4,0} = 0$  and  $a_{1,0} = -4a_{0,0}$ . At order 1 in  $\Phi$ , we get directly that  $a_{2,1} = a_{3,1} = a_{4,1} = 0$ ,  $a_{1,1} = -4a_{0,1}$  and  $r_1 = 24$  with no information on  $K_1$ . This is however obtained at the next order where we find that  $K_1 = 9/32$  minimizes  $r_2$ , which is then  $r_2 = -81/256$ . The order 2 coefficients are also obtained as a function of  $a_{0,0}$ , which is the value of the maximum of  $\Theta$ . These can then be used to determine the shape of the different

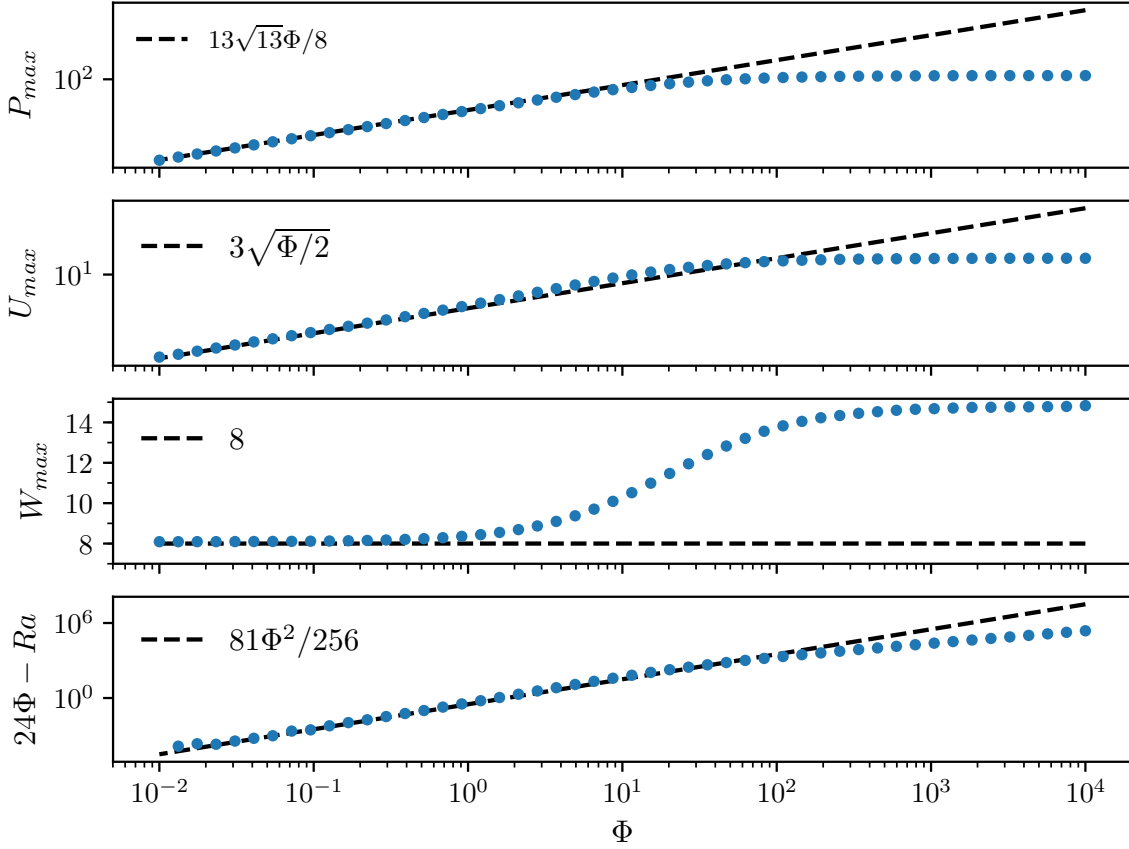


Figure A.6: Variation of the maxima of profiles of  $P$ ,  $U$  and  $W$  of the first unstable mode, that for  $\Theta$  being set to 1, as a function of  $\Phi$ . The bottom panel shows the difference between  $24\Phi$  and the critical Rayleigh number. On each plot, the solid circles are the results of the calculation using the Chebyshev-collocation method while the dashed lines are the low  $\Phi$  predictions of equations (A.62) to (A.66).

function  $\Theta$ ,  $W$ ,  $U$  and  $P$  for small values of  $\Phi$ . To leading order in  $\Phi$  we get

$$k_c = \frac{3}{4\sqrt{2}}\sqrt{\Phi} \quad (\text{A.61})$$

$$Ra_c = 24\Phi - \frac{81}{256}\Phi^2, \quad (\text{A.62})$$

$$\Theta = (1 - 4z^2)\Theta_{max}, \quad (\text{A.63})$$

$$W = 8\Theta_{max}, \quad (\text{A.64})$$

$$U = -3i\sqrt{2\Phi}z\Theta_{max}, \quad (\text{A.65})$$

$$P = \frac{z}{2}(39 - 64z^2)\Phi\Theta_{max}. \quad (\text{A.66})$$

$\Theta_{max} = a_{0,0}$  is used to normalise all profiles. Note that the shape of the temperature (eq. A.63) and vertical velocity (eq. A.64) profiles are of order 0 in  $\Phi$  and are equal to their counterpart in the steady-state translation solution (eq. A.39). The small  $\Phi$  development of the solution to the linear problem can be compared to the results obtained using the Chebyshev-collocation method for cross-validation. The match between the mode profiles is very good for  $\Phi \leq 0.1$ . Figure A.5 shows the variation of  $Ra_c$  and  $k_c$  as function of  $\Phi$  as computed by the Chebyshev-collocation approach (in solid symbols) as well as the analytical value classically obtained for

non-penetrating conditions and the small  $\Phi$  expansion. Additionally, figure A.6 shows the variation of the maximum of profiles of  $P$ ,  $U$  and  $W$ , that of  $\Theta$  being set to 1, as well as the difference between the critical Rayleigh number for uniform translation ( $24\Phi$ ) and that for a deforming mode, each as function of  $\Phi$ . It shows the consistency between the calculations using the Chebyshev-collocation approach and the low  $\Phi$  development.

At low  $\Phi$ , the wavelength of the first unstable mode tends to infinity as  $\sim 1/\sqrt{\Phi}$ , which means that deformation of the solid becomes negligible. Accordingly, the viscous stress ceases to be a limiting factor for the flow and  $Ra_c/\Phi$ , which contains no viscosity, tends to a constant value. This ratio,

$$\frac{Ra}{\Phi} = \frac{\rho\alpha\Delta T d^2}{\Delta\rho^\pm \kappa\tau_\phi} \equiv \frac{\Delta\rho_T \tau_\kappa}{\Delta\rho^\pm \tau_\phi}, \quad (\text{A.67})$$

is the ratio of the driving thermal density difference  $\Delta\rho_T$  to that involved in the phase change, times the ratio of the thermal timescale to the phase change one, and can be considered as the effective Rayleigh number in the low  $\Phi$  limit.

Figure A.7 shows the first unstable mode for different values of the phase change parameter. In the case of  $\Phi = 10^5$ , the critical Rayleigh number and wavenumber are very close to that obtained using classical non-penetrating boundary conditions (fig. A.5) and so is the first unstable mode. For  $\Phi = 10$ , the critical Rayleigh number has already decreased significantly ( $Ra_c = 190$ ), the critical wavelength significantly increased ( $\lambda_c = 4.55$ ) and the critical mode displays streamlines that cross both boundaries. For  $\Phi = 10^{-2}$ , the critical Rayleigh number is a bit less than 0.24, the critical wavelength is about 115 and streamlines are essentially vertical. At each horizontal position, this mode of convection has exactly the same shape as the linearly unstable translation mode but it is modulated laterally, with a very long wavelength that increases as  $\sim 1/\sqrt{\Phi}$  when  $\Phi \rightarrow 0$ . The fact that this makes the critical Rayleigh number smaller than that for pure solid-body translation is rather mysterious.

The critical Rayleigh number for the instability for the non-null  $k$  mode is always lower than that for pure translation, as shown by Eq. (A.62) and fig. A.5 and should therefore always be favored. This might be true in an infinite layer but, in practical cases, the horizontal direction is periodic, either in numerical models or in a planetary mantle. In that case, the minimal value of  $k$  that can be attained is  $2\pi/L$  with  $L$  the horizontal periodicity. If the value of  $k$  corresponding to the critical Rayleigh number is smaller than  $2\pi/L$ , the translation mode could still be favored. The study of the stability of the uniformly translating solution with respect to laterally varying modes is a simple extension to the stability of the conduction solution. Considering now that  $(p, \mathbf{v}, \theta)$  are infinitesimal perturbations with respect to the steady translation solution  $(p_t, w_t \hat{\mathbf{z}}, T_t)$ , the only equation to be modified compared to that treated in section A.5.1 at infinite Prandtl number is the temperature equation that now reads

$$(\text{D}^2 - k^2) \Theta - w_t \text{D}\Theta - W \text{D}T_t = \sigma \Theta \quad (\text{A.68})$$

instead of equation (A.51). Using the steady translation solution provided in section A.4.2, this equation can be implemented in the stability calculation to compute the growth rate of a deforming perturbation of wavenumber  $k$  when a steady translation solution is in place for a given Rayleigh number above the critical value for

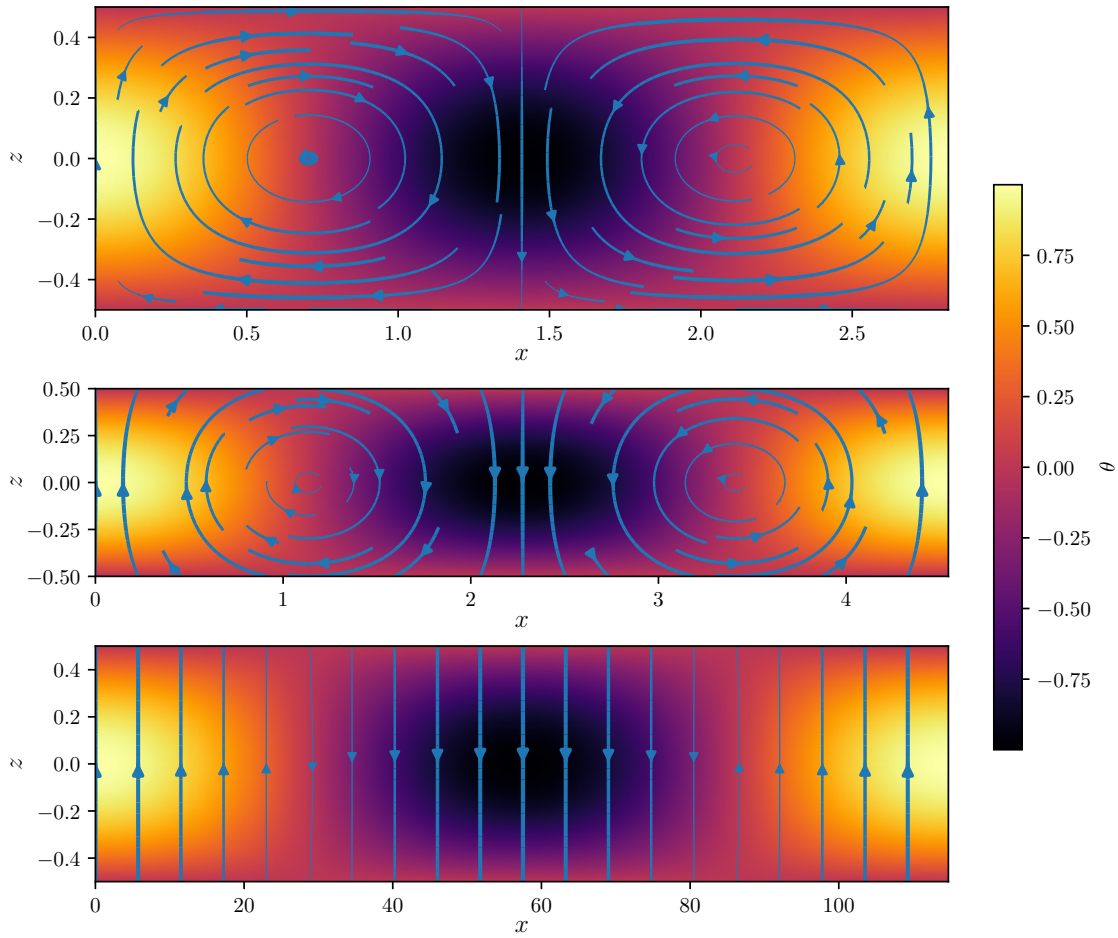


Figure A.7: First unstable mode for three different values of  $\Phi^+ = \Phi^-$ :  $10^5$  (top), 10 (middle) and  $10^{-2}$  (bottom). The color represents temperature and the flow lines thickness is proportional to the norm of the velocity. Note that for the bottom panel the axis are scaled differently owing to the large wavelength of the mode.

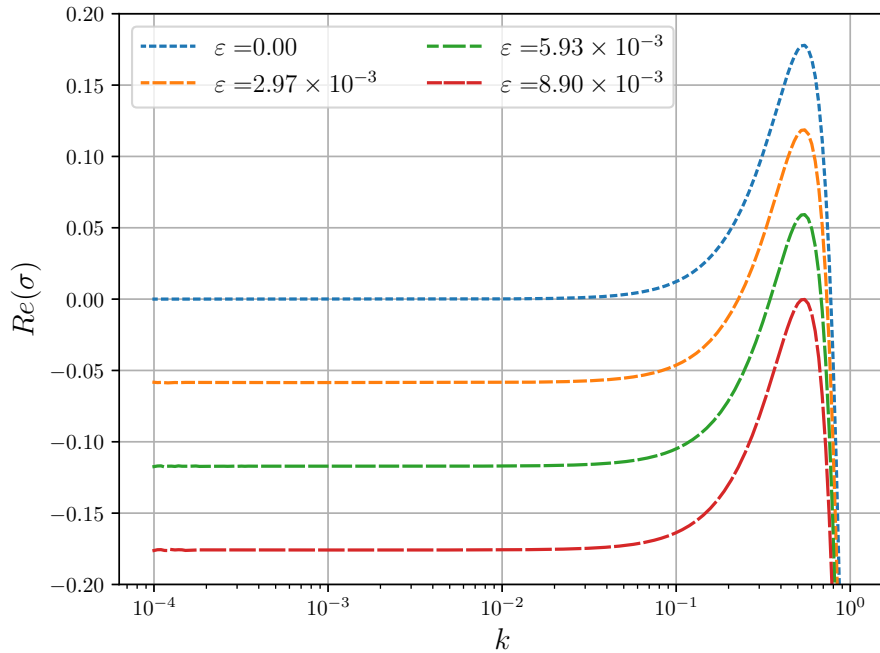


Figure A.8: Growth rate of deforming perturbation over a steady translating solution as function of the perturbation wavenumber  $k$ , for different values of the reduced Rayleigh number  $\varepsilon = (Ra - Ra_c)/Ra_c$  and for  $\Phi^+ = \Phi^- = 1$ .

the translation solution. We denote by  $\varepsilon = (Ra - Ra_c)/Ra_c$  the reduced Rayleigh number,  $Ra_c = 12(\Phi^+ + \Phi^-)$  being here the critical value for the onset of uniform translation. When  $\varepsilon$  tends to zero, the translation velocity  $w_t$  tends to zero and the system of equations tends to that solved for the stability of the steady conduction solution. But since  $\varepsilon = 0$  corresponds to the critical Rayleigh number for the translation solution that is finitely greater than the critical value for the instability with finite  $k$ , we expect a finite instability growth rate in a finite band of wave numbers. We therefore expect an infinitely slow translation solution to be unstable with respect to deforming modes. However, when the Rayleigh number is increased above the critical value for the translation mode, we expect this translation mode with a finite velocity to become more stable since perturbations with a finite  $k$  are then transported away by translation. Figure A.8 indeed shows that, for a given value of the phase change number  $\Phi$  (equal for both boundaries here), increasing the Rayleigh number above the critical value for the translation mode, and therefore the steady state translation velocity, the linear growth rate of the deforming mode decreases. For a given Rayleigh number, the growth rate curve as function of wave number displays a maximum and this maximum decreases with Rayleigh number and eventually becomes negative. There is therefore a maximum Rayleigh number beyond which the translation solution is linearly stable against any deforming perturbation. Figure A.9 shows the range of unstable modes in the  $k - \varepsilon$  space for three different values of the phase change number. The range of Rayleigh numbers above the critical one for translation that allows the finite  $k$  instabilities to develop shrinks when  $\Phi$  decreases and the translation mode becomes increasingly more relevant. Figure A.10 shows that the maximum growth rate of the instability at  $\varepsilon = 0$  varies linearly with  $\Phi$  and so does the maximum value of  $\varepsilon$  for an instability to develop. The wave number for the instability is found to be equal to that

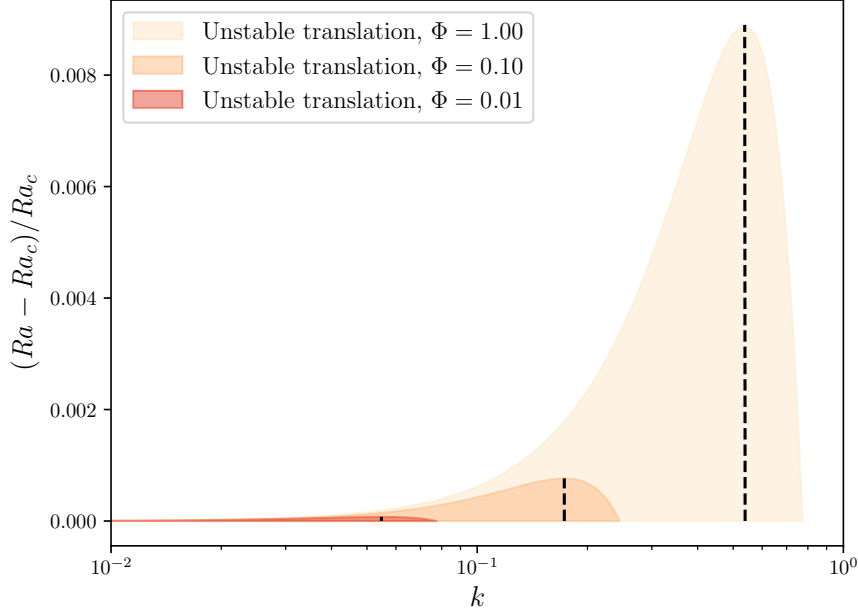


Figure A.9: Range of wave numbers as function of the reduced Rayleigh number for which the translation solution is unstable versus deforming modes. Three different shaded regions for three different values of  $\Phi$  are represented. For each shaded area, the dashed line represents the values of the wave number giving the maximum growth rate as function of the reduced Rayleigh number.

for the instability of the conductive solution (fig. A.9) and therefore varies as  $\sqrt{\Phi}$  (fig. A.5).

### A.5.2 Weakly non-linear analysis

Going beyond the linear stability is necessary to assess the behaviour of the system at Rayleigh numbers larger than the critical value, in particular to investigate the heat transfer efficiency of the convective system. We here follow the approach classically developed for weakly nonlinear dynamics (Malkus and Veronis 1958; Manneville 2004; Schlüter et al. 1965). The system of partial differential equations (A.18)- (A.20) is separated into its linear and nonlinear parts as

$$\mathbf{L}(\partial_t, \partial_x, \partial_z, Ra)\mathbf{X} = \mathbf{N}(\mathbf{X}, \mathbf{X}), \quad (\text{A.69})$$

with  $\mathbf{X} = (p; u; w; \theta)^T$  and for an infinite Prandtl case

$$\mathbf{L} = \begin{pmatrix} 0 & \partial_x & \partial_z & 0 \\ -\partial_x & \nabla^2 & 0 & 0 \\ -\partial_z & 0 & \nabla^2 & Ra \\ 0 & 0 & 1 & \nabla^2 - \partial_t \end{pmatrix}, \quad \mathbf{N}(\mathbf{X}_l, \mathbf{X}_m) = \begin{bmatrix} 0 \\ 0 \\ 0 \\ u_l \partial_x \theta_m + w_l \partial_z \theta_m \end{bmatrix}. \quad (\text{A.70})$$

The linear operator is further developed around the critical Rayleigh number as

$$\mathbf{L} = \mathbf{L}_c - (Ra - Ra_c)\mathbf{M}. \quad (\text{A.71})$$

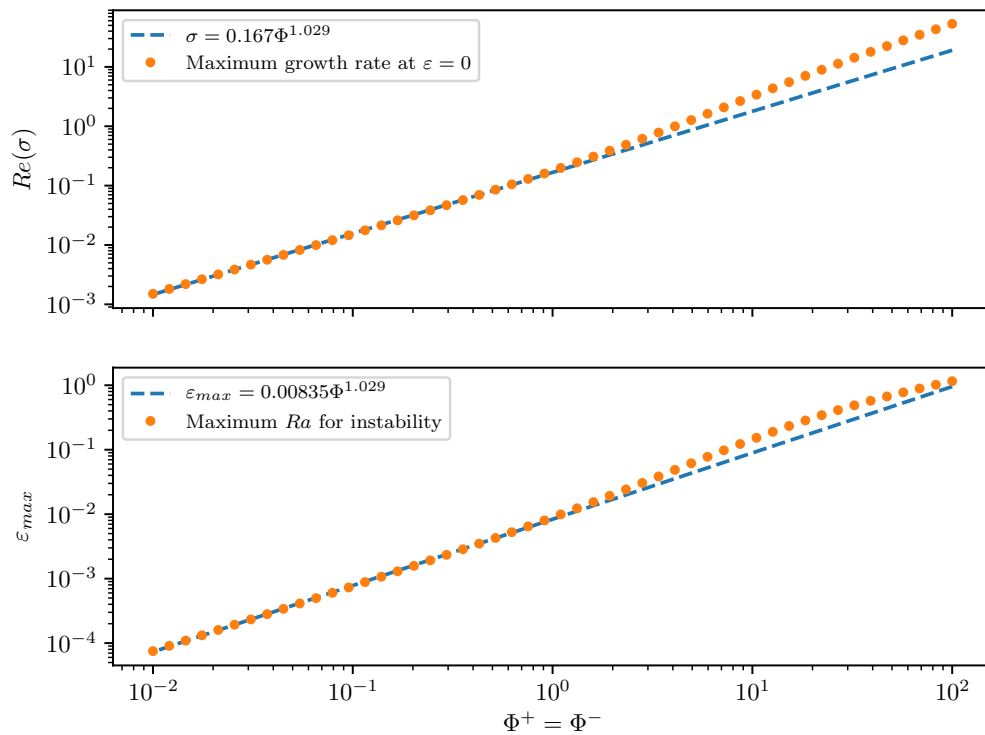


Figure A.10: Maximum growth rate for a non-null  $k$  mode at the critical Rayleigh number for the onset of the translation mode (top) and maximum reduced Rayleigh number for a positive growth rate of a deforming instability over a finite amplitude translation mode (bottom), as function of the phase change number.

By giving  $Ra_c$  as weight to the  $\theta$  part in the dot product  $\langle \bullet | \bullet \rangle$ , it can be shown that the operator  $\mathbf{L}_c$  is self-adjoint (Hermitian),  $\langle \mathbf{X}_2 | \mathbf{L}\mathbf{X}_1 \rangle = \langle \mathbf{L}\mathbf{X}_2 | \mathbf{X}_1 \rangle$  (see appendix for details). Among other things, it implies that all its eigenvalues are real and the marginal state is characterized by  $\partial_t = 0$ . The solution  $\mathbf{X}$  and the Rayleigh number are developed as

$$\mathbf{X} = \epsilon \mathbf{X}_1 + \epsilon^2 \mathbf{X}_2 + \epsilon^3 \mathbf{X}_3 + \dots \quad (\text{A.72})$$

$$Ra = Ra_c + \epsilon Ra_1 + \epsilon^2 Ra_2 + \dots \quad (\text{A.73})$$

and equation (A.69) leads to a set of equations for the increasing order of  $\epsilon$ :

$$\mathbf{L}_c \mathbf{X}_1 = \mathbf{0}, \quad (\text{A.74})$$

$$\mathbf{L}_c \mathbf{X}_2 = \mathbf{N}(\mathbf{X}_1, \mathbf{X}_1) + Ra_1 \mathbf{M}\mathbf{X}_1, \quad (\text{A.75})$$

$$\mathbf{L}_c \mathbf{X}_3 = \mathbf{N}(\mathbf{X}_1, \mathbf{X}_2) + \mathbf{N}(\mathbf{X}_2, \mathbf{X}_1) + Ra_1 \mathbf{M}\mathbf{X}_2 + Ra_2 \mathbf{M}\mathbf{X}_1, \quad (\text{A.76})$$

$$\mathbf{L}_c \mathbf{X}_n = \sum_{l=1}^{n-1} \mathbf{N}(\mathbf{X}_l, \mathbf{X}_{n-l}) + \sum_{l=1}^{n-1} Ra_l \mathbf{M}\mathbf{X}_{n-l}. \quad (\text{A.77})$$

Equation (A.74) is simply that of the linear stability problem and its solution is  $\mathbf{X}_1 = \mathbf{X}_c$  which can be suitably normalised such that the maximum value of  $W$  is 1. Taking the scalar product of equations of subsequent orders by  $\mathbf{X}_1$  and making use of the Hermitian properties of  $\mathbf{L}_c$  provides solvability conditions (Fredholm alternative) that determine the values of  $Ra_i$ . For  $Ra_1$  one gets:

$$Ra_1 = - \frac{\langle \mathbf{X}_1 | \mathbf{N}(\mathbf{X}_1, \mathbf{X}_1) \rangle}{\langle \mathbf{X}_1 | \mathbf{M}\mathbf{X}_1 \rangle}. \quad (\text{A.78})$$

The  $x$  dependence of  $\mathbf{X}_1$  is of the form  $e^{ik_c x}$ , i.e.

$$\mathbf{X}_1 = \mathbf{Z}_{1,1}(z) e^{ik_c x} + c.c., \quad (\text{A.79})$$

with  $\mathbf{Z}_{1,1}(z) = (P_{1,1}(z); U_{1,1}(z); W_{1,1}(z); \Theta_{1,1}(z))^T$  the vector composed of the four vertical modes for all four variables, at degree 1 of weakly non-linear development (first index) and first mode in the horizontal direction (second index).

Then,  $\mathbf{N}(\mathbf{X}_1, \mathbf{X}_1)$  contains two contributions to its  $x$  dependence, one constant and one in  $e^{i2k_c x}$ . It is therefore orthogonal to  $\mathbf{X}_1$  and it can then be concluded that  $Ra_1 = 0$ . The general solution to equation (A.75) is the sum of the solution to the homogeneous equation and a particular solution of the equation with a right-hand-side. Since we are seeking a solution  $\mathbf{X}_2$  which adds to  $\mathbf{X}_1$ , i.e. orthogonal to it, and since  $\mathbf{X}_1$  is the general solution to the homogeneous equation, only the particular solution is of interest. The  $x$  dependence of  $\mathbf{X}_2$  will contain a constant value of the form  $\mathbf{Z}_{2,0}(z)$  and a term of the form  $\mathbf{Z}_{2,2}(z) e^{i2k_c x}$ . Computing the scalar product of equation (A.76) by  $\mathbf{X}_1$  gives the value of  $Ra_2$ :

$$Ra_2 = - \frac{\langle \mathbf{X}_1 | \mathbf{N}(\mathbf{X}_2, \mathbf{X}_1) \rangle + \langle \mathbf{X}_1 | \mathbf{N}(\mathbf{X}_1, \mathbf{X}_2) \rangle}{\langle \mathbf{X}_1 | \mathbf{M}\mathbf{X}_1 \rangle}. \quad (\text{A.80})$$

$\mathbf{X}_2$  containing a term proportional to  $e^{i2k_c x}$  and a term independent of  $x$ ,  $\mathbf{N}(\mathbf{X}_2, \mathbf{X}_1)$  and  $\mathbf{N}(\mathbf{X}_1, \mathbf{X}_2)$  have contributions of the form  $e^{\pm ik_c x}$  which can resonate with  $\mathbf{X}_1$  and make  $Ra_2$  non-null. In that case, the amplitude parameter is, to leading order,

$$\epsilon = \sqrt{\frac{Ra - Ra_c}{Ra_2}}. \quad (\text{A.81})$$

The procedure can be extended to any higher order and the general behaviour can be predicted by recursive reasoning. In particular, it is easy to show that solutions of even and odd order contain contributions to their  $x$  dependence as even and odd powers of  $e^{ik_c x}$  up to their order value, i.e.

$$\mathbf{X}_{2n} = \sum_{l=0}^n \mathbf{Z}_{2n,2l}(z) e^{i2lk_c x} + c.c., \quad (\text{A.82})$$

$$\mathbf{X}_{2n+1} = \sum_{l=0}^n \mathbf{Z}_{2n+1,2l+1}(z) e^{i(2l+1)k_c x} + c.c., \quad (\text{A.83})$$

the vertical normal mode  $\mathbf{Z}_{n,l} = (P_{n,l}(z); U_{n,l}(z); W_{n,l}(z); \Theta_{n,l}(z))^T$  being indexed with the order  $n$  of the solution and harmonic number  $l$  in the  $x$  dependence. It also appears recursively that

$$Ra_{2n} = - \frac{\sum_{l=1}^{2n} \langle \mathbf{X}_1 | \mathbf{N}(\mathbf{X}_l, \mathbf{X}_{2n+1-l}) \rangle + \sum_{l=1}^{n-1} Ra_{2l} \langle \mathbf{X}_1 | \mathbf{M}\mathbf{X}_{2(n-l)+1} \rangle}{\langle \mathbf{X}_1 | \mathbf{M}\mathbf{X}_1 \rangle}, \quad (\text{A.84})$$

$$Ra_{2n+1} = 0. \quad (\text{A.85})$$

This is true for orders 1 and 2, as explained above and, assuming it holds up to degrees  $2n-1$  and  $2n$ , the expressions for degrees  $2n+1$  and  $2n+2$  can be predicted from equation (A.77). First, equation (A.77) of order  $2n+1$  includes on the right-hand-side only terms up to degree  $2n$  and can be used to predict the form of  $\mathbf{X}_{2n+1}$ . Each term of the form  $\mathbf{N}(\mathbf{X}_l, \mathbf{X}_{2n+1-l})$  contains only odd powers of  $e^{ik_c x}$  since it is composed of products of even (resp. odd) and odd (resp. even) polynomials of  $e^{ik_c x}$  for  $l$  even (resp. odd). Each term of the form  $Ra_l \mathbf{M}\mathbf{X}_{2n+1-l}$  is either null for  $l$  odd or an odd polynomial of  $e^{ik_c x}$  for  $l$  even. Summing up, the right-hand-side of the equation being an odd polynomial of  $e^{ik_c x}$ , the solution to the equation is of the form (A.83).

Taking the dot product of equation (A.77) of order  $2n+2$  by  $\mathbf{X}_1$  and using the Hermitian character of  $\mathbf{L}_c$  provides the equation for  $Ra_{2n+1}$ . Starting first with the last term on the right-hand-side, all the terms in the sum except the one in  $Ra_{2n+1}$  drop out either because  $Ra_l$  is null for  $l$  odd or because the dot product  $\langle \mathbf{X}_1 | \mathbf{M}\mathbf{X}_{2n+2-l} \rangle = 0$  for  $l$  even since  $\mathbf{X}_{2n+2-l}$  then contains only even powers of  $e^{ik_c x}$ . We are left with  $Ra_{2n+1} \langle \mathbf{X}_1 | \mathbf{M}\mathbf{X}_1 \rangle$ . Considering the first sum on the right-hand-side, each term  $\mathbf{N}(\mathbf{X}_l, \mathbf{X}_{2n+2-l})$  is an even polynomial of  $e^{ik_c x}$ , as the product of either two even polynomials (for  $l$  even) or two odd polynomials (for  $l$  odd). Therefore, each of these terms is orthogonal to  $\mathbf{X}_1$  and  $Ra_{2n+1} = 0$ . The same equation (A.77) $_{2n+2}$  contains only even powers of  $e^{ik_c x}$  on the right-hand-side and this justifies equation (A.82) for the order  $2n+2$ .

Finally, equation (A.84) $_{2n+2}$  is obtained by simply taking the dot product of equation (A.77) $_{2n+3}$  by  $\mathbf{X}_1$ .

An important diagnostic for convection is the heat transfer efficiency measured by the dimensionless mean heat flux density, the Nusselt number  $Nu$ . Since the temperature is uniform on each horizontal boundary and the average vertical velocity is null for the deforming mode considered here, the advective heat transfer across the horizontal boundaries is null. Therefore, the Nusselt number can easily be computed by taking the vertical derivative of the temperature at either boundary. In the Fourier decomposition used for the non-linear analysis, only the zeroth order term

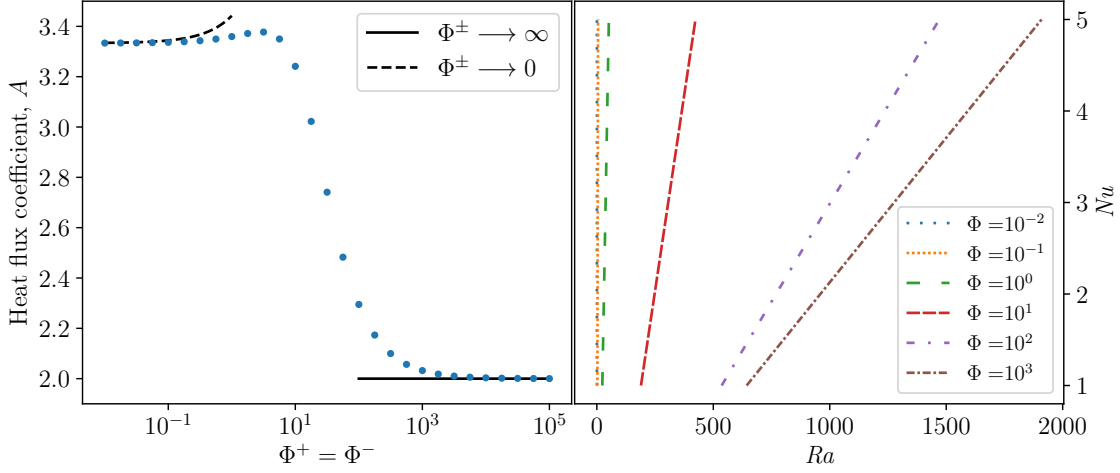


Figure A.11: Heat flux coefficient as a function of the phase change numbers, equal to each other (left), and Nusselt number as a function of Rayleigh number for different values of  $\Phi^\pm$  (right). The solid line gives the limit of two non-penetrating boundaries while the dashed line represents the first order development obtained for  $\Phi \rightarrow 0$  (eq. A.91).

in  $e^{ik_c x}$  contribute to the horizontal average and they only appear in terms that are even in the  $\epsilon$  development. Restricting ourselves here to an order 2 development, the Nusselt number can be computed as

$$Nu = 1 - \epsilon^2 D\theta_{2,0} \left( \frac{1}{2} \right) = 1 - D\theta_{2,0} \left( \frac{1}{2} \right) \frac{Ra_c}{Ra_2} \frac{Ra - Ra_c}{Ra_c} \quad (\text{A.86})$$

where equation (A.81) was used. This equation shows the classical result that the convective heat flow,  $Nu - 1$ , increases linearly with the reduced Rayleigh number  $\varepsilon = (Ra - Ra_c)/Ra_c$  for small values of  $\varepsilon$  and the determination of the coefficient of proportionality,  $A$ , is the main goal of the weakly non-linear analysis presented here. Note that  $\mathbf{N}(\mathbf{X}_2, \mathbf{X}_1)$  and  $\mathbf{N}(\mathbf{X}_1, \mathbf{X}_2)$  only have a non-zero component only along the  $\theta$  space (eq. A.70) so that, because of our definition of the dot product (§ A.8) and using equation (A.80),  $Ra_2$  is proportional to  $Ra_c$ .

The procedure just outlined can be applied to the case with classical boundary conditions. In particular, for free-slip non-penetrating boundary conditions, the problem can be solved analytically (Malkus and Veronis 1958; Manneville 2004). Starting with the vertical velocity in the critical mode as  $w_1 = \sin kx \cos \pi z$ , one gets  $\theta_1 = (\pi^2 + k^2)^{-1} \sin kx \cos \pi z$ ,  $Ra_c = (\pi^2 + k^2)^3 / k^2$ ,  $\theta_2 = (8\pi (\pi^2 + k^2))^{-1} \sin 2\pi z$ ,  $w_2 = 0$  and  $Ra_2 = (\pi^2 + k^2)^2 / 8k^2$ . This gives  $A = -D\theta_{2,0} (1/2) Ra_c / Ra_2 = 2$ .

Similarly, the low  $\Phi$  expansion of the linear mode, equations (A.61)– (A.66), can be used to compute the behaviour of coefficient  $A$  at low  $\Phi$  values. We choose  $\Theta_{max} = 1/16$  to have a normalisation consistent with the one above<sup>2</sup> and the solution

<sup>2</sup>The amplitude of  $\mathbf{X}_1$  is not defined by the linear problem and changing its normalisation, say by multiplying it by a factor  $a$ , leads to  $\mathbf{X}_2$  and  $Ra_2$  multiplied by  $a^2$ , so that by virtue of equation (A.81), the total solution  $\mathbf{X}$  is unchanged.

at order 2 is searched in the form of  $z$  polynomials, and we get, to order 1 in  $\Phi$ ,

$$\theta_2 = -\frac{z}{48} \left( z^2 - \frac{1}{4} \right) \left[ 1 + \left( 1 - \frac{\Phi}{64} \right) \cos 2k_c x \right], \quad (\text{A.87})$$

$$u_2 = -\frac{\sqrt{\Phi}}{192\sqrt{2}} \sin 2k_c x, \quad (\text{A.88})$$

$$w_2 = \frac{z\Phi}{256} \cos 2k_c x, \quad (\text{A.89})$$

$$Ra_2 = \frac{1}{320} - \frac{43\Phi}{430080}. \quad (\text{A.90})$$

The heat flux coefficient is then, to order 1 in  $\Phi$ :

$$A = \frac{4480}{1344 - 43\Phi}. \quad (\text{A.91})$$

Figure A.11 represents the value of the heat flux coefficient  $A$  as function of  $\Phi$  obtained using the Chebyshev-collocation approach described above (solid circles, see appendix A.9 for details on the calculation of non-linear terms) and the two limiting cases of  $\Phi \rightarrow \infty$  (solid line) and  $\Phi \rightarrow 0$  (dashed line), which shows a good match.

The heat flux coefficient  $A$ , which equals 2 for classical non-penetrating boundaries, tends to  $10/3$  when  $\Phi \rightarrow 0$ . This  $\sim 50\%$  increase makes the Nusselt number increase when  $\Phi$  tends to zero but the main effect comes from the decrease of the critical Rayleigh number as  $\sim 24\Phi$ , which makes the slope  $dNu/dRa$  go to infinity as  $\sim 5/36\Phi$ . This is illustrated on figure A.11 which shows the  $Nu - Ra$  relationship derived from this analysis for different values of  $\Phi$ . The heat transfer efficiency is greatly increased by decreasing  $\Phi$  for two reasons. Firstly, it makes the critical Rayleigh number decrease so that convection starts with a lower Rayleigh number. Secondly, the rate at which the Nusselt number increases with  $Ra$  above its critical value is also drastically increased when  $\Phi$  is decreased.

## A.6 Solutions with only one phase change boundary

Let us now consider the case when only one boundary is a liquid-solid phase change, the other one being subject to a non-penetrating condition. With the plane layer geometry considered here, the situation with the upper boundary a phase change is symmetrical to the one with a lower boundary a phase change. The latter is considered here since it applies to the dynamics of the icy shells of some satellites of giant planets (Čadek et al. 2016) and possibly to the Earth mantle for a large part of its history (Labrosse, Hernlund, and Coltice 2007).

The analysis is done in the same way as for the case with a phase change at both boundaries. Figure A.12 shows examples of the first unstable mode for two different values of  $\Phi^-$ . The upper one shows that when  $\Phi^- = 10$ , the convection geometry is not very different from that with a non-penetrating condition (hereafter “the classical situation”) but the streamlines are slightly open at the bottom. The horizontal wavelength at onset,  $\lambda_c = 3.57$ , is larger than the one for the classical situation ( $\lambda_c = 2\sqrt{2}$ ) and the critical Rayleigh number is smaller ( $Ra_c = 352$ ). For

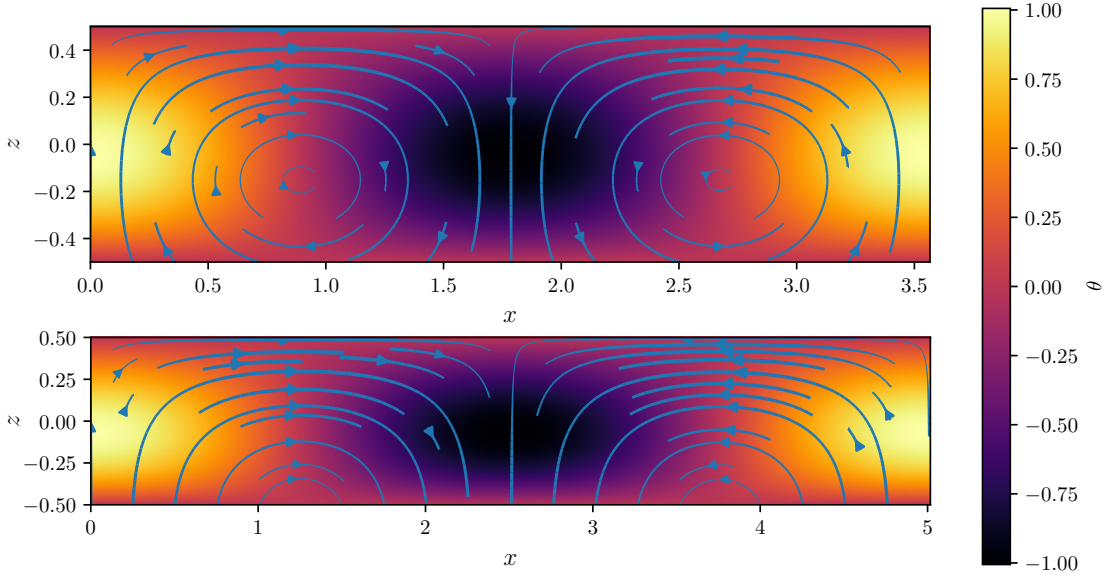


Figure A.12: First unstable mode when only the bottom boundary is a phase change interface, with  $\Phi^- = 10$  (top) and  $\Phi^- = 10^{-2}$  (bottom). The temperature anomaly compared to the conduction solution is represented in colours and streamlines have a thickness proportional to the relative norm of the velocity.

$\Phi^- = 10^{-2}$ , the streamlines are almost normal to the bottom boundary and the wavelength  $\lambda_c = 5$  is about twice the classical one, as if the solution was the upper half of a classical convective domain. However, the boundary condition imposed for temperature at the bottom is different from what would be obtained in that case and the critical Rayleigh number,  $Ra_c = 153$  is about a quarter of the classical one. This can be understood in a heuristic way: The Rayleigh number can be written as

$$Ra = \frac{\tau_\nu \tau_\kappa}{\tau_c^2} = \frac{\alpha \Delta T g d^2}{\nu \kappa}, \quad (\text{A.92})$$

with  $\tau_c$  the convective time scale associated with acceleration due to gravity,  $\tau_\nu$  the viscous time scale and  $\tau_\kappa$  the thermal diffusion time scale. Compared to the classical situation, we have the same imposed temperature gradient, hence the same  $\tau_c$ . Similarly, diffusion happens on the same vertical length scale and we have the same  $\tau_\kappa$ . On the other hand, the bottom boundary imposes no limit to vertical flow and the viscous deformation is distributed on vertical distance twice the thickness of the layer, which increases the effective viscous time scale by a factor 4. Therefore, the Rayleigh number imposed here is equivalent to a value 4 times larger in the classical situation.

Figure A.13 shows the variation of the critical Rayleigh number (top) and wave-number (bottom) as a function of  $\Phi^-$  and one can see that both tend to a finite value when  $\Phi^- \rightarrow 0$ . The mode obtained for  $\Phi^- = 10^{-2}$  is close to that limit. Contrary to the situation with a phase change at both boundaries, the presence of non-penetrating boundary condition implies that some deformation is always needed for convection to occurs, which makes viscosity still be a limiting factor at vanishing values of  $\Phi^-$ .

Considering now the weakly non-linear analysis results, figure A.14 shows that the heat flux coefficient for only one phase change boundary condition tends to a

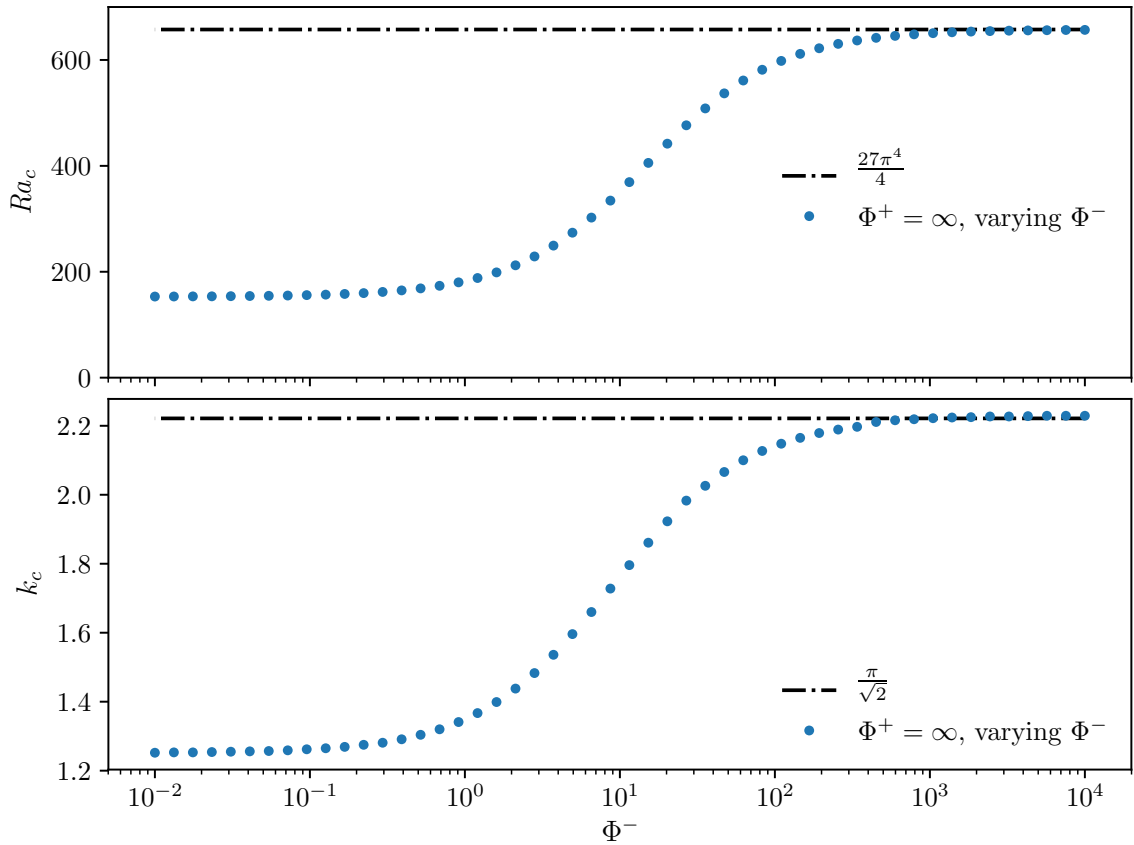


Figure A.13: Critical Rayleigh number (top) and wavenumber (bottom) as function of the phase change number for the bottom boundary  $\Phi^-$ , the top one having a non-penetrating condition. The dash dotted lines represent the classical values obtained for two non-penetrating conditions, for reference.

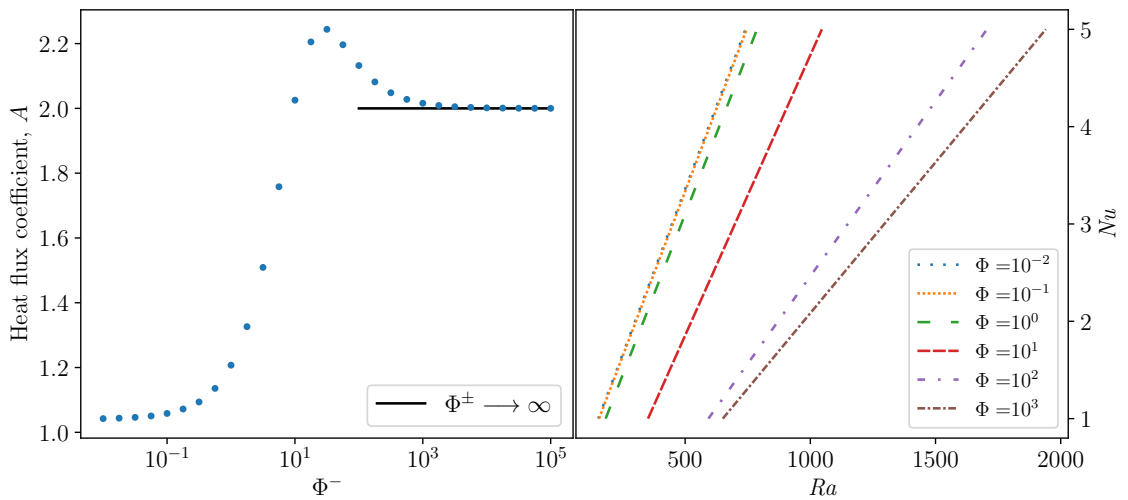


Figure A.14: Heat flux coefficient as a function of the bottom phase change number  $\Phi^-$ , the top boundary being non-penetrative (left), and Nusselt number as a function of Rayleigh number for different values of  $\Phi^-$  (right).

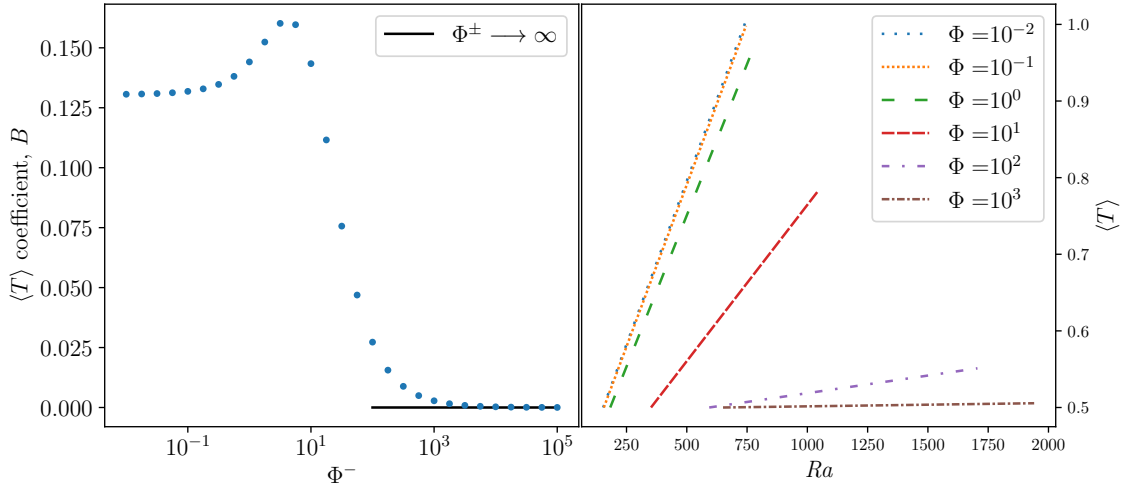


Figure A.15: Mean temperature coefficient ( $B$  defined in equation (A.93)) as function of the bottom phase change parameter  $\Phi^-$  (left) and mean temperature as function of  $Ra$  for different values of  $\Phi^-$  (right). The range of  $Ra$  values explored is the same as that used for figure A.14.

little above 1, that is about half that for the case for both non-penetrative boundaries. Combining that with a critical Rayleigh number that is about four times smaller makes  $dNu/dRa$  about twice that for the classical situation. Therefore, the efficiency of heat transfer is improved compared to the classical case, both because convection starts for a smaller Rayleigh number and because the rate of variation of the Nusselt number with  $Ra$  is about twice larger. This is illustrated on the right panel of figure A.14.

In contrary to the case with both boundaries being a phase change with equal values of  $\Phi$ , the case discussed in this section breaks the symmetry around the  $z = 0$  plane. In particular, this means that the mean temperature in the domain is not equal to the average of both boundaries,  $\langle T \rangle \neq 1/2$  in dimensionless form. As for the Nusselt number (eq. A.86), a contribution from all even orders in  $\epsilon$  is expected, and to the leading order explored here,

$$\langle T \rangle = \frac{1}{2} + \langle \theta_{2,0} \rangle \frac{Ra_c}{Ra_2} \frac{Ra - Ra_c}{Ra_c} \equiv \frac{1}{2} + B \frac{Ra - Ra_c}{Ra_c}. \quad (\text{A.93})$$

The coefficient  $B$  defined above is computed exactly for the case of both non-penetrating boundaries and as expected found to be null. Figure A.15 shows the evolution of this coefficient as function of  $\Phi^-$ . One can see that it tends to a finite positive value when in the limit  $\Phi^- \rightarrow 0$ . Therefore, for small values of  $\Phi^-$ , the average temperature is expected to be larger than  $1/2$  (figure A.15). For the same range of Rayleigh number as explored in figure A.14, figure A.15 also shows the evolution of the mean temperature at the leading order given by equation (A.93). For low values of  $\Phi^-$ , the mean temperature increases rapidly with Rayleigh number.

The asymmetry of the mean temperature for low values of  $\Phi^-$  is also expressed in the finite amplitude solution that can be plotted for a given value of  $\epsilon$ . The range of validity of such solutions as function of  $\epsilon$  depends on the order of the development. Computing the solution only up to order 3 in  $\epsilon$ , we restrict ourselves to small values of this number and figure A.16 shows the result for  $\epsilon = 5.58$  corresponding to

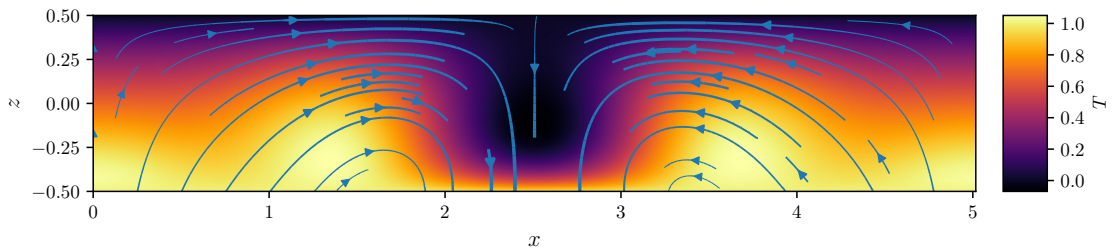


Figure A.16: Finite amplitude solution for  $\Phi^- = 10^{-2}$ ,  $\epsilon = 5.58$  and a non-penetrating boundary condition at the top.

$Nu = 1.5$ . This shows that the down-welling current is more focused than the up-welling one. This situation is similar to the case of volumetrically heated convection (e. g. E. M. Parmentier and Sotin 2000), which is not the case here. Preliminary direct numerical simulations confirm this behaviour but the full exploration of this question goes beyond the scope of the present paper.

## A.7 Conclusion

In the context of the dynamics of planetary mantles, convection can happen in solid shells adjacent to liquid layers. The viscous stress in the solid builds up a topography of the interface between the solid and liquid layers. In the absence of mechanisms to erase topography, its buoyancy equilibrates the viscous stress which effectively enforces a non-penetrating boundary condition. On the other hand, if the topography can be suppressed by melting and freezing at the interface at a faster pace than its building process, the vertical velocity is not required to be null at the interface. The non-penetrating boundary condition is then replaced by a relationship between the normal velocity, its normal gradient, and pressure (eq. A.16) and involving a dimensionless phase change number,  $\Phi$ , ratio of the phase change timescale to the viscous timescale (eq. A.15). When this number is large, we recover the classical non-penetrating condition while the limit of low  $\Phi$  authorises a large flow through the boundary.

When both boundaries are characterised by a low  $\Phi$  number, a translating, non-deforming, mode of convection is possible and competes with a deforming mode with wave number  $k$  that decreases as  $\sqrt{\Phi}$ , and therefore resembles translation with alternating up- and downward direction. The critical Rayleigh number for the onset of the deforming mode is slightly below that of the translation mode,  $Ra = 24\Phi$ , but the latter is found to be stable against a deforming instability when the Rayleigh number is  $\sim \Phi^2$  above the critical value. It is therefore likely to dominate when both boundaries are characterised by low values of  $\Phi$ . In both translating and deforming modes of convection, the heat transfer efficiency, the Nusselt number, is found to increase strongly with Rayleigh number at small values of  $\Phi$ .

When only one boundary is a phase change interface with a low value of  $\Phi$ , the wavenumber is about half and the critical Rayleigh number is about a quarter the corresponding values for the classical non-penetrating boundary condition. Close to onset, a weakly non-linear analysis shows that the Nusselt number varies linearly with the Rayleigh number with a slope that is about twice that for both non-penetrating boundary conditions. The average temperature is also found to increase

strongly with Rayleigh number and the flow geometry is strongly affected, with down-welling currents more focused than up-welling ones.

Overall, having the possibility of melting and freezing across one or both horizontal boundaries of an infinite Prandtl number fluid makes convection much easier (i.e. the critical Rayleigh number is strongly reduced), the preferred horizontal wavelength much larger and heat transfer much stronger, with important potential implications for planetary dynamics.

## Acknowledgments

We are thankful to three anonymous reviewers and editor Grae Worster for comments that pushed us to significantly clarify our paper. This research has been funded by the french Agence Nationale de la Recherche under the grant number ANR-15-CE31-0018-01, MaCoMaOc.

## A.8 A – Self-adjointness of operator $\mathbf{L}_c$

Using a Fourier decomposition for the horizontal decomposition,  $\mathbf{L}_c$  simply reads as

$$\mathbf{L}_c = \begin{pmatrix} 0 & ik & D & 0 \\ -ik & D^2 - k^2 & 0 & 0 \\ -D & 0 & D^2 - k^2 & Ra_c \\ 0 & 0 & 1 & D^2 - k^2 \end{pmatrix} \quad (\text{A.94})$$

where the time derivative has been omitted since the linear instability is found to be stationary. In a linear stability analysis, adding a growth rate  $\sigma$  on the diagonal of the matrix would not alter the adjoint calculation, as will appear below. The boundary conditions are given by equations (A.52) to (A.54). In the calculation of the dot product, the  $\theta$  part is given  $Ra_c$  as weight and the horizontal integral can be factored out:

$$\begin{aligned} \langle \mathbf{X}_2 | \mathbf{L}_c \mathbf{X}_1 \rangle &= \int e^{i(k_2 - k_1)x} dx \left[ \int_{-\frac{1}{2}}^{\frac{1}{2}} \bar{P}_2 (ikU_1 + DW_1) dz \right. \\ &\quad + \int_{-\frac{1}{2}}^{\frac{1}{2}} \bar{U}_2 (-ikP_1 + (D^2 - k^2) U_1) dz \\ &\quad + \int_{-\frac{1}{2}}^{\frac{1}{2}} \bar{W}_2 (-DP_1 + (D^2 - k^2) W_1 + Ra_c \Theta_1) dz \\ &\quad \left. + Ra_c \int_{-\frac{1}{2}}^{\frac{1}{2}} \bar{\Theta}_2 (W_1 + (D^2 - k^2) \Theta_1) dz \right] \end{aligned} \quad (\text{A.95})$$

where the overbar means complex conjugate. Since the  $x$  part poses no difficulty, we only consider the  $z$  part, which we denote as  $\langle \bullet | \bullet \rangle_z$ . Reordering the different integrals in Eq. (A.95) so that terms of  $\mathbf{X}_1$  are factored out and performing integrations by

part on each term including  $D$ , we get

$$\begin{aligned}
 \langle \mathbf{X}_2 | \mathbf{L}_c \mathbf{X}_1 \rangle_z &= \int_{-\frac{1}{2}}^{\frac{1}{2}} (-ik\bar{U}_2 + D\bar{W}_2) P_1 dz \\
 &+ \int_{-\frac{1}{2}}^{\frac{1}{2}} (ik\bar{P}_2 + (D^2 - k^2) \bar{U}_2) U_1 dz \\
 &+ \int_{-\frac{1}{2}}^{\frac{1}{2}} (D\bar{P}_2 + (D^2 - k^2) \bar{W}_1 + Ra_c \bar{\Theta}_2) W_1 dz \\
 &+ Ra_c \int_{-\frac{1}{2}}^{\frac{1}{2}} (\bar{W}_2 + (D^2 - k^2) \bar{\Theta}_2) \Theta_1 dz \\
 &+ [\bar{P}_2 W_1]_{-\frac{1}{2}}^{\frac{1}{2}} + [\bar{U}_2 D U_1]_{-\frac{1}{2}}^{\frac{1}{2}} - [U_1 D \bar{U}_2]_{-\frac{1}{2}}^{\frac{1}{2}} - [\bar{W}_2 P_1]_{-\frac{1}{2}}^{\frac{1}{2}} \\
 &+ [\bar{W}_2 D W_1]_{-\frac{1}{2}}^{\frac{1}{2}} - [W_1 D \bar{W}_2]_{-\frac{1}{2}}^{\frac{1}{2}} + Ra \left( [\bar{\Theta}_2 D \Theta_1]_{-\frac{1}{2}}^{\frac{1}{2}} - [\Theta_1 D \bar{\Theta}_2]_{-\frac{1}{2}}^{\frac{1}{2}} \right)
 \end{aligned} \tag{A.96}$$

The integral part shows that the adjoint linear system is the same as the direct one, with  $\mathbf{L}_c$  as operator. The boundary conditions are the one that allow to suppress all the boundary values in equation (A.96). The boundary conditions (A.52) to (A.54) are applied to  $\mathbf{X}_1$  to remove  $\Theta_1(\pm\frac{1}{2})$  and replace  $DU_1$  and  $P_1$ . In addition, the mass conservation equation applied to  $\mathbf{X}_2$  allows to replace  $DW_2$ . Factorizing  $W_1$ ,  $U_1$  and  $\Theta_1$  gives for the boundary conditions

$$[W_1 (-\bar{P}_2 \pm \Phi^\pm \bar{W}_2 + 2D\bar{W}_2)]_{-\frac{1}{2}}^{\frac{1}{2}} + [U_1 (-ik\bar{W}_2 + D\bar{U}_2)]_{-\frac{1}{2}}^{\frac{1}{2}} - Ra [\bar{\Theta}_2 D \Theta_1]_{-\frac{1}{2}}^{\frac{1}{2}} = 0. \tag{A.97}$$

Since  $W_1$ ,  $U_1$  and  $D\Theta_1$  can take arbitrary values on the boundaries, the differences can only be eliminated in a general manner by setting all their coefficients to 0, which gives the boundary conditions for the adjoint:

$$DU_2 + ikW_2 = 0, \tag{A.98}$$

$$\pm \Phi^\pm W_2 + 2DW_2 - P_2 = 0, \tag{A.99}$$

$$\Theta_2 = 0. \tag{A.100}$$

The adjoint problem is therefore identical to the direct one. Among other implications, all eigenvalues of  $L_c$  must be real, which is consistent with our numerical findings.

## A.9 B – Expression of the non-linear terms

Computation of the non-linear term  $\mathbf{N}(\mathbf{X}_n, \mathbf{X}_m)$  (eq. A.70) is the trickiest part of the procedure explained in section A.5.2 and deserves some details provided here. First of all, it contains only a component, referred to as  $\mathbf{N}(\mathbf{X}_n, \mathbf{X}_m)_\Theta$ . To compute it, one needs first to decompose indices  $n$  and  $m$  as

$$n = 2p + q \text{ with } p = \left\lfloor \frac{n}{2} \right\rfloor, \tag{A.101}$$

$$m = 2r + s \text{ with } r = \left\lfloor \frac{m}{2} \right\rfloor, \tag{A.102}$$

where  $\lfloor \cdot \rfloor$  denotes the floor function. In computing  $\mathbf{N}(\mathbf{X}_n, \mathbf{X}_m)_\Theta$ , one needs to account for the full (i.e. real) expression of  $\mathbf{X}_n$  and  $\mathbf{X}_m$  including the complex conjugate. They write

$$\mathbf{X}_n = \sum_{l_1=0}^p \mathbf{Z}_{n,2l_1+q}(z) e^{i(2l_1+q)kx} + c.c., \quad (\text{A.103})$$

$$\mathbf{X}_m = \sum_{l_2=0}^r \mathbf{Z}_{m,2l_2+s}(z) e^{i(2l_2+s)kx} + c.c.. \quad (\text{A.104})$$

Using eq. (A.70), we get

$$\begin{aligned} \mathbf{N}(\mathbf{X}_n, \mathbf{X}_m)_\Theta = & \sum_{l_1=0}^p \sum_{l_2=0}^q \{ [i(2l_2 + s)kU_{n,2l_1+q}\Theta_{m,2l_2+s} \\ & + W_{n,2l_1+q}D\Theta_{m,2l_2+s}] e^{i[2(l_1+l_2)+q+s]kx} \\ & + [-i(2l_2 + s)kU_{n,2l_1+q}\bar{\Theta}_{m,2l_2+s} \\ & + W_{n,2l_1+q}D\bar{\Theta}_{m,2l_2+s}] e^{i[2(l_1-l_2)+q-s]kx} \} + c.c.. \end{aligned} \quad (\text{A.105})$$

The harmonics of the first term is always positive while that of the second can be negative. Either way, each term has its complex conjugate and we solve only for the positive or null harmonics, the rest of the solution simply being obtained as the conjugate of the computed part.



# Appendix B

## Mantle convection interacting with magma oceans

This chapter is an article written by R. Agrusta, A. Morison, S. Labrosse, R. Deguen, T. Alboussière, P. J. Tackley and F. Dubuffet. It is currently under minor revision after submission to *Geophysical Journal International*. It presents numerical simulations of the thermal problem with constant thickness of the solid in cartesian geometry.

### B.1 Abstract

The presence of a magma ocean may have characterized the beginning of terrestrial planets and, depending on how the solidification has proceeded, the solid mantle may have been in contact with a magma ocean at its upper boundary, its lower boundary, or both, for some period of time. At the interface where the solid is in contact with the liquid the matter can flow through by changing phase, and this affects convection in the solid during magma ocean crystallization. Linear and weakly non linear analyses have shown that Rayleigh-Bénard flow subject to two liquid-solid phase change boundary conditions is characterized by a non-deforming translation or weakly deforming long wavelength mode at relatively low Rayleigh number. Both modes are expected to transfer heat very efficiently, at least in the range of applicability of weakly non-linear results for the deforming mode. When only one boundary is a phase change, the critical Rayleigh number is also reduced, by a factor of about 4, and the heat transfer is also greatly increased. In this study we use direct numerical simulations in two-dimensional Cartesian geometry to explore how the solid convection may be affected by these boundary conditions for values of the Rayleigh number extending beyond the range of validity of the weakly non-linear results, up to  $10^3$  times the critical value. Our results suggest that solid state convection during magma ocean crystallization may have been characterized by a very efficient mass and heat transfer, with a heat flow and velocity at the least twice the value previously thought when only one magma ocean is present, above or below. In the situation with a magma ocean above and below, we show that the convective heat flow through the solid layer could reach values of the same order as that of the black-body radiation at the surface of the magma ocean.

## B.2 Introduction

Partial or even complete melting of the silicate mantle may have occurred early in the history of rocky planets, and depending on the phase diagram involved (e.g. Boukaré, Ricard, et al. 2015; Thomas, Liu, et al. 2012), the solid mantle may have crystallised upwards and/or downwards leading to a solid mantle bounded above and/or below by molten layers, commonly called magma oceans (e.g. Debaille et al. 2007; Elkins-Tanton 2012; Labrosse, Hernlund, and Coltice 2007; Solomatov 2015). Petrological experiments and thermodynamics calculation have shown that chemical composition controls significantly the melting curves of mantle rocks (Andrault, Bolfan-Casanova, Bouhfid, et al. 2017; Boukaré, Ricard, et al. 2015; Thomas and Asimow 2013), and that the location of the first solids within the mantle depends on the slope of their melting curves compared to the isentropic temperature gradient in the magma. The solid crystalizes from the bottom if the isentropic gradient is smaller than the melting temperature gradient (e.g. Thomas and Asimow 2013) and from the top if the adiabatic gradient is larger than the melting one (e.g. Mosenfelder, Asimow, and Ahrens 2007). The comparison between the two slopes must be done locally, at each depth, and the curvature of the two temperature profiles matter. Fiquet et al. (2010) obtained a curved liquidus whereas Andrault, Bolfan-Casanova, Nigro, et al. (2011) obtained a liquidus with a nearly constant slope, for different compositions and using slightly different experimental techniques. The curved liquidus implies that the magma ocean starts crystallising at intermediate depth while the straight liquidus implies a crystallisation from the bottom up (Thomas, Liu, et al. 2012). Moreover, at the lowermost mantle conditions, crystallization may lead to the formation of solids lighter (Fe depleted) than the surrounding melt (Boukaré, Ricard, et al. 2015), and this would favor the formation of a basal magma ocean and eventually sustain the scenario with a solid bounded between two magma oceans (Boukaré, Ricard, et al. 2015; Labrosse, Hernlund, and Coltice 2007). A situation with a basal ocean is also currently encountered in icy satellites like Enceladus, Europa, Titan, where the shallow icy layer is in contact with liquid water ocean and where possibly a high-pressure ice layer underlies the buried ocean (e.g. Baland et al. 2014; Čadek et al. 2016; Grasset et al. 2000; Khurana et al. 1998; Pappalardo et al. 1998; Tobie, Choblet, et al. 2003; Tobie, Lunine, et al. 2006).

Whatever the relative position of the solid compare to the ocean is, the existence of solid-liquid phase change at the boundary of a solid mantle is thought to strongly affect its dynamics (Deguen 2013; Labrosse, Morison, et al. 2018) and this is the subject of the present paper.

Usually, convection models in solid mantles assume a non-penetrating boundary condition at the horizontal boundaries of the solid shell, where the free-surface boundary condition is modeled as a free-slip boundary condition on an undeformed surface. This approximation is valid as long as the dynamic topography generated by convective stresses is small and is affected only slowly by surface processes (Ricard, Labrosse, et al. 2014). This approximation has been used for mantle convection models as it operates in the current Earth and planets (Schubert et al. 2004), but also in the presence of a magma ocean (Ballmer et al. 2017; Maurice et al. 2017). However, at the boundary between the solid and liquid, matter may flow through by changing phase. This requires that the latent heat released in regions of freezing (inflow for the solid) is transferred efficiently to regions where it is consumed for

melting (outflow). Whether this happens depends on how fast latent heat is transferred in the liquid region compared to the rate at which topography is generated by solid viscous flow (Alboussière et al. 2010; Deguen 2013; Deguen, Alboussière, et al. 2013). Indeed, if the heat transfer in the liquid is able to erase the topography formed by viscous deformation, the lithostatic stress due to the topography variation will not balance the viscous stress of the convective solid, and the liquid-solid boundary can be considered as semi-permeable (Deguen 2013; Deguen, Alboussière, et al. 2013). This process, that leads to semi-permeable boundary condition, has been shown to strongly affect the dynamics of the solid and the associated heat transfer leading for example to a translation dynamics in the Earth’s inner core in contact with the liquid outer core (Alboussière et al. 2010; Deguen, Alboussière, et al. 2018; Deguen, Alboussière, et al. 2013; Mizzon and Monnereau 2013; Monnereau, Calvet, et al. 2010), whereas only recently, attention has been paid on its effect on the evolution of the solid mantle (Deguen 2013; Labrosse, Morison, et al. 2018; Morison et al. 2019).

Morison et al. (2019) looked at the effect of semi-permeable solid-liquid phase change boundaries on the development of the first mantle overturn, during magma ocean crystallisation of the silicate mantle of the Earth, Mars, and Moon. They show that solid-liquid phase change boundary conditions make the timescale of the first overturn decrease by several orders of magnitude compared to the case where solid-liquid phase change is not taken into account (Ballmer et al. 2017; Boukaré, E. Parmentier, et al. 2018; Maurice et al. 2017). Moreover, Labrosse, Morison, et al. (2018) performed both linear and weakly non-linear analysis to show that Rayleigh-Bénard flow in a two-dimensional (2D) Cartesian geometry, subjects to one semi-permeable boundary, representing the simplest scenario during solid mantle formation, presents an heat transfer efficiency much higher than the classical values obtained with non-penetrating boundary conditions. Moreover, their study shows that the flow is characterized by a non-deforming translation mode or weakly deforming long-wavelength mode if the flow is allowed at both boundaries of the solid mantle. Both translation and weakly deforming modes are able to transfer heat very efficiently, and may have characterized mantle dynamics during the primordial epochs of Earth or of larger size terrestrial planets.

In this study, using 2D Cartesian numerical simulations, we explore how solid-state Rayleigh-Bénard convection may be affected by the presence of one or two solid-liquid phase change(s) at horizontal boundary(ies). We compare the results of the present finite amplitude calculations to the weakly non-linear results of Labrosse, Morison, et al. (ibid.) and discuss the applicability of the latter to finite amplitude situations at high Rayleigh number, and the likely consequences of these boundaries conditions on the primordial evolution of the Earth or other terrestrial planets.

## B.3 Method

### B.3.1 Governing equations

Solid-state mantle convection is described by the system of conservation equations for mass, momentum and energy for an incompressible fluid with infinite Prandtl number and in the Boussinesq approximation. These equations, rendered dimensionless using the thickness  $H$  of the solid mantle for length, the diffusion time  $H^2/\kappa$

for time, with  $\kappa$  the thermal diffusivity,  $\kappa/H$  for velocity and  $\eta\kappa/H^2$  for pressure, with  $\eta$  the viscosity, are:

$$\nabla \cdot \mathbf{u} = 0, \quad (\text{B.1})$$

$$\nabla^2 \mathbf{u} - \nabla p + \text{Ra}(T - T_c)\mathbf{z} = 0, \quad (\text{B.2})$$

$$\frac{\partial T}{\partial t} + \mathbf{u} \cdot \nabla T = \nabla^2 T, \quad (\text{B.3})$$

with  $\mathbf{u} = (v, w)$  the velocity,  $p$  the dynamic pressure,  $T$  the temperature and  $T_c$  the steady conduction solution,  $t$  the time,  $\mathbf{z}$  the unit vector in the vertical direction and Ra the Rayleigh number:

$$\text{Ra} = \frac{\alpha g \rho_s \Delta T H^3}{\kappa \eta}, \quad (\text{B.4})$$

with  $\alpha$  the thermal expansion coefficient,  $g$  the acceleration of gravity,  $\rho_s$  the density of the solid,  $\Delta T$  the temperature difference between the lower and upper boundaries.

This set of equations neglects many of the complexities of mantle convection: in this first study, we assume a Newtonian rheology with a constant viscosity, we do not consider volumetric heat generation, all physical parameters are assumed uniform and constant and no compositional effect is included. Although we recognise the importance of these complexities to understand mantle dynamics (Schubert et al. 2004), we consider the simplest possible convective system to isolate the effects of the phase change boundary condition.

### B.3.2 Treatment of the solid-liquid phase changes

At the boundary between a solid mantle and a liquid of the same composition, a flow through the phase change can take place. Whether the flow through the phase change takes place or not depends on the latent heat transferred through the liquid region during topography variations due to solid viscous flow (Deguen, Alboussière, et al. 2013). Stresses in the solid lead to the formation of topography of the solid-liquid interface and convective heat transfer in the liquid tends to homogenize temperature and suppress that topography. On the one hand, if the topography is able to build because the heat transfer in the liquid region is slow, the radial velocity at interface is limited by the weight of the topography (classical dynamic topography balance) and the flow across the boundary is effectively inhibited. On the other hand, when heat transfer in the liquid is fast, it can destroy the topography by transporting heat from places where crystallization occurs to places where melting happens, and the flow through the boundary is allowed. To include this process, the solid-liquid phase change is accounted for by considering the variation in the stress field and the associated dynamic pressure at the phase boundary. Details can be found in previous papers (Deguen 2013; Deguen, Alboussière, et al. 2013; Labrosse, Morison, et al. 2018) and the derivation of the boundary condition is only shortly recalled here.

Across the solid-liquid boundary the total stress must be continuous and, if the topography slope and the viscous stress and dynamic pressure in the liquid side are assumed small and can be neglected, the vertical stress equilibrium acting along the undeformed phase boundary is

$$(\rho_s - \rho_l^\pm)gh^\pm + 2\eta \frac{\partial w}{\partial z} - p = 0. \quad (\text{B.5})$$

The first term is the differential stress between the solid and liquid hydrostatic pressures, with  $\rho_s$  and  $\rho_l$  the solid and liquid density respectively and  $h$  the topography height, the second term and third term ( $p$ ) are the viscous stress and the dynamic pressure on the solid side,  $w$  being vertical velocity. The  $^+$  and  $^-$  exponents refer to the upper and lower boundaries, respectively. Note that Chambat et al. (2014) argue for a discontinuity of traction across the boundary and propose to add two terms to the balance equation (B.5). A preliminary analysis has shown that these two terms are negligible for applications to mantle convection and they are omitted here for simplicity.

At the solid-liquid boundary, like any phase change, the reaction is accompanied by release and absorption of latent heat, during freezing and melting, respectively. Because the interface between solid and liquid cannot accumulate or lose heat, the discontinuity of heat flow at the interface must equilibrate the release or absorption of latent heat due to the reaction. This may be expressed by the Stefan condition,

$$\rho_s L v_\phi = -q_s + q_l, \quad (\text{B.6})$$

where the term on the left represents the heat production due to freezing or melting, with  $L$  the latent heat and  $v_\phi$  the freezing (negative for melting) rate. The right-hand-side is the heat flow difference across the boundary, and the subscript  $s$  and  $l$  refer to solid and to liquid respectively. The heat flow difference of the right-hand side is dominated by convective heat transport in the liquid side, and for the sake of simplicity the right side of eq. B.6 can be expressed by the advective heat flux on the liquid. Moreover, the freezing (or melting) rate ( $v_\phi$ ) can be approximated by the vertical velocity ( $w$ ) across the boundary, if the topography growth rate is negligible. Under these conditions eq. B.6 leads to (see Deguen, Alboussière, et al. 2013; Labrosse, Morison, et al. 2018, for details):

$$w \equiv \frac{h^\pm}{\tau_\phi}, \quad (\text{B.7})$$

$\tau_\phi$  being the characteristic phase-change time scale for transferring latent heat from region where it is released (freezing, around topography depression) to places where it is consumed (melting, around topography highs), and is defined as:

$$\tau_\phi = \frac{\rho_s L}{(\rho_l c_{pl} u_l \left( \frac{dT_l}{dz} - \frac{dT_{ad}}{dz} \right))^\pm}, \quad (\text{B.8})$$

where  $c_{pl}$  is the heat capacity,  $u_l$  the characteristic liquid velocity, and  $\frac{dT_l}{dz}$  and  $\frac{dT_{ad}}{dz}$  are the melting temperature Clapeyron slope and the isentropic gradient in the melting region, reflectively. The explicit development of equations B.7 and B.8 can be found in Deguen, Alboussière, et al. (2013). Using eq. B.7 and introducing the viscous time scale for building topography,

$$\tau_\eta = \frac{\eta}{|\rho_s - \rho_l^\pm| g H}, \quad (\text{B.9})$$

eq. B.5 becomes, in dimensionless form:

$$\pm \Phi^\pm w + 2 \frac{\partial w}{\partial z} - p = 0 \quad (\text{B.10})$$

where  $\Phi = \tau_\phi/\tau_\eta$  is the phase-change number and represents the ratio between the characteristic phase-change and viscous time scales. For a large value of  $\Phi$ , the phase change condition (eq. B.10) implies a small value of  $w$ . This can be interpreted considering that, when  $\tau_\eta \ll \tau_\phi$ , the topography forms in response to stress in the solid and the solid flow is limited by the buoyancy of the topography, which makes the vertical velocity effectively drop to zero at the boundary, which leads to an effectively non-penetrating classical free-slip boundary condition. On the other hand, for the opposite situation when  $\tau_\eta \gg \tau_\phi$ , the topography is erased faster than it is generated. The removal of the associated buoyancy leads to a non-null velocity across the interface and the boundary is permeable.

The continuity of the horizontal traction across the boundaries leads to the classical free-slip boundary condition,

$$\frac{\partial u}{\partial z} + \frac{\partial w}{\partial x} = 0. \quad (\text{B.11})$$

Note however, that contrary to the classical calculations assuming a non-penetrating boundary condition, the second term in equation (B.11) is identically null in our model.

### B.3.3 Numerical approach and set-up

The equation described in B.3.1 and B.3.2 are solved using the finite-volume code StagYY (Tackley 2008). The mass and momentum equation B.1 and B.2 are discretized as a unique linear system of equations inverted using a direct solver for sparse matrices (UMFpack for sequential calculations, MUMPS for parallel calculations; Amestoy, Duff, et al. 2001; Amestoy, Guermouche, et al. 2006), whereas the energy equation B.3 is solved in an explicit manner, using a total variation diminishing (TVD) method for the advection term.

The mechanical boundary conditions are periodic on the vertical sides, and free-slip (eq. B.11) on the top and bottom domain boundaries, where eq. B.10 is also applied. The thermal boundary conditions are the Dirichlet condition of fixed temperature of 0 and 1 at the top and bottom, respectively. However, resolving numerically the boundary layers on the melting front of the flow at low values of the phase change number ( $\Phi$ ) is difficult at large Rayleigh number. Indeed, as shown by the analytical solution for the translation mode of convection when both boundaries have a phase change, a thermal boundary layer (TBL) of thickness  $1/w$  exists in the solid side (Labrosse, Morison, et al. 2018) and since the velocity can be very large, it requires a huge number of grid points to be properly resolved. Moreover, even if extreme grid refinement can be used in the boundary layers, the stability of the explicit time-stepping scheme requires a extremely small timestep which renders calculations at high Rayleigh number inaccessible. The analytical solution for the translation mode and the weakly non-linear analysis for the deforming mode (ibid.) show however that regions where the TBL is very thin are those where flow is toward the boundary and therefore are not prone to instabilities. Moreover, the temperature difference in these TBLs are tiny. In that sense, these regions play little role in the global dynamics and can be modeled using the theory developed by Labrosse, Morison, et al. (ibid.). In that case, the thin TBL needs not to be resolved numerically and the Dirichlet boundary condition is replaced by an effective

Robin one that depends on the vertical velocity  $w$ . The Dirichlet condition that applies at the boundary is replaced by a condition that applies on the interior side of the thin boundary layer. In practice, when the flow is toward the boundary ( $w < 0$  at the bottom,  $w > 0$  at the top), the vertical temperature gradient should be null,  $\partial\theta/\partial z = 0$ , whereas flow going away from the boundary carries the information of the boundary temperature and the Dirichlet condition is applied,  $\theta = 0$ , with  $\theta$  the deviation of temperature with respect to the steady-state conduction profile. This condition is written as:

$$\Gamma^\pm\theta + (1 - \Gamma^\pm)\frac{\partial\theta}{\partial z} = 0, \quad (\text{B.12})$$

where  $\Gamma^\pm$  is a smooth approximation of the Heaviside function depending on the vertical velocity:

$$\Gamma^\pm = \frac{1}{2} \left[ 1 + \tanh \left( \pi \frac{\mp w + \frac{w_0}{2}}{\frac{w_0}{2}} \right) \right], \quad (\text{B.13})$$

with  $w_0$  the velocity range along which  $\Gamma$  varies from 0 to 1, defined depending on the problem. For a large velocity toward the boundary ( $w \ll -w_0/2$  at the bottom,  $w \gg w_0/2$  at the top),  $\Gamma \sim 0$  and we get a Neumann boundary condition,  $\partial\theta/\partial z = 0$ , whereas for flow away from the boundary or slow flow toward the boundary, we get the classical Dirichlet boundary condition,  $\theta = 0$ . Using eq. B.12 the heat carried by diffusion across the thermal boundary layer is ignored and heat transport is done entirely by advection across the boundary. A similar approach has been already used to study the convection pattern with fast surface erosion or important magmatism in hot planets (Ricard, Labrosse, et al. 2014). We checked that, for cases with intermediate velocity at the boundary that can be modeled using both boundary conditions, the results do not depend on the choice of boundary condition. We are therefore confident that the thermal boundary condition (B.12) can be used to model the phase change at high Rayleigh number.

The initial temperature conditions are described case by case in the results section B.4. The model domain has different mesh resolution depending of the problem, and it ranges from 18 to 128 grid points for unit length.

## B.4 Results

We performed 323 simulations in 2D Cartesian coordinate (the full simulation list is presented in the supplementary material) to systematically investigate the convection style, the thermal structure and heat transfer efficiency in the solid mantle when it is bounded by one or two solid-liquid phase change boundaries. We investigate the effect of the phase change ( $\Phi^\pm$ ) and Rayleigh (Ra) numbers, which allows us to have an overview of possible convection patterns during magma ocean crystallisation. In this first exploration, we do not consider the effects of many ingredients that are commonly thought to play a role in mantle convection: spherical geometry, volumetric heating, compositional variations, temperature- and depth- variation of physical properties. We make this choice in order to restrict this first study to a tractable set of independent parameters and compare the results to the well studied situation of Rayleigh-Bénard convection.

### B.4.1 Convection with a magma ocean above and below

Let us first consider the situation where both the top and bottom boundaries are the seat of a phase change between the convecting solid and the magma oceans. This situation may have happened if the solid mantle crystallized from the middle, up- and downward (Boukaré, Ricard, et al. 2015; Labrosse, Hernlund, and Coltice 2007; Thomas, Liu, et al. 2012). For simplicity, we consider only the situations with an equal value of the phase change parameter at the top and bottom boundaries, which we call simply  $\Phi$  for both sides.

#### Non-deforming translation mode

Labrosse, Morison, et al. (2018) showed that a steady-state translation mode of convection can exist when both top and bottom boundaries are phase change interfaces. In that mode, a uniform purely vertical upward or downward flow in the solid is maintained by the buoyancy associated with a nearly uniform temperature, equal to that of the boundary at which the flow enters. This analytical solution is a good test of the numerical method.

To investigate the ability to develop a translation mode, we have performed numerical simulations, in a rectangular domain with aspect ratio  $A = 4$ , with a finite small phase-change number  $\Phi = 0.01$  for both top and bottom sides. The choice of these parameters is justified by the fact that, for such a low value of  $\Phi$ , the critical Rayleigh number for the onset of the translation mode is  $Ra_{ct} = 24\Phi = 0.24$  and this mode is favored over a deforming mode if the aspect ratio of the domain is smaller than the critical wavelength of the deforming mode, which is approximately 115 (ibid.). The reduced Rayleigh number  $\varepsilon_t = (Ra - Ra_{ct})/Ra_{ct}$  investigated ranges from 0.01 to 100 (Table S1, supplementary material). The numerical results show that steady state vertical translation occurs in the solid. The dimensionless vertical velocity ( $w$ ) increases with the Rayleigh number in a way that was predicted by the analytical solution for a steady-state translation (ibid.) (Figure B.1a). Figure B.1b shows the temperature profiles obtained by the numerical simulations compared to the temperature profile predicted by the analytical solutions. Numerical solutions nicely reproduce theoretical results, and this validates our numerical method. The temperature profile obtained at low values of the reduced Rayleigh number ( $\varepsilon_t < 1$ ) diverges from the conductive profile by an amount proportional to the velocity (ibid.). At high Rayleigh numbers (high translation velocity), the profile assumes a form with a constant temperature equal to the temperature at the inflow boundary (0 for downward flow and 1 for upward flow), whereas on the opposite side the temperature drops (or rises) to the boundary temperature in a thermal boundary layer of thickness  $\delta \sim 1/w$  (ibid.). Contrary to classical Rayleigh-Bénard convection where the flow is driven by horizontal density contrast, in the translation mode, the uniform topography of each boundary,  $h = \tau_\phi w$ , is maintained by the buoyancy associated with difference between the nearly uniform temperature and conductive profile that decreases linearly with height. Moreover, in the translation mode at high Rayleigh number, heat is mainly advected by the translation, and the difference between the top and bottom conductive heat fluxes is equal to the advective heat flux (ibid.). This implies that, at high Rayleigh numbers ( $\varepsilon_t \gg 1$ ), the heat flux scales linearly with the Rayleigh number, on the contrary to classical Rayleigh-Bénard convection where the heat flux scales as  $Ra^{\frac{1}{3}}$ .

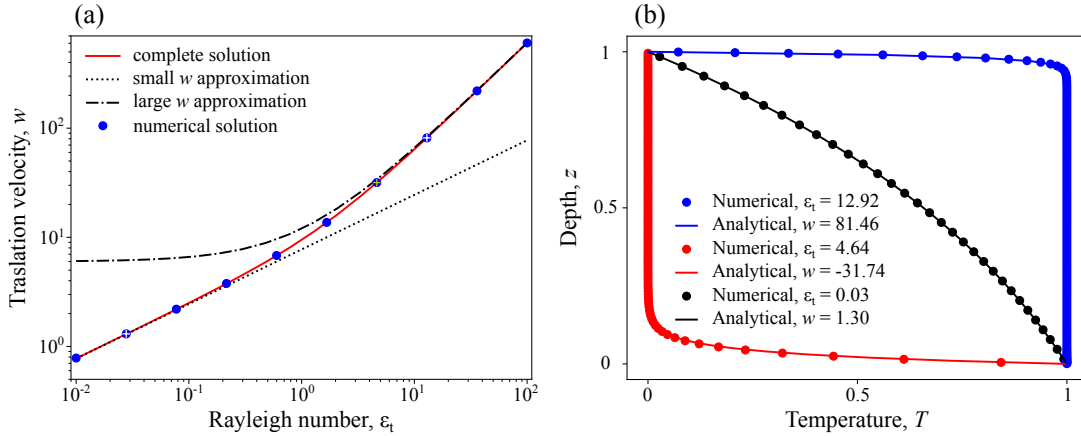


Figure B.1: Non-deforming translation mode. (a) Translation velocity ( $w$ ) plotted against the reduced Rayleigh numbers ( $\varepsilon_t$ ), compared to the theoretical predictions (Labrosse, Morison, et al. 2018). The blue symbols are the numerical simulations, and the white crosses indicate the simulations in (b). Solid, and dashed lines are the theoretical results. (b) Temperature profiles for relatively slow and fast velocities, both upward and downward compared with the theoretical profiles.

### Non-translating mode

The simulations to study the non-translating modes of convection are performed in a model domain with aspect ratio equal to the critical wavelength,  $A_c = 2\pi/k_c$ , with  $k_c$  the wavenumber for which the critical Rayleigh number is minimum.  $A_c$  increases with the decrease of the phase-change number  $\Phi$  as  $\sqrt{128\pi/9\Phi}$  for small  $\Phi$  and tends to the classical  $2\sqrt{2}$  at large  $\Phi$  (ibid.). For this study we have investigated 5 values of  $\Phi$ , ranging from  $10^{-1}$  to  $10^3$ , and the aspect ratio ranges from  $\sim 36$  to  $\sim 2.8$ , respectively. Wider and narrower aspect ratios of respectively 1.5 and 0.5 times  $A_c$  have been used, too. We performed numerical simulations with the supercritical Rayleigh number  $\text{Ra}_{sc} = \frac{\text{Ra}}{\text{Ra}_{cNt}}$  ranging from  $10^{0.25}$  to  $10^3$  (Table S2, supplementary material). The critical Rayleigh number ( $\text{Ra}_{cNt}$ ) refers to the critical Rayleigh number for the non-translating mode and must not be confused with the one for the translation mode ( $\text{Ra}_{ct} = 12(\Phi^+ + \Phi^-)$ ). In this study we use the subscript “Nt” to indicate the non-translating mode, and “t” the translation one. For low values of  $\Phi$ ,  $\text{Ra}_{cNt} \simeq \text{Ra}_{ct} - 0.3\Phi^2$ , whereas for high values of  $\Phi$ ,  $\text{Ra}_{cNt}$  increases up to reach the critical value for a classical Rayleigh-Bénard convection  $\frac{27\pi^4}{4}$  (ibid.). The limit between low and high  $\Phi$  regimes can be assumed to occur where  $24\Phi = \frac{27\pi^4}{4}$ , i.e. at  $\Phi = 27.39$ .

The temperature initial condition is:

$$T(x, z) = 1 - z + 0.05 \sin(\pi z) \cos(k_c x) \quad (\text{B.14})$$

which represents a conductive profile with a cosine perturbation of wavenumber  $k_c$ , maximum at the center ( $z = 0.5$ ) and zero at the horizontal boundaries.

Figure B.2 gives an overview of the convective flow obtained by the numerical simulations for three values of  $\text{Ra}_{sc}$  and three values of  $\Phi$ . At  $\Phi = 0.1$ , convection is mostly characterized by alternating vertical up- and downward flow, whereas at higher  $\Phi$  the flow is similar to the situation with classical free-slip boundary

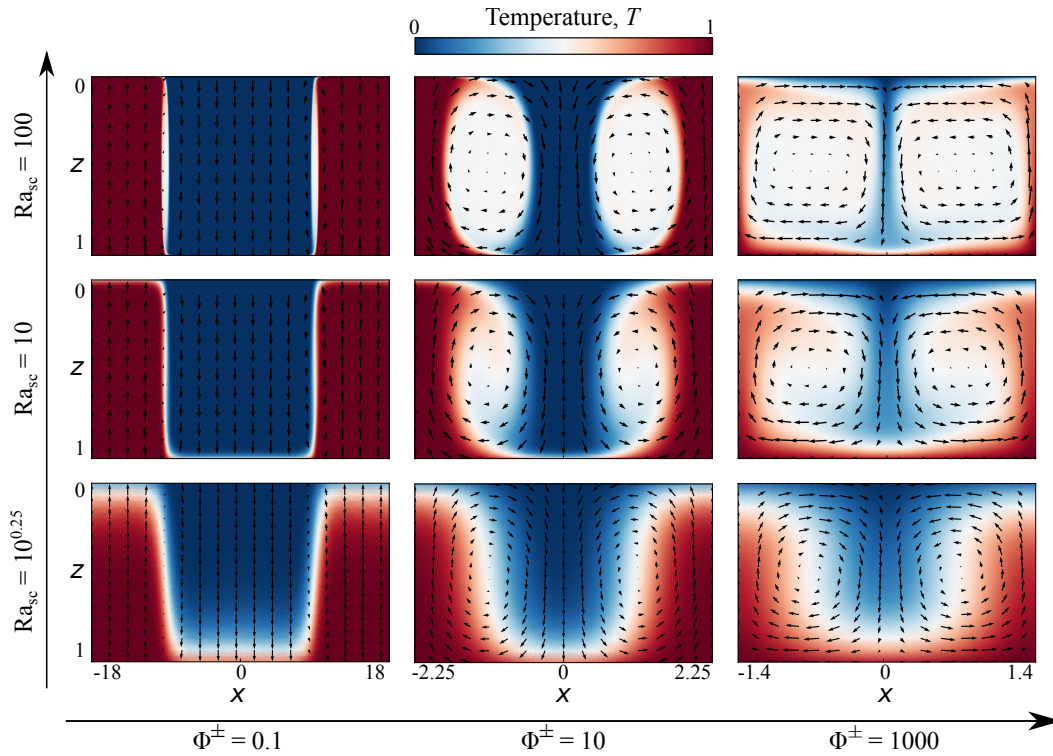


Figure B.2: Convection modes with two solid-liquid change boundaries. Snapshots of temperature (colour) and velocity (arrows) for different cases investigated. The value of  $\Phi$  increases from left to right, and the value of  $Ra_{sc}$  from the bottom to the top, as indicated by the axes. Note that the horizontal scale depends on the value of  $\Phi$ .

conditions. For intermediate cases, like for  $\Phi = 10$ , the flow is still able to pass throughout the phase changes, but it presents a substantial horizontal component compared to the lowest phase change number cases. At high values of  $\Phi$ , for example  $\Phi = 1000$ , the flow across the phase-change boundaries appears completely limited and the solution resembles the classical one for Rayleigh-Bénard convection with free-slip boundary conditions. This behavior agrees with the prediction of the weakly non-linear analysis (Labrosse, Morison, et al. 2018).

Figure B.2 shows well the effect of  $\Phi$  and  $Ra_{sc}$  on the thermal structure of the solution. For  $\Phi = 10^3$ , we observe the classical behaviour of Rayleigh-Bénard convection with the thickness of boundary layers and the associated up- and down-welling currents that decreases with  $Ra_{sc}$ . Conversely, the regions between up- and down-welling currents where the temperature is approximately uniform and close to 0.5, hereafter the isothermal cores, become thicker as  $Ra_{sc}$  increases. A markedly different behaviour is observed for low values of  $\Phi$  ( $\Phi \leq 0.1$  on the figure B.2) for which the thickness of vertical currents does not relate to the thickness of boundary layers. In addition, the boundary between the isothermal cores and the vertical currents sharpens with the increase of the Rayleigh number, and the temperature becomes more uniform in each region. To describe the thermal structure of the convective system more quantitatively, we compute the width of the isothermal core. To define the limits of the isothermal core we use the horizontal profile of the vertically averaged temperature and the limits are defined where the temperature is the

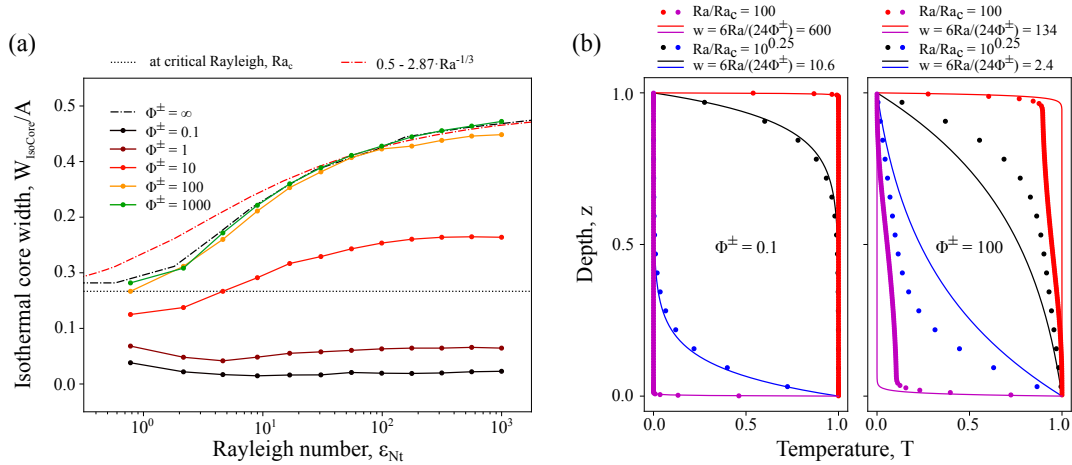


Figure B.3: Thermal structure of convection with two phase change boundaries. (a) Normalized width of the isothermal core between up- and down-welling currents as function of  $\varepsilon_{Nt}$  (see text for details). The dash-dotted and dotted black lines represent the width obtained by the numerical results for a classical free-slip Rayleigh-Bénard problem ( $\Phi^\pm = \infty$ ), and at the critical Rayleigh number. The red dash-dotted line is the predicted scaling for non-penetrating boundary condition. (b) Temperature as function of height in the up- and down-welling currents for cases at  $\Phi = 0.1$  and  $\Phi = 100$  for the  $Ra_{sc}$  as indicated in the legend. The dots represent the numerical solutions obtained from StagYY, whereas the solid lines are the profiles predicted by the theory for the pure translation solution for the same values of the Rayleigh number.

half between the mid-value and the extrema (e.g. Grigné et al. 2005). The isothermal core size normalized by the domain width is plotted against  $\varepsilon_{Nt} = Ra_{Nt} - 1$  on Figure B.3a. For high values of  $\Phi$  ( $\Phi > 100$ ) the width of the isothermal core increases with the Rayleigh number. This is the typical behaviour of classical (closed boundaries) Rayleigh-Bénard convection in which plume width decreases with the Rayleigh number value, like the thickness of boundary layers from which they originate, as  $Ra^{-\frac{1}{3}}$ . We show in Figure B.3a, for comparison, the relationship between the isothermal core width and the Rayleigh number for the classical Rayleigh-Bénard cases, as:

$$\frac{W_{IsoCore}}{A} = 0.5 - 2.87Ra^{-\frac{1}{3}} \quad (\text{B.15})$$

with  $A = 2\pi/k_c$  the aspect ratio of computational domain. Eq. B.15 is obtained by  $W_{IsoCore} + Nu^{-1} \frac{1+\sqrt{2}}{\sqrt{2}} = 0.5A$ , with  $\frac{1+\sqrt{2}}{\sqrt{2}}$  the correction due to the plume lateral heat diffusion, and assuming the classical scaling law for the dimensionless heat flux (Nusselt number,  $Nu$ ) as function of the Rayleigh number, valid for closed boundary conditions (Figure B.5a). The width of the isothermal core also increases with  $Ra$  at intermediate phase change number ( $\Phi = 10$ ) but, in that case, it saturates at a value smaller than 0.5, the maximum value that can be reached for infinitely thin plumes. On the other hand, it decreases for the smaller values of  $\Phi$ , leading to wider up- and down-welling currents.

For the non-translating mode solutions obtained with  $\Phi$  in the low range,  $\Phi < 27.39$ , the maximum and minimum temperature profile respectively of the cold and

hot current perfectly match the profile predicted by theory for the translation mode (Figure B.3b), which therefore provides a good prediction of the solution for small  $\Phi$ . The similarity between the translation and non-translation velocity at lower  $\Phi$  can be explained by the low value of the phase change number, which promotes mainly vertical flow at the expenses of the horizontal one. The numerical simulations also highlight that the non-translating mode is favored over pure translation, and prove what the linear stability analysis has suggested. Indeed the pure translation solution is unstable with respect to non translating mode, because  $Ra_{cNt}$  is always smaller than  $Ra_{ct}$  (Labrosse, Morison, et al. 2018). The similarity with the translation solution disappears when  $\Phi$  increases, with the transition that occurs for a value of  $\Phi$  somewhere between 1 and 10. For large values of  $\Phi$ , the vertical flow velocity is lower than the one predicted for the translation velocity. This agrees with colder and hotter profiles respectively for the up- and down- welling current compared to the profile predicted by the translation theory (Figure B.3b). This can be explained by the fact that the difference between  $Ra_{ct}$  and  $Ra_{cNt}$  increases as  $\sim 0.3\Phi^2$  when  $\Phi$  increases, which tends to favor the non-translating mode.

The existence of two types of solutions for the same set of parameters, one as a uniform translation and one with deformation, raises the question of their relative stability and the one that would be most likely chosen in natural situations. Labrosse, Morison, et al. (ibid.) showed that slightly above the critical Rayleigh number for the translation mode, there is a region in the  $(k, Ra)$  space where the steady translation is unstable with respect to a deforming mode. The region shrinks with the decrease of  $\Phi$ , meaning that the translation solution becomes more stable. In other words, for any value of  $\Phi$ , there is a value of the Rayleigh number above which the translation solution is stable. On the other hand, the stability of the deforming mode of convection with respect to the translation one was not studied but the increasing stability of the translation solution when increasing the Rayleigh number suggests that the deforming mode of convection could also become unstable with respect to translation. Without exploring systematically this question, we performed calculations in the same range of parameters as presented above, Rayleigh numbers,  $\Phi$  and aspect ratio  $A$ , but starting from an initial temperature condition characterized by a conductive profile with a random thermal anomaly with amplitude of 0.05 (Table S3, supplementary material). Starting with a random initial perturbation is closer to natural situations and is known to lead to different stable solutions, or to planforms with defects, in Rayleigh-Bénard convection. Figure B.4 shows snapshots of representative cases that we computed. We obtained solutions with a wavelength that differ from the one predicted by linear stability, or with up- and downwelling blocks of different width, like the case of  $Ra_{sc} = 100$  and  $\Phi = 0.1$ . We also get a translation solution in some cases, when the Rayleigh number is large enough, like for  $Ra_{sc} = 100$  and  $\Phi = 1000$ . Note that, for the models presented with  $\Phi = 0.1$  in figure B.4, despite running for a total dimensionless duration of  $\Delta t = 8.5$  for  $Ra = 10$  and for  $\Delta t = 0.05$  for  $Ra = 100$ , the system has not yet reached steady state and may still evolve toward a translation solution. In particular, the case for  $\Phi = 0.1$  and  $Ra_{sc} = 100$  shows a clear asymmetry between up- and down-welling currents, the up-welling regions gaining with time. We expect it to ultimately run in an upward translation mode.

The heat transfer efficiency of the non-translating mode of convection is studied by computing the dimensionless heat flux and the RMS velocity ( $V_{rms}$ ), for all

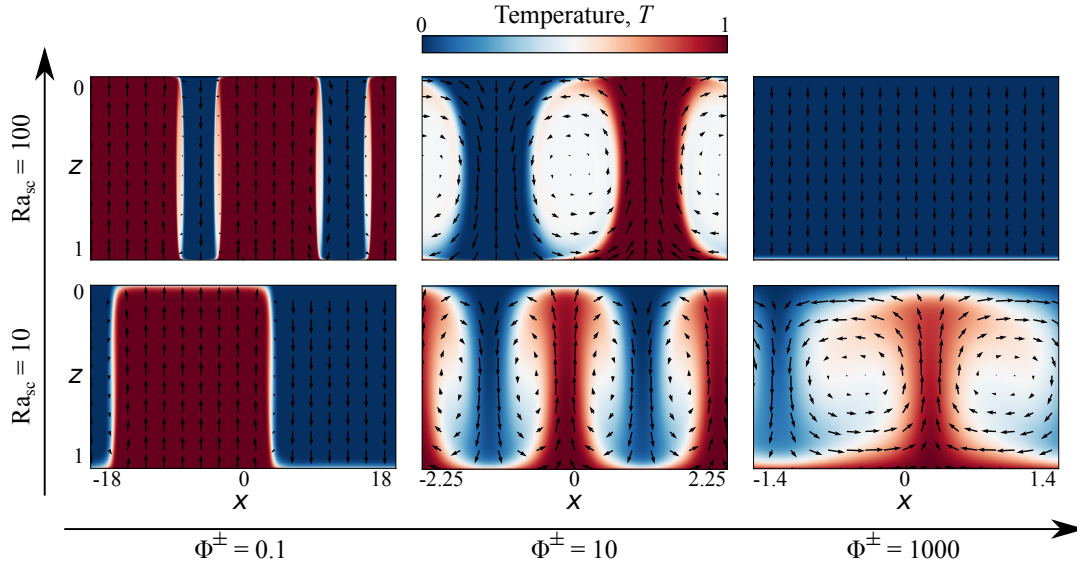


Figure B.4: Convection patterns with two solid-liquid change boundaries, obtained with a random initial perturbation. Snapshots of temperature (colour) and velocity (arrows) for different cases investigated. The phase change parameter  $\Phi$  increases from left to right, and the super-critical Rayleigh number  $Ra_{sc}$  from the bottom to the top, as indicated on the axes.

parameter sets investigated, but ignoring the simulations that show pure translation that have been discussed above and are already well explained by the analytical theory of Labrosse, Morison, et al. (ibid.). In Figure B.5 we show  $Nu$  and  $V_{rms}$  plotted against the Rayleigh number, for different values of  $\Phi$ . The case with classical boundary conditions as well as the exact solution for the translation velocity and the Nusselt number predicted by weakly non-linear analysis (ibid.) are plotted for reference, too. As expected, for  $\Phi = 1000$ , the solution roughly follows the scaling for classical Rayleigh-Bénard convection. On the other hand, for smaller values of  $\Phi$ , both  $V_{rms}$  and  $Nu$  increase more steeply with  $Ra$  than for non-penetrating boundary conditions. For  $\Phi \leq 1$ , the numerical solutions are found to closely match the prediction of the weakly non-linear analysis, for the whole range of parameters investigated, and in particular Nusselt number values in excess of  $10^3$ . This is somewhat unexpected since this first order development is only supposed to be valid very close to the onset of convection. This is another expression of the simplicity of the solution which exhibits alternative up- and down-ward translation regions, each very similar to the pure translation solution for which the velocity and Nusselt numbers increase linearly with  $Ra$  at large values of  $Ra$ . Indeed, for each set of solution with the same value of  $\Phi$  we fit the relation  $Nu = Nu_0 Ra^\alpha$ , and  $V_{rms} = V_0 Ra^\beta$ , and the resulting scaling law are shown in the plot legends. In the Rayleigh number range investigated, the exponent  $\alpha$  of 0.36 and  $\beta$  of 0.66 for the case  $\Phi = 1000$  are similar to the exponents for a classical Rayleigh-Bénard convection (e.g. Jaupart and Mareschal 2011). As  $\Phi$  decreases, both exponents tend to 1, showing the linear relationship of heat flux and velocity with the Rayleigh number, already proved for the pure translation solution (Labrosse, Morison, et al. 2018). Moreover, for cases at low phase change number ( $\Phi \leq 10$ ) the coefficient of proportionality  $Nu_0$ ,

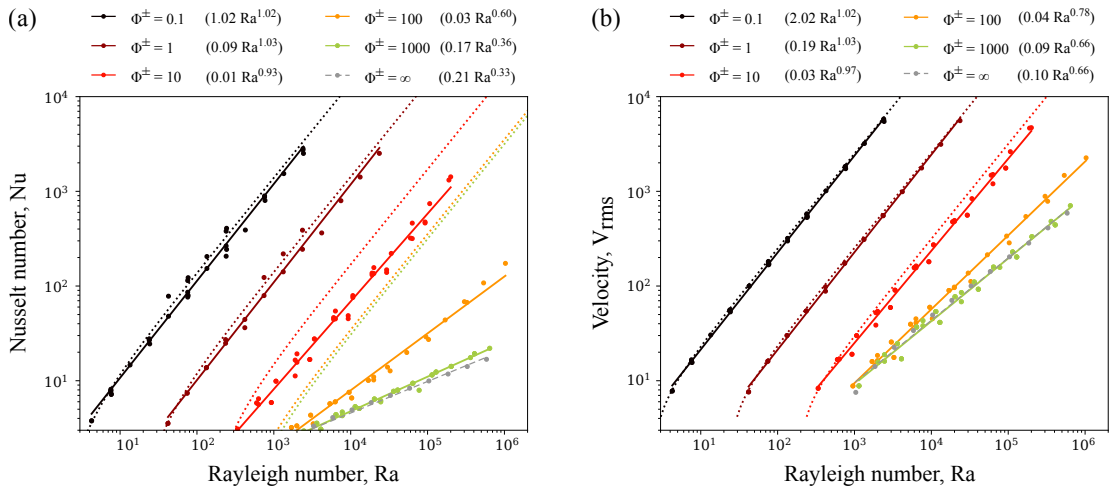


Figure B.5: Heat transfer efficiency by solid-state mantle convection bounded by two magma oceans. (a) Nusselt number and (b) RMS velocity against the Rayleigh number for different values of the phase change number, as labeled. Coloured solid symbols represent results of all cases investigated. The dotted lines represent the predictions by Labrosse, Morison, et al. (2018), using the weakly non-linear analysis for the heat flux and the exact solution of the translation mode for the velocity, whereas the gray dashed and the coloured solid lines represent the fit for each value of the phase number studied as indicated in the legend for each figures.

and  $V_0$ , both scale as  $\Phi^{-1}$ , as shown for the translation mode (Labrosse, Morison, et al. 2018). The heat flux and velocity obtained by the weakly non-linear analysis represent well the results from direct numerical simulations for very small value of  $\Phi$  ( $\Phi \leq 1$ ). On the other hand, for  $10 \leq \Phi \leq 100$ , the heat flux and RMS velocity from numerical solutions diverge at higher Rayleigh number values from analytical predictions, which is the usual behaviour for Rayleigh-Bénard convection.

#### B.4.2 Convection with a magma ocean above or below

The situation with only one boundary having a phase change is encountered in several cases. The case with a liquid ocean below the solid layer is relevant to the surface ice-shell of some icy satellites of Jupiter and Saturn (e.g. Baland et al. 2014; Čadek et al. 2016; Grasset et al. 2000; Khurana et al. 1998; Pappalardo et al. 1998; Tobie, Choblet, et al. 2003) and possibly for the early Earth with a basal magma ocean (Labrosse, Hernlund, and Coltice 2007). The case with a liquid on top of the solid may be currently relevant for high pressure ice layers below a buried ocean in the largest icy satellites (e.g. Grasset et al. 2000; Tobie, Lunine, et al. 2006) and for an upwardly crystallizing magma ocean in young terrestrial planets (Solomatov 2015). In the Cartesian geometry investigated in this paper, both situations are symmetrical to one another and we only study one of them, with a magma ocean below. This is done considering a finite value for the phase change number only at the bottom boundary ( $\Phi^-$ ), while for the top one we consider  $\Phi^+$  to be infinite, in order to impose the classical non-penetrative free-slip condition. We perform the calculations using a model domain with aspect ratio equal to the critical wavelength,  $A_c = 2\pi/k_c$ , and imposing the same initial temperature condition as

above (eq. B.14).

Before discussing all the results with only the phase change at the bottom, let us consider one case to discuss and to prove the symmetry between the situations with a magma ocean above and below. Figure B.6 shows the final snapshots of two runs with the same parameters except for the boundary conditions, one having the  $\Phi^- = \infty$  and  $\Phi^+ = 0.1$  and the other  $\Phi^- = 0.1$  and  $\Phi^+ = \infty$ . Both cases were run in a box of aspect ratio 4.978 corresponding to the wavelength of the most unstable mode at the onset of convection. After a time of about 0.05 during which convection proceeded with this initial wavelength, a transition occurred to a solution with a wavelength that is half the width of the computation domain, before resuming to a solution having the original wavelength, as displayed on the figure B.6a. As convection proceeds, the system alternates between solutions with one or two plumes. The two situations appear clearly symmetrical from one another: in the case of melting at the top, the flow is characterised by hot plumes with a cold diffuse return flow, whereas when the phase change is at the bottom, the flow is dominated by cold down-welling plumes and a diffuse hot return flow. The temperature in the return flow is equal to that of the boundary from which it originates with a boundary layer to match the opposite temperature (figure B.6b). The thickness of that boundary layer controls the heat flow in that situation and its scaling is the subject of this subsection.

For our systematic study in the case of phase change condition only at the bottom, we investigated 5 values of  $\Phi^-$ , ranging from 0.1 to 1000, with a corresponding aspect ratio between 5 and 2.8, respectively. The range of supercritical Rayleigh number ( $Ra_{sc}$ ) is from  $10^{0.025}$  to  $10^{3.25}$  (Table S4, supplementary material), the lower Rayleigh number cases allowing us a detailed comparison to the predictions of the weakly non-linear stability analysis (Labrosse, Morison, et al. 2018). For the computations at relatively high Rayleigh number ( $Ra_{sc} \geq 10^{2.75}$ ) and  $\Phi^- \leq 10$ , we applied at the bottom the Robin temperature boundary condition (eq. B.12), assuming a threshold velocity  $w_0$  based on the RMS velocity for a case without phase change at similar  $Ra_{sc}$ ,  $w_0 = 0.5V_{rms}$ . The numerical solutions for nine cases for  $\Phi^-$  of 0.1, 10 and 1000 and for  $Ra_{sc}$  of  $10^{0.25}$ , 10,  $10^3$  are shown in Figure B.7. The temperature and velocity field show that at high phase-change number ( $\Phi^- = 1000$ ), the solution does not differ from a classical case of non penetrating boundaries, and as  $Ra$  increases, the width of the isothermal core increases, which is the same behaviour we observed with phase change at both boundaries (Figure B.2, and Figure B.3a). At lower  $\Phi^-$ , a stationary cold plume, that becomes thinner as the Rayleigh number increases, characterizes the convective structure, and depending on the phase change number, at high Rayleigh number, a second cold plume can form, as shown in Figure B.7 for  $\Phi^- = 0.1$  and  $Ra_{sc} = 100$ . The formation of a secondary plume occurs at  $Ra_{sc} \geq 10^{0.5}$  for  $\Phi^- \leq 1$  and at  $Ra_{sc} \geq 10^{1.75}$  for  $\Phi^- = 1$ , and the convection shows periodic alternation of one and two cold plumes. In general, the gradual increase of the Rayleigh number and/or decrease of the phase change number leads to a strong increase of the mean temperature and a consequent progressive reduction of the thickness of the top thermal boundary layer, the formation of thin and strong cold-plumes, and the disappearance of the hot thermal boundary layer at the bottom. This pattern of convection is similar to that obtained for internally heated convection (e.g. Houseman 1988; E. M. Parmentier, Sotin, and Travis 1994; Sotin and Labrosse 1999), even though no volume heating is included in the present cal-

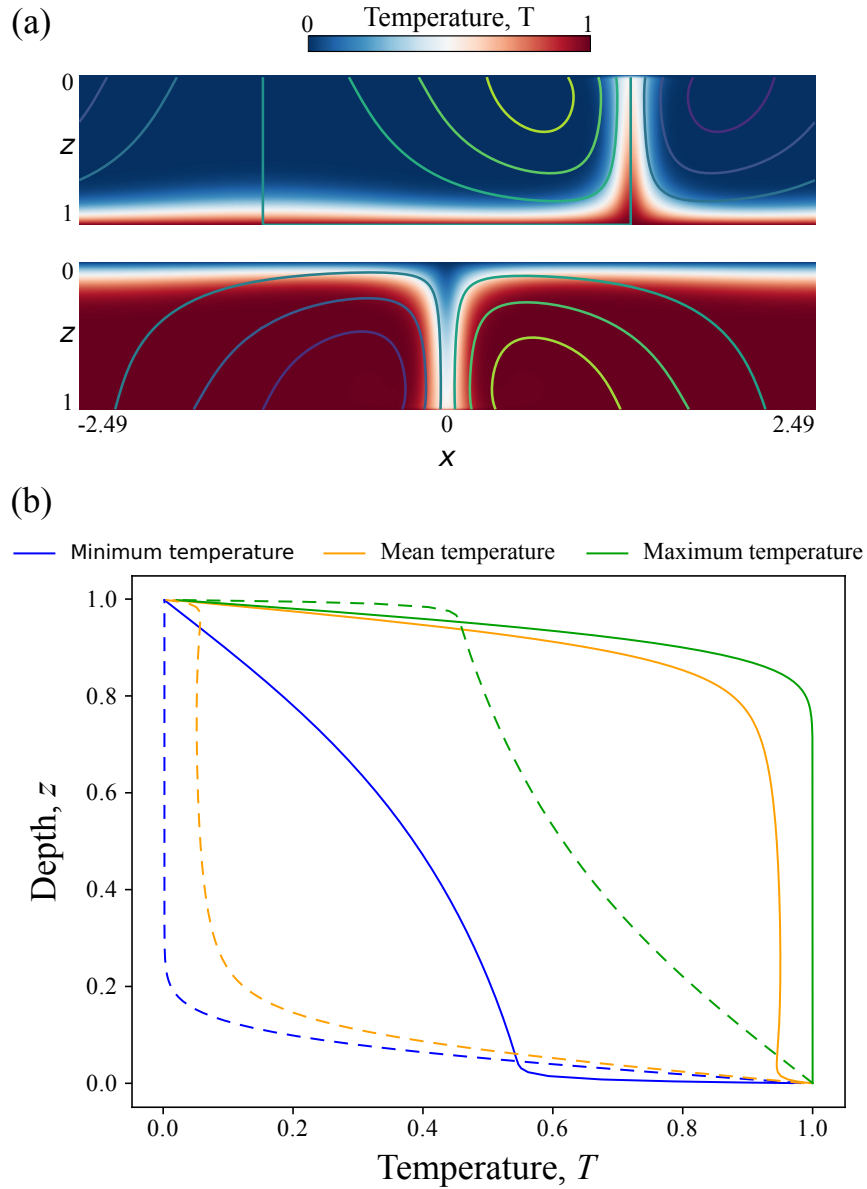


Figure B.6: Solution for convection bounded by a liquid above or below. (a) Snapshots show the temperature field in colour and the streamlines at the end of the run ( $t = 0.18$ ), with a phase change boundary condition above (top) or below (bottom), (b) The vertical profiles of minimum, mean and maximum temperature. The dashed and solid lines represent the profiles for the case with a magma ocean above and below, respectively. The Rayleigh number is  $Ra = 10^4$ . We used the horizontal periodicity of the solution to avoid the plume in the upper panel to be on the boundary, which it originally was.

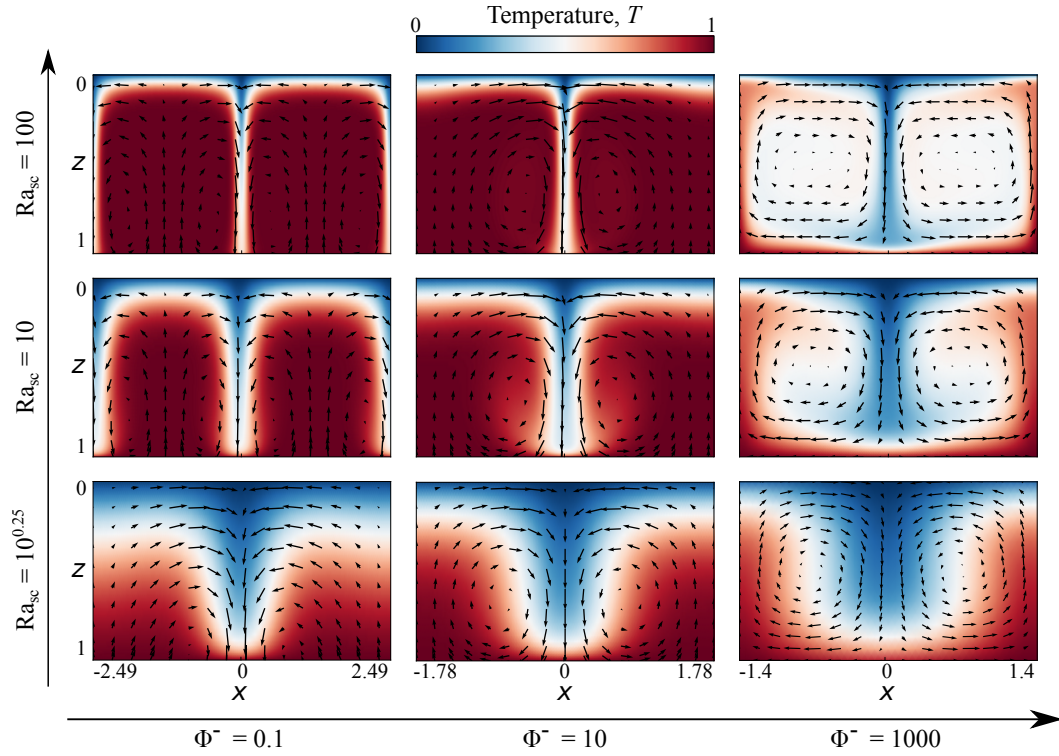


Figure B.7: Convection patterns obtained with a phase change only at the bottom boundary. Snapshots of temperature (colour) and velocity (arrows) for different case investigated.  $\Phi^-$  increases from left to right, and  $Ra_{sc}$  from the bottom to the top, as indicated by the axes. Note that the horizontal scale depends on the value of  $\Phi^-$ .

culations.

Let us now study how the Nusselt number ( $Nu$ ) and the average temperature ( $\langle T \rangle$ ) vary at low Rayleigh numbers ( $Ra_{sc} \leq 10^{0.25}$ ). Figure B.8 shows  $Nu$  and  $\langle T \rangle$  plotted against the Rayleigh number, for different values of  $\Phi^-$ , together with the prediction of the weakly non-linear analysis (Labrosse, Morison, et al. 2018). The weakly non-linear analysis is found to provide good predictions only close to the critical Rayleigh number, as expected, the range of validity being somewhat larger for the average temperature than for the Nusselt number. For large values of  $\Phi^-$ , the average temperature is close to 0.5, like for classical Rayleigh-Bénard convection, while at low  $\Phi^-$  it increases more steeply as the Rayleigh number increases. The fact that the average temperature is larger than 0.5 is again similar to the situation encountered for internally heated convection.

The Nusselt number ( $Nu$ ), the RMS velocity ( $V_{rms}$ ) and the average temperature ( $\langle T \rangle$ ) at higher Rayleigh numbers are plotted on figure B.9. The  $Nu$  and  $V_{rms}$  variations are bounded between the low value of the classical Rayleigh-Bénard convection with non-penetrative conditions and the high value for low phase change number ( $\Phi^- = 0.1$ ). The scaling law for the Nusselt Number, RMS velocity and temperature are, for  $\Phi^- = 0.1$ :

$$Nu = 0.37Ra^{0.33}, \quad (B.16)$$

$$V_{rms} = 0.2Ra^{0.66}, \quad (B.17)$$

$$\langle T \rangle = 1.0 - 2.64Ra^{-0.33}. \quad (B.18)$$

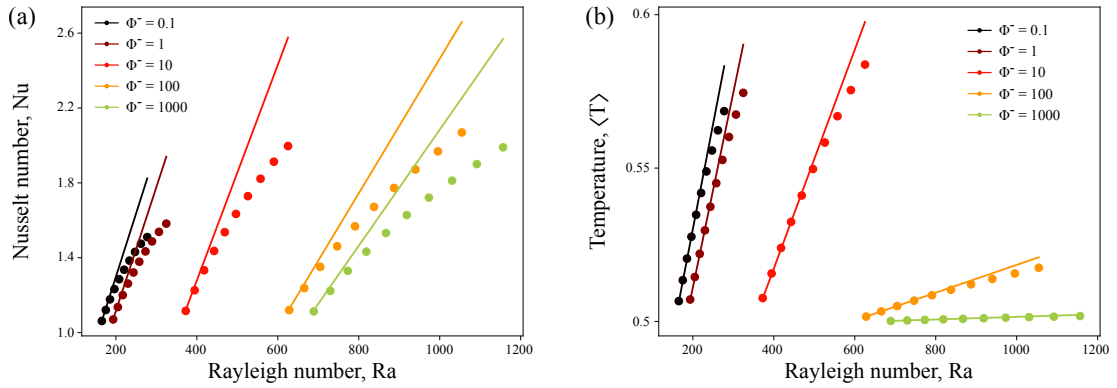


Figure B.8: Heat flux and average temperature for a Rayleigh number close to the critical value for convection bounded by only one phase change boundary. (a) Nusselt number and (b) average temperature against the Rayleigh number. The lines represent the predictions of the weakly nonlinear analysis.

We obtained the same scaling laws for Nu and  $\langle T \rangle$  as that obtained by Ricard, Labrosse, et al. (2014) for mantle convection subject to fast erosion or magmatism at its surface. This indicates that different physical processes can lead to a similar physics. Moreover, as shown on figure B.9, the pre-factors in the scaling laws for the Nusselt number and the RMS velocity (equations B.16 and B.17) are about twice their counterpart for the case with non-penetrating boundary conditions, indicating a much larger heat and mass transfer when a phase change is permitted at the boundary. As suggested by Labrosse, Morison, et al. (2018), because there is not limit to vertical flow at the bottom, the Rayleigh number is equivalent to four times the Rayleigh number of the classical not-permeable case. The ratio between the pre-factors is similar to what would be expected from this simple heuristic. Results for  $\Phi^- \geq 10$  are close to that for non-penetrative boundary conditions, at least at low values of the Rayleigh number. Increasing its value makes the heat flow at the bottom increase which makes the mean temperature increase further eventually leading to a transition to a fully open bottom boundary. This transition appears to take place at  $10^4 < Ra < 10^5$  for  $\Phi^- = 10$ , and likely at higher Ra for  $\Phi^- \geq 100$ . We suspect that, for large enough Rayleigh numbers, all scaling laws collapse to the one obtained in the small  $\Phi^-$  limit, the results obtained here for intermediate values of  $\Phi^-$  ( $\Phi^- = 10, 100$ ) being transitional.

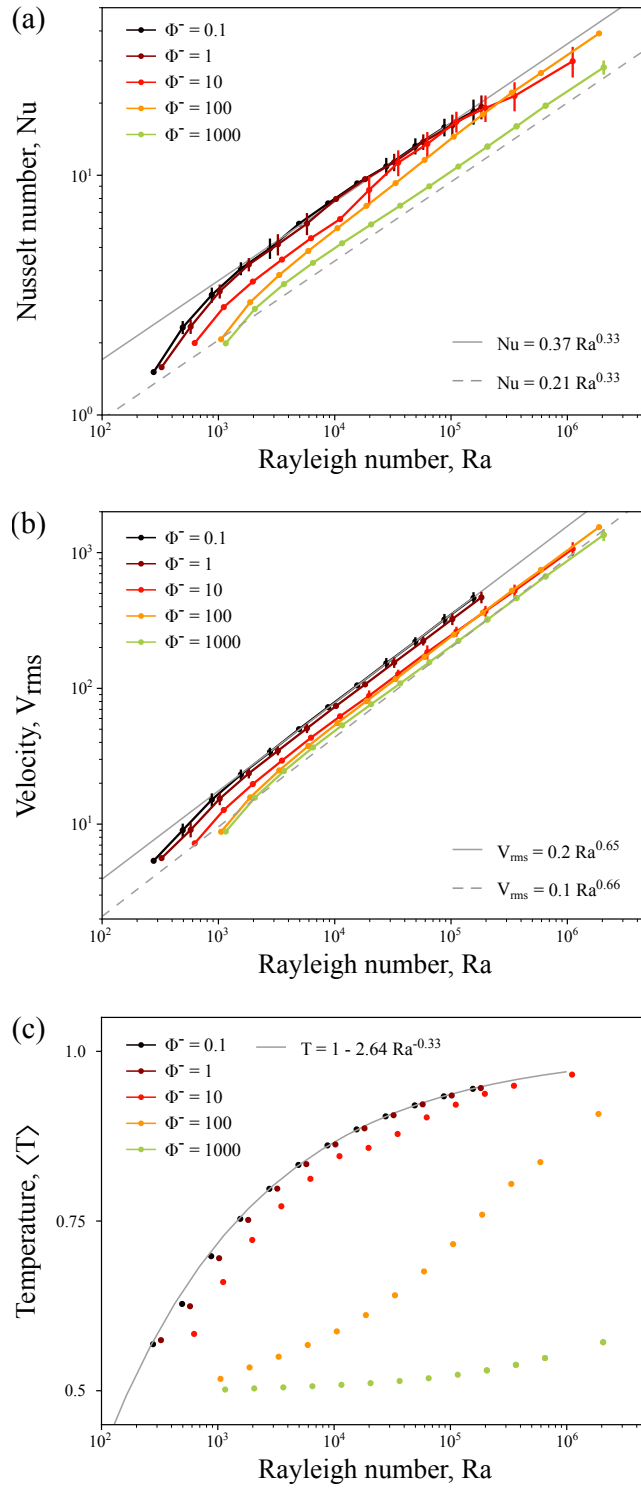


Figure B.9: Heat and mass transfer characteristics for mantle convection with a solid-liquid phase change at the bottom. (a) Nusselt number, (b) RMS velocity, and (c) average temperature, against the Rayleigh number. The gray solid line represents the fit for the simulation for  $\Phi^- = 0.1$ , and the grey dashed line the classical non-penetrative free-slip case as already shown on figure B.5.

## B.5 Discussion

In this study we have investigated the dynamics of a solid mantle bounded between two magma oceans or in contact with one at the bottom. The mantle is modeled as a two-dimensional layer of infinite Prandtl number fluid and the solid-liquid phase change at either or both boundaries is taken into account by imposing a boundary condition allowing a flow through the boundary. This boundary condition is controlled by a phase change parameter,  $\Phi$ , which allows the system to go from easy flow-through at low  $\Phi$  values to classical non-penetration at large  $\Phi$ .

In many ways, the setup we used is too simplistic to be directly applied to planetary mantles but the effects of the phase change boundary condition are so drastic that it calls for a systematic study on these effects on the simplest situation before including some of the complexities of mantle convection. Let us discuss here a few of these complexities, that may be required to include in future models, depending on the planetary object of applications, the Earth or icy satellites.

The first obvious limitation concerns the chosen geometry, cartesian instead of a spherical shell. Running models in a spherical shell is possible using StagYY (Tackley 2008) but it is quite costly in three dimensions. Using the spherical annulus geometry (Hernlund and Tackley 2008) is readily possible and is the target of a future study. Compared to the situation investigated in the present paper in which the horizontal scale of the flow can tend to infinity when the phase change numbers of both boundaries are decreased, up to the uniform translation mode, the spherical shell geometry imposes a maximum wavelength that corresponds to the spherical harmonics degree 1. This mode is indeed found to be preferred when both boundaries have a low value of  $\Phi$  (Deguen 2013; Morison et al. 2019), which corresponds to a spherical translation mode. Opposite to the situation of the translation mode in cartesian velocity, a translation in spherical geometry is characterised by a zero horizontal average of the vertical velocity. Even if this mode of convection is predicted by the linear stability analysis, its form at finite amplitude remains to be studied.

In the case with only a basal magma ocean, the dynamics is controlled by the top boundary layer, as in internally heated convection, and we expect a similar behaviour in spherical shell geometry. The main difference between the two geometries is that the situations with a magma ocean on top is not strictly symmetrical to the one with a magma ocean below in spherical geometry, although the behaviours of each situation can be qualitatively predicted from the other.

Pursuing with geometrical effects, the dynamics that is modeled here should also be accompanied with the net motion of the boundaries as the magma oceans freeze or, possibly, the solid mantle remelts. The importance of this aspect depends on the velocity of the boundary motion relative to the flow velocity in the solid. During the crystallisation of a top magma ocean, both velocities may be comparable and the net freezing has been included in the study of Morison et al. (2019) about the onset of convection. In the case of a basal magma ocean only, the net motion of the interface is expected to be slow and separation of time-scales should apply. Nevertheless, the net motion of the interfaces is important, particularly when dealing with the long term evolution of the mantle. This is also associated with the evolution of the composition of magma oceans and the solid that crystallises from it. These effects have been included in the numerical model and are the subject of our current studies.

Another simplification of the present model is that we consider all physical properties uniform whereas most vary with pressure and temperature in planetary mantles. Among these, the most important one is undoubtedly the viscosity. In the case of a magma ocean above and below, the whole solid is close to the melting temperature and we do not expect its variations to affect the solutions too much, in particular since the solutions in that case have a very large wavelength with little deformation. The situation with only a basal magma ocean is quite different since the surface boundary is the one at the lowest temperature and therefore the highest viscosity but is also the one which provides the buoyancy source for the flow. Taking into account the temperature-dependence of the viscosity, we expect to obtain the same regimes as with classical boundary conditions: the small viscosity contrasts regime, the transitional regime and the stagnant-lid regime (Moresi and Solomatov 1995). The regime boundaries should however be displaced compared to the classical case, as is the value of the Rayleigh number for the onset of convection. The significance of this effect remains to be investigated.

By far, the most important limitation of the present results comes from neglecting variations of composition and their effect on the melting temperature and the implied two-phase flow dynamics. First of all, as we assume incompressibility in the framework of the Boussinesq approximation, temperature gradients should in fact be interpreted as super-isentropic temperature gradients, or gradient of the potential temperature. In this context, a curved liquidus as obtained by (Fiquet et al. 2010) that allows crystallisation to start in the mid-mantle (Boukaré, Ricard, et al. 2015; Mosenfelder, Asimow, Frost, et al. 2009), could in fact lead to a decrease of melting temperature with depth in the deep mantle. Considering first the situation where crystallisation indeed starts in the mid-mantle, the upward crystallisation proceeds much faster than the downward one, owing to the rapid heat transfer to the atmosphere, and we expect a temperature profile in the solid following the liquidus (Morison et al. 2019). As soon as the convective instability sets in, the matter at the bottom of the solid layer, which is at the highest temperature, should remelt on its way up. Treating properly this problem requires including two-phase flow dynamics, as done by Boukaré and Ricard (2017), and goes beyond the current paper. We expect however that taking into account remelting of hot solid as it moves up should enhance heat transfer even more than what is obtained in the present results, which should then be considered as conservative.

The situation with only a basal magma ocean (BMO) is less problematic. The existence of a BMO requires the isentropic gradient to be steeper than the melting temperature gradient. This has been proposed for the magma (Boukaré, Ricard, et al. 2015; Mosenfelder, Asimow, Frost, et al. 2009) and it is also possible for the solid. Of course, we expect that an up-welling current getting close to the upper boundary may eventually cross the solidus, leading to partial melting and volcanism as it is happening in the current mantle. This process is likely to be more pervasive with a basal magma ocean since the whole mantle, except for focused down-welling currents, is then predicted to have a potential temperature similar to that of the lower boundary. Some effort has been conducted in the recent years to account for volcanism and plutonism in large scale mantle convection models (e.g. Agrusta et al. 2015; Lourenço et al. 2018) and we expect that similar processes can coexist with a basal magma ocean. Again, the present result not taking these effects into account should be considered as conservative in terms of heat flow.

The model presented in this paper neglect the effects of variations of composition even though Labrosse, Hernlund, and Coltice (2007) proposed that fractional crystallisation at the base of the mantle could lead to formation of dense piles at the bottom of the mantle. This behaviour is in fact expected to develop late in the history of the mantle, when enough of the BMO has already crystallised. The present results should apply early in the history, when the variations of composition are too small to significantly affect mantle dynamics. They may also apply to the ice layers of icy satellites in which very little salt is expected to enter.

Having laid down the most important limitations that we can identify, we can still use the scaling laws obtained for the Nusselt number as function of the Rayleigh number to evaluate the heat flux and to quantify the impact that a permeable solid-liquid change boundary might have had on the thermal evolution of both bottom magma ocean and core, and on the surface magma ocean. Combining the definition of Nusselt number, Rayleigh number, and their scaling relationship  $\text{Nu} = \gamma \text{Ra}^\beta$ , the heat flux  $Q$  can be evaluated by the following equation:

$$Q = \gamma \left( \frac{\alpha g \rho_s}{\kappa \eta} \right)^\beta k H_s^{3\beta-1} (T_{\text{bottom}} - T_{\text{top}})^{\beta+1}, \quad (\text{B.19})$$

with  $k = \rho_s C_p \kappa$  the thermal conductivity,  $\gamma$  and  $\beta$  the fitting coefficients and that depend on the phase change number  $\Phi$  and the problem considered. Their values are given in the Figure B.5a for the case with 2 magma oceans and in the eq. B.16 for the case of a solid in contact with only one magma ocean.  $T_{\text{bottom}}$  and  $T_{\text{top}}$  are the bottom and top potential temperature, respectively. Obviously, the super-isentropic temperature difference depends on the thickness of the solid mantle and we follow a very simple scenario similar to that of Morison et al. (2019), assuming that the top and bottom boundaries are at the liquidus temperature. We assume that crystallisation starts at a depth of 2500 km, first upward with both magma oceans then downwards with only a basal magma ocean. For any thickness of the crystallised mantle we can compute the predicted heat flow from equation (B.19) for different values of the  $\Phi$  parameters. Although simplistic, this scenario allows us to compare a conservative estimate of heat transfer by solid-state convection in the early mantle to that at present and draw some implications.

For simplicity, we consider all physical parameters constant and in particular the liquidus temperature gradient,  $\partial_r T_L \simeq -0.93 \text{Kkm}^{-1}$  (Andrault, Bolfan-Casanova, Nigro, et al. 2011), the isentropic temperature gradient,  $\partial_r T_L \simeq -0.17 \text{Kkm}^{-1}$  (Katsura et al. 2004), which allow us to relate the super-isentropic difference to the thickness of the layer as  $\Delta T \equiv T_{\text{bottom}} - T_{\text{top}} = 0.76H$  with  $H$  in km and  $\Delta T$  in K. For the other parameters, we use  $g = 9.8 \text{ms}^{-2}$ ,  $\alpha = 210^{-5} \text{K}^{-1}$ ,  $\kappa = 10^{-6} \text{m}^2 \text{s}^{-1}$ ,  $\rho_s = 410^3 \text{kgm}^{-3}$ ,  $C_p = 10^3 \text{Jkg}^{-1} \text{K}^{-1}$  and, for the viscosity, either  $\eta = 10^{18} \text{Pas}$ , possibly representative of the situation where the solid is close to the solidus, or  $\eta = 10^{22} \text{Pas}$ , similar to the present-time mantle viscosity.

Figure B.10 shows the results of this simple calculation. The choice of parameters makes the heat flux density for a completely solid mantle, using the classical boundary conditions and the large viscosity,  $q = 98 \text{mWm}^{-2}$ , similar to the present day value,  $q = 90 \text{mWm}^{-2}$  (Jaupart, Labrosse, et al. 2015), represented as a red dot on the figure. Decreasing the viscosity obviously leads to a larger heat flux. Having a basal magma ocean makes the heat flux 76% larger, with  $\gamma = 0.37$  instead of  $\gamma = 0.21$  as pre-factor in the scaling relation (B.19). The most spectacular result is

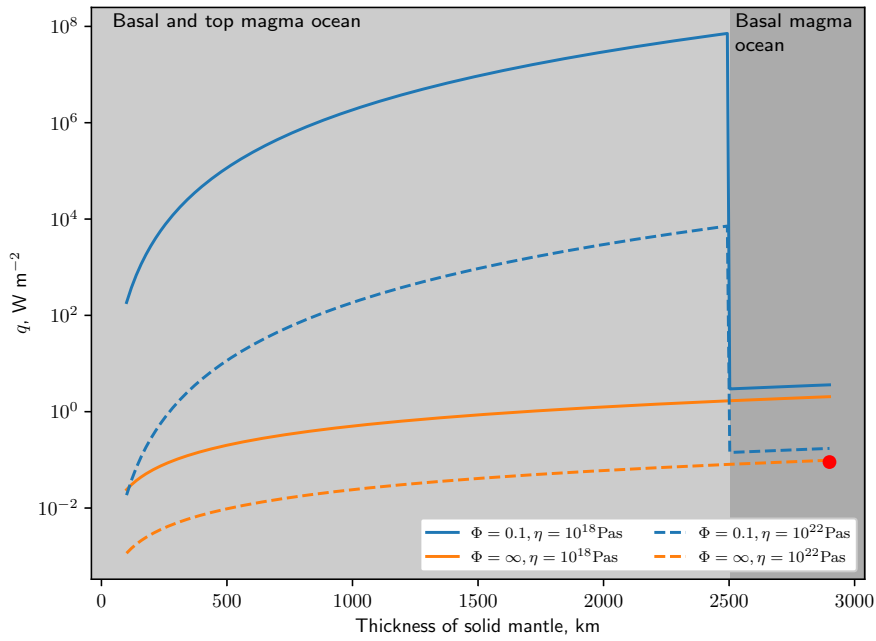


Figure B.10: Heat flux density predicted as a function of the thickness of crystallised mantle. For a thickness lower than 2500 km, we assume the existence of magma oceans above and below. For a thicker solid mantle, we assume only a basal magma ocean. The orange curves are computed using the scaling law obtained for  $\Phi = 0.1$ , the blue ones are computed with the scaling law obtained without the effect of the phase change boundary condition. Solid and dashed curves are for different values of the solid mantle viscosity, as labeled. The red dot represents the present day value of the mean surface heat flux.

obtained with magma oceans above and below. As a comparison, a magma ocean with a surface temperature of  $T_s = 3000\text{K}$  not surrounded by an atmosphere radiates  $q = 4.6\text{MWm}^{-2}$  into free space. This value is obtained for a convecting solid mantle of  $1200\text{km}$  thickness. Including an early atmosphere on top of the magma ocean makes its surface heat flow decrease significantly (e.g. Hamano et al. 2013; Lebrun et al. 2013; Salvador et al. 2017) so that the value just quoted is in fact a maximum achievable surface heat flux. On the other hand, the value  $\Phi = 0.1$  used to compute the results shown on figure B.10 is likely to be overestimated, possibly by orders of magnitude. It appears therefore that if both magma oceans existed at some point in the early times, convection in the solid mantle is not a limiting factor for the cooling of the deep Earth. The reason for the ease of heat transport in that case lies in the peculiar mode of convection that develops with no or very little deformation, the viscosity playing therefore no role in the process.

## B.6 Conclusions

In this study we have investigated the dynamics of a solid mantle bounded between two magma oceans or in contact with one at the bottom, with a semi-permeable phase-change at the solid-liquid boundary(ies). We explored systematically the parameter space to compare with and extend the results of the weakly non-linear analysis of Labrosse, Morison, et al. (2018). For the case when the solid is bounded above and below by magma oceans, we recover the two modes of convection predicted by Labrosse, Morison, et al. (ibid.): a steady-state up- or down-ward non-deforming translation and a deforming mode. Extending the previous results from Labrosse, Morison, et al. (ibid.) to high values of the Rayleigh number shows that the solution at small values of  $\Phi$  takes the form of alternating up- and down-ward translating blocks separated by thin deformation bands (isothermal core width  $\sim 1$ ). The two vertically moving blocks have a vertical velocity and a thermal structure that closely resemble the exact analytical solution for the pure translation mode (ibid.). Both convection modes are characterised by a very efficient heat transfer, in which the Nusselt number scales linearly with the Rayleigh number, whereas in the classical situation of Rayleigh-Bénard convection with non-penetrating boundary conditions, it scales as  $\text{Ra}^{1/3}$ . Consequently, we find that the predictions from the weakly non-linear analysis predict very well the behavior of the solution for the whole range of calculations performed in this study, with a Nusselt number as high as  $3 \cdot 10^3$ .

The situation with a magma ocean above and below the solid mantle may have occurred early in the history of Earth-or-larger-sized rocky Planets (Boukaré, Ricard, et al. 2015; Labrosse, Hernlund, and Coltice 2007; Thomas, Liu, et al. 2012). Assuming efficient mixing of the magma ocean, we expect the value of  $\Phi$  to be less than 0.01. Applying the present results to that situation suggests that heat and mass transfer would rapidly grow to values that are orders of magnitude larger than any rate encountered in the solid mantle after full crystallisation of magma oceans, of the same order or even larger than the black body heat flow at the surface of a bare magma ocean. This would promote a heat flow from the deep interior to the surface magma ocean so large that the basal magma ocean and the core would cool faster than previously thought, fast enough to drive an early dynamo.

A magma ocean that simply cools by radiating heat into space would solidify completely in a few thousand years (Monteux et al. 2016). Considering the effect

of a dense atmosphere can elongate this period to about 10 Myr at Earth position (e.g. Abe 1997; Hamano et al. 2013; Lebrun et al. 2013; Salvador et al. 2017). Longer timescales can be reached for planets closer to their star (e.g. Hamano et al. 2013; Salvador et al. 2017). It is however difficult to explain with these models the apparent longevity of the Martian magma ocean (Debaille et al. 2007). Our result suggest that the possibility of phase change between the crystallising mantle and the magma ocean allows for a very efficient heat transfer by convection in the solid. This means that the contribution of the heat flow from the deepest part of the planet to the magma ocean thermal budget may not be as negligible as usually assumed. If the mantle crystallizes upward from the bottom and is in contact with only one magma ocean, the heat flux scaling obtained here would suggest a heat flow a factor of two larger than that obtained for classical non-penetrating conditions, for the same Rayleigh number. The importance of that heat flow depends then crucially on the values of poorly constrained parameters such as the viscosity of the solid mantle. On the other hand, it is quite possible that a basal magma ocean formed on Mars owing to the density inversion between olivine and silicate melt at about 8 GPa (e.g. Agee and Walker 1988, 1993; Ohtani 1983). In that case, the heat flow across the solid mantle could be orders of magnitude larger, of the same order as the radiative surface heat flux, and contribute significantly to keep the surface magma ocean liquid, as long as the basal magma ocean has not crystallised. This could help making the magma ocean on Mars last  $\sim 100$ My (Debaille et al. 2007). Heat is not the only player in this scenario since fractional crystallisation would also lead to transfer of FeO between the top and basal magma oceans changing their freezing temperature (Andrault, Bolfan-Casanova, Bouhifd, et al. 2017). A full model including FeO exchange is therefore necessary to test whether this scenario could make the surface magma ocean live longer.

Considering now the case of only one magma ocean, the situation applies for the present time on icy satellites and possibly for a part of the history of the Earth (Labrosse, Hernlund, and Coltice 2007). We only studied here the situation with a magma ocean below the solid mantle but the case with a magma ocean above is its symmetrical in the cartesian geometry considered here (fig. B.6). The results presented above show that the form of convection and the thermal structure are dramatically modified and heat and mass transfer are greatly enhanced when phase melting and freezing occurs at one boundary, even though these effects are not as drastic as in the case of two phase change boundaries. In the case of a basal magma ocean that has been investigated thoroughly here, the dynamics and thermal structure bears many similarities with internally heated convection, with narrow cold plumes descending from the upper boundary and broad high temperature return flow elsewhere. Even though volumetric heating is not included in these calculation, the bottom boundary layer is completely suppressed and no hot plume can develop. This suggests that the dynamics of the surface ice shells of icy satellites and possibly of the early Earth mantle are entirely dominated by down-welling currents, leaving no role to hot plumes. In the case of the Earth mantle, the situation is certainly more complex with fractional crystallisation at the bottom possibly leading to compositional stratification, a situation that deserves further study.

In terms of heat transfer, we find that the dimensionless heat flux, the Nusselt number, scales with the Rayleigh number with an exponent equal to  $1/3$ , which is the same as for classical non-penetrating conditions, but with a pre-factor about 76%

higher. This means that, for the same Rayleigh number, the thermal evolution with a basal magma ocean should be about twice faster than without, and this imply that thermal evolution models, involving a basal magma ocean, should take that effect into account. The parameterisation of the heat flow at the bottom of the solid mantle cannot rely on the existence of a boundary layer, as was assumed by Labrosse, Hernlund, and Coltice (2007), since heat transfer happens by advection through the boundary. We expect however that, as compositionally dense material fractionally crystallizing at the bottom starts to accumulate (*ibid.*), the dynamics of the bottom of the solid mantle strongly departs from the one shown here.

## Acknowledgements

This research has been funded by the French Agence Nationale de la Recherche under the grant number ANR-15-CE31-0018-01, MaCoMaOc.

# Bibliography

- Abe, Y. (1997). “Thermal and chemical evolution of the terrestrial magma ocean”. In: *Phys. Earth Planet. Inter.* 100.1-4, pp. 27–39. DOI: 10.1016/S0031-9201(96)03229-3.
- Abe, Y. and T. Matsui (1986). “Early evolution of the Earth: Accretion, atmosphere formation, and thermal history”. In: *J. Geophys. Res. Solid Earth* 91.B13, E291–E302. DOI: 10.1029/JB091iB13p0E291.
- Agee, C. B. and D. Walker (1988). “Mass balance and phase density constraints on early differentiation of chondritic mantle”. In: *Earth Planet. Sci. Lett.* 90.2, pp. 144–156. DOI: 10.1016/0012-821X(88)90097-0.
- Agee, C. B. and D. Walker (1993). “Olivine flotation in mantle melt”. In: *Earth Planet. Sci. Lett.* 114.2-3, pp. 315–324. DOI: 10.1016/0012-821X(93)90033-6.
- Agrusta, R., A. Tommasi, D. Arcay, A. Gonzalez, and T. Gerya (2015). “How partial melting affects small-scale convection in a plume-fed sublithospheric layer beneath fast-moving plates”. In: *Geochem. Geophys. Geosyst.* 16.11, pp. 3924–3945.
- Alboussière, T., R. Deguen, and M. Melzani (2010). “Melting-induced stratification above the Earth’s inner core due to convective translation.” In: *Nature* 466, pp. 744–747. DOI: 10.1038/nature09257.
- Amestoy, P., I. Duff, J. L’Excellent, and J. Koster (2001). “A Fully Asynchronous Multifrontal Solver Using Distributed Dynamic Scheduling”. In: *SIAM J. Matrix Anal. Appl.* 23.1, pp. 15–41. DOI: 10.1137/S0895479899358194.
- Amestoy, P., A. Buttari, J.-Y. L’Excellent, and T. Mary (2019). “Performance and Scalability of the Block Low-Rank Multifrontal Factorization on Multicore Architectures”. In: *ACM Trans. Math. Softw.* 45.1. DOI: 10.1145/3242094.
- Amestoy, P., A. Guermouche, J.-Y. L’Excellent, and S. Pralet (2006). “Hybrid scheduling for the parallel solution of linear systems”. In: *Parallel Comput.* 32.2, pp. 136–156. DOI: 10.1016/j.parco.2005.07.004.
- Andrault, D., N. Bolfan-Casanova, M. A. Bouhifd, A. Boujibar, G. Garbarino, G. Manthilake, M. Mezouar, J. Monteux, P. Parisiades, and G. Pesce (2017). “Toward a coherent model for the melting behavior of the deep Earth’s mantle”. In: *Phys. Earth Planet. Inter.* 265, pp. 67–81.
- Andrault, D., N. Bolfan-Casanova, G. L. Nigro, M. A. Bouhifd, G. Garbarino, and M. Mezouar (2011). “Solidus and liquidus profiles of chondritic mantle: Implication for melting of the Earth across its history”. In: *Earth Planet. Sci. Lett.* 304.1-2, pp. 251–259. DOI: 10.1016/j.epsl.2011.02.006.
- Andrault, D., S. Petitgirard, G. Lo Nigro, J.-L. Devidal, G. Veronesi, G. Garbarino, and M. Mezouar (2012). “Solid–liquid iron partitioning in Earth’s deep mantle”. In: *Nature* 487.7407, pp. 354–357. DOI: 10.1038/nature11294.

- Baland, R.-M., G. Tobie, A. Lefèvre, and T. V. Hoolst (2014). “Titan’s internal structure inferred from its gravity field, shape, and rotation state”. In: *Icarus* 237.0, pp. 29–41. DOI: 10.1016/j.icarus.2014.04.007.
- Ballmer, M. D., D. L. Lourenço, K. Hirose, R. Caracas, and R. Nomura (2017). “Reconciling magma-ocean crystallization models with the present-day structure of the Earth’s mantle”. In: *Geochem. Geophys. Geosyst.* 18.7, pp. 2785–2806. DOI: 10.1002/2017GC006917.
- Bercovici, D. and Y. Ricard (2014). “Plate tectonics, damage and inheritance”. In: *Nature* 508, pp. 513–516. DOI: 10.1038/nature13072.
- Bercovici, D. and G. Schubert (1988). “Geoid and topography for infinite Prandtl number convection in a spherical shell”. In: *J. Geophys. Res.* 93, pp. 6430–6436. DOI: 10.1029/JB093iB06p06430.
- Bouffard, M., S. Labrosse, G. Choblet, A. Fournier, J. Aubert, and P. J. Tackley (2017). “A particle-in-cell method for studying double-diffusive convection in the liquid layers of planetary interiors”. In: *J. Comput. Phys.* 346, pp. 552–571. DOI: 10.1016/j.jcp.2017.06.028.
- Boukaré, C.-E. and Y. Ricard (2017). “Modeling phase separation and phase change for magma ocean solidification dynamics”. In: *Geochem. Geophys. Geosyst.* 18.9, pp. 3385–3404. DOI: 10.1002/2017GC006902.
- Boukaré, C., Y. Ricard, and G. Fiquet (2015). “Thermodynamics of the MgO-FeO-SiO<sub>2</sub> system up to 140 GPa: Application to the crystallization of Earth’s magma ocean”. In: *J. Geophys. Res. Solid Earth* 120.9, pp. 6085–6101. DOI: 10.1002/2015JB011929.
- Boukaré, C., E. Parmentier, and S. Parman (2018). “Timing of mantle overturn during magma ocean solidification”. In: *Earth Planet. Sci. Lett.* 491, pp. 216–225. DOI: 10.1016/j.epsl.2018.03.037.
- Braginsky, S. I. and P. H. Roberts (1995). “Equations governing convection in earth’s core and the geodynamo”. In: *Geophys. Astrophys. Fluid Dyn.* 79.1-4, pp. 1–97. DOI: 10.1080/03091929508228992.
- Čadež, O., G. Tobie, T. Van Hoolst, M. Massé, G. Choblet, A. Lefèvre, G. Mitri, R.-M. Baland, M. Běhounková, O. Bourgeois, and A. Trinh (2016). “Enceladus’s internal ocean and ice shell constrained from Cassini gravity, shape, and libration data”. In: *Geophys. Res. Lett.* 43.11, pp. 5653–5660. DOI: 10.1002/2016GL068634.
- Canuto, C., M. Yousuff Hussaini, A. Quarteroni, and T. A. Zang (1985). *Spectral Methods in Fluid Dynamics*. Springer Series in Computational Physics.
- Caracas, R., K. Hirose, R. Nomura, and M. D. Ballmer (2019). “Melt–crystal density crossover in a deep magma ocean”. In: *Earth Planet. Sci. Lett.* 516, pp. 202–211. DOI: 10.1016/j.epsl.2019.03.031.
- Chambat, F., S. Benzoni-Gavage, and Y. Ricard (2014). “Jump conditions and dynamic surface tension at permeable interfaces such as the inner core boundary”. In: *C.R. Geosci.* 346.5-6, pp. 110–118. DOI: 10.1016/j.crte.2014.04.006.
- Chandrasekhar, S. (1961). *Hydrodynamic and hydromagnetic stability*. Oxford.
- Christensen, U. R. (1985). “Thermal evolution models for the Earth”. In: *J. Geophys. Res. Solid Earth* 90.B4, pp. 2995–3007. DOI: 10.1029/JB090iB04p02995.
- Christensen, U. R. and D. A. Yuen (1989). “Time-dependent convection with non-Newtonian viscosity”. In: *J. Geophys. Res.* 94.B1, pp. 814–820. DOI: 10.1029/JB094iB01p00814.

- Coltice, N., M. Moreira, J. Hernlund, and S. Labrosse (2011). “Crystallization of a basal magma ocean recorded by Helium and Neon”. In: *Earth Planet. Sci. Lett.* 308.1-2, pp. 193–199. DOI: 10.1016/j.eps1.2011.05.045.
- Crank, J. (1984). *Free and moving boundary problems*. Oxford University Press Oxford [Oxfordshire] ; New York, 425 p.
- Cross, M. C. and P. C. Hohenberg (1993). “Pattern Formation outside of equilibrium”. In: *Rev. Modern Phys.* 65.3, pp. 851–1112.
- Davaille, A. and C. Jaupart (1993). “Transient high-Rayleigh-number thermal convection with large viscosity variations”. In: *J. Fluid Mech.* 253, pp. 141–166.
- Davies, G. F. (1979). “Thickness and thermal history of continental crust and root zones”. In: *Earth Planet. Sci. Lett.* 44.2, pp. 231–238. DOI: 10.1016/0012-821X(79)90171-7.
- Davies, G. F. (1988). “Ocean bathymetry and mantle convection: 1. Large-scale flow and hotspots”. In: *J. Geophys. Res. Solid Earth* 93.B9, pp. 10467–10480. DOI: 10.1029/JB093iB09p10467.
- Davies, J. and D. Davies (Nov. 2009). “Earth’s surface heat flux”. In: *Solid Earth Discuss.* 1. DOI: 10.5194/sed-1-1-2009.
- Davis, T. A. (2004). “Algorithm 832: UMFPACK V4.3—an Unsymmetric-Pattern Multifrontal Method”. In: *ACM Trans. Math. Softw.* 30.2, pp. 196–199. DOI: 10.1145/992200.992206.
- Debaille, V., A. D. Brandon, Q. Z. Yin, and B. Jacobsen (2007). “Coupled  $^{142}\text{Nd}$  –  $^{143}\text{Nd}$  evidence for a protracted magma ocean in Mars”. In: *Nature* 450, p. 525.
- Deguen, R. (2013). “Thermal convection in a spherical shell with melting/freezing at either or both of its boundaries”. In: *J. Earth Sci.* 24.5, pp. 669–682. DOI: 10.1007/s12583-013-0364-8.
- Deguen, R., T. Alboussière, and S. Labrosse (2018). “Double-diffusive translation of Earth’s inner core”. In: *Geophys. J. Int.*
- Deguen, R., T. Alboussière, and P. Cardin (2013). “Thermal convection in Earth’s inner core with phase change at its boundary”. In: *Geophys. J. Int.* DOI: 10.1093/gji/ggt202.
- Dormy, E. (1997). “Modelisation Numerique De La Dynamo Terrestre”. PhD thesis. IGP.
- Elkins-Tanton, L. T. (2012). “Magma Oceans in the Inner Solar System”. In: *Annu. Rev. Earth Planet. Sci.* 40.1, pp. 113–139. DOI: 10.1146/annurev-earth-042711-105503.
- Elkins-Tanton, L. T., S. Burgess, and Q. Z. Yin (2011). “The lunar magma ocean: Reconciling the solidification process with lunar petrology and geochronology”. In: *Earth Planet. Sci. Lett.* 304.3-4, pp. 326–336. DOI: 10.1016/j.eps1.2011.02.004.
- Elkins-Tanton, L. T., E. M. Parmentier, and P. C. Hess (2003). “Magma ocean fractional crystallization and cumulate overturn in terrestrial planets: Implications for Mars”. In: *Meteorit. Planet. Sci.* 38.12, pp. 1753–1771. DOI: 10.1111/j.1945-5100.2003.tb00013.x.
- Elkins-Tanton, L. T., S. E. Zaranek, E. M. Parmentier, and P. C. Hess (2005). “Early magnetic field and magmatic activity on Mars from magma ocean cumulate overturn”. In: *Earth Planet. Sci. Lett.* 236.1-2, pp. 1–12. DOI: 10.1016/j.eps1.2005.04.044.

- Fiquet, G., A. L. Auzende, J. Siebert, A. Corgne, H. Bureau, H. Ozawa, and G. Garbarino (2010). “Melting of peridotite to 140 gigapascals.” In: *Science* 329.5998, pp. 1516–8. DOI: 10.1126/science.1192448.
- Gaidos, E. J. and F. Nimmo (2000). “Planetary science: Tectonics and water on Europa”. In: *Nature* 405.6787, pp. 637–+.
- Gomi, H., K. Ohta, K. Hirose, S. Labrosse, R. Caracas, M. J. Verstraete, and J. Hernlund (2013). “The high conductivity of iron and thermal evolution of the Earth’s core”. In: *Phys. Earth Planet. Inter.* 224, pp. 88–103. DOI: 10.1016/j.pepi.2013.07.010.
- Grasset, O., C. Sotin, and F. Deschamps (2000). “On the internal structure and dynamics of Titan”. In: *Planet. Space Sci.* 48.7–8, pp. 617–636.
- Grigné, C., S. Labrosse, and P. J. Tackley (2005). “Convective heat transfer as a function of wavelength: Implications for the cooling of the earth”. In: *J. Geophys. Res. B: Solid Earth* 110.3, pp. 1–16. DOI: 10.1029/2004JB003376.
- Guo, W., G. Labrosse, and R. Narayanan (2012). *The Application of the Chebyshev-Spectral Method in Transport Phenomena*. Springer-Verlag Berlin. DOI: 10.1007/978-90-481-9809-2.
- Hamano, K., Y. Abe, and H. Genda (2013). “Emergence of two types of terrestrial planet on solidification of magma ocean.” In: *Nature* 497.7451. DOI: 10.1038/nature12163.
- Harten, A. (1983). “High resolution schemes for hyperbolic conservation laws”. In: *J. Comput. Phys.* 49.3, pp. 357–393. DOI: 10.1016/0021-9991(83)90136-5.
- Haynes, W. M. and D. R. Lide (2011). *CRC Handbook of Chemistry and Physics*. 92nd ed. ProQuest Ebook Central ATO Loan. Baton Rouge : CRC Press. ISBN: 9781439855126.
- Hernlund, J. and A. McNamara (2015). “7.11 - The Core–Mantle Boundary Region”. In: *Treatise on Geophysics (Second Edition)*. Ed. by G. Schubert. Second Edition. Oxford: Elsevier, pp. 461–519. DOI: 10.1016/B978-0-444-53802-4.00136-6.
- Hernlund, J. and P. Tackley (Dec. 2008). “Modeling mantle convection in the spherical annulus”. In: *Phys. Earth Planet. Inter.* 171.1-4, pp. 48–54. DOI: 10.1016/j.pepi.2008.07.037.
- Hess, P. C. and E. M. Parmentier (1995). “A model for the thermal and chemical evolution of the Moon’s interior: implications for the onset of mare volcanism”. In: *Earth Planet. Sci. Lett.* 134.3-4, pp. 501–514. DOI: 10.1016/0012-821X(95)00138-3.
- Holmes, A. (1913). *The age of the Earth*. English. Harper ; London.
- Houseman, G. (1988). “The dependence of convection planform on mode of heating”. In: *Nature* 332.6162, pp. 346–349. DOI: 10.1038/332346a0.
- Huang, Y., V. Chubakov, F. Mantovani, R. L. Rudnick, and W. F. McDonough (2013). “A reference Earth model for the heat-producing elements and associated geoneutrino flux”. In: *Geochem. Geophys. Geosyst.* 14.6, pp. 2003–2029. DOI: 10.1002/ggge.20129.
- Jarvis, G. T. and D. P. McKenzie (1980). “Convection in a compressible fluid with infinite Prandtl number”. In: *J. Fluid Mech.* 96, pp. 515–583.
- Jaupart, C., S. Labrosse, F. Lucazeau, and J.-C. Mareschal (2015). “7.06 - Temperatures, Heat, and Energy in the Mantle of the Earth”. In: *Treatise on Geophysics (Second Edition)*. Ed. by G. Schubert. Second Edition. Oxford: Elsevier, pp. 223–270. ISBN: 978-0-444-53803-1. DOI: 10.1016/B978-0-444-53802-4.00126-3.

- Jaupart, C. and J.-C. Mareschal (2011). *Heat generation and transport in the Earth*. Cambridge: Cambridge University Press, p. 464.
- Jeffreys, H. (1930). “The instability of a compressible fluid heated below”. In: *Math. Proc. Camb. Phil. Soc.* 26, pp. 170–172.
- Katsura, T., H. Yamada, O. Nishikawa, M. Song, A. Kubo, T. Shinmei, S. Yokoshi, Y. Aizawa, T. Yoshino, M. J. Walter, and E. Ito (2004). “Olivine-Wadsleyite transition in the system (Mg,Fe)SiO<sub>4</sub>”. In: *J. Geophys. Res.* 109, B02209. DOI: 10.1029/2003JB002438.
- Khurana, K. K., M. G. Kivelson, D. J. Stevenson, G. Schubert, C. T. Russell, R. J. Walker, and C. Polansky (Oct. 1998). “Induced magnetic fields as evidence for subsurface oceans in Europa and Callisto”. In: *Nature* 395.6704, pp. 777–780. DOI: 10.1038/27394.
- King, E. M., S. Stellmach, and J. M. Aurnou (2012). “Heat transfer by rapidly rotating Rayleigh–Bénard convection”. In: *J. Fluid Mech.* 691, pp. 568–582. DOI: 10.1017/jfm.2011.493.
- Koker, N. de, G. Steinle-Neumann, and V. Vlček (2012). “Electrical resistivity and thermal conductivity of liquid Fe alloys at high P and T, and heat flux in Earth’s core”. In: *PNAS* 109.11, pp. 4070–4073. DOI: 10.1073/pnas.1111841109.
- Korenaga, J. (2011). “Clairvoyant geoneutrinos”. In: *Nat. Geosci.* 4, pp. 581–582. DOI: 10.1038/ngeo1240.
- Labrosse, S., J. Hernlund, and N. Coltice (2007). “A crystallizing dense magma ocean at the base of the Earth’s mantle.” In: *Nature* 450.7171, pp. 866–869. DOI: 10.1038/nature06355.
- Labrosse, S. (2002). “Hotspots, mantle plumes and core heat loss”. In: *Earth Planet. Sci. Lett.* 199.1, pp. 147–156. DOI: 10.1016/S0012-821X(02)00537-X.
- Labrosse, S. (2015). “Thermal evolution of the core with a high thermal conductivity”. In: *Phys. Earth Planet. Inter.* 247. Transport Properties of the Earth’s Core, pp. 36–55. DOI: 10.1016/j.pepi.2015.02.002.
- Labrosse, S., J. Hernlund, and K. Hirose (2015). “Fractional Melting and Freezing in the Deep Mantle and Implications for the Formation of a Basal Magma Ocean”. In: *The Early Earth*. American Geophysical Union (AGU). Chap. 7, pp. 123–142. ISBN: 9781118860359. DOI: 10.1002/9781118860359.ch7.
- Labrosse, S., A. Morison, R. Deguen, and T. Alboussière (2018). “Rayleigh – Bénard convection in a creeping solid with melting and freezing at either or both its horizontal boundaries”. In: *J. Fluid Mech.* 846, pp. 5–36. DOI: 10.1017/jfm.2018.258.
- Lasbleis, M., R. Deguen, P. Cardin, and S. Labrosse (2015). “Earth’s inner core dynamics induced by the Lorentz force”. In: *Geophys. J. Int.* 202, pp. 548–563. DOI: 10.1093/gji/ggv155.
- Lay, T., J. Hernlund, and B. A. Buffett (2008). “Core–mantle boundary heat flow”. In: *Nat. Geosci.* 1, pp. 25–32. DOI: 10.1038/ngeo.2007.44.
- Lebrun, T., H. Massol, E. Chassefière, A. Davaille, E. Marcq, P. Sarda, F. Leblanc, and G. Brandeis (2013). “Thermal evolution of an early magma ocean in interaction with the atmosphere”. In: *J. Geophys. Res. E: Planets* 118.6, pp. 1155–1176. DOI: 10.1002/jgre.20068.
- Lekic, V., S. Cottaar, A. Dziewonski, and B. Romanowicz (2012). “Cluster analysis of global lower mantle tomography: A new class of structure and implications for chemical heterogeneity”. In: *Earth Planet. Sci. Lett.* 357–358, pp. 68–77.

- Lister, J. R. and B. A. Buffett (1995). “The strength and efficiency of thermal and compositional convection in the geodynamo”. In: *Phys. Earth Planet. Inter.* 91.1. Study of the Earth’s Deep Interior, pp. 17–30. DOI: 10.1016/0031-9201(95)03042-U.
- Lord Kelvin (1864). “On the Secular Cooling of the Earth”. In: *Trans. R. Soc. Edinburgh* XXIII, pp. 167–169.
- Lourenço, D. L., A. B. Rozel, T. Gerya, and P. J. Tackley (2018). “Efficient cooling of rocky planets by intrusive magmatism”. In: *Nat. Geosci.* 11.5, pp. 322–327. DOI: 10.1038/s41561-018-0094-8.
- Lucazeau, F. (2019). “Analysis and Mapping of an Updated Terrestrial Heat Flow Data Set”. In: *Geochem. Geophys. Geosyst.* 20. DOI: 10.1029/2019GC008389.
- Malkus, W. and G. Veronis (1958). “Finite amplitude cellular convection”. In: *J. Fluid Mech.* 4, pp. 225–260.
- Manneville, P. (2004). *Instabilities, Chaos and Turbulence - An introduction to non-linear dynamics and complex systems*. London: Imperial College Press.
- Maurice, M., N. Tosi, H. Samuel, A.-C. Plesa, C. Hüttig, and D. Breuer (2017). “Onset of solid-state mantle convection and mixing during magma ocean solidification”. In: *J. Geophys. Res. Planets*. DOI: 10.1002/2016JE005250.
- McKenzie, D. P., J. M. Roberts, and N. O. Weiss (1974). “Convection in the Earth’s mantle: towards a numerical simulation”. In: *J. Fluid Mech.* 62, pp. 465–538.
- Mizzon, H. and M. Monnereau (2013). “Implication of the lopsided growth for the viscosity of Earth’s inner core”. In: *Earth Planet. Sci. Lett.* 361, pp. 391–401. DOI: 10.1016/j.epsl.2012.11.005.
- Monnereau, M. and F. Dubuffet (2002). “Is Io’s mantle really molten?” In: *Icarus* 158, pp. 450–59.
- Monnereau, M., M. Calvet, L. Margerin, and A. Souriau (2010). “Lopsided Growth of Earth’s Inner Core”. In: *Science* 328.5981, pp. 1014–1017. DOI: 10.1126/science.1186212.
- Monteux, J., D. Andraut, and H. Samuel (2016). “On the cooling of a deep terrestrial magma ocean”. In: *Earth Planet. Sci. Lett.* 448, pp. 140–149. DOI: 10.1016/j.epsl.2016.05.010.
- Moresi, L. and V. Solomatov (1995). “Numerical investigation of 2D convection with extremely large viscosity variations”. In: *Phys. Fluids* 7.9, pp. 2154–2162. DOI: 10.1063/1.868465.
- Morison, A., S. Labrosse, R. Deguen, and T. Alboussière (2019). “Timescale of overturn in a magma ocean cumulate”. In: *Earth Planet. Sci. Lett.* 516, pp. 25–36. DOI: 10.1016/j.epsl.2019.03.037.
- Mosenfelder, J. L., P. D. Asimow, D. J. Frost, D. C. Rubie, and T. J. Ahrens (2009). “The MgSiO<sub>3</sub> system at high pressure: Thermodynamic properties of perovskite, postperovskite, and melt from global inversion of shock and static compression data”. In: *J. Geophys. Res.* 114.1, pp. 1–16. DOI: 10.1029/2008JB005900.
- Mosenfelder, J. L., P. D. Asimow, and T. J. Ahrens (2007). “Thermodynamic properties of Mg<sub>2</sub>SiO<sub>4</sub> liquid at ultra-high pressures from shock measurements to 200 GPa on forsterite and wadsleyite”. In: *J. Geophys. Res. Solid Earth* 112.B6.
- Nomura, R., H. Ozawa, S. Tateno, K. Hirose, J. Hernlund, S. Muto, H. Ishii, and N. Hiraoka (2011). “Spin crossover and iron-rich silicate melt in the Earth’s deep mantle”. In: *Nature* 473, pp. 199–202. DOI: 10.1038/nature09940.

- Ohtani, E. (1983). “Melting temperature distribution and fractionation in the lower mantle”. In: *Phys. Earth Planet. Inter.* 33.1, pp. 12–25. DOI: 10.1016/0031-9201(83)90003-1.
- Pappalardo, R. T., J. W. Head, R. Greeley, R. J. Sullivan, C. Pilcher, G. Schubert, W. B. Moore, M. H. Carr, J. M. Moore, M. J. S. Belton, and D. L. Goldsby (1998). “Geological evidence for solid-state convection in Europa’s ice shell”. In: *Nature* 391.6665, pp. 365–368.
- Parmentier, E. M. (1978). “Study Of Thermal-Convection In Non-Newtonian Fluids”. In: *J. Fluid Mech.* 84, pp. 1–11.
- Parmentier, E. M. and C. Sotin (2000). “Three-dimensional numerical experiments on thermal convection in a very viscous fluid: Implications for the dynamics of a thermal boundary layer at high Rayleigh number”. In: *Phys. Fluids* 12.3, pp. 609–617.
- Parmentier, E. M., C. Sotin, and B. J. Travis (1994). “Turbulent 3-D thermal convection in an infinite Prandtl number, volumetrically heated fluid: implications for mantle dynamics”. In: *Geophys. J. Int.* 116.2, pp. 241–251. DOI: 10.1111/j.1365-246X.1994.tb01795.x.
- Parmentier, E., S. Zhong, and M. Zuber (2002). “Gravitational differentiation due to initial chemical stratification: origin of lunar asymmetry by the creep of dense KREEP?” In: *Earth Planet. Sci. Lett.* 201.3-4, pp. 473–480. DOI: 10.1016/S0012-821X(02)00726-4.
- Pedlosky, J. (1987). *Geophysical Fluid Dynamics*. New York: Springer-Verlag.
- Perry, J. (1895). “On the Age of the Earth”. In: *Nature* 51, pp. 341–342. DOI: 10.1038/051341b0.
- Pozzo, M., C. Davies, D. Gubbins, and D. Alfè (2014). “Thermal and electrical conductivity of solid iron and iron–silicon mixtures at Earth’s core conditions”. In: *Earth Planet. Sci. Lett.* 393, pp. 159–164. DOI: 10.1016/j.epsl.2014.02.047.
- Ribe, N. (2007). “Analytical approaches to mantle dynamics”. In: *Treatise on Geophysics*.
- Ricard, Y. (2015). “7.02 - Physics of Mantle Convection”. In: *Treatise on Geophysics (Second Edition)*. Ed. by G. Schubert. Second Edition. Oxford: Elsevier, pp. 23–71. ISBN: 978-0-444-53803-1. DOI: 10.1016/B978-0-444-53802-4.00127-5.
- Ricard, Y., S. Labrosse, and F. Dubuffet (2014). “Lifting the cover of the cauldron: Convection in hot planets”. In: *Geochem. Geophys. Geosyst.*, pp. 4617–4630. DOI: 10.1002/2014GC005556.Received.
- Ricard, Y. and C. Vigny (1989). “Mantle dynamics with induced plate tectonics”. In: *J. Geophys. Res.* 94.B12, pp. 17543–17559. DOI: 10.1029/JB094iB12p17543.
- Richter, F. M. (1986). “Kelvin and the Age of the Earth”. In: *J. Geol.* 94.3, pp. 395–401.
- Righter, K., R. L. Hervig, and D. A. Kring (1998). “Accretion and core formation on Mars: molybdenum contents of melt inclusion glasses in three SNC meteorites”. In: *Geochim. Cosmochim. Acta* 62.12, pp. 2167–2177. DOI: 10.1016/S0016-7037(98)00132-X.
- Roberts, P. H. and E. M. King (Sept. 2013). “On the genesis of the Earth’s magnetism”. In: *Rep. Prog. Phys.* 76.9, p. 6801. DOI: 10.1088/0034-4885/76/9/096801.

- Salvador, A., H. Massol, A. Davaille, E. Marcq, P. Sarda, and E. Chassefière (2017). “The relative influence of H<sub>2</sub>O and CO<sub>2</sub> on the primitive surface conditions and evolution of rocky planets”. In: *J. Geophys. Res.* 122.7, pp. 1458–1486. DOI: 10.1002/2017JE005286.
- Schlüter, A., D. Lortz, and F. Busse (1965). “On the Stability of Steady Finite Amplitude Convection”. In: *J. Fluid Mech.* 23, pp. 129–144.
- Schubert, G., D. L. Turcotte, and P. Olson (2004). *Mantle convection in the Earth and Planets*.
- Sleep, N. H. (1990). “Hotspots and mantle plumes: Some phenomenology”. In: *J. Geophys. Res. Solid Earth* 95, pp. 6715–6736. DOI: 10.1029/JB095iB05p06715.
- Sleep, N. H. (2000). “Evolution of the mode of convection within terrestrial planets”. In: *J. Geophys. Res. Planets* 105.E7, pp. 17563–17578. DOI: 10.1029/2000JE001240.
- Smolarkiewicz, P. K. and L. G. Margolin (1998). “MPDATA: A Finite-Difference Solver for Geophysical Flows”. In: *J. Comput. Phys.* 140.2, pp. 459–480. DOI: 10.1006/jcph.1998.5901.
- Soderlund, K. M., B. E. Schmidt, J. Wicht, and D. D. Blankenship (Jan. 2014). “Ocean-driven heating of Europa’s icy shell at low latitudes”. In: *Nat. Geosci.* 7.1, pp. 16–19. DOI: 10.1038/ngeo2021.
- Sohl, F., H. Hussmann, B. Schwentker, T. Spohn, and R. D. Lorenz (2003). “Interior structure models and tidal Love numbers of Titan”. In: *J. Geophys. Res.* 108.E12.
- Solomatov, V. (2015). “Chapter 4 Magma Oceans and Primordial Mantle Differentiation”. In: *Treatise on Geophysics*. Vol. 9. Elsevier, pp. 91–119.
- Sotin, C. and S. Labrosse (1999). “Three-dimensional thermal convection in an iso-viscous, infinite Prandtl number fluid heated from within and from below: Applications to the transfer of heat through planetary mantles”. In: *Phys. Earth Planet. Inter.* 112.3-4, pp. 171–190. DOI: 10.1016/S0031-9201(99)00004-7.
- Stacey, F. D. and D. E. Loper (1983). “The thermal boundary-layer interpretation of D” and its role as a plume source”. In: *Phys. Earth Planet. Inter.* 33.1, pp. 45–55. DOI: 10.1016/0031-9201(83)90006-7.
- Strutt, J. W. ( R. (1916). “On Convection Currents in a Horizontal Layer of Fluid, when the Higher Temperature is on the Under Side”. In: *Phil. Mag.* 32.192, pp. 529–546. DOI: 10.1080/14786441608635602.
- Tackley, P. (2000). “Self-consistent generation of tectonic plates in time-dependent, three-dimensional mantle convection simulations, 2. Strain weakening and asthenosphere”. In: *Geochem. Geophys. Geosyst.* 01.23.
- Tackley, P. (2008). “Modelling compressible mantle convection with large viscosity contrasts in a three-dimensional spherical shell using the yin-yang grid”. In: *Phys. Earth Planet. Inter.* 171.1-4, pp. 7–18. DOI: 10.1016/j.pepi.2008.08.005.
- Thomas, C. W. and P. D. Asimow (2013). “Direct shock compression experiments on premolten forsterite and progress toward a consistent high-pressure equation of state for CaO-MgO-Al<sub>2</sub>O<sub>3</sub>-SiO<sub>2</sub>-FeO liquids”. In: *J. Geophys. Res.* 118.11, pp. 5738–5752. DOI: 10.1002/jgrb.50374.
- Thomas, C. W., Q. Liu, C. B. Agee, P. D. Asimow, and R. A. Lange (2012). “Multi-technique equation of state for Fe<sub>2</sub>SiO<sub>4</sub>melt and the density of Fe-bearing silicate melts from 0 to 161 GPa”. In: *J. Geophys. Res. Solid Earth* 117.B10. DOI: 10.1029/2012JB009403.

- Tobie, G., G. Choblet, and C. Sotin (2003). “Tidally heated convection: Constraints on Europa’s ice shell thickness”. In: *J. Geophys. Res.* 108, p. 5124. DOI: 10.1029/2003JE002099.
- Tobie, G., J. I. Lunine, and C. Sotin (2006). “Episodic outgassing as the origin of atmospheric methane on Titan”. In: *Nature* 440.7080, pp. 61–64. DOI: 10.1038/nature04497.
- Tosi, N., A. C. Plesa, and D. Breuer (2013). “Overturn and evolution of a crystallized magma ocean: A numerical parameter study for Mars”. In: *J. Geophys. Res. E: Planets* 118.7, pp. 1512–1528. DOI: 10.1002/jgre.20109.
- Turcotte, D. L. and E. R. Oxburgh (1967). “Finite amplitude convective cells and continental drift”. In: *J. Fluid Mech.* 28, pp. 29–42.
- Turcotte, D. L. and G. Schubert (Apr. 2002). *Geodynamics - 2nd Edition*, p. 472. DOI: 10.2277/0521661862.
- Ulvrova, M., S. Labrosse, N. Coltice, P. Raback, and P. J. Tackley (2012). “Numerical modelling of convection interacting with a melting and solidification front: Application to the thermal evolution of the basal magma ocean”. In: *Phys. Earth Planet. Inter.* 207, pp. 51–66.
- Wasson, J. T. and P. H. Warren (1980). “Contribution of the Mantle to the Lunar Asymmetry”. In: *Icarus* 44, pp. 752–771. DOI: 10.1016/0019-1035(80)90142-6.
- Weideman, J. A. C. and S. C. Reddy (2000). “A MATLAB differentiation matrix suite”. In: *ACM Trans. Math. Software* 26.4, pp. 465–519. DOI: 10.1145/365723.365727.
- Wolstencroft, M., J. Davies, and D. Davies (2009). “Nusselt–Rayleigh number scaling for spherical shell Earth mantle simulation up to a Rayleigh number of 10<sup>9</sup>”. In: *Phys. Earth Planet. Inter.* 176.1, pp. 132–141.
- Wood, J. A., J. Dickey J. S., U. B. Marvin, and B. N. Powell (1970). “Lunar anorthosites and a geophysical model of the moon”. In: *Geochim. Cosmochim. Acta Supplement 1*, p. 965.
- Zahnle, K. J., J. F. Kasting, and J. B. Pollack (1988). “Evolution of a steam atmosphere during earth’s accretion”. In: *Icarus* 74.1, pp. 62–97. DOI: 10.1016/0019-1035(88)90031-0.
- Zhang, N., E. M. Parmentier, and Y. Liang (2013). “A 3-D numerical study of the thermal evolution of the Moon after cumulate mantle overturn: The importance of rheology and core solidification”. In: *J. Geophys. Res. Planets* 118.9, pp. 1789–1804. DOI: 10.1002/jgre.20121.
- Zhong, S., E. M. Parmentier, and M. T. Zuber (2000). “A dynamic origin for the global asymmetry of lunar mare basalts”. In: *Earth Planet. Sci. Lett.* 177.3-4, pp. 131–140. DOI: 10.1016/S0012-821X(00)00041-8.



# List of Figures

1.1	Values of Urey number acceptable with classical thermal evolution models . . . . .	18
1.2	Formation of a BMO owing to crystals settling at intermediate depth . . . . .	21
1.3	Translation mode for the inner core . . . . .	23
1.4	Most unstable modes of convection with phase change boundary condition . . . . .	23
2.1	Problem setup . . . . .	26
2.2	Dynamic topography at the boundaries . . . . .	28
3.1	Eigenmodes with non-penetrative top boundary . . . . .	42
3.2	Eigenmodes with flow-through top boundary . . . . .	43
3.3	Critical Rayleigh and degree for varying $\Phi^-$ . . . . .	44
3.4	Critical Rayleigh and degree for varying $\Phi^+$ . . . . .	44
3.5	Critical Rayleigh and degree for varying $\Phi^+ = \Phi^-$ . . . . .	45
3.6	Neutral Rayleigh of several modes vs aspect ratio, flow-through at bottom boundary . . . . .	45
3.7	Neutral Rayleigh of several modes vs aspect ratio, flow-through at top boundary . . . . .	46
3.8	Neutral Rayleigh of several modes vs aspect ratio, flow-through at both boundaries . . . . .	46
3.9	Frame in a degree-one translation case . . . . .	47
4.1	Oscillations on temperature field obtained with MPDATA . . . . .	52
4.2	Staggered grid used in StagYY . . . . .	53
4.3	Temperature fields and streamlines in $(\Phi^-, Ra/Ra_c)$ space . . . . .	57
4.4	Temperature fields and streamlines in $(\Phi^-, \gamma)$ space . . . . .	58
4.5	Mean temperature vs Ra for various $\Phi^-$ . . . . .	59
4.6	RMS velocity vs Ra for various $\Phi^-$ . . . . .	59
4.7	Nu vs Ra for various $\Phi^-$ . . . . .	60
4.8	Temperature fields and streamlines in $(\Phi^+, Ra/Ra_c)$ space . . . . .	62
4.9	Temperature fields and streamlines in $(\Phi^+, \gamma)$ space . . . . .	63
4.10	Mean temperature vs Ra for various $\Phi^+$ . . . . .	64
4.11	RMS velocity vs Ra for various $\Phi^+$ . . . . .	64
4.12	Nu vs Ra for various $\Phi^+$ . . . . .	65
4.13	Temperature fields and streamlines in $(\Phi^\pm, Ra/Ra_c)$ space . . . . .	68
4.14	Temperature fields and streamlines in $(\Phi^\pm, \gamma)$ space . . . . .	69
4.15	Idealized temperature field in the translation regime . . . . .	70
4.16	Mean temperature vs Ra for various $\Phi^\pm$ . . . . .	70

LIST OF FIGURES

---

4.17	RMS velocity vs Ra for various $\Phi^\pm$ . . . . .	71
4.18	Nu vs Ra for various $\Phi^\pm$ . . . . .	71
6.1	Temperature and composition reference profiles for the stability analysis	98
6.2	Growth time of the most unstable mode for the Earth, Mars, and the Moon . . . . .	105
6.3	Most unstable convection modes . . . . .	107
6.4	Destabilization timescale of several harmonics degree . . . . .	108
6.5	Compositional/thermal cases destabilization timescale ratio . . . . .	109
6.6	Growth time of the most unstable mode versus Stokes time . . . . .	110
6.7	Effect of the partition coefficient on the destabilization timescale . . . . .	112
7.1	Temperature and compositional fields 1/3 . . . . .	124
7.2	Temperature and compositional fields 2/3 . . . . .	125
7.3	Temperature and compositional fields 3/3 . . . . .	126
7.4	Time series . . . . .	127
A.1	Dynamic topography at the boundaries . . . . .	134
A.2	Instability growth rate $\sigma$ as a function of $Ra/Ra_c$ . . . . .	140
A.3	Finite amplitude velocity in the translation mode. . . . .	141
A.4	Temperature profile in the translation mode . . . . .	142
A.5	Critical Rayleigh number and wavenumber as function of the phase change numbers . . . . .	145
A.6	Variation of the maxima of profiles as a function of $\Phi$ . . . . .	147
A.7	First unstable mode for three different values of $\Phi^+ = \Phi^-$ . . . . .	149
A.8	Growth rate of deforming perturbation over a steady translating solution . . . . .	150
A.9	Range of wave numbers as function of the reduced Rayleigh number . . . . .	151
A.10	Maximum growth rate for a non-null $k$ mode at the critical Rayleigh number for the onset of the translation mode . . . . .	152
A.11	Heat flux coefficient as a function of the phase change numbers and Nusselt number as a function of Rayleigh number . . . . .	155
A.12	First unstable mode when only the bottom boundary is a phase change interface . . . . .	157
A.13	Critical Rayleigh number and wavenumber as function of the phase change number . . . . .	158
A.14	Heat flux coefficient as a function of the bottom phase change number and Nusselt number as a function of Rayleigh number for different values of $\Phi^-$ . . . . .	158
A.15	Mean temperature coefficient as function of the bottom phase change parameter . . . . .	159
A.16	Finite amplitude solution for $\Phi^- = 10^{-2}$ , $\epsilon = 5.58$ and a non-penetrating boundary condition at the top. . . . .	160
B.1	Velocity and temperature of translation mode . . . . .	173
B.2	Convection modes with two phase change boundaries . . . . .	174
B.3	Thermal structure with two phase change boundaries . . . . .	175
B.4	Convection patterns with two phase change boundaries from a random noise . . . . .	177

B.5	Heat transfer efficiency with two phase change boundaries . . . . .	178
B.6	Convective patterns with one phase change boundary . . . . .	180
B.7	Convection patterns with phase change at the bottom . . . . .	181
B.8	Heat transfer efficiency with phase change at the bottom . . . . .	182
B.9	Heat and mass transfer with phase change at the bottom . . . . .	183
B.10	Heat flux as a function of solid mantle thickness . . . . .	187

## LIST OF FIGURES

---

# List of Tables

5.1	Dimensionless parameters for the Top Magma Ocean evolution. . . .	81
5.2	Dimensionless parameters for the Basal Magma Ocean evolution. . .	87
5.3	Dimensionless parameters for the dynamics of the solid. . . . .	92
6.1	Symbols used in the EPSL paper . . . . .	99
7.1	Parameters used for the long-term simulation . . . . .	123